Active species identification of iron-based homogeneously and heterogeneously catalyzed reactions

Dissertation

Vorgelegt von

Roland Schoch

Fakultät für Naturwissenschaften
Universität Paderborn

Zur Erlangung der Würde eines
Doktors der Naturwissenschaften (Dr. rer. nat.)
im Department Chemie

2017

Promotionskommission

Prof. Dr. Jan Paradies	Vorsitz
Prof. Dr. Matthias Bauer	Erstgutachter
Prof. Dr. Wolfgang Kleist	Zweitgutachter
Prof. Dr.-Ing. Hans-Joachim Warnecke	

Einreichung:	31. Mai 2017
Verteidigung:	12. Juli 2017

Ich bin immer noch verwirrt, aber auf einem höheren Niveau.

Enrico Fermi

EIDESSTATTLICHE ERKLÄRUNG

Hiermit versichere ich, die vorliegende Arbeit selbständig angefertigt und keine anderen als die von mir angegebenen Hilfsmittel verwendet zu haben. Wörtliche und sinngemäße Zitate wurden als solche gekennzeichnet und die Genehmigungen zur Veröffentlichung der urheberrechtlich geschützten Publikationen wurden eingeholt.

PADERBORN, 26. MAI 2017   ROLAND SCHOCH

ABSTRACT

Precious metal-based catalyst systems have dominated the market over the last decades, due to their superior catalytic performance. Since economic and ecologic circumstances recently changed, a replacement of noble metals by non-precious alternatives gets inevitable. Because of its non-toxicity, availability and stable low price, iron came to the fore.

In this work, iron-based catalysts in homogeneous cross-coupling reactions and in heterogeneous carbon monoxide oxidation were subject of investigation. In both applications multiple analytical techniques were used to gain insights into the working principle of the respective catalysts. Standard techniques, like UV/Vis-, Raman- and Mößbauer spectroscopy, X-ray powder diffraction and specific surface area determination according to the BET method, were combined with X-ray absorption fine structure spectroscopy. Thereby, information about oxidation state, coordination geometry, local and electronic structure of iron could be obtained - independent on the state of aggregation of the sample.

For cross-coupling reactions, this information enables the identification of the catalytically active species by investigation of the activation process. During this process, the iron precursor is reduced and iron in the oxidation state of +I could be observed acting as catalytically active center. Furthermore, originating from these findings the clarification of the reaction mechanism was possible by in-operando spectroscopy.

In case of application in carbon monoxide oxidation, model catalysts were synthesized and compared in their structure as well as in their catalytic activity to obtain a correlation between theses parameters. One of the catalysts was prepared by impregnation of the alumina support material with an iron salt. In the synthesis procedure of the other catalysts, the same iron precursor was reduced by three different metal organic compounds (PhMgBr, $AlPh_3$ and PhLi) to generate iron nanoparticles. Apart from their comparable size, these iron nanoparticles differ in the second metal, which was introduced in the reduction process and is now present on their surface. Alumina as support material was impregnated by these nanoparticles and after calcination at 600 °C the catalysts were applied in carbon monoxide oxidation reaction and showed pronounced differences in catalytic performance. These differences could be correlated to structural variations determined by multiple analytic techniques and structural and electronic requirements could be ascertained, which are a prerequisite for a highly active catalyst.

KURZZUSAMMENFASSUNG

Seit einigen Jahrzehnten dominieren Edelmetallkatalysatoren den Markt aufgrund ihrer überlegenen katalytischen Aktivität. Jedoch fordern sowohl ökonomische als auch ökologische Faktoren zunehmend den Einsatz von alternativen Katalysatoren bestehend aus unedlen Metallen. Eine vielversprechende Alternative bildet Eisen, ein ungiftiges sowie in großen Mengen auf der Erde verfügbares und seit Jahren gleichbleibend günstiges Metall.

Aus diesem Grund wurden in der vorliegenden Arbeit eine homogen katalysierte Kreuzkupplungsreaktion und die heterogen katalysierte Kohlenstoffmonoxidoxidation an Eisenkatalysatoren untersucht. In beiden Anwendungsgebieten wurden durch Kombination mehrerer analytischer Methoden neuartige Einblicke in die Arbeitsweise der jeweiligen Katalysatoren erhalten. Um dies zu erreichen, wurden Standardtechniken wie UV/Vis-, Raman- und Mößbauerspektroskopie, die Bestimmung der spezifischen Oberfläche sowie Röntgenpulverdiffraktometrie mit röntgenabsorptionsspektroskopischen Untersuchungen am Synchrotron kombiniert. Dadurch wurden unabhängig vom Aggregationszustand Informationen über den Oxidationszustand, die Koordinationsgeometrie, die lokale und die elektronische Struktur des Eisens erhalten.

In Kreuzkupplungsreaktionen ermöglichten diese Informationen eine Identifikation der katalytisch aktiven Spezies durch Untersuchung der Aktivierungsprozesse am Präkatalysator. Während dieses Vorgangs wurde die Eisenvorstufe mittels einer Grignardverbindung reduziert wobei Eisen in der Oxidationsstufe +I als katalytisch aktive Spezies bestimmt werden konnte. Des Weiteren gelang es ausgehend von diesen Erkenntnissen durch in-operando Spektroskopie den Reaktionsmechanismus zu formulieren.

Des Weiteren wurden Katalysatoren zur Oxidation von Kohlenstoffmonoxid hergestellt und ihre jeweilige Struktur mit der katalytischen Aktivität korreliert. Einer dieser Katalysatoren wurde durch Imprägnierung des Aluminiumoxidträgers mit einem Eisensalz synthetisiert. Im Präparationsverlauf der anderen drei Katalysatoren wurde das gleiche Eisensalz durch drei unterschiedliche Metallorganyle (PhMgBr, $AlPh_3$, PhLi) reduziert, um Eisennanopartikel zu erzeugen. Neben ihrer vergleichbaren Größe unterscheiden sich die Nanopartikel in ihrem Zweitmetall, das während des Reduktionsprozesses eingeführt wurde und nun auf der Partikeloberfläche vorhanden ist. Die Nanopartikel wurden ebenfalls auf den Aluminiumoxidträger aufgebracht und nach einer Kalzinierung bei 600 °C in der katalytischen Oxidation von Kohlenstoffmonoxid getestet. Die vier Katalysatoren zeigten stark variierende katalytische Aktivitäten, welche mithilfe der angewendeten analytischen Methoden strukturellen und elektronischen Merkmalen zugeordnet wurden. Somit konnten die Grundvoraussetzungen für einen aktiven Eisenkatalysator ermittelt werden.

Ångstrømquelle Karlsruhe (ANKA)

XAS
- February 03-10 2012
- September 05-10 2012
- May 23-29 2013
- October 27-31 2013
- May 14-17 2014

- June 03-06 2014
- May 19-23 2015
- November 12-14 2015
- February 23-27 2016

Berliner Elektronenspeicherring-Gesellschaft für Synchrotronstrahlung (BESSY II)

- June 13-15 2012
- October 14-22 2012

- July 27 - August 04 2013
- August 25-31 2014

Deutsches Elektronensynchrotron (DESY)

Doris

A1
- March 09-12 2012
- September 17-21 2012

X1
- May 10-15 2012
- September 28 - October 02 2012

PETRA III

P65
- June 02-06 2016
- July 25 - August 02 2016
- September 15-20 2016

European Synchrotron Radiation Facility (ESRF)

BM23
- July 18-24 2012
- September 05-08 2012
- June 12-17 2016

BM25A
- December 05-09 2013
- July 09-14 2014

ID26
- June 19-27 2012
- July 18-24 2012
- February 21-26 2013
- March 25 - April 01 2013
- November 13-19 2013
- April 14-21 2015

Publications in journals

1. M. Bauer, R. Schoch, L. Shao, B. Zhang, A. Knop-Gericke, M. G. Willinger, R. Schloegl, D. Teschner: "Structure-Activity Studies on Highly Active Palladium Hydrogenation Catalysts by X-ray Absorption Spectroscopy", *J. Phys. Chem. C* **2012**, *116*, 22375-22385.

2. M. A. Gotthardt, A. Beilmann, R. Schoch, J. Engelke, W. Kleist: "Post-synthetic immobilization of palladium complexes on metal-organic frameworks - a new concept for the design of heterogeneous catalysts for Heck reactions", *RSC Advances* **2013**, *3*, 10676-10679.

3. E. Suljoti, R. Garcia-Diez, S. I. Bokarev, K. M. Lange, R. Schoch, B. Dierker, M. Dantz, K. Yamamoto, N. Engel, K. Atak, O. Kühn, M. Bauer, J.-E. Rubensson, E. F. Aziz: "Direct Observation of Molecular Orbital Mixing in a Solvated Organometallic Complex", *Angew. Chem. Int. Ed.* **2013**, *52*, 9841-9844; "Direkte Untersuchung von Orbitalwechselwirkungen in gelösten metallorganischen Komplexen", *Angew. Chem.* **2013**, *125*, 10024-10027.

4. R. Schoch, W. Desens, T. Werner, M. Bauer: "X-ray Spectroscopic Verification of the Active Species in Iron-Catalyzed Cross-Coupling Reactions", *Chem. Eur. J.* **2013**, *19*, 15816-15821.

5. K. S. M. Salih, S. Bergner, H. Kelm, Y. Sun, A. Grün, Y. Schmitt, R. Schoch, M. Busch, N. Deibel, S. Bräse, B. Sarkar, M. Bauer, M. Gerhards, W. R. Thiel: "Trinuclear Diamagnetic Nickel(II) Complexes with Bridging 3-Arylpyrazolato Ligands", *Eur. J. Inorg. Chem.* **2013**, 6049-6059.

6. E. Keceli, M. Hemgesberg, R. Grünker, V. Bon, C. Wilhelm, T. Philippi, R. Schoch, Y. Sun, M. Bauer, S. Ernst, S. Kaskel, W. R. Thiel: "A series of amide functionalized isoreticular metal organic frameworks", *Microporous and Mesoporous Mater.* **2014**, *194*, 115-125.

7. M. A. Gotthardt, R. Schoch, T. S. Brunner, M. Bauer, W. Kleist "Design of Highly Porous Single-Site Catalysts through Two-Step Postsynthetic Modification of Mixed-Linker MIL-53(Al)", *ChemPlusChem* **2014**, *80*, 188-195.

8. R. Schoch, H. Huang, V. Schünemann, M. Bauer: "A New Iron-Based Carbon Monoxide Oxidation Catalyst: Structure-Activity Correlation", *ChemPhysChem* **2014**, *15*, 3768-3775.

9. M. A. Gotthardt, R. Schoch, S. Wolf, M. Bauer, W. Kleist: "Synthesis and characterisation of bimetallic metal-organic framework Cu-Ru-BTC with HKUST-1 structure", *Dalton Trans.* **2015**, *44*, 2052-2056.

10. R. Schoch, M. Bauer: "Pollution Control Meets Sustainability: Structure-Activity Studies on New Iron Oxide-Based CO Oxidation Catalysts", *ChemSusChem* **2016**, *9*, 1996-2004.

Talks

1. R. Schoch, M. Bauer: "CO oxidation on iron model catalysts: Insights into the mechanism by X-ray absorption and X-ray emission spectroscopy", EuropaCat XI, Lyon (France), September 3, 2013.

2. R. Schoch, M. Bauer: "A new iron based CO oxidation catalyst: Structure-activity correlation", 24th North American Meeting (NAM) of the Catalysis Society, Pittsburgh (USA), June 17, 2015.

Poster presentations

1. R. Schoch, M. Bauer: "CO oxidation on iron model catalysts: Insights into the mechanism by X-ray spectroscopy", CaSuS, Braunfels, June 26-28, 2012.

2. R. Schoch, M. Bauer: "CO oxidation by supported iron catalysts: A multidimensional spectroscopic approach", Bunsentagung, Karlsruhe, May 9-11, 2013.

3. R. Schoch, M. Bauer: "CO oxidation on iron model catalysts: Insights into the mechanism by X-ray absorption and X-ray emission spectroscopy", EuropaCat XI, Lyon (France), September 1-6, 2013.

4. R. Schoch, M. Bauer: "Entwicklung und mechanistische Untersuchung neuer Fe-basierter Katalysesysteme für umweltrelevante CO-Oxidationsreaktionen", Stipendiatentreffen der Carl-Zeiss-Stiftung, Oberkochen, 2013.

5. R. Schoch, M. Bauer: "CO oxidation on iron model catalysts: Insights into the mechanism by X-ray spectroscopy", 46. Jahrestreffen Deutscher Katalytiker, Weimar, March 13-15, 2013.

6. R. Schoch, M. Bauer: "X-ray spectroscopy and metal organic frameworks", Deutsche Zeolithtagung, Paderborn, February 26-28, 2014.

7. <u>R. Schoch</u>, M. Bauer: "The active species in iron cross-coupling reactions by X-ray absorption spectroscopy", 47. Jahrestreffen Deutscher Katalytiker, Weimar, March 12-14, 2014.

8. <u>R. Schoch</u>, M. Bauer: "A new iron based CO oxidation catalyst: Structure-activity correlation", XAFS16, Karlsruhe, August 23-28, 2015.

9. <u>R. Schoch</u>, M. Bauer: "Valence-to-core X-ray emission as powerful tool to elucidate structural details of transition metal complexes", Koordinationschemie-Tagung, Paderborn, March 22-24, 2015.

10. <u>R. Schoch</u>, M. Bauer: "A new iron based CO oxidation catalyst: Structure-activity correlation", 48. Jahrestreffen Deutscher Katalytiker, Weimar, March 11-13, 2015.

11. <u>R. Schoch</u>, M. Bauer: "Iron based CO oxidation catalyst: A structure-activity correlation", 26th ATC 2017: Industrial Inorganic Chemistry, Frankfurt a. Main, February 23 & 24, 2017.

12. <u>R. Schoch</u>, M. Bauer: "Iron based CO oxidation catalyst: A structure-activity correlation", 50. Jahrestreffen Deutscher Katalytiker, Weimar, March 15-17, 2017.

TABLE OF CONTENTS

Page

CHAPTER

<div align="right">

1

</div>

<div align="right">

INTRODUCTION

</div>

1.1 Outline

K nowledge about the active species is a crucial step for the improvement and aimed design of highly active catalysts. Due to a dominant position of precious metal-based catalysts, there is only rather negligible knowledge about the active species and processes during reactions of non-precious metal-based catalysts. Even though precious metals show a superior catalytic activity, there are a number of reasons why precious metals may have to be replaced in the next years for economical and ecological causes. These circumstances call for alternative catalyst systems. Since non-precious metals exhibit a smaller catalytic activity than current precious metal-based systems, an all the better understanding of the reaction mechanisms and structural requirements, that distinguish a good catalyst from an insufficient one, have to be gained. This was neglected in the past years, which is why in the presented work X-ray absorption fine structure spectroscopy (XAFS) was applied in combination with more common techniques like (diffuse reflection) UV/Vis, Raman and Mößbauer spectroscopy, X-ray powder diffraction (XRD) and specific surface area determination. Through application of these analytical methods, the active species of iron-based catalysts could be identified in homogeneous as well as heterogeneous reactions. In homogeneous catalysis, iron was applied as catalyst in cross-coupling reactions, while as a heterogeneous model reaction the oxidation of carbon monoxide was used.

Because of this rather exceptional combination of applications, this thesis is divided into two subdivisions: iron applied in homogeneous catalysis (chapter 2) and also in heterogeneous catalysis (chapter 3). This partition is also reflected in this chapter, since in addition to catalysis in general and the justification why iron is used as substitute of precious

metals, an overview on homogeneous iron catalyzed cross-coupling reactions as well as on heterogeneous catalyzed emission control is given. The reason for the application of iron as catalyst in two completely different fields during this thesis lies in their preparation method. For homogeneous cross-coupling reactions, a threevalent iron precursor was reduced by a Grignard compound forming an iron +I species, which was proved to be the starting point of the cross-coupling reaction mechanism cycle. The preparation of the heterogeneous catalyst is based on this reduction process, since addition of an excess of reducing compound leads to iron nanoparticles. Iron clusters were also obtained through application of organometallic reducing agents based on lithium and aluminum as an alternative to Grignard reagent. These small particles were used as defined initial species for the synthesis of alumina-supported catalysts with varying loadings in carbon monoxide oxidation. In addition, one catalyst was synthesized by impregnation of the support with iron precursor directly. All prepared catalyst systems exhibit different activities, which could be assigned to structural characteristics. Thus, a correlation between structure and catalytic performance as well as the identification of the catalytically active species could be gained.

1.2 Catalysis

The development of catalysts and their targeted application in chemical syntheses and environment protection was undoubtedly one of the greatest economical successes in the last centuries. Today, our daily life is inconceivable without products, which were manufactured using catalytic processes - be it in the fabrication of fuels, pharmaceuticals, cosmetics, clothes (e.g. synthetic fibers), building materials or in food processing. Therefore, a rough overview over the beginnings and the evolution of catalysis will be given in the following.

1.2.1 Historical review

Catalytic reactions were already used in ancient times, for example in the fermentation of sugar for ethanol production or in the formation of acidic acid from ethanol, although knowledge about the precise processes (biocatalysis via enzymes) was lacking[1]. During the centuries, discoveries based on catalytic processes were made regularly, which sometimes even found their way into daily live. One early example is the Döbereiner's lamp from 1823, where the reaction of zinc metal and sulfuric acid was used to produce hydrogen[2]. The hydrogen was lead over a platinum sponge, on which surface the reaction of hydrogen with atmospheric oxygen was catalyzed. Through the formed heat excessive hydrogen could be ignited to produce a flame. In 1835, Jöns Jacob Berzelius formulated a first description of the phenomenon catalysis, where he covered a number of reactions that only proceed in the presence of a substance which remains unaffected. In case of the oxidation of hydrogen

in Döbereiner's lamp he suggested, that the platinum sponge would awake the "dozing" gases[3]. For the first time he used the term "katalysis", which he borrowed from the Greek word for "to untie". This shows, that he considered the bond breaking as the crucial step. He explained the formulation "catalytic power" as follows[4]:

"This is a new power to produce chemical activity belonging to both inorganic and organic nature, which is surely more widespread than we have hitherto believed and the nature of which is still concealed from us. When I call it a new power, I do not mean to imply that it is a capacity independent of the electrochemical properties of the substance. On the contrary, I am unable to suppose that this is anything other than a kind of special manifestation of these, but as long as we are unable to discover their mutual relationship, it will simplify our researches to regard it as a separate power for the time being. It will also make it easier for us to refer to it if it possesses a name of its own. I shall therefore, using a derivation well-known in chemistry, call it the catalytic power of the substances, and the decomposition by means of this power catalysis, just as we use the word analysis to denote the separation of the component parts of bodies by means of ordinary chemical forces. Catalytic power actually means that substances are able to awaken affinities which are asleep at this temperature by their mere presence and not by their own affinity."

60 years later (1895), Friedrich Wilhelm Ostwald observed more profound, that a catalyst cannot start a chemical reaction which is not taking place without it and a catalyst accelerates a chemical reaction without influencing its equilibrium. Furthermore, he was able to include processes like the release of supersaturation, catalysis in homogeneous and heterogeneous mixtures and by enzymes in the phenomena "catalysis"[5]. Like Justus von Liebig before him, he compared a catalyst with oil on a machine or with a whip on a tired horse[6]. For his fundamental findings, Friedrich Wilhelm Ostwald was awarded with the Nobel Prize for chemistry in 1909[7]. Already in 1898 Rudolf Knietsch realized Ostwald's findings in an industrial process. The employee of BASF, applied a vanadium oxide based catalyst for the production of sulfuric acid, the so-called "contact process"[3]. In 1903, Fritz Haber started to search a way to produce ammonia from its elements and succeeded in 1909 in a laboratory scale[8]. Due to the poor yield and a catalyst material, which was not suitable for a large industrial application (osmium), Haber won "Badische Anilin- und Sodafabrik" (BASF) to this process. In the following two years, Alwin Mittasch under the guidance of Carl Bosch tested about 3000 different catalysts in 6500[9] to 20.000[3] experiments (numbers differ depending on source). Mittasch found an iron oxide sample from Sweden as surprisingly active and designed a catalyst, which is in main features still used today. In 1908, BASF applied for a patent[10] and in 1913 the first industrial plant started operation[8]. Already in 1909, Friedrich Wilhelm Ostwald found a way to use ammonia for the synthesis of nitric acid by application of a platinum/rhodium net as catalyst[3].

All these early applications are based on heterogeneous catalysts, which means that the used catalyst has another state of aggregation than the reactants and products. Important processes using homogeneous catalysts, where the catalyst exhibits the same state of aggregation, were developed only few decades later. As a starting point the development of hydroformylation by Otto Roelen in 1938 can be considered - even though he did not realize, that he discovered a homogeneously catalyzed reaction[3]. Roelen helped to develop as coworker of Franz Fischer and Hans Tropsch the production of alkanes and alkenes from synthesis gas (H_2 and CO) using iron and cobalt catalysts, when he realized that after addition of ethylene to the synthesis gas, propanal is formed in higher yield. In fact, cobalt formed with hydrogen and carbon monoxide a cobalt-cabonylhydride complex in the reactor, which acts as active species in the synthesis of aldehydes. Roelen applied 1938 for a patent and was afterwards involved in the implementation of this process at Hoechst. During the 1950s, Sir Geoffrey Wilkinson synthesized a rhodium-based complex, which was successfully applied as catalyst for hydrogenation, hydroformylation and hydrosylation in an industrial scale[3]. Also in 1950s, Karl Ziegler applied mixed catalysts, consisting of a transition metal complex and an alkyl aluminum compound, in ethene polymerization reaction under mild conditions (atmospheric pressure). Giulio Natta successfully adapted this "Ziegler catalyst" for the polymerization of propene in the same year. Before the development of "Ziegler-Natta-catalysts", these polymerizations required pressures between 2000 and 3000 bar[3].

In addition to the definitions made hitherto, it was assumed, that a catalyst remains unaffected after reaction. Today it is known, that a catalyst forms chemical bonds to the reactants during reaction process, which are loosened after formation. This would have no influence on an ideal catalyst, but in nature competitive reactions take place, which change a catalyst until deactivation. In some cases a catalyst can be regenerated but often it has to be exchanged. Therefore, the stability and with this the time a catalyst can be used represents an important factor especially for industrial implementation[9,11,12].

By application of catalysts the amount of energy necessary for a reaction progress can be decreased significantly due to a reduction of the activation energy. Furthermore, a suited catalyst can affect the selectivity of a reaction, which leads to a higher yield of the desired product[13,14]. This allows the preparation of a wide product range generated from the same reactants, simply by variation of the catalyst. One example, which demonstrates the influence of a catalyst, is the reaction of hydrogen and carbon monoxide (so-called synthesis gas). As can be seen in figure 1.1, significant different products can be generated by the exchange or the combination of active metals[1,3]. Another approach to influence product selectivity is the ligand modification of a complex as demonstrated by the example of nickel catalyzed cyclooligomerization of butadiene, shown in figure 1.2. In dependence of the used ligands, different ring sizes can be obtained. Both examples show, that catalysis provides the ability to synthesize a desired product, whereas unwanted by-products were avoided or
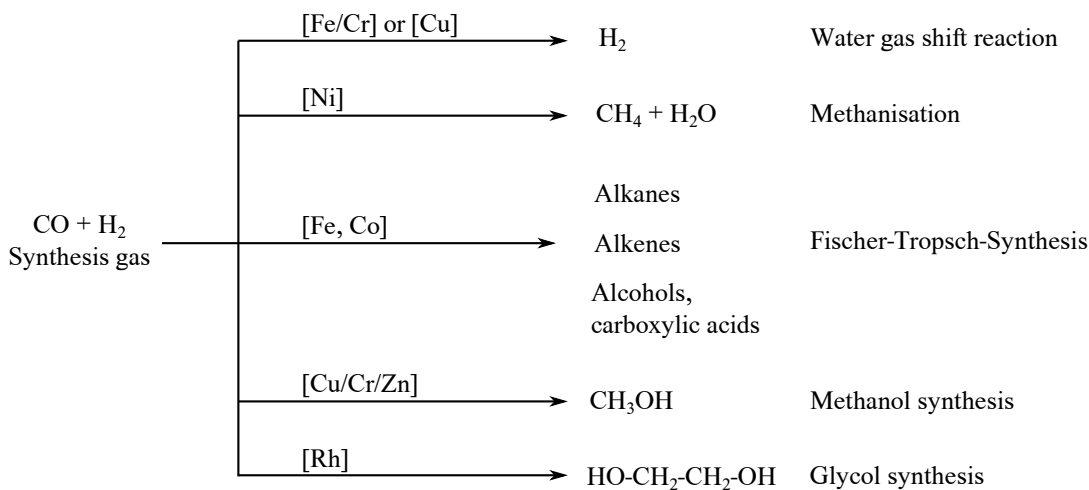
FIGURE 1.1. Influence of the catalyst on the obtained product at the example of synthesis gas[1,3].
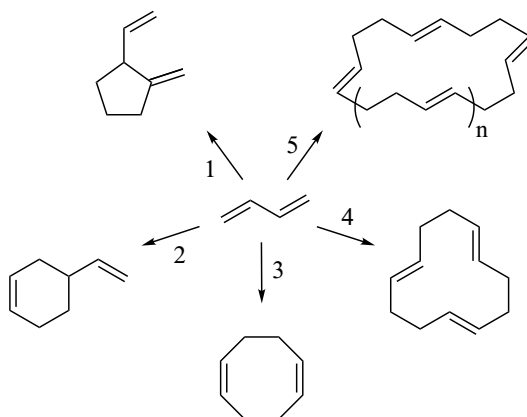
FIGURE 1.2. Influence of the ligand system on the obtained product at the example of nickel catalyzed cyclooligomerization of butadiene. (1) [NiCl(o−tolyl)(PEt$_3$)$_2$], (2) [Tricyclohexylphophine] (PCy$_3$), (3) [Triphenylphosphite] (P(OPh$_3$)), (4) [nickel bis(acrylonitrile) + triethylaluminum (AlEt$_3$)], (5) Allyl complexes[3].

at least suppressed. The points mentioned so far - increased energy efficiency, maximized product yield, higher selectivity, which means a prevention of waste - together with the possibility to use renewable feedstocks due to the feasibility to use new synthesis routes show, that catalysis fulfills all requirements to be considered as "green chemistry"[15].

The importance catalysis gained in the following years is also reflected in the number of Nobel Prizes, that were awarded for discoveries in this field. Since Ostwald in 1909 about 17 further researchers were awarded for their work in the development of theoretical models, diverse applications and the inventions of methods for the investigation of catalysts[16].

1.2.2 Classification

Due to their mode of action, catalysts are divided according to their physical state, in which they are working. This results in two main groups: heterogeneous and homogeneous catalysts. In addition, transition forms are existing - for example homogeneous catalysts attached to solids (also termed as immobilized) and biocatalysts (enzymes)[1,8,11,17]. A more specified division is given in the following and in figure 1.3.
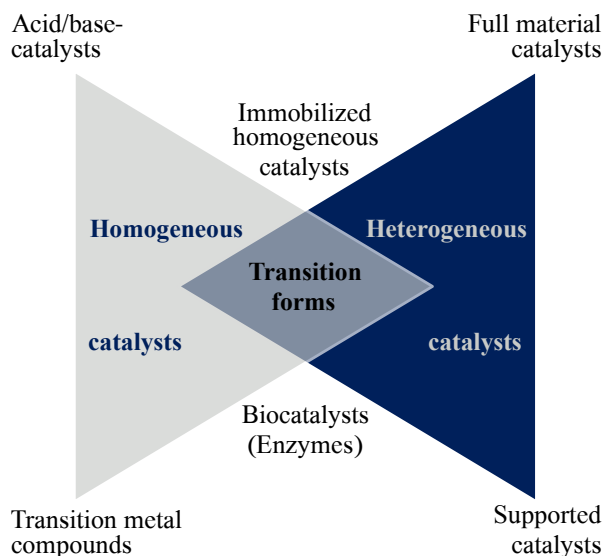
FIGURE 1.3. Division of catalysts in homogeneous, heterogeneous catalysts and transition forms.

Heterogeneous and homogeneous catalysis represents complimentary positions in chemical industry. Most major industrial products are fabricated via heterogeneous catalysts, e.g. gasoline, ammonia, sulfuric acid or nitric acid. Homogeneous catalysts are mainly used for the production of fine chemicals, pharmaceuticals and agrochemicals - products with smaller production values and more complex chemical structures[3]. Whereas in heterogeneous catalysts a phase boundary is present between the catalyst material and the reactants and solely surface atoms are catalytically active, homogeneous catalysts are in the same phase like the reactants. Therefore, homogeneous catalysts have a higher degree of disposition, due to the fact that every single atom is accessible and catalytically active. With this, homogeneous catalysts show a higher catalytic performance referred to the applied amount of metal. Furthermore, interactions between catalyst and reactant molecule are significantly simplified. Due to mobility of molecules a spacial approach from all directions is possible and there is a higher probability for collisions between substrate molecules[18,19]. In contrast to heterogeneous catalysts, a reaction at a homogeneous catalyst center does not lead to a blockade of a catalytically active center nearby, which allows low catalyst concentrations and mild reaction conditions. Homogeneous catalyzed reactions are mainly kinetically controlled

in contrast to reactions at heterogeneous catalysts, which are mainly diffusion-controlled and occur at structurally defined centers. These facts in combination with the application of various spectroscopic methods allow the determination of the reaction mechanisms and with this, the design of catalysts with high product selectivities[1].

Apart from these positive properties of homogeneous catalysis, there are also some considerable disadvantages. In industrial applications higher temperatures are used for reactions to increase the reaction velocities and with this the throughput of a product. Because of the small temperature tolerance of metalorganic complexes, homogeneous catalyzed reactions are limited to working temperatures below 200 °C[1]. The major problem in application of homogeneous catalysts lies in their separation from the product. Here, very cost-intensive and energy demanding methods like distillation, crystallization, precipitation, liquid-liquid-extraction or rather complex methods like ion exchange processes have to be applied[3]. In comparison, heterogeneous catalysts can be separated more easily by filtration, centrifugation or by application of fixed bed catalysts[1,18,20].

There are numerous approaches to combine the advantages of homogeneous catalysts in activity, selectivity and modifiability with the easy way of separation and stability of heterogeneous catalysts[18,19]. The majority of these approaches is based on the idea to use metalorganic complexes, that are highly active in homogeneous applications, immobilized on solid supports with high specific surface areas. One of the most prominent examples for these solid supports are zeolites - microporous aluminosilicates[21,22]. Here, the catalytically active species can for example be introduced into the zeolite pore system by adsorption of a suitable precursor followed by transformation into the desired catalytic center (ship-in-a-bottle synthesis)[23]. Another approach is the immobilization of molecular complexes on solid surfaces[24], whereby inorganic (e.g. silica gels or oxides)[25,26] as well as organic (e.g. monolithic porous polymers)[27–29] supports are used. Also biological catalysts can be immobilized to increase their robustness and recyclability[30–32]. When coordination polymers based on metals and bi- or trivalent aromatic carboxylic acids were described for the first time[33], they were meant to be used in gas purification[34], separation[35] and in gas storage applications[35–37], due to their porous structure on a molecular scale. But because of their enormous specific surface area induced by their unique molecular structure[38,39] and their diffusional properties[40,41], metal organic frameworks (MOFs) have also a high potential in catalysis. There are mainly three approaches, how MOFs can be utilized as catalysts: Firstly, they can be used as support for a catalytically active species[42–44]. Secondly, transition metals can be introduced by coordination on functional groups present in the linker molecules after MOF synthesis (post-synthetic modification)[45–48]. Thirdly, the metal which builds up the scaffold shows in several MOFs free coordination sites, which can also act as catalytically active centers[49,50]. Unfortunately, in most cases the activity decreases when a homogeneous catalyst is fixed onto a support[20].

Because of these facts heterogeneous catalysts are widely used in industrial processes[14] and the market share of homogeneous catalysts is estimated to only 10-15 %[20]. In general, the market for catalysts has become enormous in the last decades. In about 90 % of all chemical processes catalysts were applied[51]. In table 1.1 several processes and the used catalysts are listed exemplarily. Beside applications in petrochemical industry, like petroleum refinement or natural gas processing, and in chemical industry, heterogeneous catalysts were also used in more unapparent branches like food industry and for the production of pharmaceuticals. The probably most prominent application in society undoubtedly is in exhaust gas reduction of automobiles. But catalyst application in environmental protection is also realized in stationary setups, e.g. at coal-fired or gas power plants[8,11,12,52,53]. Furthermore, catalysts are also necessary in emerging areas like fuel cells[54–56], green chemistry[57–59], nanotechnology[60] and biorefining respectively biotechnology[61–65]. The worldwide trade volume of solid catalysts is estimated to about 15 billion US $[3,20].

TABLE 1.1. Examples for catalyzed industrial processes and the used catalysts at a glance.

Process	Catalyst
Sulfuric acid	V[66]
Ammonia	α-Fe[17]
	Recently: Ru/C-based[67–69]
Nitric acid	Pt/Rh- resp. Pt/Pd/Rh-alloy[70]
Hydrodesulfurization	Co/Mo- or Co/Ni-oxides[71]
Hydrocracking	Pt[72]
Isomerization	Pt[73,74]
Three-way-catalyst	Pt, Rh, Pd[8]

1.3 Exchange of noble metals

The majority of catalysts which are used in industrial applications are based on noble metals as active species, which can also be seen in table 1.1. Noble metals undisputed show the highest catalytic activities and best performances in a large number of chemical reactions. However, the use of noble metals leads to constantly increasing problems: First of all, noble metals are, compared to other metals, rare in the earth's crust (see figure 1.4)[75]. Secondly, the extraction is complex and is associated with tremendous power requirement and highly reactive chemicals[76]. These two points always result in high cost for noble metals. Thirdly, the prices for noble metals even increased in the last decades, inter
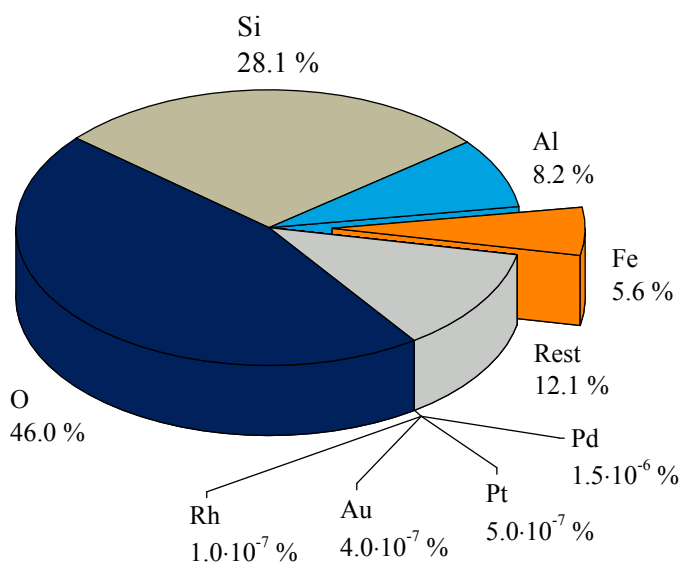
FIGURE 1.4. Occurence of elements in earth's crust with focus on iron compared to selected noble metals[75].

alia induced by the growing demand in other industrial fields, like electronic industry[77], but also in the field of renewable energy (fuel cells[78,79], biomass conversion[80,81]), as shown in figure 1.5[82]. Finally, there are still discussions about the biological compatibility of noble metals, when released into the environment[83–86]. These economical and ecological drawbacks are compensated to a certain extent by the considerable catalytic activity of noble metals. Through modification of the catalyst structure, a larger surface area and with this a higher amount of accessible catalyst sites can be achieved. This leads to an increased efficiency of the catalyst and allows the application of a smaller amount of noble metals as active species to obtain equal performance. However, a full compensation of the price increase with these methods is not possible[87].

Consequently, new catalyst materials have to be developed based on metals, that are available in a sufficient amount in the earth's crust, simply extractable without high energy effort and easily recyclable. Furthermore, these metals have to be ecologically harmless or better: biocompatible - to avoid contamination of the environment. Beside manganese, copper and cobalt, iron seems to be a promising alternative to noble metals. Iron is the second most abundant metal in earth's crust (see figure 1.4)[75], its extraction, refinement and recycling is relatively straightforward and is not connected to the use of aggressive chemicals or high energy requirement[76]. Since iron as refined metal is not traded at the stock exchange, it is no subject of speculative fluctuations[3]. This kept the price very stable at a low level in the last years, as shown by means of the share prices for iron ore in figure 1.5. The mass fraction of iron in iron ore is depending on its origin about 45 wt%[88], therefore, the share price of

9
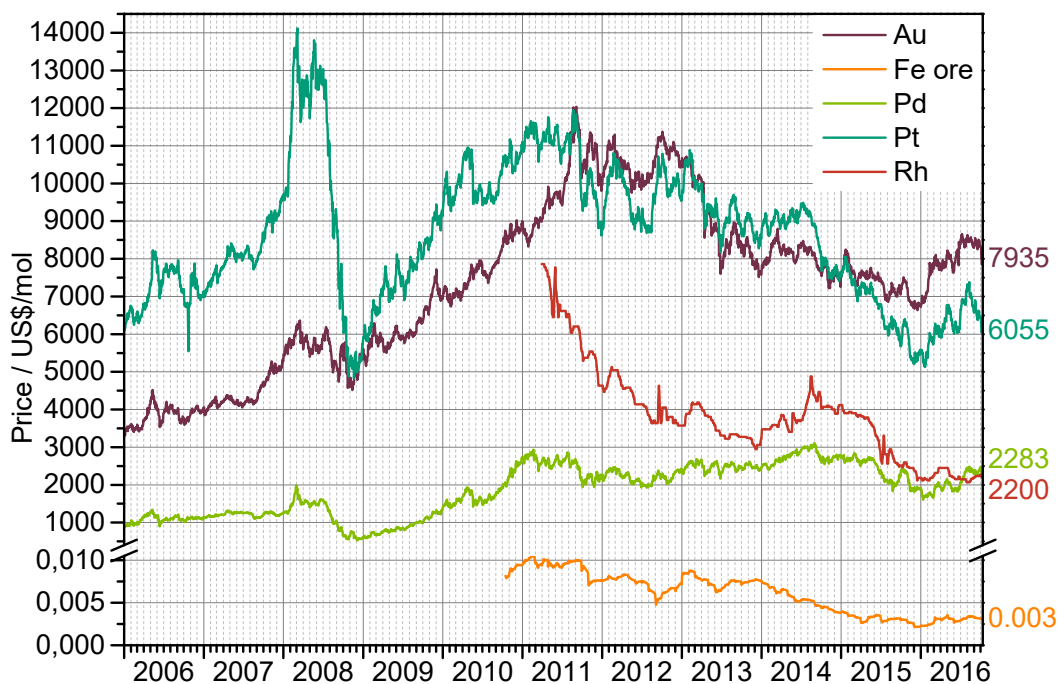
FIGURE 1.5. Molar share prices of noble metals (Au, Pd, Pt, Rh) compared with Fe ore in the last decades[82].

iron ore can at least be considered as an indicator. Furthermore, iron is absolutely non-toxic - even biocompatible, since iron-containing enzymes are essential for a various biological systems and functions[89–92]. Unfortunately, the catalytic activity of iron significantly lags behind the activity of noble metals so far. To determine the catalytic performance of a catalyst, the turnover-frequency (TOF) is one of the most significant values, since it gives the number of catalyzed conversions per number of catalyst centers and time[93].

$$TOF = \frac{number\ of\ conversions}{number\ of\ catalyst\ centers \cdot time} \quad \left[\frac{1}{s}\right]$$

Using this number, a performance comparison of different catalysts is possible. Here, a Pt/Pd/Rh-based system typically used in three-way catalysts should be compared with the activity of commercial available iron oxide nanoparticles (NANOCAT®) in CO oxidation. Since TOFs of a particular three-way catalyst are not published, probably for competitive reasons, typical values had to be used for calculation, which were found in the *Handbook of Heterogeneous Catalysis*[94]. Therefore, the exhaust gas of a spark ignition engine at 2000 rpm with 18 Nm and 425 °C is used exemplary. At these conditions a total exhaust gas flow of 16.53 $\frac{l}{s}$ and a CO concentration of 0.55 vol% is measured. With the presumption of full removal of CO at this temperature (ideal operating temperatures for three-way catalysts are between 350-650 °C[11]) and consideration of CO as ideal gas, 4.059 $\frac{mmol}{s}$ are oxidized. A typical catalyst, which will here be used as an example, has a volume of 1.24 l and a total

10

precious metal loading of 2.232 g (1.8 $\frac{g}{l}$). The metal atoms are highly distributed, which allows the assumption, that every atom is catalytically active[94]. A typical composition rate referred to weight of Pt:Pd:Rh is 1:16:1, whereby Rh is not active in CO oxidation (but important for NO_x removal)[94]. This allows a calculation of the molar amount of Pt and Pd. Relating the amount of oxidized CO per second on the quantity of Pt and Pd centers gives a turnover frequency of 0.21 $\frac{1}{s}$.

As example for an iron-based catalyst, commercial available Fe_2O_3 nanoparticles NANOCAT® from MACH I, Inc.® are used. These nanoparticles have an average particle size of 3 nm and with 250 $\frac{m^2}{g}$ a relatively high specific surface area. Hajaligol et al. investigated these nanoparticles with respect to their catalytic activity in CO oxidation and found full conversion at 350 °C[95] with a total gas flow of 1000 $\frac{ml}{min}$ and a CO concentration of 3.44 vol%. Together with the assumption that, due to the small particle size, every iron atom is accessible and with this all of the used 50 mg Fe_2O_3 is catalytically active, the calculation of a turnover frequency of 0.08 $\frac{1}{s}$ is possible.

Comparison of the two turnover frequencies shows, that the TOF of the iron-based catalyst (0.08 $\frac{1}{s}$) is about one power of ten smaller than the one of a commercial three-way catalyst (0.21 $\frac{1}{s}$). To achieve the same amount of conversions per second of a three-way catalyst, ten times more iron sites would be necessary. Considering the prices for precious metals and for iron ore, which differ of about six powers of ten (see figure 1.5), the application of a higher amount of iron to achieve a catalyst with the same performance will still be less expensive than the noble metal-based catalyst - even in consideration of the costs for the refinement of iron ore. However, the increased demand of catalytically active metal centers would increase the weight of the catalyst. Nowadays, the weight of an automobile is a very important factor for its conception, since it is directly connected to fuel consumption and to driving performance. Using the three-way catalyst mentioned above as example, 10.766 g iron would have to be used for the catalyst instead of 2.108 g precious metal (Pt, Pd). The repercussion of a weight increase of 8.658 g is relatively negligible.

In the following, iron will be discussed in homogeneous cross-coupling reactions and exhaust gas removal, as two application examples in very essential fields.

1.3.1 Iron in homogeneous catalysis

A comparable situation to exhaust gas removal with respect to the use of precious metals as active species in catalysts can be found in organic synthesis. Catalysis and in particular iron catalyzed processes become more and more relevant - even in industrial processes. As mentioned above, only 10-15 % of all catalytic reactions in industry are catalyzed homogeneously[20]. Whereas heterogeneous catalysts are mainly used for the production of bulk chemicals in huge quantities, homogeneous catalysts are applied in productions of fine and specialty chemicals, where the molecular structure is very demanding, e.g. due

to the incorporation of several functional groups or through the presence of sophisticated steric centers. Additional costs caused through complex catalyst recovery are in this case compensated by high prices for these chemicals. Therefore, homogeneous catalysis is mainly applied for the production of fragrances and flavors, pharmaceuticals and agrochemicals[3].

For the preparation of these in most cases highly complex molecules, a whole arsenal of different reactions have to be applied[3,18]. One of the most important steps in synthesis is the formation of C-C-bonds. These reactions have become a fundamental tool during the last decades[89]. In the majority of C-C-bond formation reactions heavy or precious metals are applied as catalysts. Beside noble metals like palladium, rhodium, iridium or ruthenium, transition metals of the first period like cobalt, nickel, molybdenum or copper are mainly used[3]. The advantages of these metals regarding activity and functional group tolerance are explored extensively and documented in numerous publications[96,97]. Whereas the prices for precious metals like palladium complicate their application and especially an upscale towards industrial standards[98], various toxicity aspects taint the use of heavy metals like e.g. nickel for the production of consumer goods and healthcare products[99]. In addition, structurally complex and with this expensive ligands are usually necessary for the application of these metals as catalysts[89].

Advantages of iron as alternative to precious metals were exhaustively outlined above. In addition to the ecological and economical factors already mentioned, another point has to be stated: Many iron salts used as catalyst precursor are commercially available or their simple synthesis is described in literature[98].

Effective processes were developed in the last few years, which are able to compete with noble metal catalyzed reactions[89,98]. There are numerous fields, where iron is already established as catalytically active compound for C-C-bond formations[98,100]: Besides substitutions and additions, aldol reactions and polymerizations are feasible by application of an iron catalyst as well as isomerizations and rearrangements. Nonetheless, this dissertation will focus on iron-catalyzed cross-coupling reactions.

1.3.1.1 Iron-catalyzed cross-coupling reactions

Within the multifaceted possibilities for generation of carbon-carbon and carbon-heteroatom bonds, cross-coupling reactions facilitated through application of transition metal catalysts have gained an indispensable tool[101]. In general, a nucleophilic organometallic compound (R-M) interacts in a cross-coupling reaction with an electrophilic organic halide (R'-X) under formation of a new carbon-carbon bond (R-R') and of the corresponding metal salt.

$$R-M + R'-X \longrightarrow R-R' + M-X$$
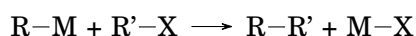
First investigations of an aryl-Grignard compound homo coupling catalyzed by iron were reported by Kharash and Fields already in 1941[102]. After the description of an iron catalyzed vinylation of Grignard reagents with vinyl halides by Tamura and Kochi in

1971[103,104] and the groundbreaking findings of the groups of Corriu[105] and Kumada[106] in the field of nickel-catalyzed cross-coupling reactions in 1972, the interest in iron-catalyzed cross-coupling reactions was awakened. In the following years, the catalyst could be described as an Fe(I)-species, that was formed from the Fe(III)-consisting starting compound through reduction by Grignard reagent[107]. By application of ethylmagnesium bromide a significant amount of ethane and ethylene was formed during reaction. These side-products could be attributed to the presence of β-hydrogen atoms in ethylmagnesium bromide. A first mechanistic proposal was given by Kochi et al. in 1974, as can be seen in figure 1.6.
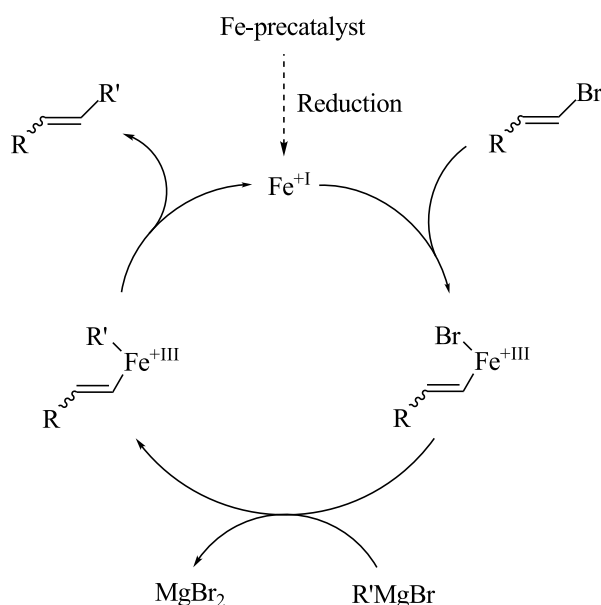
FIGURE 1.6. First mechanism of iron-catalyzed cross-coupling reaction proposed by Kochi et al.[108].

He also reported, that a detailed mechanistic description of the cross-coupling process is difficult, since all intermediates are extremely unstable and in practice nearly impossible to isolate[108–110]. Based on this proposal, Molander et al. extended the application area to aryl Grignard reagents in 1983. Furthermore, they proved that an excess of alkenyl halide, as initially described by Kochi, is not necessary for the reaction[111]. The still limited scope of iron-catalyzed cross coupling reactions was significantly widened by Cahiez and Avedissian, by introduction of *N*-methyl-2-pyrrolidone (NMP) as co-solvent. Highly probable, NMP stabilizes organometallic iron intermediates through coordination, which results in an increase in yield[112]. Numerous reports cover the distinct functional group tolerance of iron-catalyzed cross coupling reactions. Even in presence of esters, enones, ethers, ketones, carbamates, acetals, lactones, alkyl chlorides and protected amines the cross coupling with Grignard reagents proceeds in high yields[113,114]. Free alcohol groups can be tolerated simply by protection through deprotonation - and with this, the generation of the corresponding

magnesium salt[115,116]. This wide functional group tolerance is not connected to a reduced catalytic activity. For example, cross-coupling reactions of vinyl halides proceed chemo- and stereoselective with high yields and nearly independent of the use of vinyl iodides, bromides and chlorides. Furthermore, the configuration of the vinylic double bond has no significant effect. Vinyl-vinyl as well as aryl-vinyl cross-couplings can be achieved in satisfying yields. Reactions with cyclic alkenyl halides and cyclic Grignard reagents can also be carried out with sufficient amount of product[117]. In addition, bromothioethers were reported to be useful electrophiles for the coupling of secondary Grignard compounds[118]. Aryl electrophiles can also widely be used for iron-catalyzed cross-coupling reactions with excellent yields. The range comprises benzene derivatives, substituted with electron-withdrawing groups and many heterocyclic compounds[117].

There are numerous approaches to optimize the coupling protocol to obtain easy to handle reactions with satisfying turnovers. To achieve this, for example coordinating compounds were added to stabilize active intermediates. Through addition of N,N,N',N'-tetramethylenediamine (TMEDA), secondary alkyl halides could be coupled with aryl Grignard reagents, as Nakamura et al. first reported in 2004[119]. This was a groundbreaking discovery, since alkyl electrophiles show a poor reactivity - even with palladium or nickel catalysts[120,121]. This is due to their small driving force to add oxidatively to the metal center and the proclivity of the formed fragment to undergo destructive β-hydrogen-elimination[122–125]. To facilitate the application of palladium or nickel as catalysts, special designed ligands and careful tuning of the reaction conditions are necessary to obtain satisfying yields for the coupling of primary and secondary alkyl electrophiles[126].

In case of iron-catalyzed cross-coupling reactions of primary and secondary halide substrates under mild conditions, the simple iron salt $FeCl_3$, pretreated with amines can be applied, as Bedford et. al reported in 2005[127]. The preliminary treatment was carried out using triethyl-amine, TMEDA and 1,4-diazabicyclo[2.2.2]octane (DABCO or TEDA) and permits β-hydrogen-elimination. Cahiez et al. applied hexamethylenetetramine (HMTA) in combination with TMEDA to facilitate the coupling of primary and secondary bromides and iodides in good to excellent yields[128,129]. By addition of polyethylene glycol (PEG) iron nanoparticles of 7-13 nm in size were stabilized, which were generated in-situ through reduction of $FeCl_3$ with Grignard compound. The yields for the coupling of alkyl halides with aryl Grignard agents are comparable to the reaction conditions without stabilization of the nanoparticles by PEG (4-12 nm) and allow the conclusion, that iron nanoparticles are the catalytic active species in the coupling reaction[130].

Bica and Gärtner developed an advancement, which permits an easy work-up and catalyst recovery procedure[131]. They used an iron-containing ionic liquid, whose hydrophobic nature permits reaction without inert atmosphere and isolation of the catalyst through phase separation followed by decantation.

Another approach for the optimization of the coupling protocol represents the variation of the metal in the organometallic reducing reagent. Iron-catalyzed coupling of organomanganese compounds shows very related reaction profiles. Alkenylation of organomanganese compounds can also be carried out under high chemo- and stereoselectivity[132]. However, the yields and selectivities are generally high, the obtained reaction rates are significantly smaller[133]. The first efficient aryl-aryl coupling was reported by Knochel et al. in 2005. They applied organocopper reagents to suppress homodimerization of the organometallic compound, which increased the amount of the desired aryl-aryl product[134,135]. In contrast, application of triethylaluminum and n-butyllithium leads to no significant formation of product. Boronic acids, stannanes and trialkylzinc compounds as coupling reagents also showed no reaction[136–138]. The explanation for these findings can be ascertained with a look on the reaction mechanism. Various speculations were made about the oxidation state of the catalytically active iron species - from Fe(0) to Fe(+I)[103,104,107–109] and even to "super-ate" complexes consisting of Fe(+II) species[140,141]. Around the year 2000, Bogdanovic et al. reported in a series of papers about the generation of an inorganic Grignard compound, during iron-catalyzed cross-coupling reactions. In course of the formation, iron is inserted into the magnesium-carbon bond and is reduced through homo-coupling of two organic residues. Application of four equivalents of Grignard reagent lead to a cluster species with the formal composition [Fe(MgX)$_2$][142–145]. As further products, alkanes, the corresponding alkenes and the homodimers originating from the Grignard compound were obtained. The formal oxidation state of the iron species is in course of the reduction process decreased to a negative charge, presumably Fe(-II). According to a mechanistic proposal made by Fürstner and Leitner[136,137,139] sketched in figure 1.7, this highly nucleophilic species is subsequently able to add oxidatively to aryl halides, also favored by the absence of stabilizing ligands,
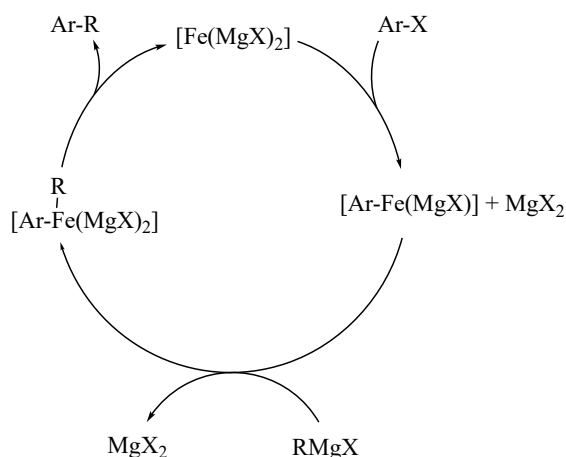
FIGURE 1.7. Re-evaluated mechanistic concept of the iron-catalyzed cross-coupling reaction reported by Fürstner and Leitner[136,137,139].

15

under formation of a zerovalent compound referred to iron. In a next step, the zerovalent iron compound is alkylated by excess of Grignard agent followed by a reductive coupling of the organic ligands forming the product and regeneration of the propagated Fe(-II) species. Apart from the proposed oxidation state of the active species, these findings are in large parts identical to the reduction process reported by Smith and Kochi in 1976[107].

Direct spectroscopic investigations of the active species are complicated through the extremely high reactivity, the paramagnetic character and the thermal instability of the iron species, which results in rapid aging[139]. Through different experimental approaches evidence for the scenario proposed by Fürstner and Leitner[136,137,139] could be gained. Zerovalent iron as catalytically active species could be ruled out by application of Fe(0) species as catalyst[146,147]. In this approach nearly no reaction was observed comparing to the application of reduced catalyst system. Another evidence for the proposed mechanism was obtained by the observation that finely dispersed Fe(0) particles slowly dissolve in THF in presence of an excess Grignard reagent. The resulting solution shows significant performance in cross-coupling reactions[148,149]. A further control experiment was carried out by Jonas and Schieferstein[150–153]. In this experiment a structurally well-defined nucleophilic iron compound was synthesized - $Li_2[Fe(C_2H_4)_4]$. The formal iron oxidation state in this complex of -II corresponds to the assumed oxidation state of iron in the proposed mechanism. The reaction rates and product yields in cross-coupling are comparatively high. In contrast, the highly nucleophilic complex $Na_2Fe(CO)_4$, in which iron also carries the formal oxidation state -II, did not show any activity[154].

Fe^{+III}

Reduction — ArMgX

Ar-Ar

Fe^n

Ar-Alkyl

Elimination

Alkyl-X

Electron transfer

$\left\{ \begin{array}{l} Ar\text{-}Fe^{n+1} \\ Alkyl^{\bullet} \end{array} \right\}$

$\left\{ \begin{array}{l} X\text{-}Fe^{n+1} \\ Alkyl^{\bullet} \end{array} \right\}$

MgX_2 ArMgX

Transmetallation

FIGURE 1.8. Radical related mechanistic catalysis cycle suggested by Nakamura, Bedford, Cossy and Cahiez.

16

Due to the instability of the active species and the impossibility of isolation, there are still controversial discussions about the detailed reaction mechanism of iron-catal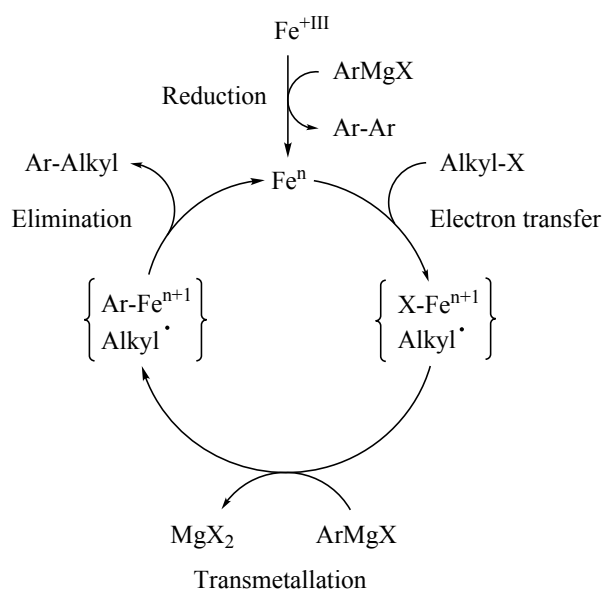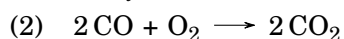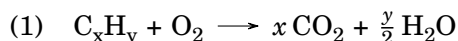yzed cross-coupling reactions. Because of the paramagnetic nature of iron, its low concentration and the absence of chromophoric ligands, the number of analytical and spectroscopic methods is limited and an unquestionable reaction mechanism still missing. While Hayashi assumes a classic catalytic cycle similar to the proposals of Kochi and Fürstner, containing oxidative addition, transmetallation and reductive elimination (see figure 1.7), Nakamura, Bedford, Cossy and Cahiez suppose a radical related pathway, as pictured in figure 1.8[100].

1.3.2 Exhaust gas catalysis

Industrial growth and the resulting increasing environmental pollution and destruction dictated legislative demands to decrease exhaust gas emissions of automobiles, heavy-duty traffic, stack gas from power stations and gaseous effluents from processes generated by petroleum refining and chemical industries. The first emission limits for automobiles were established in the USA in 1975 and in Germany in 1985 and are continuously decreased since then[8,155]. Induced by this, the market for automobile catalysts has undergone extraordinary expansion. More than 30 % of the worldwide market of solid catalysts can be attributed to the environmental sector and even more than 90 % of this share are used in mobile applications. Since their introduction, emissions of carbon monoxide, unburnt hydrocarbons and nitric oxides could be reduced by more than 90 %[87,156].

1.3.2.1 Spark ignition engines

The first catalyst systems which were introduced in 1975 were designed for spark ignition engine driven automobiles. These systems consisted of platinum and palladium on an alumina support and were used for the oxidation of unburnt hydrocarbons and carbon monoxide. During the 1980s the reduction of nitric oxides under formation of water and nitrogen was also implemented in the catalyst systems, resulting in the well-known "three-way catalysts", which are used until now[94,155]. The oxidation of unburnt hydrocarbons and carbon monoxide on the one hand and at the same time the reduction of nitric oxides on the other are only possible in the same catalyst system by tuning the amount of oxygen present in the exhaust gas. The processes can be expressed in these overall chemical equations[11]:

(1) $C_xH_y + O_2 \longrightarrow x\,CO_2 + \frac{y}{2}\,H_2O$

(2) $2\,CO + O_2 \longrightarrow 2\,CO_2$

(3) $2\,CO + 2\,NO \longrightarrow 2\,CO_2 + N_2$ $HC + 2\,NO \longrightarrow CO_2 + \frac{1}{2}\,H_2O + N_2$

Oxidative and reductive conditions at the same time are possible through the control of the air-to-fuel-ratio in the combustion chamber of the engine and an oxygen sensor in the exhaust gas stream, the so-called lambda sensor. The window in which the air-to-fuel ratio - named lambda-value - has to be adjusted is very narrow. If the air-to-fuel ratio is

too small (lambda < 1, so-called rich conditions), the combustion is incomplete and more unburnt hydrocarbons and carbon monoxide are formed. On the other hand, if the air-to-fuel ratio is too large (lambda > 1, so-called lean conditions) more oxidized components - nitric oxides - can be found in the exhaust gas stream. Only with a lambda value of 1, which corresponds to a stoichiometric air-to-fuel rate of 14.7, hydrocarbons and carbon monoxide are oxidized and nitric oxides are reduced, resulting in the formation of carbon dioxide, water and nitrogen[11,87,94,155].

A three-way catalyst nowadays consists of a ceramic α-cordierite ($Mg_2Si_5Al_4O_{18}$) honeycomb monolith, because this material is very stable against thermal shock. The monolith is coated with a thin layer of a γ-alumina and cerium oxide mixture - the washcoat. Both oxides work as a stabilizer and due to their high surface area as a carrier for the catalytically active precious metal species. In addition, cerium oxide act as oxygen reservoir to suppress inevitable oxygen fluctuations and with this helps to stabilize lambda. The catalytically active components - platinum, palladium and rhodium particles - are highly distributed on the γ-alumina/cerium oxide surface[8,94].

1.3.2.2 Diesel engines

An application of a three-way catalyst for the removal of toxic substances from exhaust gas of compression ignition engines (diesel engines) is not possible, due to a different air-to-fuel ratio and the ignition method of the air-fuel mixture. Furthermore, the exhaust gas composition of a diesel engine is more complex, since particular matter is present as well as gaseous, liquid and solid matter[94,155].

During the 1990s ceramic monoliths with a washcoat as support for platinum and palladium as catalytically active species were introduced in passenger cars in the EU and heavy-duty trucks in the US. Through these oxidation catalysts the emission of hydrocarbons, carbon monoxide and most of the solid matter were removed. Despite the oxidative properties of these catalysts, compounds like NO or SO_2 were not converted to even more toxic substances like NO_2 or SO_3[94,155,157]. First pioneering experiments, in which the exhaust gas leaving the oxidizing catalyst was lead over a second catalyst consisting of copper exchanged mordernite (a natural abundant zeolite mineral, $Na_2Al_2Si_{10}O_{24}\cdot 7\,H_2O$)[76] were applied in 1984 by Volkswagen[158]. Not oxidized hydrocarbons were used for the reduction of nitric oxides, which lead to the name "hydrocarbon selective reduction" (HC-SCR). Due to the complex control of the needed amount of hydrocarbons for a full removal of both nitric oxides and hydrocarbons themselves, ammonia is used as reduction compound in current applications (NH_3-SCR). Because of the dangers connected with the transport of ammonia in vehicles, aqueous solutions of urea (32.5 % urea, 67.5 % deionized water[159]) are used and carried along in separate tanks, as can be seen in figure 1.9. Urea is decomposed using an acidic precatalyst under formation of ammonia, which is then injected into the oxidized

exhaust gas stream. The reduction of nitric oxides is carried out by application of titania-supported $V_2O_5-WO_3$ catalysts[94,155,157]. This system is currently used in heavy-duty diesel trucks as well as in several automobiles e. g. under the name AdBlue® (Germany) or DEF (USA)[159]. Nowadays, a particulate filter is placed in the exhaust gas stream as well for the removal of particulate matter. Another approach shows promising results in the removal of nitric oxides: nitric oxide storage catalysts (NSR), which was originally invented by Toyota Laboratories in the 1990s[160]. Centerpiece of this approach is a storage catalyst which consists of barium carbonate on its surface. Under lean conditions, produced nitric oxide binds on the catalyst forming barium nitrate on the surface. By switching the working conditions of the engine to rich conditions for a short period of time, barium carbonate is recovered and the generated nitric oxide is reduced to nitrogen and water using a conventional three-way catalyst[161,162].
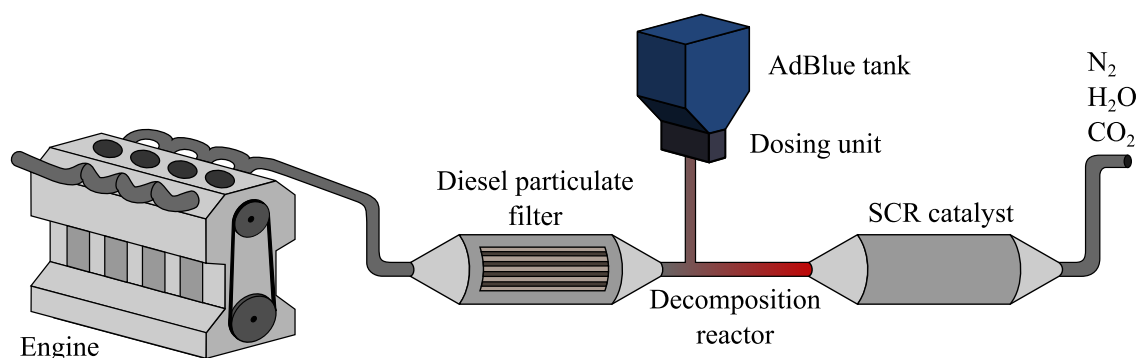
FIGURE 1.9. Scheme of the exhaust gas treatment for SCR catalysis.

1.3.2.3 CO-oxidation as key reaction

Since carbon monoxide is the most toxic gas component in the exhaust gas mixture of combustion engines and it is emitted with the highest share of all components[11,155], its oxidation can be considered to be a key reaction in emission reduction. Worldwide a huge amount of carbon monoxide is emitted every year (1.09 billion tons in 2000[163]), mainly from traffic, power plants, industrial and domestic activities - nearly anywhere where incomplete combustion of hydrocarbons is possible.

The toxicity of carbon monoxide is based on its binding strength to transition metals like iron. In human body, iron-based complexes are the main component in enzymes responsible for the transportation of gases in blood (hemoglobin) and binding in muscles (myoglobin)[164]. The coordination of iron in these enzymes is realized by nitrogen atoms in heme ligands, leaving coordination sites vacant, where oxygen and carbon dioxide can bind reversibly. Since the binding affinity of carbon monoxide to iron is 200 times greater than of oxygen,

inhalation of even small amounts lead to a blocking of binding sites and inhibits oxygen transport. First symptoms for carbon monoxide poisoning can be detected with 35 ppm, concentrations of 100 ppm and higher are considered as dangerous to human health[165]. Beside its toxicity, carbon monoxide is also a precursor for ground level ozone, which can trigger serious respiratory problems[163].

Due to the absence of possible side products, carbon monoxide oxidation can be carried out without great effort or complex instruments. In the last years, carbon monoxide oxidation was established as a standard test reaction for the determination of the activity of heterogeneous emission reduction catalysts. Because of these reasons, carbon monoxide oxidation was used for the catalysts presented in this dissertation[166–172].

1.4 Analytical methods

For the determination and identification of present species in the catalyst, a variety of analytical methods were applied in this work. Beside rather common methods like specific surface determination after BET theory, X-ray powder diffraction, Mößbauer- or optical spectroscopy, X-ray absorption spectroscopy represents an indispensable tool in catalyst investigation. Since Mößbauer spectroscopy plays only a minor role in the presented work and optical spectroscopy is well known theoretically and in its application[173], the following section focuses on specific surface area determination, X-ray powder diffraction and X-ray absorption spectroscopy.

1.4.1 Specific surface area determination

To determine the activity of heterogeneous catalysts a detailed knowledge about the material surface is indispensable, since the number and nature of accessible catalyst sites is directly connected to the catalyst performance[8,174,175]. Furthermore, knowledge about the presence, size distribution and geometry of pores in the solid catalyst or its support are of importance for the determination of molecular transportation type and reaction pathways[176–179].

To determine the specific surface area, gas is adsorbed on the solid's surface at low temperature. The amount of gas, that is physisorbed on the surface, is detected by reduction of the gas pressure and can be correlated to the surface area. Hereby, physical adsorption or physisorption occurs as an interphacial phenomenon whenever a solid surface is exposed to gas as demonstrated in figure 1.10. The difference to chemisorption lies in the absence of chemical bonds of physisorbed molecules between the adsorptive and the surface[180,181]. The forces, which are involved in this process, are mainly the same as those responsible e.g. for the condensation of vapor and the deviations from ideal gas behavior[181], which are in detail: the long-range London dispersion forces, the short-range intermolecular repulsion[180] and specific molecular interactions (e.g. polarization and field dipole) as a result of particular
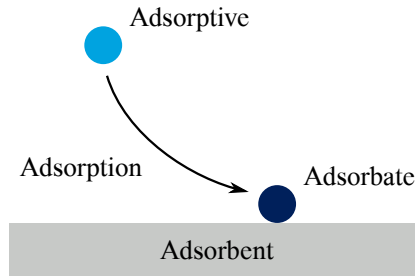
FIGURE 1.10. Terms and definitions for physisorption[180,181].

geometric and electronic properties of adsorbent and adsorptive[182]. Thereby, the amount n of adsorbed gas molecules is dependent on the equilibrium pressure p, the temperature T and the nature of the gas-solid system[180].

$$n = f(p, T, system) \tag{1.1}$$

With the gas kept at a constant temperature under its critical point, a formulation of an adsorption isotherm is possible:

$$n = f\left(\frac{p}{p^0}\right)_T \tag{1.2}$$

p^0: Saturation pressure of the adsorptive at temperature T

The adsorption isotherm is therefore a relation between the amount of adsorbed gas molecules and the equilibrium pressure at temperature T.

The mechanism of the adsorption process is in a large extent controlled by the pore size and its geometry, which therefore influences the shape of the adsorption isotherm[181]. Three distinctive processes could be identified, which occur during adsorption on a surface: monolayer-multilayer adsorption, micropore filling and capillary condensation[183]. According to IUPAC the shapes of the adsorption isotherm can be classified in six types schematically shown in figure 1.11[182].

Type I: microporous adsorbents, micropore filling (pore size < 2 nm[184])

Type II: monolayer-multilayer adsorption on an open surface of non-porous or macroporous (pore size > 50 nm[184]) adsorbents

Type III: no identifiable monolayer (weak adsorbent-adsorbate interactions)

Type IV: mesoporous adsorbents (2-50 nm[184]), hysteresis loop associated with capillary condensation

Type V: rare, at low $\frac{p}{p^0}$ $\approx$ Type III: relative weak adsorbent-adsorbate interactions at higher $\frac{p}{p^0}$: molecular clustering followed by nanopore filling

Type VI: steps representative for layer-by-layer adsorption on a highly uniform surface (step height = layer capacity)
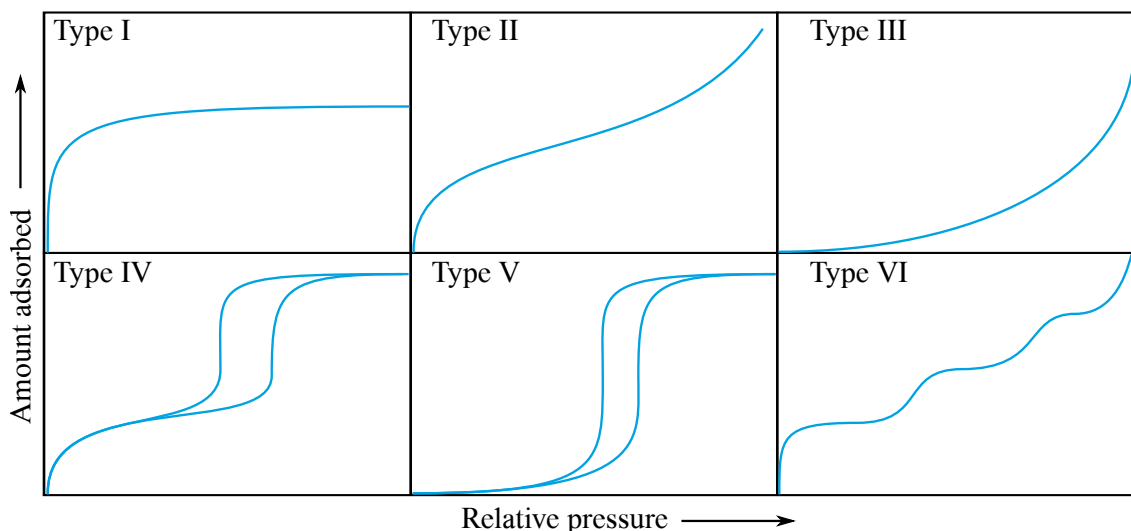
FIGURE 1.11. Types of physisorption isotherms according to IUPAC[180,182].

Mainly two different experimental procedures for the measurement of adsorption isotherms are common: 1) Detection of the amount of removed gas from the surface (volumetric or manometric method)[185] or 2) direct measurement of the weight difference of the adsorbent (gravimetric method)[180]. In both cases, the surface of the sample has to be cleaned from residual physisorbed molecules preliminary to the measurement. Since adsorption forces of physisorbed molecules are significantly weaker than of chemisorbed molecules no ultra high vacuum or other very harsh conditions are required to obtain a satisfying clean surface[181]. This means under realistic conditions, pressures in the range of a few millibars and slightly elevated temperatures for several hours. Many different techniques are available for the determination of gas adsorption data based on the recorded adsorption isotherm and especially for the ascertainment of the specific surface area[186,187]. The choice of the suitable method depends on the purpose of the measurement and the operational requirements[181]. Figure 1.12 shows a schematic assembly of an adsorption experiment[182].

The BET method[188,189], named after their developers Stephen Brunauer, Paul Hugh Emmett and Edward Teller, is widely used for evaluation of the surface area of catalysts and support materials[8] - despite known shortcomings and theoretical limitations, the most significant will be mentioned in the following[176,178,179]. Commercial available user-friendly equipment and the use of liquid nitrogen as adsorptive, which is a standard substance in laboratories, made the BET method become a standard technique[180,181]. In its original form, the BET theory[188] was basically an extension of Langmuir's kinetic treatment of monolayer adsorption on an array of identical sites. Langmuir's concept of an ideal localized monolayer was widened to include the formation of either a finite or infinite number of
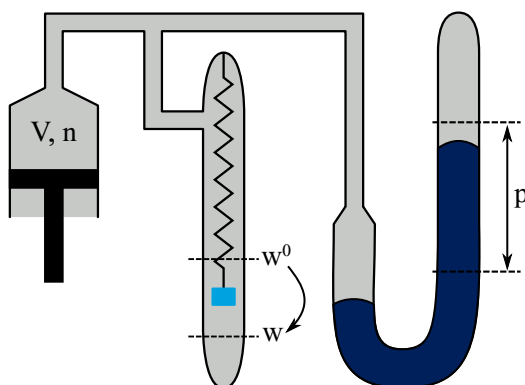
FIGURE 1.12. Schematic arrangement of a simultaneous volumetric and gravimetric adsorption experiment[182].

adsorption layers[180,181]. Today, it is generally accepted, that the BET theory is based on an oversimplified model[180]. Due to its empirical manner and the application of several assumptions, certain conditions have to be fulfilled before the "BET area" represents a meaningful surface area[176,178].

One of the most fundamental assumptions was already adopted from the Langmuir model and includes a planar surface composed of a set of uniform sites. The occupation probability of these sites is independent from the occupancy of neighboring sites, which makes all sites equivalent[8,181]. Adsorbed atoms/molecules of one layer are considered to act as adsorption sites for the atoms/molecules of the next layer. The occupation probability of sites in layers higher than one is zero unless all underlying sites are occupied[180,181]. To elucidate further assumptions and simplifications in the BET theory, it is unavoidable to comprehend the theoretical background. This should be presented here in a succinct manner. At a given temperature T the equilibrium pressure p is attained, when the rate of condensation (adsorption) is equal to the rate of evaporation (desorption). This steady state can be formulated as follows[180,181]:

$$(1.3) \qquad a_i \cdot p \cdot \theta_{i-1} = b_i \cdot \theta_i \cdot exp\left(-\frac{E_i}{RT}\right)$$

θ_{i-1}, θ_i: Fractions covered in the i-1th and ith layers

a_i, b_i: Adsorption and desorption constants

E_i: Energy of adsorption

Each layer has its own set of a_i, b_i and E_i values, but to simplify the summation of the adsorbed amounts of gas, all layer parameters after the first one are considered to be constant. Furthermore, the energy of adsorption is equated to liquefaction energy ($E_i = E_L$)[8,180], which implies that E_i is independent from the surface coverage θ_i. At this point the fundamental assumption of an uniform array of equal adsorption sites, mentioned above, and the absence of lateral interactions between adsorbed atoms/molecules are implemented[181]. By

the simplification, that all multilayer have the same thickness at $p = p^0$, the formulation of the BET equation is possible[8,180,188].

(1.4)
$$\frac{\frac{p}{p^0}}{n \cdot \left(1 - \frac{p}{p^0}\right)} = \frac{1}{n_m \cdot C} + \frac{C-1}{n_m \cdot C} \frac{p}{p_0}$$

n: Amount of adsorbed gas

n_m: Monolayer capacity

C: Empirical constant, related to E_i by equation $C = exp\left(\frac{E_i - E_L}{RT}\right)$

To evaluate the BET surface area, the adsorption isotherm has to be transformed into the "BET plot" and the monolayer capacity n_m - the maximum number of absorbed molecules in one layer - has to be extracted. To obtain the BET graph, $\frac{p/p^0}{n(1-p/p^0)}$ is plotted against p/p^0. Afterwards a linear regression can be adjusted in a limited part of the adsorption isotherm with the slope $s = \frac{C-1}{n_m C}$ and intercept $i = \frac{1}{n_m C}$, which yield $n_m = \frac{1}{s+i}$ and $C = \frac{s}{i} + 1$[8,181]. Knowledge about the monolayer capacity n_m allows the calculation of the specific surface area (a_{BET}).

(1.5)
$$a_{BET} = n_m L \sigma$$

L: Avogadro constant

σ: Area occupied by each adsorbate atom/molecule

To gain knowledge about the area each atom/molecule occupies in a completed monolayer (σ), another assumption has to be applied, after which adsorbed gas exhibits on the surface liquid-like packaging[187]. The calculation of σ is possible using the density of the bulky liquid of the adsorptive at operational temperature. Many attempts were made to achieve a precise definition of σ for a wide range of adsorption systems. However, the specific value of σ depends at least partially on the adsorptive-adsorbent system[183,190–192]. There are indications that $\sigma(N_2)$ varies up to 25 % from one surface to another, leading to the simplification to use $\sigma(N_2) = 0.162\ nm^2$, as already Emmett and Brunauer proposed[8,180,187,188]. In fact, comparison between the values for a_{BET,N_2} and independently determined clusters by electron microscopy show a size discrepancy of 20 %[176,178,193].

Caused by the assumptions, which were necessary to establish the BET method, there are several discrepancies from reality. One significant deviation is the incompatibility of the BET model with topologically heterogeneous surfaces[8,178]. These surfaces are exhibited by most adsorbents and do not show the equal occupation probabilities for every site of an adsorption layer[180]. Furthermore, BET method does not take lateral interactions between molecules into consideration and all higher layers were regarded to have liquid-like properties. This contradicts experimental and theoretical studies, which could show that adsorbate-adsorbate interactions take place in a significant extent long before monolayer coverage is completed[194,195]. Another important point is the range of the adsorption isotherm,

which is considered in the linear adjustment for the determination of the monolayer capacity (n_m). This range rarely exceeds $\frac{p}{p^0} \approx 0.35$ [8,175,176,178] and can in some systems only be improved by restricting the number of adsorption layers[180]. In general, the BET method is only applicable, when significant macropore filling can be excluded[8].

As mentioned before, nitrogen is mainly used in commercial available equipments and is accepted as standard BET adsorptive. On one hand, this is due to practical reasons, since liquid nitrogen is usually available in laboratories. On the other hand, nitrogen is considered to be the most suitable adsorbate for standard surface area determinations of non-porous, macroporous or mesoporous solids[8,180]. This is explainable through the fact, that its multilayer isotherm is relatively insensitive to differences in adsorbent structure[8]. Dependencies of this type between nitrogen and the surface cannot be considered by the BET method and are therefore disregarded[176,178].

Despite these rather negative facts, determination of the BET surface area evolved to be a standard technique for porous solid samples, which allows a straightforward measurement and a very good comparability between different samples. For these reasons, surface areas given in this thesis were ascertained using the BET method.

1.4.2 X-ray powder diffraction

X-ray powder diffraction has emerged to be the main characterization tool whenever solid materials with a long range order are synthesized. Nowadays, commercial available diffractometers are utilized in almost every laboratory[196]. Powder diffraction is a non-contact and non-destructive characterization method to obtain information about crystal structures, phase compositions or microstructures[197]. Since powder diffractograms can be recorded in a relatively short time, the method is also predestined for product control during synthesis[196]. The properties of X-ray radiation enable the implementation of studies under non-ambient conditions - e.g. high of low temperatures and elevated pressures - which allows in-situ, in-operando and time-resolved studies[197].

In general, to produce X-ray radiation for powder diffraction in a laboratory, two metal electrodes enclosed in a vacuum chamber are used, arranged as shown in figure 1.13 (both tube designs shown are explained later). As cathode a heated tungsten filament is used and a high negative potential between 30-60 kV[197,199]) is applied. The free electrons produced in this way are accelerated toward the anode, which is normally at ground potential. During the bombardment of electrons on the anode, two processes occur[198,200]: a) The electrons collide with a series of anode atoms and loose kinetic energy, which is emitted as X-ray radiation. Because each electron looses its energy in a unique way, a continuous X-ray spectrum is emitted, which is also known as white spectrum or "Bremsstrahlung" and shown in figure 1.14[197,198]. Due to its low intensity, this type of radiation cannot be used for diffraction measurements[198]. b) When the energy of the accelerated electrons exceed a
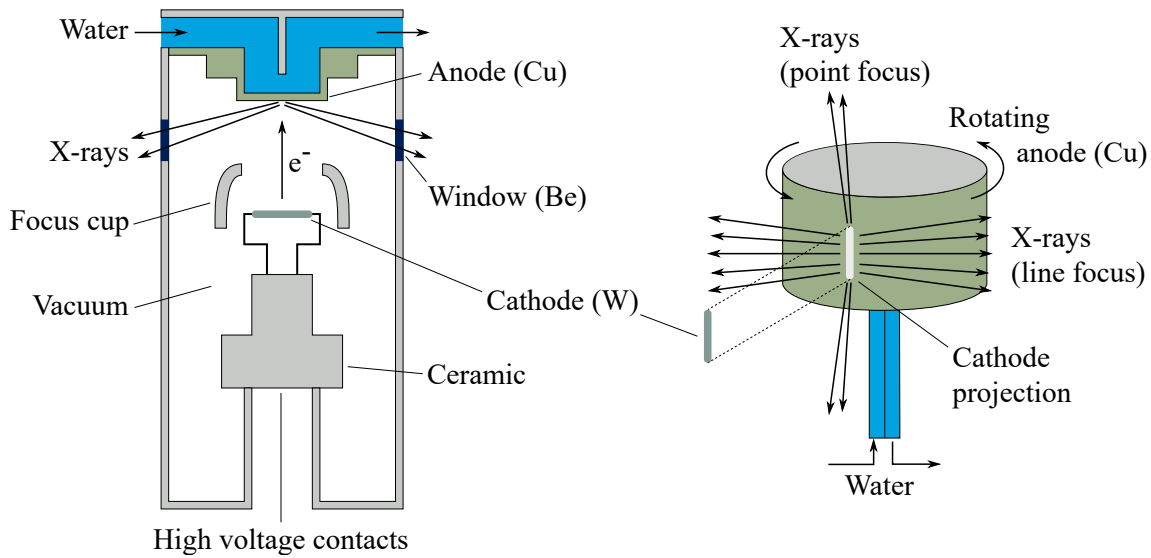
FIGURE 1.13. Schematic assembly of a sealed X-ray tube (left) and a tube with a rotating anode (right)[197–199].

certain threshold value, which is depending on the anode element, an electron of the anode atom K shell is ejected. The exited state generated in this way relaxes through transition of an outer shell electron to the K shell under emission of an X-ray fluorescence photon with an energy equal to the difference of these two electron energy levels[198]. The sharp peaks, which emerge in the spectrum according to these transition processes, arise superimposed
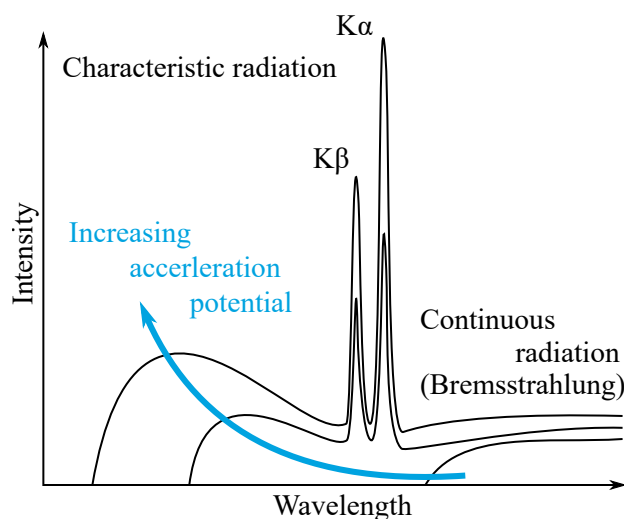
FIGURE 1.14. X-ray fluorescence spectrum of a copper anode dependent on acceleration potential of the electron beam[197,198].

to the continuous spectrum and are anode element specific. Thus, these lines are called characteristic lines and can be classified according to their formation process. An electron transition from L to K shell is called Kα radiation. Thereby, Kα radiation consists of two transition processes: Kα_1 ($2p_{\frac{1}{2}} \rightarrow 1s_{\frac{1}{2}}$) and K$\alpha_2$ ($2p_{\frac{3}{2}} \rightarrow 1s_{\frac{1}{2}}$). A transition $2p_{\frac{2}{2}} \rightarrow 1s_{\frac{1}{2}}$ does not occur due to selection rules, where $\Delta l = 0, \pm 1, \pm 2, ...$[199]. Another electron transition from an M level to K shell is called Kβ radiation[200]. Due to the number of M shell energy levels, several discrete lines exist, which are energetically very close to distinguish. The intensity of Kα_1 exceeds that of Kα_2 by the factor of about two, whereby the intensity of the combined K$\alpha_{1,2}$ radiation is about five times higher than Kβ. Hence, Kα radiation is used for powder diffraction experiments[197,199].

The X-ray yield of the electron beam is only less than 1 % in these tubes, the majority is consumed as heat, although the anode is water cooled during operation[198]. The anode metal has to fulfill both, being a good conductor for heat and electricity and also having a suitable high melting point[197,199]. Usually copper is used, but molybdenum, chromium, iron, cobalt and silver are also applied as anodes depending on the experiment and on the desired energy[196,197]. Operation of X-ray tubes with these anodes leads to wavelengths in range of approximately 0.1-5 Å (125 keV-2.5 keV)[197].

The two tube types, which are in common use today are the sealed tube and the rotating anode tube. Their schematic assemblies are shown in figure 1.13. The construction of a standard sealed tube is relatively easy and more or less maintenance-free. The typical electron beam current is about 10-50 mA with an input power of 0.5-30 kW[199]. In contrast, the setup of a rotating anode X-ray tube is rather complex. Due to the constant rotating of the anode disk, a more effective cooling is achieved. This allows an increased input power of 15-18 kW and in some instances 50-60 kW, which is up to 20 times higher than in a standard sealed tube. The increased input power leads to higher brightness and much better resolved diffraction pattern. On the other hand, the durability of seals and bearings that operate in high vacuum are limited, which makes this type of X-ray tube more vulnerable for defects and with this more expensive in maintenance[199]. Another X-ray source with significant higher intensity and much better signal-to-noise ratio is a synchrotron. Because of a higher photon flux, considerable shorter measuring time is needed. An advantage is the possibility to vary the X-ray energy. This allows to exploit the phenomenon, that the scattering efficiency decreases, if the radiation energy is close to the absorption edge of an element. The so-called "anomalous scattering" enables to suppress the diffraction pattern e.g. of the support material to obtain a detailed view on the sample signals[201].

To obtain a diffraction pattern, X-ray photons are scattered elastically by atoms in periodic lattice planes, separated by a certain distance. Scattered monochromatic X-ray photons, which are in phase, interfere constructively leading to an increase of their recorded intensity in the diffractogram[200,202]. X-ray radiation penetrates deeply into the material

and the photons are all reflected in the same direction. As can be seen in the left scheme of figure 1.15, the photon which is scattered at a deeper plane travels a longer distance - namely $\overline{CB}$ before and $\overline{BD}$ after reflection.
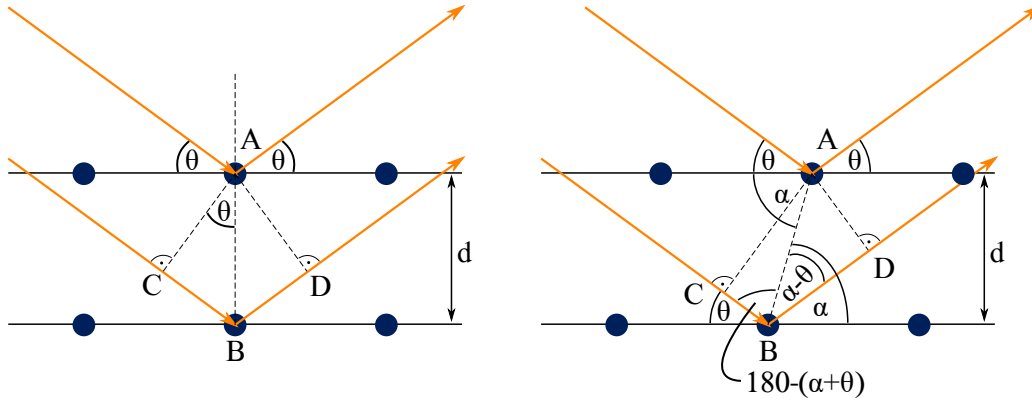
FIGURE 1.15. Scattering process of X-ray photons on periodic lattice planes. Left: Atoms of the planes are positioned directly above each other; Right: Consideration of a shift between the planes[202].

Constructive interference occurs, if $\Delta = \overline{CB} + \overline{BD}$ is an integer multiple $n = \pm 1, \pm 2, ...$ of the incident wavelength λ. That means, sharp intensity maxima emerge only at special angles, where $\Delta = n\lambda$ holds and no intensity can be detected between these angles. As easily can be seen geometrically:

$$(1.6) \qquad \Delta = 2dsin(\theta)$$

A combination of these two equations lead to the Bragg equation[200,202]:

$$(1.7) \qquad n\lambda = 2dsin(\theta)$$

> n=1, 2, 3, ...: Integer, called order of reflection
> λ: X-ray wavelength
> d: Distance between lattice planes
> θ: Incidence angle of the incoming X-rays

Although it leads to the correct solution, this derivation of the Bragg equation is simplified since X-rays are not reflected by planes in reality, but are scattered by electrons bound to these atoms[202]. The assumption made at the beginning of the derivation is not very far from reality, due to the fact, that crystal planes contain discrete atoms separated by regimes with low electron probability of presence. This again leads to a periodic lattice, where the X-ray photons are scattered. Another deficiency in the derivation can be found in the presumption, that atoms of one plane lie exactly above atoms in the plane below[202]. A more general derivation shows that Bragg equation is valid even in consideration of shifted

planes. As sketched in figure 1.15, in this case the longer distance of the second photon, which is scattered at a deeper plane, can be described by:

$$n\lambda = \overline{AB} \cdot cos\left[180° - (\alpha + \theta)\right] + \overline{AB} \cdot cos(\alpha - \theta)$$

(1.8)
$$n\lambda = \overline{AB} \cdot \left[-cos(\alpha + \theta) + cos(\alpha - \theta)\right]$$

Implementation of relations from trigonometry:

(1.9)
$$cos(\alpha + \theta) = cos(\alpha)\,cos(\theta) - sin(\alpha)\,sin(\theta)$$

(1.10)
$$cos(\alpha + \theta) = cos(\alpha)\,cos(\theta) + sin(\alpha)\,sin(\theta)$$

lead to:

(1.11)
$$n\lambda = \overline{AB} \cdot \left[2sin(\alpha)\,sin(\theta)\right]$$

Inserting relation $d = \overline{AB} \cdot sin(\alpha)$ lead to the known Bragg equation:

(1.12)
$$n\lambda = 2d\,sin(\theta)$$

Knowledge about the angle θ allows calculation of the lattice spacing, which is characteristic for a certain compound[200].

During the measurement, the X-ray source as well as the detector are moved, which enables to scan the intensity of the diffracted radiation as a function of the angle 2θ[200]. Investigations of powdered samples are possible, since the powder consists of very small crystallites, which are orientated coincidentally. This means, a very small part of these crystallites is always oriented in a way, that a certain crystal plane is in the right angle θ to constructively interfere with the incident beam, as sketched in figure 1.16. Moreover, rotation of the sample during measurement increases the number of crystallites, that contribute to diffraction, which leads to a higher signal-to-noise ratio[200]. Instead of Bragg reflexes detected in form of defined points known from single crystal diffraction, lines in form of Debye-Scherrer rings were obtained[203] during the measurement.
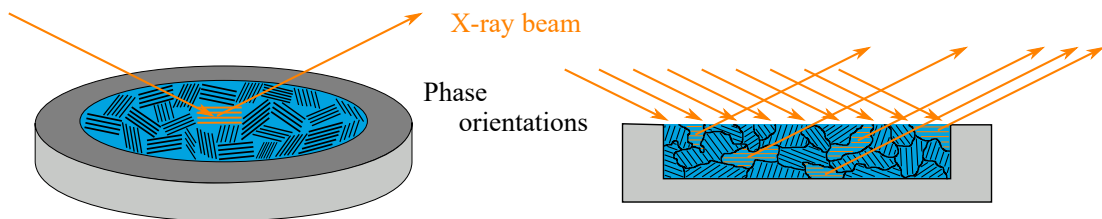
FIGURE 1.16. Schematic view on a powdered sample, which consists of randomly orientated small single crystals. A small part of these single crystals are always oriented in the right angle to obtain a diffraction pattern[200].

There are mainly two instrumental configurations, which are used for recording X-ray powder diffractograms[197]:

a) The measurement in reflection mode, also called Bragg-Brentano geometry, is the most common configuration. Here, a flat plate sample holder is used, which rotates constantly to increase the signal-to-noise ratio, as explained before. During the measurement the X-ray tube is fixed and sample as well as detector are moved on a circle in the velocity ratio 1:2, which is called $\theta/2\theta$ geometry (mainly used at older instruments). As an alternative, the sample is fixed and X-ray tube as well as detector are moved with the same speed on a cycle, which is called θ/θ geometry, and is shown in figure 1.17. The sample holder in this configuration is easily and fast prepared, but the surface-flattening process of the sample often induced a preferred orientation and preparation under inert atmosphere is difficult. Furthermore, in $\theta/2\theta$ geometry sample can fall out the holder during rotation[197].
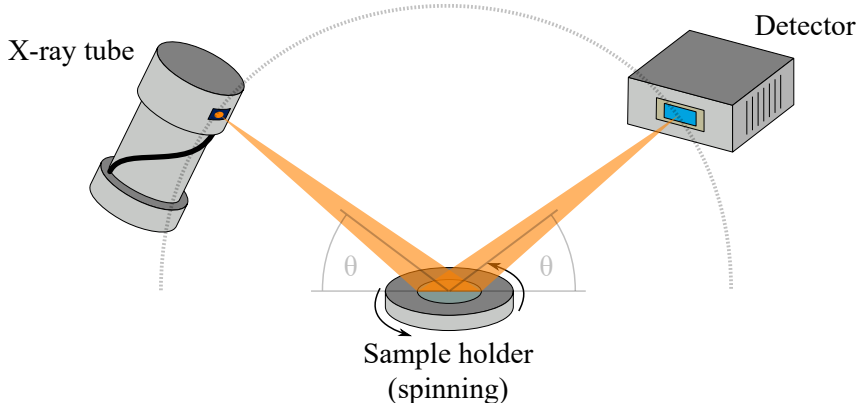
FIGURE 1.17. Schematic assembly of a Bragg-Brentano setup. X-ray tube and detector move along the cycle in the same speed during measurement

b) In transmission configuration the X-ray beam is focused using a curved single crystal not onto the sample, but onto the detector beyond, as sketched in figure 1.18. Because of this, a thin flat sample holder or a thin walled glass capillary filled with the sample is required for this geometry. Although preparation of the sample in a glass capillary is more complex, no preferred orientations were induced during the process. Also it is possible to handle air sensitive samples. As a disadvantage, a significant part of the X-ray photons are scattered diffusively from the glass walls and the alignment of the capillary has to be carried out very carefully, since its axis has to be co-linear to the one of the diffractometer[197].

Both instrumental configurations can also be used for in-situ, in-operando or time resolved investigations[196,197,204]. Application of an appropriate cell, exemplary shown in figure 1.19, allows experiments under control of temperature, pressure and atmosphere. This facilitates monitoring of dynamic processes like phase transitions, chemical formations, precipitations and reactions with gas phase depending on time, temperature or atmosphere
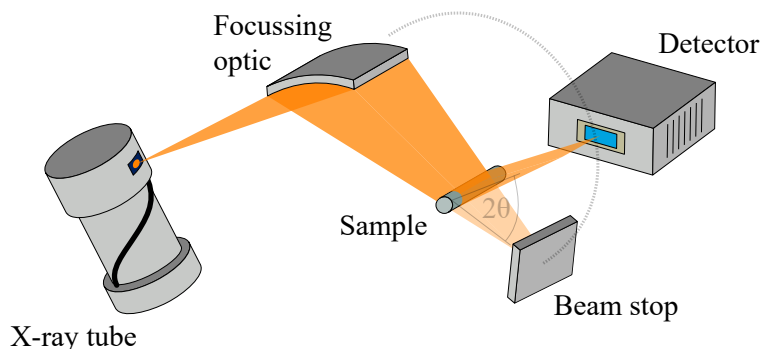
FIGURE 1.18. Scheme of a transmission geometry setup. During the measurement, only the detector is moved along the pictured cycle.

composition[197,204]. To follow these dynamic processes, short measuring times are required since under normal conditions recording of a diffraction pattern takes minutes up to several hours[196]. Therefore, on one hand, a high X-ray flux is necessary, which can be realized using a rotating anode instead of a standard X-ray tube, that allows measuring times of about a thousandth of that with a standard X-ray tube[196]. On the other hand, conventional detectors (mostly scintillation counters e. g. based on thallium-doped sodium iodide crystals[197]) have to be replaced by new developed ones (scintillation counters on basis of yttrium aluminum perovskite or germanium resp. silicon-based solid-state detectors[197]), which allow measurements down to millisecond regime[204]. An experimental setup for in-situ studies is shown in figure 1.19 for Bragg-Brentano geometry[205,206]. An alternative setup is common, using a capillary flushed with gas, which is warmed by a heat blower. In
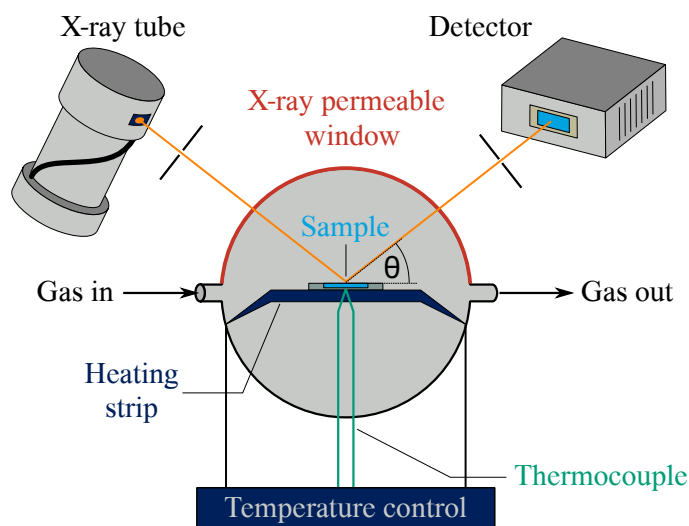
FIGURE 1.19. Example of an in-situ X-ray diffraction cell in Bragg-Brentano geometry[205,206].

reflection geometry relatively large sample diameters (5-15 mm) are needed and concentration gradients occur, when gas is lead through the sample. Furthermore, the sample moves out of the focus point of the beam through volume expansion or contraction, induced by chemical reaction or sintering processes[196]. Therefore, reflection geometry should only be used when a gas flow through the sample is of less importance - for example calcinations, phase transitions or reduction-oxidation reactions[196].

The identification of a phase in a diffraction pattern is based on graphical comparison of the diffraction reflex positions and their relative relations with a database (most commonly used: International Center of Diffraction Data ICDD)[196]. Furthermore, through determination of absolute intensities, a quantitative analysis is possible. This is rather complex, since the scattering power of a diffraction line and an instrumental scaling factor, depending on measuring time, sample amount, X-ray intensity, aperture, etc. have to be calculated preliminary[196]. Solid samples often consist of nanocrystalline and defect-rich phases, which cause significant line broadening in diffractograms. Narrow diffraction peaks are only observable for samples, which posses very long range order. Already below a crystal size of 100 nm line broadening occurs[196]. Therefore, the relation between crystal size and diffraction peak form can be used to determine the dimension of the reflecting plane in the sample[200]. This can be achieved by application of the Scherrer equation[196,200,207]:

$$(1.13) \qquad\qquad D = \frac{K\lambda}{\beta cos\theta}$$

D: Crystallite size in the direction perpendicular to the reflecting plane

K: Crystallite shape form factor (spherical: K=0.94, often taken as 1)

λ: X-ray wavelength

β: FWHM (full width at half maximum) of the diffraction peak

θ: Bragg angle corresponding to the diffraction peak

The estimation of the particle size via Scherrer equation provides a quick but not always reliable view on the particle size, since it results in crystallite size (more precise: in coherent scattering domain size) - not in a grain or particle size. Since one particle can consist of more than one coherent scattering domains, the value calculated via Scherrer equation is erroneous[196,200]. By now, better methods based on improved models for the determination of the particle size are available[200,208–210].

To investigate multiphase crystalline samples, a full X-ray powder pattern analysis - better known as Rietveld analysis - can be carried out. Through consideration of the whole diffraction pattern, a great amount of information can be achieved at once[211–213]. Due to the huge number of iterable parameters, an input model is required in form of single crystal data. Therefore, this method is mainly used for refinement of crystalline phases and quantitative multiphase analysis[196] and could not be applied in the systems presented

in this dissertation. There are numerous articles published, exploring all aspects of this technique since the first report in 1967[211] and still important improvements could be made in the last years[196].

1.4.3 X-ray absorption fine structure spectroscopy

X-ray absorption fine structure spectroscopy (XAFS) is the only technique that gives information about electronic and structural properties of a catalyst - even in presence of reactants and under reaction conditions. Techniques like X-ray diffraction require long-range order of the sample but provide mainly geometric information. In contrast, X-ray photoelectron spectroscopy as well as any other electron spectroscopy method provides electronic information but requires ultra-high vacuum, which does not allow measurements under reaction conditions[214]. Another advantage of XAFS as applied here lies in the use of hard X-rays, since their penetration properties give a high number of degrees of freedom with respect to cell design and experimental setup. There are four ways X-rays interact with materials: elastic scattering, inelastic scattering and absorption are the most common ones. At very high energies ($> 1.022\ MeV$) also the generation of electron-positron pairs is possible through colliding particles. This process is mainly used for the synthesis of new particles in high-energy physics[215].

Elastic scattering - also called coherent, unmodified or Rayleigh scattering - occurs, when a photon of a certain energy impinges on a sample, interacts with the electrons and a photon of the same energy is emitted in another spacial direction[216]. In a classic attempt of explanation, the incident electromagnetic wave causes an oscillation of the atom bound electrons. These generate thereby their own secondary wave field of identical frequency[215].

Inelastic scattering - also called incoherent, modified or Compton scattering - occurs, when the scattered photon has not the same energy (generally lower energy) than the incident photon. This is due to an energy transfer usually from the photon to the sample by inducing electronic transitions (excitations)[216].

In an absorption process the photon incidents on the sample and transfers its energy to sample electrons. While the photon is consumed in this process, the sample electrons are excited from lower atomic levels to higher ones, leaving vacancies in their original levels as shown in figure 1.20. This so-called photoionization process is also possible through excitation by electrons, which is then named ionization process[216]. In both cases, the generated vacancies in lower energy levels are refilled by electron transitions from higher energy levels after a short time. The difference between these two energy levels is released in this relaxation process and can be emitted radiatively by emission of fluorescence radiation, which is characteristic for the absorbing element. Assuming that the electron vacancy was generated in the K shell (1s orbital), the fluorescence transitions are named dependent on the origin of the relaxing electron: K_α ($L \rightarrow K$), K_β ($M \rightarrow K$). Further possible transitions
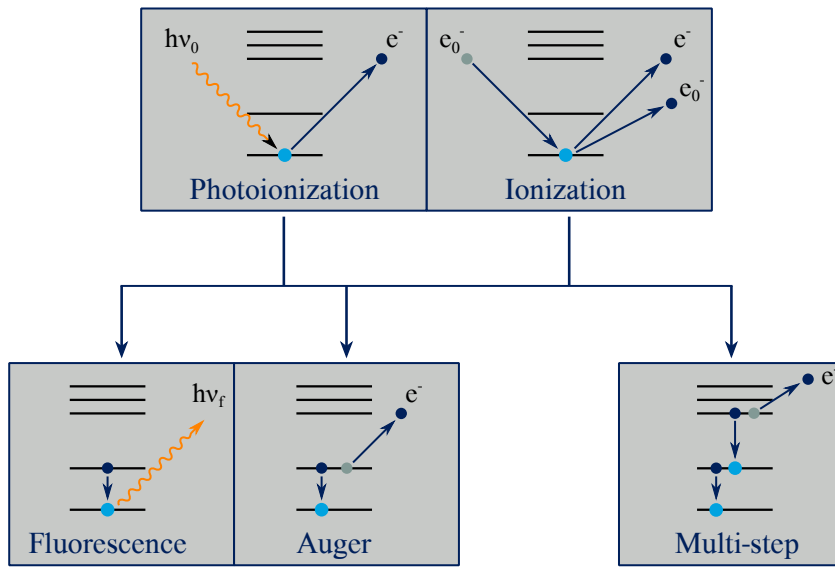
FIGURE 1.20. Interactions of photons ($h\nu$) and electrons (e_0^-) with atomic core levels.

and more detailed notations are given in figure 1.21. The ratio of emitted X-rays to the number of generated electron vacancies is called fluorescence yield or radiative probability. The value of fluorescence yield increases with higher atomic numbers and is significantly larger for K emission than for L or subsequent line emissions. For this reason, K emission line is mainly used. Only for elements with high atomic number L shell emission is preferred, since excitation of a K shell electron requires a lot of energy and the L shell emission is of sufficient intensity.
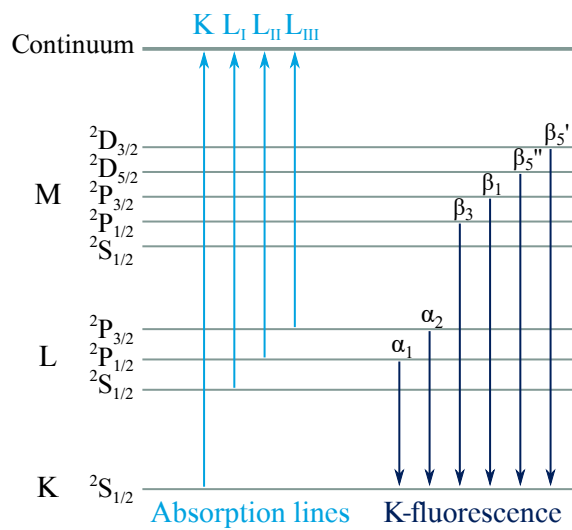
FIGURE 1.21. Selected absorption edges and fluorescence lines[216].

Moreover, non-radiative relaxation by emission of an Auger electron is possible [215,216]. The generated electron vacancy is filled by an electron from an energetically higher atomic level, while simultaneously another electron is ejected usually from the same higher atomic level from which the relaxing electron came from. Therefore, through Auger spectroscopy information can be obtained about the involved energy levels by detection of the kinetic energy of the escaping electron [215,216]. Since electrons are detected, ultra high vacuum is required for the measurements. In some cases, a cascade of radiative and non-radiative relaxations due to many single- and multi-electron processes occurs, which lead to photons emitted in X-ray, UV-Vis and infrared wavelengths, electron ejections and heat pulses [215,216].

All three phenomena are closely related and occur at the same time, but during an XAFS experiment focus lies on the energy dependence of the absorption coefficient and there is usually no detection of scattering intensity versus angle as in scattering experiments [215].

1.4.3.1 Phenomenological description of XAFS spectra

The basic physical parameter detected in XAFS is the X-ray absorption coefficient $\mu(E)$ [215]. When a collimated beam of monochromatic X-rays travels through matter, its intensity is reduced because of interactions with the material. The loss in intensity is proportional to the original beam intensity and to the material thickness [214,216].

$$(1.14) \qquad dI = -\mu I dx$$

integration gives Lambert-Beer's law:

$$(1.15) \qquad \frac{I}{I_0} = exp\left(-\mu(E)X\right)$$

I: Transmitted intensity

I_0: Incident intensity

$\mu(E)$: Linear absorption coefficient

X: Material thickness

Assuming a free atom is exposed to X-rays, its absorption coefficient $\mu(E)$ decreases continuously smooth with higher energies. This trend is due to a decrease of probability of photoelectric absorption, which is directly proportional to the absorption coefficient and beside coherent and incoherent scattering the dominant factor in the energy range of interest in XAFS [215,217]. Since no analytic expression is valid for this process, only a rough approximation can be given [217]:

$$(1.16) \qquad \sigma = \text{constant} \cdot \frac{Z^n}{E^{3.5}}$$

σ: Photoelectric absorption cross section

Z: Atomic number

n: Exponent, varies between 4 and 5

E: Photon energy

Thus, the absorption coefficient decreases approximately with $\frac{1}{E^3}$ [214,215]. At specific energies characteristic for the illuminated element, sharp increases of the absorption - called absorption edges - take place and are shown in figure 1.22, the corresponding electron transitions are displayed in figure 1.21 [215,216]. At these absorption edges, the X-ray energy ($h\nu$) is equal to the binding energy (E_b) of an atom electron. The electron is ejected from low energy bound states and its kinetic energy is defined to be equal zero-point energy (also called minor potential) [214]. With higher radiation energy, the electron leaves the atom with a kinetic energy $E_{kin} = h\nu - E_b$ (photoelectric effect). For a free atom, no further structure can be detected in absorption spectrum (see figure 1.22, left) [200]. In presence of atoms near to the absorbing atom, the generated photoelectron, which has both particle as well as wave character, can be scattered back to the absorbing atom. Due to interferences between the outgoing and the backscattered photoelectron, the absorption coefficient varies periodically and a fine structure arises in the absorption spectrum, as sketched in figure 1.22 [200,216].
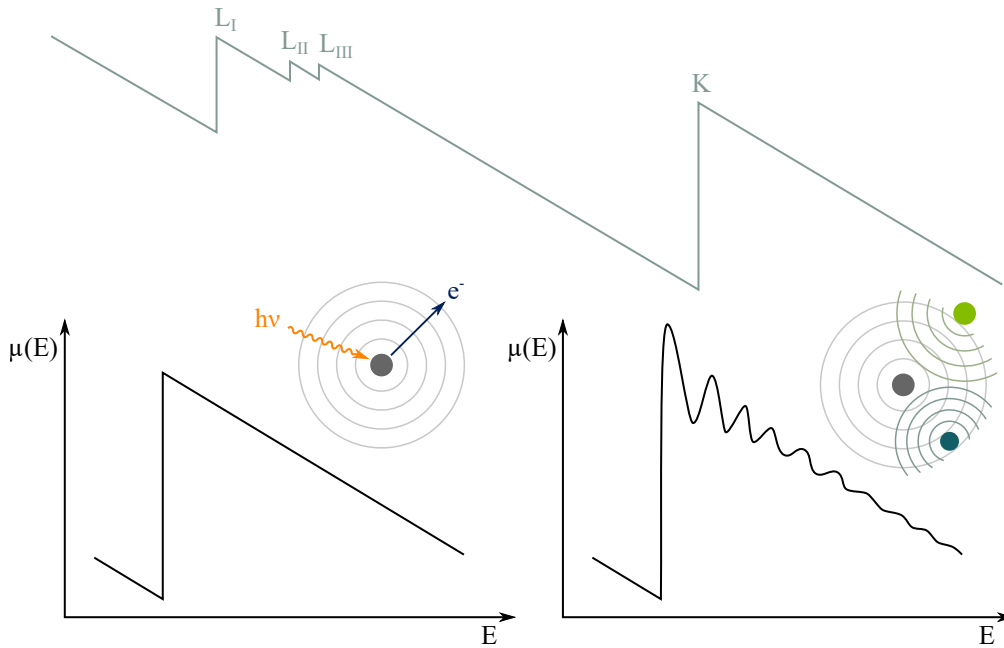
FIGURE 1.22. Schematic presentation of the absorption coefficient versus energy and the influence of nearby atoms on the spectrum [216].

This fine structure extents from about 40 eV up to 1000 eV above the absorption edge with amplitudes up to a few tenth (1-20 %) of the edge jump[216]. Usually, the energy range around only one absorption edge is recorded during a measurement. For this, the most pronounced absorption edge - usually the K-edge, in case of heavier elements also L_{III} - is selected to obtain higher signal-to-noise ratios.

In general, an absorption spectrum can be divided into three ranges, as demonstrated in figure 1.23:
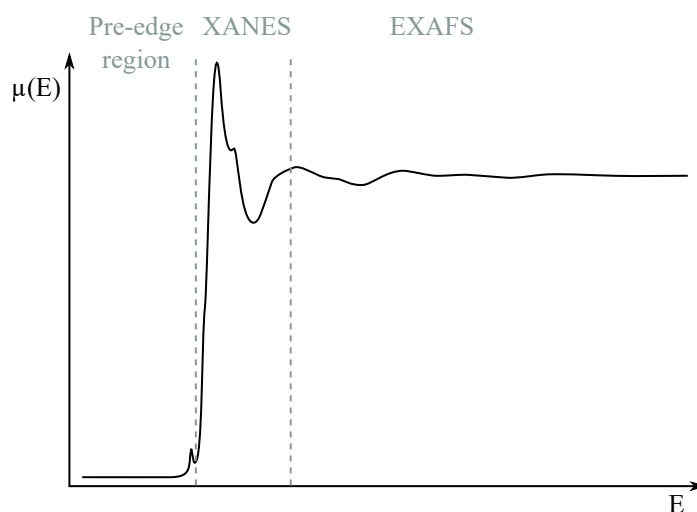
FIGURE 1.23. Categorization of an absorption spectrum in pre-edge-, XANES- and EXAFS-region[215]

The pre-edge region usually contains one or more signals at around 15-20 eV below the absorption edge[218], caused mainly by electric dipole transitions of a 1s electron to $nd - (n+1)p$ hybridized orbitals. The origin of pre-edge peak is often misinterpreted as pure $1s \rightarrow nd$ transition, which represents electric quadrupole[219]. This type of transition occurs only with significant smaller probability (and therefore signal intensity) than electric dipole transition, which includes $1s \rightarrow np$ transitions. Due to the dependence on $nd - (n+1)p$ hybridization, the pre-edge peak signal intensity is strongly influenced by the number of coordinating atoms and their geometry[218]. The affinity to hybridize can be estimated by application of the character tables of the corresponding point groups[219]. If the absorbing atom is coordinated tetrahedrally (point group T_d), which exhibits the most intense pre-edge peak signals, $p_{x,y,z}$ and $d_{xy,xz,yz}$ orbitals belong to the same irreducible representation (T_2). This allows a formation of a hybridized orbital and the electric dipole transition of a 1s electron to the p component of the $nd - (n+1)p$ hybridized orbital. On the contrary, in case of octahedrally coordinated environment (point group O_h), no irreducible representation exists to which both d and p orbitals belong. Therefore, no hybridization is possible and only electric quadrupole transitions occur[219]. The assignment of transitions, which cause

37

pre-edge signals is possible through theoretical calculations. The pre-edge signal energy can additionally be used as a probe for determining the oxidation state of the absorbing atom.

This is also possible directly by determination of the absorption edge energy in X-ray absorption near edge structure (XANES) region, but depending on the structure of the atom, transitions can occur in the edge jump region. This complicates accurate determination of the "real" absorption energy and can be avoided by the use of the pre-edge signal as a reference value (if available). As mentioned above, the absorption edges represent the photoionization of a low energy electron, excited into continuum. Both pre-edge and edge energy are related to the oxidation state of the absorbing atom[200,216]. With increasing oxidation state both signals shift to higher energies, since the core electrons are more strongly bound to a higher (positive) charged ion. Therefore, electromagnetic excitation respectively photoionization requires more energy[218]. A shift of the absorption edge can additionally be influenced by the amount and lengths of chemical bonds to the absorbing metal, since in this way electron density of involved orbitals can be influenced[215]. In general, quantitative analysis by theoretical calculations without reference spectra can only be carried out with significant error, although the accuracy increases in the last years as theoretical methods have improved. If reference spectra are available, a linear combination XANES fit can be carried out to model the sample spectra from its references and respective contribution proportions can be obtained[215].

In the extended X-ray absorption fine structure (EXAFS) region of the absorption spectrum, the local structure around the absorbing atom can be studied element specific through analysis of the oscillations after the edge and the first resonant signal ("white line"). Thus, information about distances, number and type of neighboring atoms are accessible, as outlined in section 1.4.3.5[220,221]. Since no long-range order is required in the sample, XAFS spectroscopy can be applied to manifold systems - for example solutions, liquids, molecular gases, amorphous substances, glasses and quasicrystals. This versatility enables applications in a wide range of disciplines: physics, chemistry, biology, medicine, engineering, environmental science, material science and geology[215,216].

1.4.3.2   Development of XAFS

The first absorption edge was measured by Maurice de Broglie, the older brother of quantum mechanics pioneer Luis de Broglie in 1913[222]. After turning a crystalline sample in an X-ray beam, absorption edges of Ag and Br were measured accidentally, since the crystal worked as monochromator lattice and tuned the energy of the beam falling onto the photographic plate. Due to this phenomenon, the first intense peak after the absorption edge is called "white line"[215]. In 1920, Hugo Fricke observed the first "fine structure" - energy dependent variations in the absorption coefficient $\mu(E)$ in vicinity of the X-ray absorption K-edges of magnesium, iron and chromium[223]. At the same time Gustav Hertz reported the same

behavior for L-edge absorption of caesium and neodymium[224]. In the following years further experiments[225–227] and many refinements of the experimental technique[228–231] were carried out and even first attempts were made to explain the found phenomenon[232–235]. Nonetheless, disagreements about the theoretical explanation of this phenomenon existed for the next 50 years[215,236]. Around 1970 Dale Sayers, Edward A. Stern and Farrel W. Lytle developed a sound and viable theory of XAFS, which allows to extract the local structure information from measurements[237–240]. One of the first catalyst systems XAFS was applied on, was copper-chromium catalyst supported on alumina for automobile exhaust gas emission reduction in 1974[241]. Not all of the high expectations in this promising technique could be fulfilled at that time. This was mainly due to the complex data analysis, which was not always without ambiguity. Nonetheless, XAFS proved to be a powerful and versatile tool, when applied with care[221,242].

1.4.3.3 Synchrotron radiation

The development and improvement of XAFS spectroscopy was directly connected to the growth of synchrotron radiation facilities[215,243,244]. The first utilizable synchrotron radiation facilities became accessible around 1970 - at the same time Sayers, Stern and Lytle published their theoretical work and XAFS proved its potential as analytic tool. Synchrotrons were originally developed for high-energy physics experiments and were only subsequently modified to generate high-energy electromagnetic radiation[215]. For XAFS spectroscopy an X-ray beam is required, that can be finely tuned in energy over a wide range with constant intensity. Laboratory XAFS spectrometers were developed and commercially available only years after the discovery of fine structure[221]. Since these spectrometers are equipped with an X-ray tube as source, only the continuous Bremsstrahlung of relatively low intensity in combination with a monochromator and focusing units can be employed. Thus, experiments with laboratory X-ray sources are only possible to a limited extend. Nevertheless, laboratory spectrometers were applied successfully in low-energy domain experiments. Despite this, synchrotron radiation is clearly preferred, due to its higher intensity (10^3 times higher than characteristic lines of a laboratory X-ray tube and factor 10^6 over continuous radiation), energy adjustability over a wide energy range with continuous spectrum, high collimation, flux and brilliance[216]. As a result, nearly all XAFS experiments are performed at synchrotron radiation facilities nowadays[215].

Since notions like flux, intensity and brilliance are often used associated with synchrotrons and synchrotron radiation, a short definition of these terms should be given here (see also figure 1.24). Flux is the total number of photons in the beam per second. Intensity means number of photons per time and area - therefore flux per area. Brilliance is defined as number of photons per time, source area and source angular divergence. This means a brilliant source emits many photons per second with a small source size and a small angular

divergence. To achieve a small source area and a small angular divergence of the X-ray beam, a low emittance is required, which means a small spacial spread of the electrons in the synchrotron orbit.
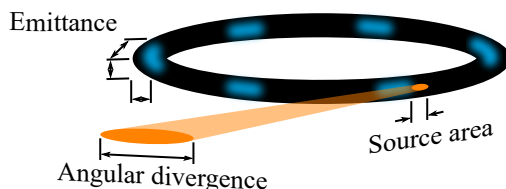
FIGURE 1.24. Definitions of parameters necessary for calculation flux, intensity and brilliance of an X-ray source.

In a synchrotron, charged particles are accelerated closely to the speed of light within an evacuated pipe on a circular orbit, guided by vertical magnetic fields. Wherever the trajectory bends, the charged particles are accelerated radially, which means in this case change of velocity vector and accelerating charged particles emit electromagnetic radiation, as described by Maxwell equations[215]. Since charged particles are brought on a circular orbit, they continuously loose a large amount of energy through radiation. Therefore, it was regarded as nuisance from particle physicists, since their particle beams loose a significant amount of kinetic energy caused by the parasitic radiation. In the first years, synchrotron radiation research was entirely dependent on high-energy physics experiments. But because of the benefits of XAFS and other related techniques and the early success of synchrotron radiation research, "second generation" sources designed solely for the production of X-rays were built[215]. In contrast to synchrotrons used by high-energy physicists, where protons or heavier ions were accelerated, electrons are used as charged particles at these facilities due to their higher efficiency in radiation output. In second generation synchrotrons, radiation is generated by bending magnets (see figure 1.25). In addition, "insertion devices" such as wigglers and undulators are introduced in third generation synchrotrons to further enhance the characteristics of the emitted radiation ($\sim 10^4$ higher brightness than binding magnets)[215] and to increase the yield in radiation by generating X-rays also on straight parts of the orbit. Fourth generation sources are currently the latest development. They will exceed the performance of previous sources by one or more orders of magnitude in essential parameters like brightness, coherence and shortness of pulse duration[245]. The most promising approaches are the development of storage rings with even lower emittance (spatial position distribution of electrons in the synchrotron orbit) than third generation sources and short wavelength free-electron lasers (FELs), which allow the generation of sub-picosecond pulses with full transverse coherence[245]. The intensity of the laser is high enough to typically destroy the sample instantly, but the flux is sufficient to generate a full diffraction pattern before[215].
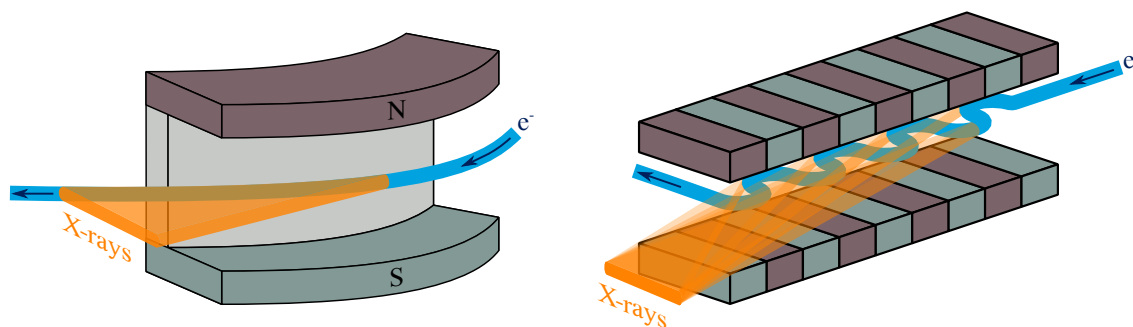
FIGURE 1.25. Schematic assembly of a bending magnet (left) and an insertion device (right) used to generate X-ray radiation at a synchrotron. The main difference between wigglers and undulators is the number of alternating magnet pairs.

1.4.3.4 Experimental modes

There are mainly two different experimental modes available for the measurement of XAFS spectra: transmission and fluorescence.

In transmission mode the X-ray flux is detected before and after the beam has passed the sample, as can be seen in figure 1.26. The relation between incident and transmitted flux or intensity is expressed in the Lambert-Beer's law $\mu(E)X = ln(\frac{I_0}{I})$ (see above in 1.4.3.1). In experiments, not the real beam fluxes can be measured, but the signals from the used ionization chambers are directly proportional. The passing beam ionizes a certain amount of the gas, that is filled in the ionization chamber. The generated charged particles are accelerated towards electrodes, which are put on high potential and the measured current is thus proportional to the amount of ionized gas atoms and also to the intensity of the beam. This imprecision with regard to data acquisition is invalid since the signal of the transmitted beam intensity is normalized on the incident beam intensity[215]. The absorption step of the spectrum measured in transmission geometry is related to the sample concentration. Since
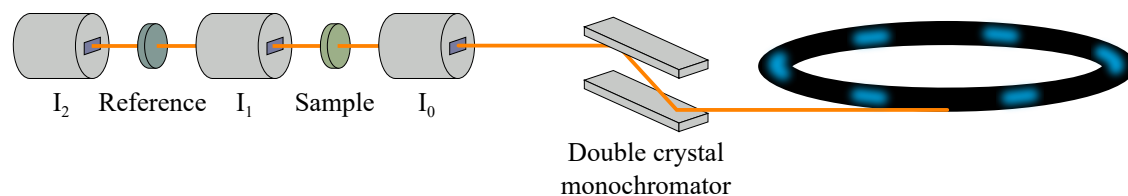
FIGURE 1.26. Schematic assembly of a transmission mode geometry. Through measurement of a reference (usually a metal foil) simultaneously to the sample measurement, energy drifts of the monochromator can be ruled out.

41

a certain edge step height is needed for data processing, investigations of very low sample concentrations are not possible.

In contrast to transmission mode geometry, no minimum sample concentration is necessary in fluorescence mode. In this case, the detector is placed 90° in horizontal plane to the incident beam and the sample is turned by 45° with respect to the beam and towards the detector as demonstrated in figure 1.27[215]. Very small concentrations of absorbing atoms can be measured, since the amount of detected fluorescence photons can be summed up easily. Due to the geometrically limited ratio of detected fluorescence photons, the quality of the obtained spectrum is normally not as high as a spectrum measured in transmission mode. The signal of the fluorescence detector (I_f) is normalized on the incident beam signal of the ionization chamber I_0. Since the operation principle of these two detector types is not comparable, an extinction of both data acquisition imprecisions does not occur, which is visible in slightly corrected Debye-Waller factors[215].
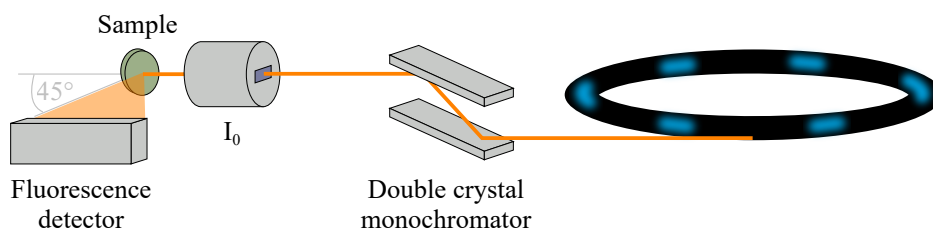
FIGURE 1.27. Schematic assembly of a fluorescence mode geometry.

Measurement of most XAFS spectra is carried out in step scan mode, which means the double crystal monochromator moves step by step to the different energies and stays there until the scan of this energy is finished. In this mode one spectra is collected on a time scale of minutes up to hours. Although quick XAFS (QXAFS) allows measurements in second to sub-second time ranges, due to a continuously moving double crystal monochromator during a spectrum, even shorter time scales can be necessary for the investigation of time-dependent phenomena. To achieve this, dispersive and ultrafast XAFS can be applied[215].

In dispersive XAFS a polychromatic beam impinges onto a bended polychromator crystal to obtain a range of Bragg angles focused on the sample (see figure 1.28). The beams of energies depending on their scattering angle pass through the sample simultaneously at different angles and are measured by a position-sensitive detector. With one X-ray shot a complete XAFS spectrum can be recorded, while no mechanical motion is required. Generally, the measurements are carried out in transmission geometry. If the flux is sufficient and the detector system is fast enough, the progress of a reaction can be followed simply by measurements after varying delay times[215].

There are several different modifications of ultrafast XAFS measurements known. One of the most common is optical pump - X-ray probe. Here, the sample is perturbed by a
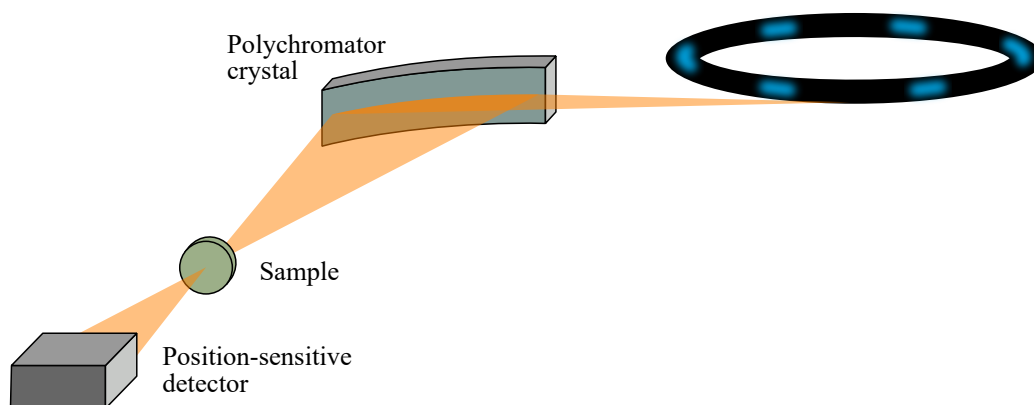
FIGURE 1.28. Schematic assembly of a dispersive mode geometry. A polychromatic beam falls on a bended polychromator crystal, which focuses the beam on the sample. Since the angle corresponds to the energy, the transmitted beam is detected dependent on position.

laser pulse and after a defined delay time measured by X-ray absorption spectroscopy. After full relaxation or replacement of the system, this sequence is repeated under variation of energy and time delay. In this way, XAFS spectra of different (very short) delay times can be obtained[215]. In another approach, the equilibrium of a system is disturbed by a fast pressure jump or rapid reactant mixing, followed by a protocol similar to optical pump - X-ray probe[215].

1.4.3.5 Theory of EXAFS

The fine structure in the EXAFS region is a quantum mechanic phenomenon based on the X-ray photoelectric effect and the interference between the generated photoelectron wave with the photoelectron wave backscattered from neighboring atoms. These quantum interferences cause an energy-dependent periodic variation of X-ray absorption probability, which is proportional to the measurable X-ray absorption coefficient. The sinusoidal oscillations of the absorption coefficient vary between total construction (the two waves are fully in phase) and total destruction (the two waves are exactly out of phase). Through analysis of these modulations, information can be extracted about structure, atomic number, structural disorder and thermal motions of nearby atoms[200,214–216].

Many derivations for the theoretical description of EXAFS were presented in the last years, varying in applied approximations[237,246,247]. One of the simplest is the well accepted "short-range single-electron single-scattering" approach[238,240,246–251], in which one electron is scattered once before returning to the absorbing atom and multiple scattering processes are excluded, as demonstrated hereinafter. To isolate and to normalize the fine structure from the spectra, the absorption coefficient as a function of the photon energy $\mu(E)$ is

subtracted by the atomic background $\mu_0(E)$ and afterwards the difference is normalized to $\mu_0(E)$. Finally, the energy dependent EXAFS function is obtained[214,216]:

$$(1.17) \qquad \chi(E) = \frac{\mu(E) - \mu_0(E)}{\mu_0(E)}$$

$\chi(E)$: Isolated and normalized fine structure dependent on E

$\mu(E)$: Absorption coefficient

$\mu_0(E)$: Atomic background

The atomic background $\mu_0(E)$ is not the absorption coefficient of a physically isolated atom, but of an atom, whose effects caused by nearby atoms, are "switched off"[218]. In the next step, the EXAFS signal $\chi(E)$ has to be transferred from E- into k-space to obtain $\chi(k)$. To achieve this, the photon energy E has to be converted into the photoelectron wave number k. By application of the equation, which describes the photoelectric effect

$$(1.18) \qquad E_{kin} = h\nu - E_b$$

in combination with de Broglie equation ($\lambda = \frac{h}{p}$) and the wave vector definition $k = \frac{2\pi}{\lambda}$, the kinetic energy E_{kin} can be expressed as follows[216]:

$$(1.19) \qquad E_{kin} = \frac{p^2}{2m} = \frac{\hbar^2 k^2}{2m} \qquad \text{whereby } \hbar = \frac{h}{2\pi}$$

p: Electron momentum

m: Electron mass

h: Planck's constant

Insertion into the initial equation 1.18 and resolving to k gives:

$$(1.20) \qquad k = \sqrt{\frac{2m}{\hbar^2}(E - E_b)}$$

E: photon energy ($E = h\nu$)

E_b: Electron binding energy

The resulting function $\chi(k)$, which describes the fine structure can be expressed as a summation over all interference pattern scattered off neighboring atoms. To reflect the periodic oscillations of the fine structure, sine functions are applied for each shell. The scattering intensity of the photoelectron is reflected in the multiplied amplitude factor:

$$(1.21) \qquad \chi(k) = \sum_{j=1}^{shells} A_j(k) \cdot sin\Phi_{ij}(k)$$

$A_j(k)$: Amplitude, scattering intensity of the jth shell

The argument of the sine function Φ_{ij} consists of the interatomic distance between the absorbing and the scattering atoms and a factor accounting for the total phase shift.

(1.22)
$$sin\Phi_{ij}(k) = sin\left[2kr_j - \phi_{ij}(k)\right]$$

r_j: Distance absorbing atom - atoms in the jth shell

$\phi_{ij}(k)$: Total phase shift

The total phase shift $\phi_{ij}(k)$ is equal to the phase shift of the backscattering atom plus twice that of the absorbing atom (outgoing and returning photoelectron)[214,216]:

(1.23)
$$\phi_{ij}(k) = 2\phi_i(k) + \phi_j(k)$$

$\phi_i(k)$: Phase shift of the absorbing atom

$\phi_j(k)$: Phase shift of the scattering atoms in the jth shell

Under consideration of relation 1.22, $\chi(k)$ can be rephrased:

(1.24)
$$\chi(k) = \sum_{j=1}^{shells} A_j(k) \cdot sin\left(2kr_j + \phi_{ij}(k)\right)$$

As can be easily seen from the equation 1.24, each coordination shell contributes to the sum in form of a sine function multiplied by an amplitude. In EXAFS analysis, all sine functions have to be considered[200]. The amplitude of each contribution contains diverse structural information:

(1.25)
$$A_j(k) = N_j S_i(k) F_j(k) exp\left(-2\sigma_j^2 k^2\right) exp\left(-\frac{2r_j}{\lambda_j(k)}\right)\frac{1}{kr_j^2}$$

Insertion in relation 1.24 gives the EXAFS equation:

(1.26)
$$\chi(k) = \sum_j N_j S_i(k) F_j(k) exp\left(-2\sigma_j^2 k^2\right) exp\left(-\frac{2r_j}{\lambda_j(k)}\right)\frac{sin\left(2kr_j + \phi_{ij}(k)\right)}{kr_j^2}$$

In the following all individual components will be explained[214,216]:

N_j: Number of backscattering atoms in the jth coordination shell. As coordination shell, atoms are considered, which are of the same type and in the same distance. In fcc or hcp metals, the number of backscatterers is $N_j = 12$, whereby in small particles the number decreases with the particle size, due to the increasing amount of surface atoms with a smaller amount of neighbors.

$F_j(k)$: Backscattering amplitude from each of the N_j neighboring atoms in j^{th} shell. Since the backscattering process is resonant in nature, the backscattering amplitude is enhanced, when the energy of the photoelectron is equal to orbital energies of the backscattering atom[214]. As each atom has its unique electron configuration, the backscattering pattern is element specific.

σ_j: Debye-Waller factor - accounts for static (σ_{stat}) and dynamic (σ_{vib}) disorders of the system. Static disorder is a consequence of slightly varying distances between atoms of

the same coordination shell and the absorbing atom. Dynamic disorder is caused by lattice vibrations of the atoms and is therefore temperature-dependent. Since this contribution can be suppressed by measurements at low temperature, determination of both, σ_{stat} and σ_{vib} is possible.

$\frac{1}{kr_j}$: Distance dependency of oscillation amplitude. Term reflects the decrease in intensity of the outgoing photoelectron wave with larger distance to the absorbing atom. This means that scattering contributions in EXAFS are mainly dominated by next and nearest neighbors, while contributions from more distant shells are represented weakly.

$sin\left(2kr_j + \Phi_{ij}(k)\right)$: Sinusoidal oscillation as a function of interatomic distances ($2kr_j$) and the phase shift (ϕ_{ij}).

Two components in the EXAFS equation account for inelastic scattering processes, which occur as the photoelectron is excited by the absorbing atom and cause a decrease of the photoelectron wave amplitude[216].

$S_i(k)$: Amplitude reducing factor - accounts mainly for multiple excitations (so-called many-body effects) in the absorbing atom i. The photoelectron looses kinetic energy by imparting energy to another electron of the atom and appears at a higher binding energy in the spectrum. This electron - so-called "passive electron" - is excited to a higher unoccupied state (shake-up) or even to an unbound state (shake-off), as sketched in figure 1.29[200,216]. Since the total absorption rate remains the same, this additional absorption process implies a loss of intensity of the primary photoelectron resulting in a reduced EXAFS amplitude[216].

$exp\left(-\frac{2r_j}{\lambda_j(k)}\right)$: This component accounts for the excitation of neighboring environment (atoms, intervening medium) by the excited photoelectron. Due to these interactions, the photoelectron life time is reduced as a function of its inelastic mean free path length $\lambda_j(k)$, which also reduces the EXAFS amplitude[214,216].
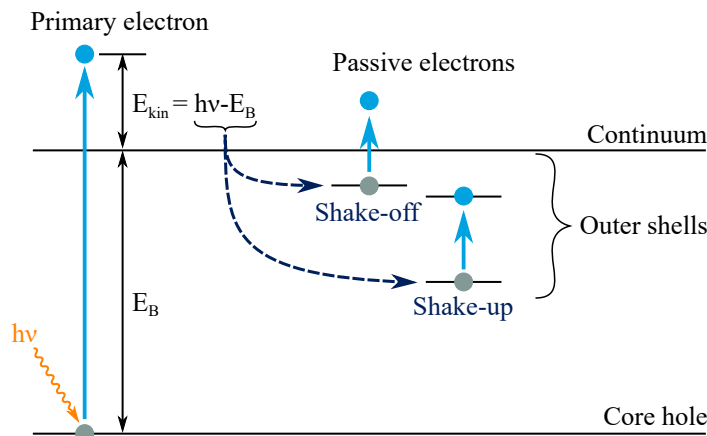
FIGURE 1.29. Shake-up and shake-off processes in the X-ray absorbing atom.

The structure determination of a system depends on the feasibility to resolve the data into individual waves corresponding to the different neighbors[216]. Through Fourier transformation of $\chi(k)$, a radial distribution function dependent on the distance (R) can be obtained. A straightforward Fourier transformation yields in an inaccurate radial distribution function, where the phase shift causes incorrect coordination shell distances and wrong intensities due to element specific backscattering amplitude. Regarding the total phase shift and the backscattering amplitude separately, the corresponding Fourier transform becomes[200,237]:

$$(1.27) \qquad \theta(R) = \frac{1}{\sqrt{2\pi}} \int_{k_{min}}^{k_{max}} k^n \chi(k) \frac{exp\left(-i\phi(k)\right)}{F_j(k)} exp\left(i2kR\right) dk$$

$\theta(R)$: Probability to find an atom at distance R

k^n: Weighting factor to distinguish between high and low Z scatterers to emphasis the important scatterer[214].

By Fourier transformation, a complex function is obtained, of which the absolute part determines the number of backscattering atoms and the disorder (reflected in Debye-Waller factor). The imaginary part can be used for absorber-scatterer distance calculation[214]. Through inverse Fourier transformation using a restricted part in R, coordination shells can be isolated. The so-called Fourier filtering is very useful in data analysis and standards obtainment, but has to be handled with care, since important contributions could be cut out in this way.[214].

1.4.3.6 Data reduction

In the following, an overview of the process of EXAFS data analysis is provided. This process can be divided into four steps of data reduction[214,218]:

a) Pre-edge background removal

b) Atomic background removal and data normalization

c) Conversion into k-space

d) Fourier transformation

But before the fine structure can be extracted and analyzed, the experimental data have to be converted into a spectrum. Dependent on the experimental mode, which was chosen for the measurement, there are differences in data processing.

For transmission mode, according to Lambert-Beer's law, the absorption coefficient is proportional to the natural logarithm of the incident beam intensity referred to the transmitted intensity: $\mu(E) \sim ln\frac{I_0}{I}$. In contrast, for data collected in fluorescence mode, the absorption coefficient is proportional to the fluorescence intensity normalized by the incident intensity: $\mu(E) \sim \frac{F}{I_0}$.

a) Pre-edge background removal   Since in EXAFS analysis only the energy region above the absorption edge is of interest, all contributions of lower energy absorption edges and Compton-scattering to the absorption coefficient $\mu(E)$ have to be subtracted. Usually, a Victoreen-spline is used to model the shape of the pre-edge region, but also simple linear or quadratic polynomials can be used. Afterwards, the fitted function is extrapolated beyond the edge to the end of the spectrum (as demonstrated in figure 1.30) and subtracted, resulting in the "elemental absorption coefficient" as already described by Lytle, Sayers and Stern in 1975[218,239].
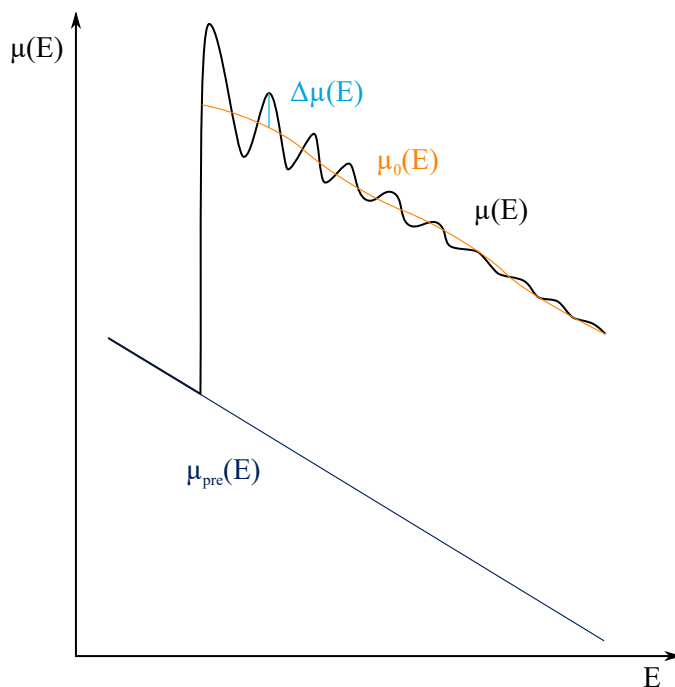
FIGURE 1.30. Schematic procedure for pre-edge and atomic background removal.

b) Atomic background removal and data normalization   As outlined in section 1.4.3.5, to obtain the isolated fine structure, the absorption coefficient of the sample $\mu(E)$ has to be subtracted by the absorption coefficient of the same atom, but in an isolated surrounding without any backscatterer. This so-called atomic background $\mu_0(E)$ is generally not known, because it can not be calculated or is accessible experimentally. Since in the "elemental absorption coefficient" obtained after subtraction of the pre-edge background still "background factors" (spectrometer baseline, beam harmonics, elastic scattering, etc.) in the EXAFS spectrum are present, a discrete background removal is necessary, as shown schematically in figure 1.30. Therefore, the atomic background $\mu_0(E)$ is often approximated as the smooth part of the measured total absorption $\mu(E)$. Various fitting procedures were developed for this purpose, but the most common ones are polynomial splines or B-splines.

These functions are defined over a set of intervals, whereby each interval contains a polynomial and the nodes of each interval are tied, so the function is continuous across the nodes. By application of a least squares fitting procedure, low frequency background components can be removed from $\mu(E)$ without affecting the higher frequent EXAFS oscillations. Subsequently, the difference is normalized by the atomic background. The quality of this procedure can be determined by inspecting the Fourier transformation. When the used polynomial order or the number of intervals are set too high, parts of the EXAFS oscillations are removed as well. On the other hand, when the polynomial order or the number of intervals is too low, background artifacts cause signals at a unphysical distance around 1 Å in the Fourier transformation[216,218].

c) Conversion into k-space To convert $\chi(E)$ into k-space, the relation $k = \sqrt{\frac{2m}{\hbar^2}(E - E_b)}$ derived in equation 1.20, section 1.4.3.5 has to be applied. In this case, the electron binding energy E_b corresponds to the edge energy of the spectrum and this value is needed in this equation to calculate k. In general, the first inflection point in the first derivative of the spectrum is used for this purpose[216].

d) Fourier transformation In the last step, after selection of a suitable k-interval in $\chi(k)$ the Fourier transformation can be carried out. Very small k values lead to artifacts at unphysical short distances in R-space, while too large k values yield in a small signal-to-noise ratio.

Fit of the obtained experimental EXAFS spectra can be carried out in k-space or in R-space[252]. Main advantages lie in the fit in k-space, since truncation errors during Fourier transformation can be avoided, noise built-up problem is minimized and the variance in R-space has only one maxima, which makes the least squares iterative process during spectrum fit much more stable[214,216]. Throughout the fit, it is important to know the maximal number of freely iterable parameters to avoid overdeterminacy. According to Nyquist theorem, the so-called variance is defined as follows[253]:

$$(1.28) \qquad N_{ind} = \frac{2\Delta k \Delta R}{\pi} + 2$$

N_{ind}: Number of independent points, variance

Δk: Range in k-space usable for analysis

ΔR: Range in R-space usable for analysis

Usually, the variance as well as the number of actually used parameters are considered in the fitting error calculation.

IRON IN HOMOGENEOUS CROSS-COUPLING REACTIONS

T he determination of the active species in iron catalyzed cross-coupling reactions as key step for the elucidation of the reaction mechanism was subject of discussions in the last decades. Iron shows a noteworthy catalytic performance when added to the reactants in presence of a Grignard compound. Literature is in agreement, that the initial iron species are reduced by the Grignard agent, but publications differ in the formed species, its oxidation state and subsequently in the proposed reaction mechanism. This fact can be explained by the limited number of analytic and spectroscopic techniques that can be applied - inter alia due to air and moisture sensitivity of the formed species and the paramagnetism of iron. Five proposed catalytic active species and reaction mechanisms are used as hypotheses in the following publication.

2.1   Active Species Verification in Cross-Coupling Reactions

By quantitative determination of the formed homocoupling product of the Grignard compound during addition of one, two, three and four equivalents of reduction agent, the amount of electrons transfered to iron could be calculated. These results were combined with UV/Vis-, Raman- and XAFS spectroscopy, to get access to the intermediate stages during the reduction process of iron and the formation of the catalytic active species. Addition of three equivalents of Grignard compound lead to a stable species, which could not be further reduced by addition of a fourth equivalent. This species was identified to be the catalytic active compound by application in cross-coupling reactions. A structural clarification was carried out by application of EXAFS analysis, which allowed to present a reaction mechanism based on the found results.

Participations in this publication

W. Desens & T. Werner: Quantification of biphenyl;
R. Schoch & M. Bauer: XAFS analysis, UV/Vis spectroscopy, Raman spectroscopy, quantification of biphenyl

X-ray Spectroscopic Verification of the Active Species in Iron-Catalyzed Cross-Coupling Reactions

Roland Schoch,[a] Willi Desens,[b] Thomas Werner,*[b] and Matthias Bauer*[a]

53

COMMUNICATION
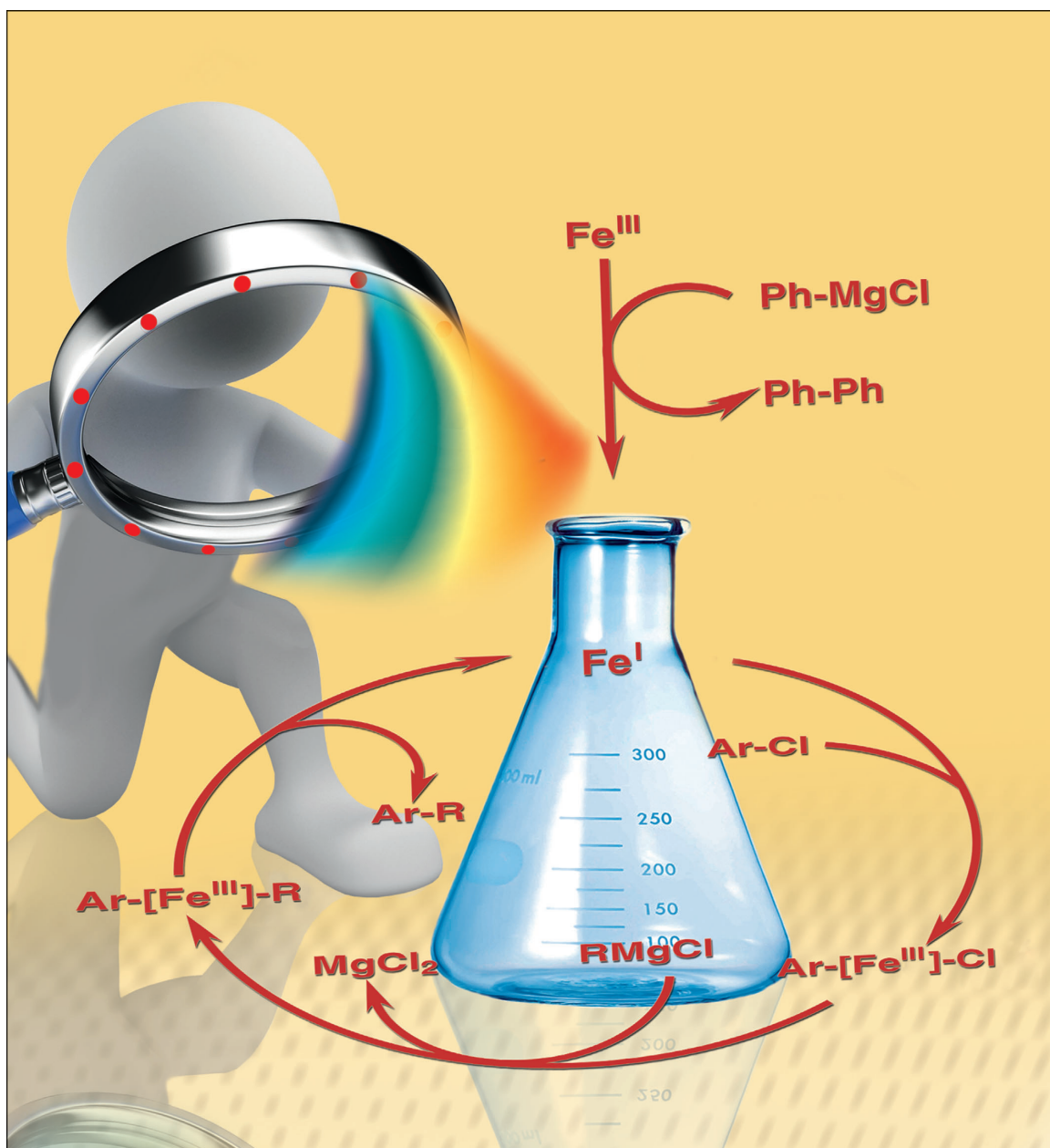
Over the past two decades iron catalysis has become a powerful tool in organic synthesis.[1] Cross-coupling reactions doubtless rank among the most important of these reactions, because they allow effective formation of carbon scaffolds.[1f,h–q,2] Nowadays, these transformations are a standard tool for the preparation of fine chemicals and biologically active compounds on both laboratory and industrial scales.[1d] Although cross-coupling reactions are dominated by palladium complexes, iron complex catalysts offer an alternative of increasing importance due to their easy accessibility, short reaction times and broad functional group tolerance.[1b,g] Under established conditions alkyl or aryl Grignard reagents are coupled with aryl chlorides, triflates and tosylates.[1e,g,n,2a,3a]

Despite the importance of iron-catalyzed cross-coupling reactions and intensive investigations, the mechanism of this reaction is still subject to ongoing discussion.[1m,3] Spectroscopic studies are very limited due to the paramagnetic character of the species formed.[3a] Hence, mechanistic findings are mainly based on investigations of potential intermediates.[3a] In contrast to palladium-catalyzed cross-couplings, for which detailed mechanistic knowledge exists,[4] this gap prevents the directed development of improved iron catalysts for cross-coupling reactions.

X-ray absorption spectroscopy represents a method to bridge this gap.[5] It provides element specific clarification of local structure and oxidation state of metal centers through EXAFS (extended X-ray absorption fine structure) and XANES (X-ray absorption near edge structure) spectroscopy.[6] Employing these methods, the type and number of ligands as well as their distance from the catalytically active metal center can be determined in situ.[7] Despite these advantages, which were already used for investigations of different cross-coupling and Grignard reactions,[5,8] to the best of our knowledge no XAS investigations on iron-catalyzed cross-coupling reactions have been reported to date. This is even more surprising, because this type of investigation would enable a comparison of the five suggested mechanisms proposed to date for this type of cross-coupling:[3a]

1) Kochi et al.[9] postulate a "soluble iron species" of unspecified oxidation state, which exists as an aggregate complexed by Grignard compounds. In this case, Fe−Fe pairs characteristic of a metal cluster would be expected in the EXAFS analysis.

2) Bogdanovic et al.[10] suggest a heterobimetallic inorganic Grignard complex [Fe^{-II}(MgCl)$_2$]$_n$, which would show Fe−Mg pairs in the EXAFS spectrum.

3) Fürstner et al.[11] describe the formation of Fe^{II} organoferrates [R$_n$Fe^{+II}]$^{2-n}$. This type of compound would exhibit only Fe–C contributions to the radial distribution function.

4) Noda et al.[12] propose diaryl Fe^{II} compounds stabilized by TMEDA, which would show similar EXAFS characteristics to the organoferrates described in point 3).

5) Norrby et al.[3b] suppose a catalytically active Fe^{I}-species, which is not further structurally specified.

Herein, these proposals will be discussed on the basis of X-ray-spectroscopic investigations. According to the literature,[10] a maximum amount of four equivalents Grignard compound are required to form the active iron species. Analogously, the reaction products of iron(III)-acetylacetonate Fe(acac)$_3$ and one to four equivalents phenylmagnesiumchloride PhMgCl in THF/NMP were examined to identify the species formed through activation of the pre-catalyst Fe(acac)$_3$.[13]

Figure 1 shows the energy-calibrated XANES spectra during addition of 1–4 equivalents of PhMgCl to Fe(acac)$_3$ in THF/NMP. To emphasize small changes, the first derivatives[14] of the spectra are displayed as well. Two spectral regions can be distinguished: The pre-edge signal (prepeak)[15] at an energy of 7.10–7.11 keV (signal A) and the absorptions edge at a range of 7.11–7.12 keV (signals B and C). The prepeak position of the pre-catalyst Fe(acac)$_3$ is located at 7.106 keV and shifts after addition of one equivalent PhMgCl to a smaller value of 7.104 keV. Whereas this prepeak is caused by a 1s→3d transition, the decreased resonance energy reflects the transition from an s^{0}d^5 to an s^{0}d^6 electron configuration, which corresponds to a reduction from Fe^{III} to Fe^{II}. This energy does not change with addition of further equivalents, but the prepeak intensity and the shape and energy of the absorption edge (signals B and C)

[a] R. Schoch, Prof. Dr. M. Bauer
Fachbereich Chemie, TU Kaiserslautern
Erwin-Schrödinger-Str. 54, 67663 Kaiserslautern (Germany)
Fax: (+49) 631-205-4676
E-mail: bauer@chemie.uni-kl.de
[b] W. Desens, Dr. T. Werner
Leibniz-Institut für Katalyse e.V. an der Universität Rostock
Albert-Einstein-Str. 29a, 18059 Rostock (Germany)
Fax: (+49) 381-1281-51326
E-mail: thomas.werner@catalysis.de
Supporting information for this article is available on the WWW under http://dx.doi.org/10.1002/chem.201303340.
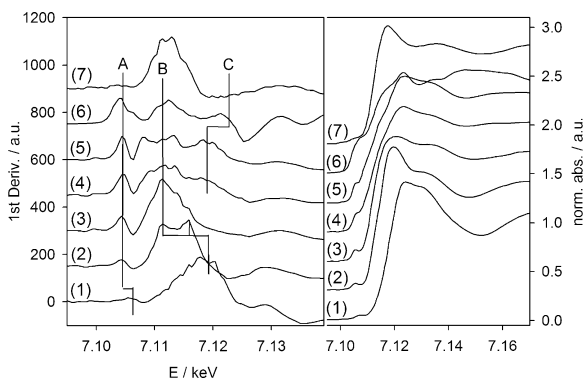

Figure 1. XANES spectra (right) and their derivatives (left) of the pre-catalyst Fe(acac)$_3$ (1) and after addition of one to four equivalents (2–5) PhMgCl in comparison to Fe^0 (6) and under reaction conditions (7).

T. Werner, M. Bauer et al.

changes in a systematic way. The first derivative of the pre-catalyst spectra shows only one signal (B), which shifts significantly in energy after addition of one equivalent of PhMgCl and then exhibits an Fe[II] characteristic doublet structure.[14] With addition of the second equivalent, the higher-energetic signal of the doublet disappears. A related spectrum to the resulting first derivative is not known in the literature so far. With addition of three equivalents, another signal appears in the derivative, which can also be found in the spectrum of an iron foil (Fe[0]). The addition of the fourth equivalent causes no further changes in the spectrum, indicating that the activation of the catalyst is finished after the addition of three equivalents PhMgCl.

Although the XANES spectra of the active species might lead to speculation about a metalloide species due to the presence of the signals A, B and C, the shape and position of the signals deviate from that of an Fe[0] species. Even size-effects do not cause considerable changes in spectra of Fe[0] nanoparticles compared with spectra of a bulk Fe foil.[16] Hence the broadened shape of the prepeak signal is not the result of Fe[0] nanoparticle formation.[17] The rather distinct separation of the prepeak from the main-edge indicates a certain ionic character. Because the Fe[0] and Fe[II] oxidation states can be excluded due to the XANES shape, the spectra of three and four equivalents of PhMgCl are thus assigned to an oxidation state of Fe[I], in keeping with the findings of Adams et al. in iron-catalyzed Negishi reactions.[18]

This argument is supported by quantification of the organic redox product biphenyl (Ph−Ph). It is formed by an oxidative coupling of two Ph[−] during the reduction of Fe[III]. Because β-hydride elimination can be excluded as side path, the number of electrons transferred to iron can be determined by quantification of the Ph−Ph formed by means of gas chromatography.[19] Because no organo-halide is present

as potential coupling reagent at this stage, reversible redox-pairs can be excluded.[18] Fe(acac)$_3$ was treated with 1–10 equiv PhMgCl and the resulting reaction mixtures were analyzed by quantitative GC.[20] In presence of one equivalent of PhMgCl, full conversion to biphenyl was observed. It is likely, that the phenyl-anion reduced Fe[III] to Fe[II] under formation of a phenyl-radical, two of which can couple forming the biphenyl observed. Analogous homo-couplings of Grignard compounds in presence of Fe[III]-complexes have already observed.[18, 20] With the addition of two equivalents of PhMgCl, only 65 % of the theoretical amount of biphenyl is formed through reduction of Fe[III] to Fe[I] (Table 1, entry 2). This suggests a formal alteration of the oxidation state from +3 to +1.7. In contrast, the addition of three equivalents of Grignard reagent leads to a formal change in oxidation state from +3 to +1. If one equivalent of Fe(acac)$_3$ is converted with an excess of four or ten equivalents PhMgCl, only small differences in the formed oxidation states are visible compared to addition of three equivalents.

The trends observed in the XANES spectra and the results of the GC investigations are reflected in the EXAFS spectra as shown in Figure 2. The nuclearity of the iron compound formed during the activation process and the nature of the ligands coordinated to the metal core can both be extracted from the EXAFS spectra. In course of the activation, the EXAFS signal is dominated by iron–iron contributions because of the high backscattering amplitude of iron. The coordination number of iron follows no regular behavior, as can be seen in Table 1. Based on the Fe−Fe coordination number of 0.7 obtained after reaction with one equivalent of PhMgCl the formation of dimers can be deduced. The iron–iron distance of 2.55 Å is consistent with the partial reduction of the iron centers deduced from the XANES spectra and literature values (2.46–2.69 Å) for Fe[II] dimers

Table 1. Structural parameters, obtained through fitting of the experimental EXAFS spectra.

Entry	Sample	Abs−Bs[a]	N(Bs)[b]	R(Bs)[c] [Å]	σ[d] [Å]	R[e] [%]	Transferred e[−] oxidation state of Fe
1	Fe(acac)$_3$	Fe−O(acac)	*6*	1.99±0.02	0.067±0.007	24.10	–
		Fe−C	*6*	2.93±0.03	0.084±0.008		
2	+1 equiv PhMgCl	Fe−O(acac)	3.9±0.2	2.04±0.02	0.081±0.004	19.85	1.0 equiv
		Fe−O(THF/NMP)	2.0±0.2	2.20±0.02	0.039±0.004		+2.0
		Fe−Fe	0.7±0.3	2.55±0.03	0.100±0.040		
3	+2 equiv PhMgCl	Fe−C(Ph)	1.4±0.1	1.94±0.02	0.112±0.011	7.97	1.3 equiv
		Fe−O(THF/NMP)	0.4±0.1	2.19±0.02	0.032±0.003		+1.7
		Fe−Fe	5.1±0.5	2.42±0.02	0.102±0.010		
		Fe−Mg	1.6±0.3	2.74±0.03	0.097±0.040		
4	+3 equiv PhMgCl	Fe−C(Ph)	1.1±0.1	1.97±0.02	0.032±0.003	23.32	2.0 equiv
		Fe−O(THF/NMP)	1.5±0.1	2.07±0.02	0.039±0.004		+1.0
		Fe−Fe	2.0±0.4	2.55±0.03	0.112±0.011		
		Fe−Mg	0.5±0.3	2.62±0.03	0.032±0.015		
5	+4 equiv PhMgCl	Fe−C(Ph)	0.8±0.1	1.95±0.02	0.059±0.006	19.03	2.3 equiv
		Fe−O(THF/NMP)	1.4±0.1	2.10±0.02	0.032±0.003		+0.7
		Fe−Fe	2.6±0.4	2.52±0.02	0.112±0.011		
		Fe−Mg	1.0±0.3	2.59±0.03	0.050±0.015		
7	Reaction cond. (+4 equiv PhMgCl+10 equiv **1b**)	Fe−C(Ph)	1.5±0.1	1.93±0.02	0.112±0.011	10.29	–
		Fe−O(THF/NMP)	0.4±0.1	2.14±0.02	0.045±0.004		
		Fe−Fe	6.7±0.4	2.44±0.02	0.100±0.040		
		Fe−Mg	1.8±0.3	2.80±0.03	0.097±0.040		

[a] Abs=X-ray absorbing atom, Bs=backscatterer (neighbor atom). [b] Number of neighbor atoms; italicized numbers are crystallographic values. [c] Distances Abs−Bs. [d] Debye–Waller factor, considers static and vibronic disorder. [e] Quality of the fit.
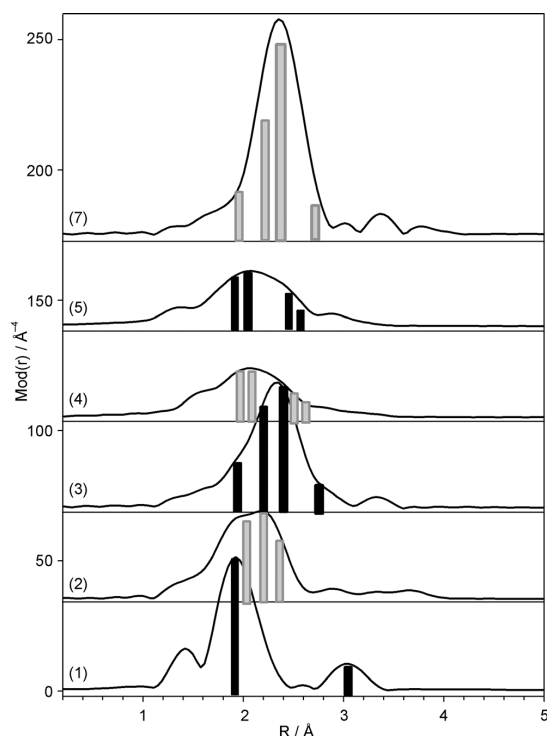
55

Active Species in Iron-Catalyzed Cross-Coupling Reactions

COMMUNICATION

Figure 2. Fourier-transformed EXAFS spectra of the pre-catalyst Fe-(acac)₃ (1) after addition of one to four equivalents PhMgCl (2–5) and under reaction conditions (7) with 2-chloropyridine as coupling reagent. The constitutive shells are indicated as bars.[21]

with direct Fe–Fe contact and bridging C- or N-containing ligands (e.g., [Fe(mes)₂]₂ or [Fe(tim)]₂).[22] With two equivalents PhMgCl the number of iron–iron contacts increases to 5.1. Thereby the presence of iron-clusters with a size of 13 ± 2 atoms can reasonably be assumed.[23] GC quantification of the biphenyl formed, suggests a formal oxidation number of +1.7.[23] A fractional oxidation number, such as 1.7, cannot be realized in a molecular compound and supports the cluster formation hypothesis. The iron–iron distance of 2.42 Å extracted, on the other hand, is in the lower range of documented values for multinuclear Fe^{II} compounds[24] and supports the ascertained number electrons transferred. Surprisingly, the addition of three and four equivalents PhMgCl causes a decrease in aggregation from Fe₁₃ to Fe₃₋₄. The oxidation state determined from GC analysis is Fe^I, which is verified by the Fe–Fe distance of 2.53 Å.[25] In general the error in the determination of the iron core size by EXAFS spectroscopy is small, because the Fe–Fe coordination number excludes the presence of larger clusters.
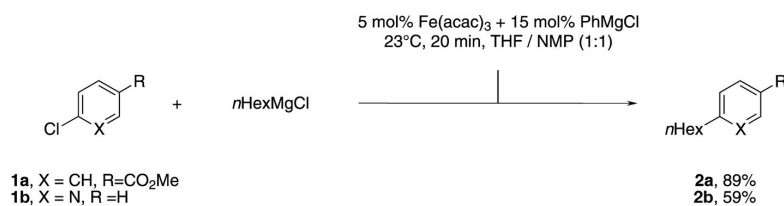
Besides Fe–Fe pairs, contributions of the lighter atoms present (Table 1) also provide information about the ligands stabilizing the iron core. After addition of one equivalent of PhMgCl, Fe–O contributions are found, which can be assigned to the pre-catalyst Fe(acac)₃.[26] Because all PhMgCl

was consumed by the formation of Ph-Ph, the coordination of phenyl residues can be excluded. The coordination number of four determined agrees well with UV/Vis measurements, which indicated that 65% Fe–O(acac) signal signal remained.[27] In addition to the first Fe–O shell, a second contribution of a lighter backscatterer at a distance of 2.2 Å could be detected, which is attributed to bridging, neutral ligands like THF or NMP.[28] NMP is known to stabilize small nanoparticles.[29] Further contributions, which could indicate coordinating MgX groups, were not found after addition of one equivalent of PhMgCl. This changes with addition of the second equivalent PhMgCl. Raman and UV/Vis-measurements detect only marginal Fe–O(acac) contributions.[30] An Fe–C bond with a length of 1.94 Å can be deduced, which suggest an average of 1.4 coordinating phenyl residues.[31] The sterically demanding aryl groups coordinate to Fe^I at a distance of 2.0 Å.[18,32] Because 1.3 equivalents of phenyl anion were consumed forming Ph–Ph, 0.7 equivalents remain formally available. To obtain an EXAFS coordination number of 1.4, the phenyl groups must act as bridging ligands. Furthermore, every iron center is stabilized by 1.6 Mg atoms at a distance of 2.74 Å, which can be attributed to Fe–Mg(–Cl) according to literature.[10] The coordination is complemented through coordination of 0.5 THF/NMP ligands at a distance of 2.2 Å.[28b]

Although addition of a third equivalent PhMgCl causes significant alterations in the Fe–Fe core, the coordination numbers in the ligand shells change only slightly. The number of coordinating Ph⁻ residues decrease to one because two equivalents of Ph⁻ are consumed in reduction process the Fe–C coordination number obtained by EXAFS coincides exactly with the quantitative GC analysis results. In contrast, the number of THF/NMP ligands increases slightly, whereas their distance from the Fe–Fe core decreases by 0.12 to 2.07 Å. These Fe–O distances are known for ether compounds coordinating on low-valent iron-centers.[8a,b] The Fe–Mg coordination number decreases to 0.5 when three equivalents of PhMgCl are used, accompanied by a shorter bond length of 2.62 Å. This relatively short distance is characteristic for a strong covalent interaction between magnesium ligands and an Fe₃ core.[8a,33]

Through addition of a fourth equivalent of PhMgCl, no further structural changes were observed. The results of the EXAFS analysis correspond to the XANES evaluation. Both methods together with GC analysis, Raman and UV/Vis spectroscopy demonstrate that only three equivalents of reduction reagent PhMgCl are necessary to form the catalytically active species. Furthermore the data show that in contrast to iron-catalyzed Negishi couplings, the active species is not characterized by Fe–X (X=Cl⁻, Br⁻) bonds, but by Fe–R (R=Ph⁻) bonds.[18]

Finally, after structural determination of the species formed in the activation process, the catalytic activity of these species was demonstrated. Hereto 5 mol% Fe(acac)₃ were converted with 15 mol% PhMgCl (Scheme 1). In presence of the in situ formed catalyst a cross-coupling reaction between aryl halide **1a** and nHexMgCl to form product **2a**

© 2013 Wiley-VCH Verlag GmbH & Co. KGaA, Weinheim **www.chemeurj.org** 15819

T. Werner, M. Bauer et al.

Scheme 1. Test reactions and yields.

1a, X = CH, R=CO₂Me
1b, X = N, R =H

2a, 89%
2b, 59%

with a yield of 89% could be conducted. The yield of an analogous reaction with *n*HexMgBr is documented with 91% yield in ref. [2a]. In general, cross-coupling of heterocyclic compounds with *n*HexMgCl is possible under similar reaction conditions. The conversion of the pyridine derivate **1b** leads to product **2b** in moderate yield of 59% (Scheme 1). However, with *n*HexMgBr a 91% yield could be achieved.[34]

The XANES spectrum of the spectroscopic "resting state" under reaction conditions as applied in the first example is shown in Figure 1. It displays the same spectral signatures as the spectrum of an Fe^{II} species with two equivalents PhMgCl. Nevertheless, EXAFS data imply the formation of larger nanoparticles as indicated by a higher Fe—Fe coordination number.

Although XAS only gathers the average spectra of all species present in the reaction mixture, the mechanism displayed in Scheme 2 can be deduced based on the spectroscopic and catalytic data presented. In the first step the pre-catalyst Fe(acac)₃ is reduced to the catalytically active Fe^I species with an oxidation state. Subsequently an oxidative addition of the organohalide occurs, associated with a change of the oxidation state from Fe^I to Fe^{III}. The spectroscopic observation of Fe^{II} substantiates the presence of Fe nanoparticles in this case. In their core, Fe^I centers persist. Averaged with the Fe^{III} centers from the oxidative addition on the particle surface this yields a mean oxidation
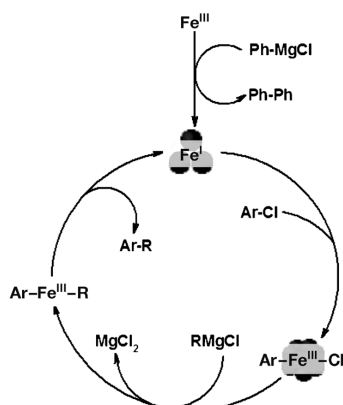
state of Fe^{II}. The averaged Fe—Fe coordination number corresponds to a cluster diameter of approximately 10 Å.[23c] Clusters of that size exhibit a surface atom (Fe^{III}) to bulk atom (Fe^I) ratio of 1:1,[35] which would result in an observed Fe^{II}.

Subsequent transmetallation and ensuing reductive elimination with release of the product and regeneration of the active catalyst has not been experimentally demonstrated so far, but is certainly plausible. Based on XAS results, a composition of Fe₃(MgCl)₃L₃ is possible. The oxidation state obtained from XANES spectra and GC analysis is Fe^I, which is in agreement with the recent study of Norrby et al. who also found that the Grignard reagent alone can only reduce the iron pre-catalyst to Fe^I.[36]

The XAS results presented allow the assessment of the non-spectroscopic mechanistic studies of iron cross-coupling reactions reported to date. Based on the oxidation state of Fe^I for the active species determined by XANES and GC analysis, it is possible to preclude hypotheses 2,[10] 3[11] and 4,[12] because these species have oxidation states of −II and +II. Nevertheless the suggestion of Bogdanovic et al.[10] postulates a structure element with an Fe—Mg bond, which was also advanced by Kochi.[9] The proposal assumes an agglomeration, the extent of which could only be demonstrated to be very small by the EXAFS results described herein. The oxidation state found agrees with that established by Norrby.[3b]

Comparisons with related studies[37] suggest that the oxidation state of the active species depends on the nature of the Grignard reagent, which is based on coordination of the organic Grignard reagent. Further systematic studies to this point are planned for the near future.

Experimental Section

X-ray absorption measurements were carried out at beamlines XAS and X1 at the synchrotrons ANKA (Karlsruhe) and HASYLAB (Hamburg). All measurements at the Fe K edge (7.112 keV) were performed in transmission under application of a Si(111) double crystal monochromator and N₂-filled ionization chambers in a cell, which allows for work under inert conditions. Details of the experimental procedure and treatment of the date are found in the Supporting Information, as well as details of the GC analysis and sample preparation.

Acknowledgements

Scheme 2. Proposed mechanism of Fe-catalyzed cross-coupling reactions.

Active Species in Iron-Catalyzed Cross-Coupling Reactions

COMMUNICATION

[1] a) C. Bolm, J. Legros, J. Le Paih, L. Zani, *Chem. Rev.* **2004**, *104*, 6217–6254; b) W. M. Czaplik, M. Mayer, J. Cvengros, A. J. von Wangelin, *ChemSusChem* **2009**, *2*, 396–417; c) *Iron Catalysis in Organic Chemistry* (Ed.: B. Plietker), Wiley-VCH, Winheim, **2008**; d) M. Beller, A. Zapf, W. Mägerlein, *Chem. Eng. Technol.* **2001**, *24*, 575–582; e) O. M. Kuzmina, A. K. Steib, D. Flubacher, P. Knochel, *Org. Lett.* **2012**, *14*, 4818–4821; f) R. Martin, A. Fürstner, *Angew. Chem.* **2004**, *116*, 4045–4047; *Angew. Chem. Int. Ed.* **2004**, *43*, 3955–3957; g) E. Nakamura, N. Yoshikai, *J. Org. Chem.* **2010**, *75*, 6061–6067; h) R. B. Bedford, E. Carter, P. M. Cogswell, N. J. Gower, M. F. Haddow, J. N. Harvey, D. M. Murphy, E. C. Neeve, J. Nunn, *Angew. Chem.* **2013**, *125*, 1323–1326; *Angew. Chem. Int. Ed.* **2013**, *52*, 1285–1288; i) D. Castagnolo, M. Botta, *Eur. J. Org. Chem.* **2010**, 3224–3228; j) S. K. Ghorai, M. Jin, T. Hatakeyama, M. Nakamura, *Org. Lett.* **2012**, *14*, 1066–1069; k) B. Scheiper, M. Bonnekessel, H. Krause, A. Fürstner, *J. Org. Chem.* **2004**, *69*, 3943–3949; l) G. Seidel, D. Laurich, A. Fürstner, *J. Org. Chem.* **2004**, *69*, 3950–3952; m) A. Fürstner, A. Leitner, *Angew. Chem.* **2002**, *114*, 632–635; *Angew. Chem. Int. Ed.* **2002**, *41*, 609–612; n) A. Fürstner, M. Méndez, *Angew. Chem.* **2003**, *115*, 5513–5515; *Angew. Chem. Int. Ed.* **2003**, *42*, 5355–5515; o) S. Kawamura, T. Kawabata, K. Ishizuka, M. Nakamura, *Chem. Commun.* **2012**, *48*, 9376–9378; p) Z. Mo, Q. Zhang, L. Deng, *Organometallics* **2012**, *31*, 6518–6521.

[2] a) A. Fürstner, A. Leitner, M. Mendez, H. Krause, *J. Am. Chem. Soc.* **2002**, *124*, 13856–13863; b) H. Shinokubo, K. Oshima, *Eur. J. Org. Chem.* **2004**, 2081–2091.

[3] a) B. D. Sherry, A. Fürstner, *Acc. Chem. Res.* **2008**, *41*, 1500; b) J. Kleimark, A. Hedström, P.-F. Larrson, C. Johansson, P.-O. Norrby, *ChemCatChem* **2009**, *1*, 152–161; c) K. Weber, E.-M. Schnöckelborg, R. Wolf, *ChemCatChem* **2011**, *3*, 1572–1577; d) Q. Ren, S. Guan, F. Jiang, J. Fang, *J. Phys. Chem. A* **2013**, *117*, 756–764; e) J. K. Kochi, *J. Organomet. Chem.* **2002**, *653*, 11–19.

[4] N. Miyaura, *Cross-Coupling Reactions: A Practical Guide; Topics in Current Chemistry*, Springer, Berlin, **2002**.

[5] L. E. Aleandri, B. Bogdanović, C. Dürr, S. C. Huckett, D. J. Jones, U. Kolb, M. Lagarden, J. Rozière, U. Wilczok, *Chem. Eur. J.* **1997**, *3*, 1710–1718.

[6] a) H. Bertagnolli, T. S. Ertel, *Angew. Chem.* **1994**, *106*, 15–37; *Angew. Chem. Int. Ed. Engl.* **1994**, *33*, 45–66; b) M. P. Feth, C. Bolm, J. P. Hildebrand, M. Köhler, O. Beckmann, M. Bauer, R. Ramamonjisoa, H. Bertagnolli, *Chem. Eur. J.* **2003**, *9*, 1348–1359.

[7] a) M. Bauer, G. Heusel, S. Mangold, H. Bertagnolli, *J. Synchrotron Radiat.* **2010**, *17*, 273–279; b) M. Bauer, C. Gastl, *Phys. Chem. Chem. Phys.* **2010**, *12*, 5575–5584.

[8] a) L. E. Aleandri, B. Bogdanovic, A. Gaidies, D. J. Jones, S. Liao, A. Michalowicz, J. Roziere, A. Schott, *J. Organomet. Chem.* **1993**, *459*, 87–93; b) W. Hörner, H. Bertagnolli, *J. Organomet. Chem.* **2002**, *649*, 128–135.

[9] M. Tamura, A. Kochi, *J. Am. Chem. Soc.* **1971**, *93*, 1487–1489.

[10] a) L. E. Aleandri, B. Bogdanovic, P. Bons, C. Dürr, A. Gaidies, T. Hartwig, S. C. Huckett, M. Lagarden, U. Wilczok, R. A. Brand, *Chem. Mater.* **1995**, *7*, 1153–1170; b) B. Bogdanovic, M. Schwickardi, *Angew. Chem.* **2000**, *112*, 4788–4790; *Angew. Chem. Int. Ed.* **2000**, *39*, 4610–4612.

[11] A. Fürstner, R. Martin, *Chem. Lett.* **2005**, *34*, 624–629.

[12] D. Noda, Y. Sunada, T. Hatakeyama, M. Nakamura, H. Nagashima, *J. Am. Chem. Soc.* **2009**, *131*, 6078–6079.

[13] In scenario 2 a β-hydride elimination is assumed to be necessary to form the appropriate compound. However with R = Ph other mechanisms are also conceivable that may lead to this species. Therefore, scenario 2 should be regarded as a possible reaction mechanism in the present studies with R = Ph.

[14] I. Arčon, J. Kolar, A. Kodre, D. Hanžel, M. Strlič, *X-Ray Spectrom.* **2007**, *36*, 199–205.

[15] M. Wilke, F. Farges, P.-E. Petit, G. E. Brown, F. Martin, *Am. Mineral.* **2001**, *86*, 714–730.

[16] F. Jiménez-Villacorta, E. Céspedes, M. Vila, A. Muñoz-Martín, G. R. Castro, C. Prieto, *J. Phys. D* **2008**, *41*, 2050091–2050098.

[17] D. Bazin, J. J. Rehr, *J. Phys. Chem. B* **2003**, *107*, 12398–12402.

[18] C. J. Adams, R. B. Bedford, E. Carter, N. J. Gower, M. F. Haddow, J. N. Harvey, M. Huwe, M. Á. Cartes, S. M. Mansell, C. Mendoza, D. M. Murphy, E. C. Neeve, J. Nunn, *J. Am. Chem. Soc.* **2012**, *134*, 10333–10336.

[19] See Supporting Information for details.

[20] M. P. Shaver, L. E. N. Allan, H. S. Rzepa, V. C. Gibson, *Angew. Chem.* **2006**, *118*, 1263–1266; *Angew. Chem. Int. Ed.* **2006**, *45*, 1241–1244.

[21] Details of the data analysis can be found in the Supporting Information.

[22] a) H. Müller, W. Seidel, H. Görls, *J. Organomet. Chem.* **1993**, *445*, 133–136; b) F. A. Cotton, L. M. Daniels, J. H. Matonic, C. A. Murillo, *Inorg. Chim. Acta* **1997**, *256*, 277–282; c) C. R. Hess, T. Weyhermüller, E. Bill, K. Wieghardt, *Angew. Chem.* **2009**, *121*, 3758–3761; *Angew. Chem. Int. Ed.* **2009**, *48*, 3703–3706; d) M. M. Olmstead, P. P. Power, S. C. Shoner, *Inorg. Chem.* **1991**, *30*, 2547–2551.

[23] a) X. Liu, M. Bauer, H. Bertagnolli, E. Roduner, J. van Slageren, F. Phillipp, *Phys. Rev. Lett.* **2006**, *97*, 2534011–2534014; b) A. I. Frenkel, C. W. Hills, R. G. Nuzzo, *J. Phys. Chem. B* **2001**, *105*, 12689–12703; c) A. Jentys, *Phys. Chem. Chem. Phys.* **1999**, *1*, 4059–4063; d) A. M. Beale, B. M. Weckhuysen, *Phys. Chem. Chem. Phys.* **2010**, *12*, 5562–5574.

[24] A. Klose, E. Solari, C. Floriani, A. Chiesi-Villa, C. Rizzoli, N. Re, *J. Am. Chem. Soc.* **1994**, *116*, 9123–9135.

[25] T. Nguyen, W. A. Merrill, C. Ni, H. Lei, J. C. Fettinger, B. D. Ellis, G. J. Long, M. Brynda, P. P. Power, *Angew. Chem.* **2008**, *120*, 9255–9257; *Angew. Chem. Int. Ed.* **2008**, *47*, 9115–9117.

[26] J. Iball, C. H. Morgan, *Acta Crystallogr.* **1967**, *23*, 239–244.

[27] See Figure SI3 in the Supporting Information.

[28] a) M. Bauer, S. Müller, G. Kickelbick, H. Bertagnolli, *New J. Chem.* **2007**, *31*, 1950–1959; b) H. Felkin, P. J. Knowles, B. Meunier, *Chem. Commun.* **1974**, 44.

[29] This is the result of additional XAS measurments, in which much larger particles are found when no NMP is used.

[30] See Figures SI2 and SI3 in the Supporting Information.

[31] a) A. Fürstner, R. Martin, H. Krause, G. Seidel, R. Goddard, C. W. Lehmann, *J. Am. Chem. Soc.* **2008**, *130*, 8773–8787; b) K. Jonas, L. Schieferstein, C. Krüger, Y.-H. Tsay, *Angew. Chem.* **1979**, *91*, 590–591; *Angew. Chem. Int. Ed. Engl.* **1979**, *18*, 550–551; c) G. S. D. King, *Acta Crystallogr.* **1962**, *15*, 243–251.

[32] C. Ni, B. D. Ellis, J. C. Fettinger, G. J. Long, P. P. Power, *Chem. Commun.* **2008**, *0*, 1014–1016.

[33] H. Felkin, P. J. Knowles, B. Meunier, *J. Organomet. Chem.* **1978**, *146*, 151–167.

[34] A. Fürstner, A. Leitner, M. Mendez in Iron catalyzed cross coupling reactions of aromatic compounds, Vol. US 20030220498 A1, **2003**.

[35] C. Batchelor-McAuley, C. E. Banks, A. O. Simm, T. G. J. Jones, R. G. Compton, *ChemPhysChem* **2006**, *7*, 1081–1085.

[36] A. Hedström, E. Lindstedt, P.-O. Norrby, *J. Organomet. Chem.* DOI: 10.1016/j.jorganchem.2013.04.024.

[37] A. Welther, M. Bauer, M. Mayer, A. Jacobi von Wangelin, *ChemCatChem* **2012**, *4*, 1088–1093.

CHEMISTRY

A EUROPEAN JOURNAL

Supporting Information

X-ray Spectroscopic Verification of the Active Species in Iron-Catalyzed Cross-Coupling Reactions

Roland Schoch,[a] Willi Desens,[b] Thomas Werner,*[b] and Matthias Bauer*[a]

chem_201303340_sm_miscellaneous_information.pdf

Electronic Supplementary Information

EXAFS measurements and data analysis

EXAFS and XANES measurements were performed at beamlines XAS and X1 at the synchrotrons ANKA (Karlsruhe) and HASYLAB (Hamburg) under ambient conditions. A Si(111) double crystal monochromator was used for measurements at the Fe K-edge (7.112 keV). The spectra were recorded in transmission mode with ionisation chambers filled with nitrogen gas. The individual pressures were adjusted to optimize the signal to noise ratio. Energy calibration was performed with an iron metal foil. To avoid mistakes in the XANES region due to small changes in the energy calibration between two measurements, all spectra were corrected to the theoretical edge energy of iron foil, which was measured every scan. The solid state $Fe(acac)_3$ sample was embedded in a polyethylene matrix and pressed into a pellet. Liquid samples were measured in a specially designed transmission sample cell for air and moist sensitive samples, which is equipped with tabs to be connected to a schlenk line. The cell can be evacuated under elevated temperature and flushed with argon prior to the measurements. Air sensitive samples can be filled in with syringes under inert conditions.[1]

To determine the smooth part of the spectrum, corrected for pre-edge absorption, a piecewise polynomial was used. It was adjusted in such a way that the low-R (<1 Å) components of the resulting Fourier transform were minimal. After division of the background–subtracted spectrum by its smooth part, the photon energy was converted to photoelectron wave numbers k. The resulting $\chi(k)$-function was weighted with k^3. Data analysis was performed in k-space according to the curved wave formalism of the EXCURVE98 program with XALPHA phase and amplitude functions.[2] The mean free path of the scattered electrons was calculated from the imaginary part of the potential (VPI set to –4.00). The amplitude reduction factor was adjusted to AFAC = 0.8 using the known XRD data of $Fe(acac)_3$.[3]

Data analysis was carried out on Fourier filtered spectra. The applied range was 3-15 Å^{-1} in k-space and 1-3.2 Å in r-space, resulting in a number of 16 independent fit-parameters according to the Nyquist criterion $N_{ind}=2\Delta k\Delta R/\pi$. The maximum number of adjusted parameters was 13, therefore overdetermacy could be ensured.[4] The unfiltered spectra are shown in figure SI1. In the fitting procedure, the shells were adjusted successively, and finally iterated together. The significance of each shell

S1

was checked by means of the reduced χ^2.[4] In case of 2, 3 and 4 added equivalents, the addition of a second light scatterer shell increased the quality of the fits by 35 %, 23 % and 28 % respectively, thus it is statistically significant. In order to exclude the existence of local minima in the fit, mapping of the coordination numbers of the individual shells against die others was applied pair-wise. To check the k^3-weighted results, k-weightings of 1 and 2 were evaluated, too. The results were identical within the error bar.
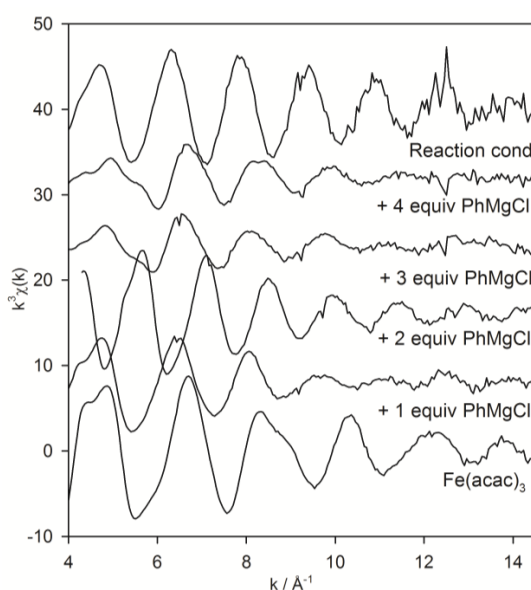
Figure SI1. Unfiltered $k^3 \cdot \chi(k)$ EXAFS spectra of the pre-catalyst $Fe(acac)_3$ in THF/NMP and after addition of 1–4 equiv PhMgCl and under reaction conditions (see below). Spectra were shifted for better comparison on the ordinate.

Raman measurements and data analysis

Raman spectra were recorded with a Bruker RFS 100/S Fourier Transform spectrometer with an air-cooled NIR Nd:YAG laser with a wavelength of 1064 nm and a power between 50–800 mW. The scattered light intensity was recorded with a high-sensitivity Ge diode (cooled with liquid nitrogen). For each spectrum 1000 scans were accumulated (spectral resolution 4 cm^{-1}). A Raman quartz cuvette was used. The concentration of the investigated samples were identical to those subjected to the EXAFS measurements.

In figure SI2 the background-corrected Raman spectra are shown. All spectra were recorded for identical concentrations of iron. The most important vibration

S2

bands for the present paper can be found in the region around 450 and 990 cm^{-1}, the first one being attributed to the Fe-O stretching band of Fe(acac)$_3$,[5] while the second corresponds to a C_6H_5 ring deformation.
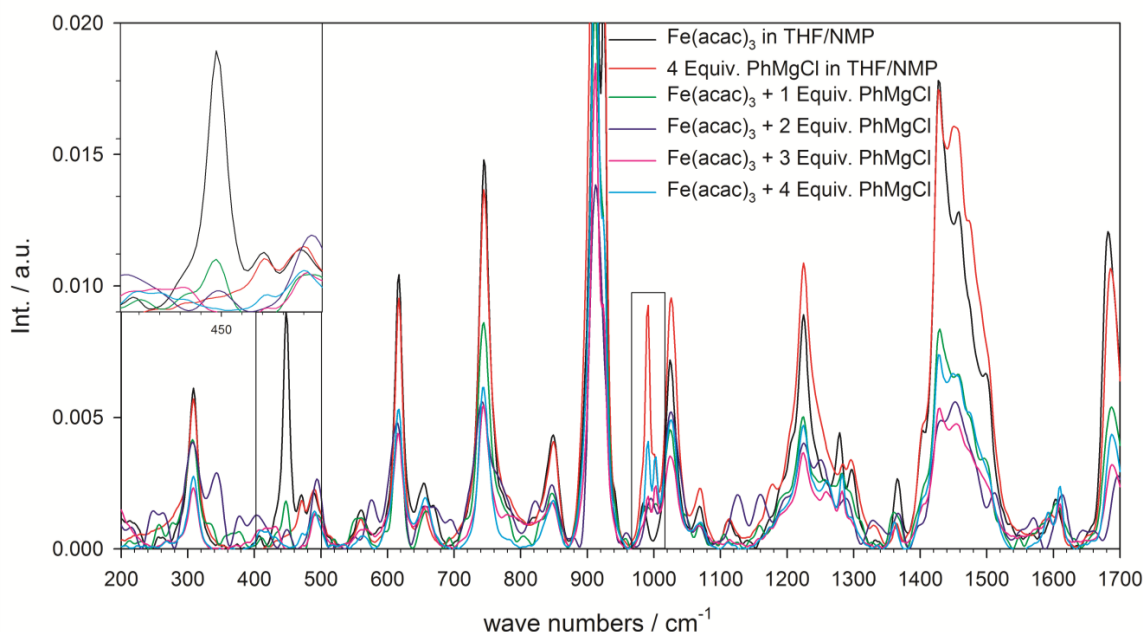
Figure SI2. Raman spectra of the pre-catalyst Fe(acac)$_3$ in THF/NMP and after addition of one to four equivalents PhMgCl. Vibration bands around 450 cm^{-1} are shown enlarged.

It is obvious from figure SI2, that for one equivalent PhMgCl added to Fe(acac)$_3$ intensity remains for the Fe-O stretching band of Fe(acac)$_3$, while it is almost negligible with a second equivalent and vanishes for three and four equivalents. Thr prominent role of the species after addition of two equivalents is represented in some additional bands (e.g. at 337, 576, 820 cm^{-1}), which are not visible in the other spectra. Especially the bands at low wavenumbers are assigned to nanoparticular species.

The results are therefore in accordance with the EXAFS results, where remaining Fe(acac)$_3$ structures were concluded with one equivalent PhMgCl. Most of the iron centers with two equivalents are located within Fe$_{13}$ clusters and the EXAFS signal is thus dominated by this compound. Therefore EXAFS spectrsocopy is not able to detect possible minor contributions of remaining Fe(acac)$_3$, which are completely consumed after the addition of a third and fourth equivalents PhMgCl.

UV/Vis measurements and data analysis

UV-Vis-measurements were recorded with an Ocean Optics USB2000 CCD spectrometer on a spectral range of 200 – 850 nm at ambient conditions (20°C) with a spectral resolution of 2.5 nm (600 l/mm grating, 2048 pixel CCD, 50 µm slit), using a optically transparent cuvette allowing Schlenk conditions in a cuvette holder as provided by OceanOptics.

In figure SI3 the UV/Vis spectra are shown. All spectra were recorded for identical concentrations of iron. $Fe(acac)_3$ in THF/NMP is characterized by two absorption bands at 353 and 435 nm in accordance with the literature.[6,7] As already found in the Raman investigation, after the addition of a first equivalent PhMgCl a significant contribution of $Fe(acac)_3$ remains. From the value of the absorption at 435 nm it can be estimated that around 65% (0.58:0.87) of the transitions characteristic for initial Fe-O(acac) still take place, while after the addition of a second equivalent <10% of $Fe(acac)_3$ is remaining (evaluated by Lambert-Beer's law). With a third and fourth equivalent PhMgCl, no absorption bands characteristic for $Fe(acac)_3$ can be observed.
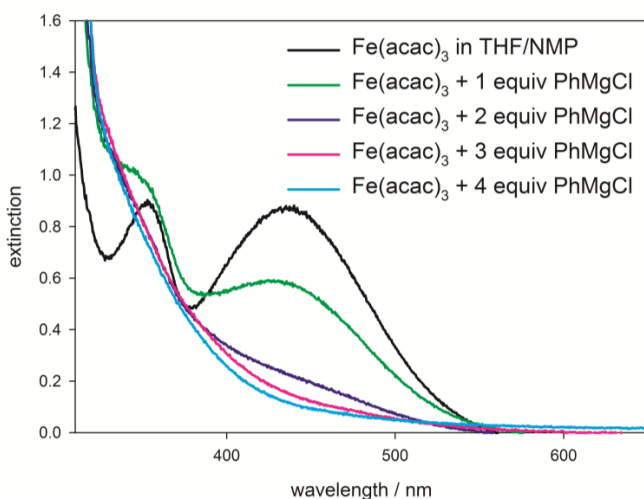
Figure SI3. UV/Vis spectra of the pre-catalyst $Fe(acac)_3$ in THF/NMP and after addition of one to four equivalents PhMgCl.

Sample preparation

All procedures were performed under air and moisture free conditions. $Fe(acac)_3$ was dissolved in a mixture of N-methylpyrrolidone and THF with a volume ratio of 1:1

(spectrum **1** in the main text) according to the procedure of Nakamura et al.[8] to obtain a solution of $c = 0.15$ mol·L^{-1}. A fresh 2.0 mol·L^{-1} solution of PhMgCl in THF (Sigma-Aldrich) was added under argon by a syringe in mole ratios of 1:1 (spectrum **2** in the main text), 1:2 (spectrum **3** in the main text), 1:3 (spectrum **4** in the main text) and 1:4 (spectrum **5** in the main text) with respect to Fe(acac)$_3$ and allowed to equilibrate at -10 °C for 10 minutes before the solution was filled at room temperature into a heat dried and evacuated cell which allows measurements under argon atmosphere. Reaction conditions in case of the XAS measurements (spectrum **7** in the main text) means that to the species that is formed with four equivalents PhMgCl, 10 equivalents **1b** were added to investigate the product of the oxidative addition step.

Quantitative GC-Analysis

Quantitative GC analyses were performed on an Agilent 7890A GC system equipped with a HP-5 column (30 m x 250 μm x 0.25 μm) and FID detector whereas for qualitative GC analysis a mass detector 5975C inert XL MSD from Agilent was used. For the latter an ionization potential of 70 eV was applied. Temperature program: 40°C for 2 min, then 25°C/min to 300°C for 3 min.

To obtain information concerning possible reactions between Fe(acac)$_3$ and Grignard reagent, 1-10 equiv PhMgCl (2M in THF) were added to 1 equiv Fe(acac)$_3$ in THF/NMP (1:1) analyzing the mixture via GC-MS after acid hydrolysis (1M HCl) (Table 1). In all cases the generation of biphenyl was observed and quantitative GC analysis with hexadecane as internal standard. In presence of 1 equiv PhMgCl full conversion to biphenyl was detected (Entry S1). It is obvious, that Fe(III) is reduced to Fe(II) by a phenyl anion under formation of a phenyl radical. The detected biphenyl is formed through coupling of two phenyl radicals. Similar homo-couplings of Grignard reagents in presence of Fe(III) complexes were already observed by Gibson et al.[9] Upon addition of 2 equiv PhMgCl only 65% of the amount of biphenyl, which would be expected for a reduction from Fe(III) to Fe(I), is formed (Entry S2). This conforms to an oxidation state amendment from +3 to only +1.7. In contrast addition of 3 equiv Grignard leads to a significant alteration of the iron oxidation state from Fe(III) to Fe(I) (Entry S3). If 1 equiv Fe(acac)$_3$ reacts with an excess of 4 respectively 10 equiv PhMgCl (Entries S4 and S5), only a slight change to lower oxidation state is

observed compared to the addition of 3 equiv of the Grignard reagent (Entry S3), based on the amount of formed biphenyl.

Table 1. Proposed Fe oxidation state based on the formation of biphenyl in the conversion of Fe(acac)$_3$ with 1-10 equiv PhMgCl.

Entry	equiv PhMgCl	Yield Ph-Ph [%][b]	Transfered electrons	Fe (averaged oxidation state)	Residual PhMgCl
S1	1.0	>99	1.0 equiv	+2.0	0.0 equiv
S2	2.0	65	1.3 equiv	+1.7	0.7 equiv
S3	3.0	66	2.0 equiv	+1.0	1.0 equiv
S4	4.0	77	2.3 equiv	+0.7	1.7 equiv
S5	10.0	78	2.4 equiv	+0.6	7.6 equiv

[a] Reaction conditions: 1 equiv Fe(acac)$_3$, THF/NMP (1:1) c(Fe(III)) = 0.15 mol/L, 23 °C, 20 min.
[b] Determined by GC with hexadecane as internal standard.

```
File       :D:\Agilent GC MS\Data\2011\06_2011\WDP181.D
Operator   : WD
Acquired   : 17 Jun 2011  18:48     using AcqMethod CARBONATE_1.M
Instrument :    GCMS 5975C
Sample Name: WDP181
Misc Info  :
Vial Number: 42
```
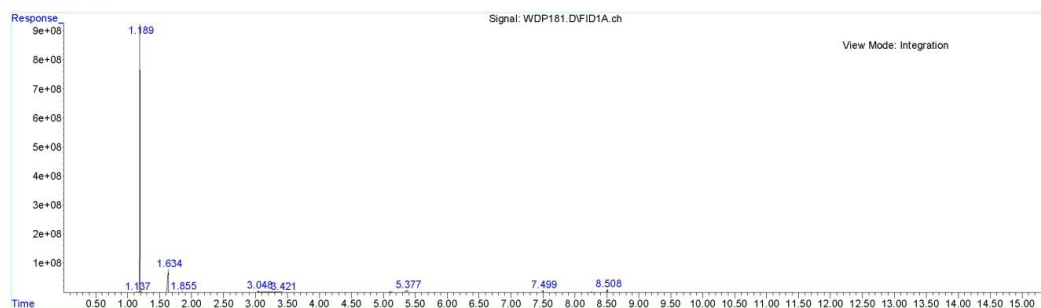


```
File       :D:\Agilent GC MS\Data\2011\06_2011\thw91_2.D
Operator   : thw
Acquired   : 1 Jun 2011  18:07     using AcqMethod CARBONATE_1.M
Instrument :    GCMS 5975C
Sample Name: thw91 2
Misc Info  :
Vial Number: 132
```


S6
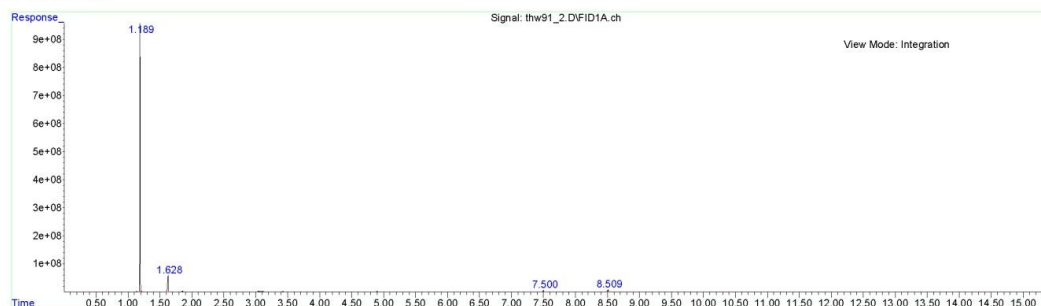
```
File      :D:\Agilent GC MS\Data\2011\06_2011\thw91_3.D
Operator  : thw
Acquired  : 1 Jun 2011  18:32    using AcqMethod CARBONATE_1.M
Instrument :    GCMS 5975C
Sample Name: thw91 3
Misc Info  :
Vial Number: 133
```
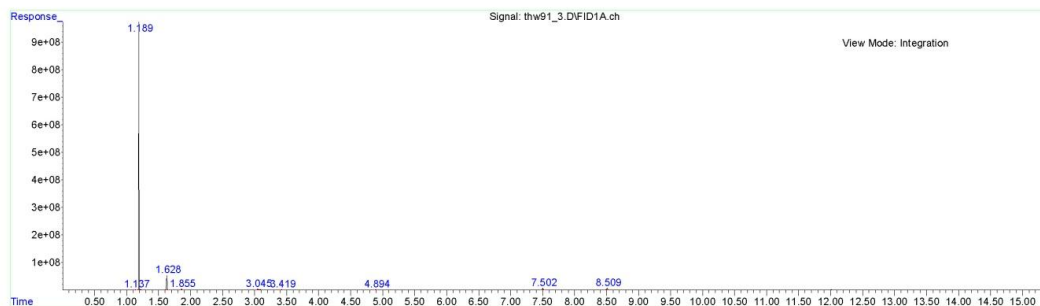


```
File      :D:\Agilent GC MS\Data\2011\06_2011\thw91_4.D
Operator  : thw
Acquired  : 1 Jun 2011  18:56    using AcqMethod CARBONATE_1.M
Instrument :    GCMS 5975C
Sample Name: thw91 4
Misc Info  :
Vial Number: 134
```
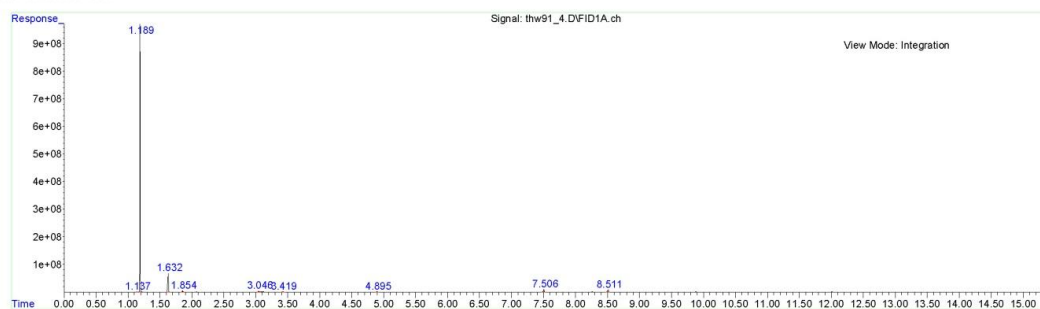


```
File      :D:\Agilent GC MS\Data\2011\06_2011\thw91_5.D
Operator  : thw
Acquired  : 1 Jun 2011  19:21    using AcqMethod CARBONATE_1.M
Instrument :    GCMS 5975C
Sample Name: thw91 5
Misc Info  :
Vial Number: 135
```
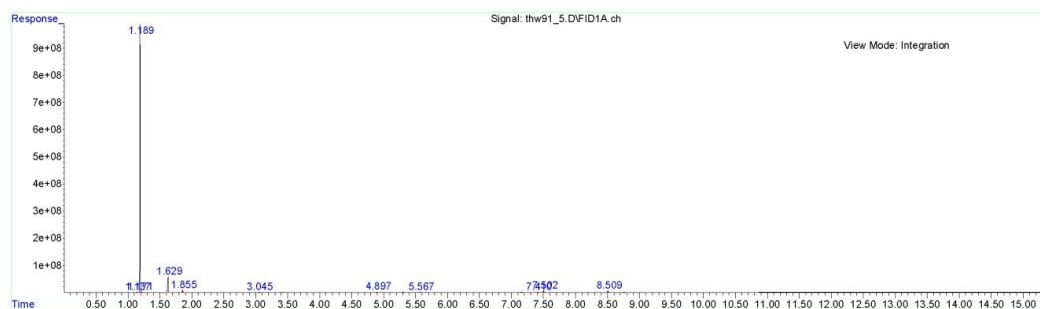

Performed test reactions:

All procedures were performed under air and moisture free conditions. THF was dried over Na/Benzophenone and freshly distilled before use. Anhydrous *N*-methylpyrrolidone (99.5%) was purchased by Alfa Aesar and used as received. All

other chemicals were purchased by Sigma Aldrich and used as received without further purification.

4-Hexylmethylbenzoat (1a)

PhMgCl (0.26 mL, 2M in THF, 0.52 mmol) was added drop wise to a solution of Fe(acac)$_3$ (1 equiv, 72 mg, 0.20 mmol) in THF (1.6 mL) and NMP (1.6 mL) at 23°C. After 20 min THF (3 mL) and methyl 4-chlorobenzoate (588 mg, 3.45 mmol) were added. After 5 min nHexMgCl (1.7 mL, 2M in THF, 3.4 mmol) was added drop wise. The reaction mixture was stirred for 20 min, quenched with aq. HCl (1M, 5 mL) and extracted with Et$_2$O (3×5 mL). The combined organic layers were dried (MgSO$_4$), rotary evaporated and chromatographed (SiO$_2$, cyclohexane:EE 75:1) to afford methyl 4-hexylbenzoate (676 mg, 3.07 mmol, 89%) as a colorless oil. R$_f$ (SiO$_2$, Cyclohexane:EE 20:1) = 0.50. ^{1}H NMR (300 MHz, CDCl$_3$): δ = 0.88 (t, J = 7.0 Hz, 3H), 1.26–1.35 (m, 6H), 1.59–1.64 (m, 2H), 2.65 (t, J = 7.7 Hz, 2H), 3.89 (s, 3H), 7.22–7.26 (m, 2H), 7.92–7.96 (m, 2H) ppm. ^{13}C{^{1}H} NMR (75 MHz, CDCl$_3$): δ = 14.0, 22.5, 28.9, 31.1, 31.6, 36.0, 51.9, 127.6, 128.4, 129.6, 148.5, 167.2 ppm.

S8

Desens WDP 185 B_4849 13C CDCl3 130618.309
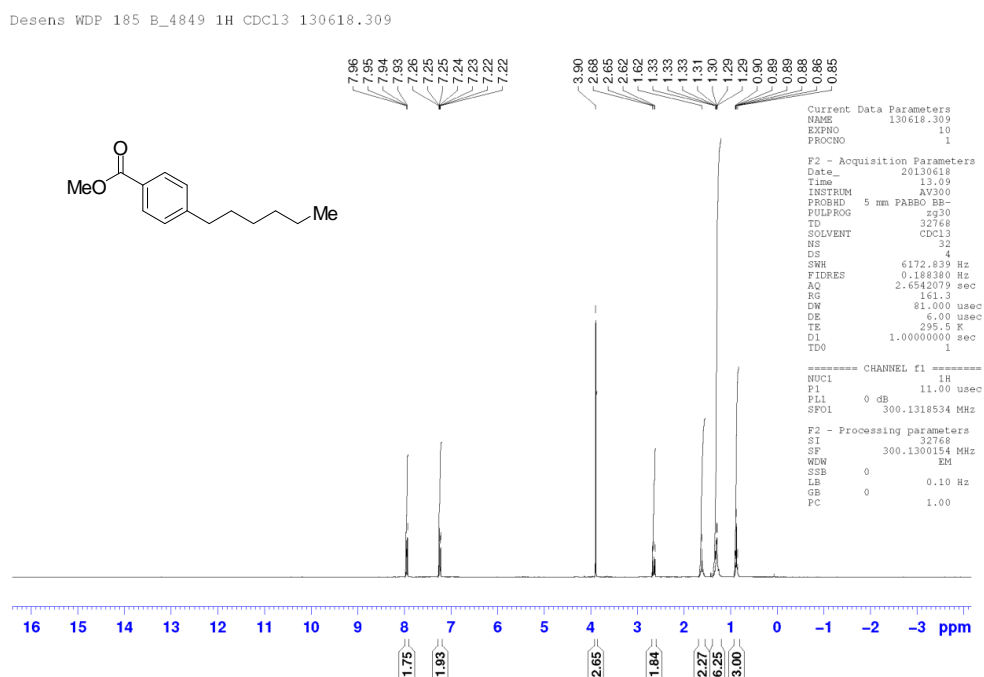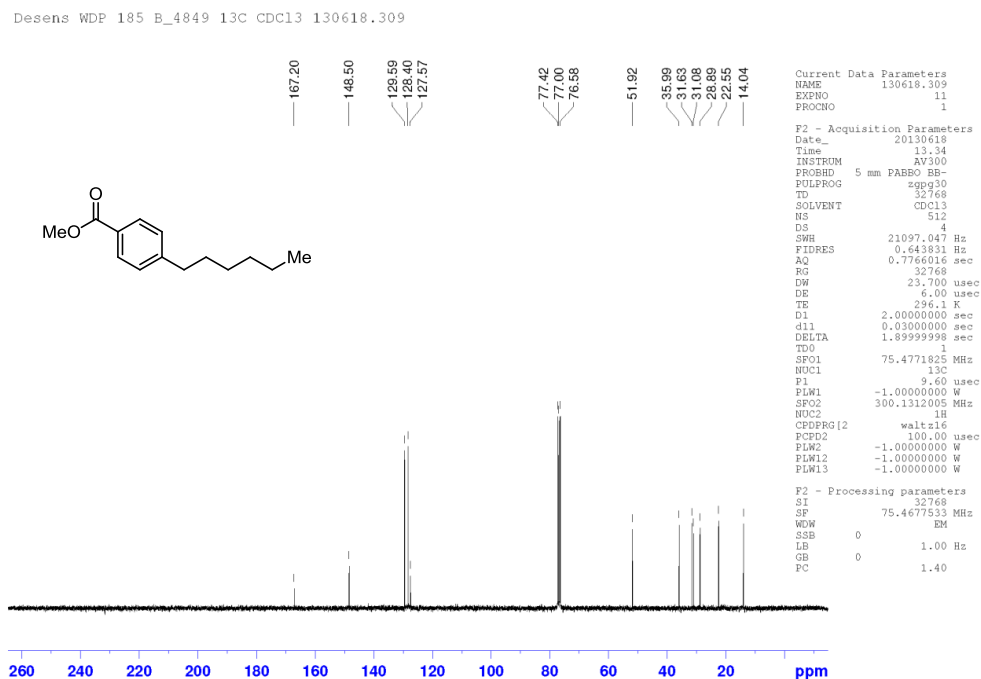
2-Hexylpyridine (2b)

PhMgCl (3 equiv, 0.26 mL, 2M in THF, 0.52 mmol) was added dropwise to a stirred solution of Fe(acac)$_3$ (1 equiv, 59 mg, 0.17 mmol) in THF (0.55 mL) and NMP (0.55 mL). at 23°C. After 30 min 2-chloropyridine (408 mg, 3.59 mmol) was adjoined to the solution. After 5 min *n*HexMgCl (2.37 mL, 2M in THF, 4.74 mmol) was added dropwise. The reaction mixture was stirred for 60 min, quenched with a saturated solution of NH$_4$Cl (5 mL) and extracted with Et$_2$O (4×5 mL). The combined organic layers were dried (MgSO$_4$), rotary evaporated and chromatographed (SiO$_2$, Cyclohexane with 1% NEt$_3$) to afford 2-hexylpyridine (352 mg, 2.16 mmol, 60%) as a colorless oil. R$_f$ (SiO$_2$, Cyclohexane with 1% NEt$_3$) = 0.03 ^{1}H NMR (300 MHz, CDCl$_3$): δ = 0.83–0.89 (m, 3H), 1.25–1.38 (m, 6H), 1.65–1.76 (m, 2H), 2.76 (m, 2H), 7.04–7.08 (m, 1H), 7.10–7.13 (m, 1H), 7.55 (dt, J = 1.86 Hz, J = 7.65 Hz, 1H), 8.50 (qd, J = 0.91 Hz, J = 4.92 Hz, 1H) ppm. ^{13}C{^{1}H} NMR (75 MHz, CDCl$_3$): δ = 14.0, 22.5, 29.0, 29.8, 31.6, 38.4, 120.7, 122.6, 136.1, 149.1, 162.5 ppm.

S9

Desens WDP687B 1H CDCl3 130621.326

Desens WDP687B 13C CDCl3 130621.326

S10

References:
[1] T.S. Ertel, H. Bertagnolli, S. Hückmann, U. Kolb, D. Peter, *Appl. Spectrosc.* **1992**, *46*, 690; M. Newville, P. Livins, Y. Yacoby, J.J. Rehr, E.A. Stern, *Phys. Rev. B* **1993**, *47*, 14126.
[2] N. Binsted, S.S. Hasnain, *J. Synchrotron Rad.* **1996**, *3*, 185.
[3] J. Iball, C.H. Morgan, *Acta Cryst.* **1967**, *23*, 239.
[4] M. Bauer, H. Bertagnolli, *J. Phys. Chem. B* **2007**, *111*, 13756 and references herein.
[5] K. Nakamoto, *Infrared and Raman Spectra of Inorganic and Coodination Compounds* **1986.**
[6] M. Handa, H. Miyamoto, T. Suzuki, K. Sawada and Y. Yukawa, *Inorg. Chim. Acta* **1992**, *203*, 61.
[7] M. Bauer, Th. Kauf, J. Christoffers and H. Bertagnolli, *Phys. Chem. Chem. Phys.* **2005**, *7*, 2664.
[8] S. K. Ghorai, M. Jin, T. Hatakeyama and M. Nakamura, *Organic Letters* **2012**, *14*, 1066.
[9] M. P. Shaver, L. E. N. Allan, H. S. Rzepa and V. C. Gibson, *Angew. Chem. Int. Ed.* **2006**, *45*, 1241.

IRON IN HETEROGENEOUS CATALYSIS

The heterogeneous catalyst synthesis applied in this thesis is based on the homogeneous cross-coupling catalyst system presented in chapter 2. By addition of an excess of Grignard compound, the reduction of the threevalent iron precursor continues until small cluster of a size between 5 and 12 nm are formed[130]. Small particles are desirable in the preparation of heterogeneous catalysts, due to their high specific surface area. Furthermore, the activity of iron in heterogeneous catalysis in exhaust gas emission reduction and oxidation reactions is already known and subject of several publications in the last decades[254–258]. The second metal (magnesium), introduced through application of a Grignard compound during the reduction process, can be found on the particle surface, as EXAFS analysis and the results of the publication presented in chapter 2 suggested. The formed nanoparticles were brought on a support material by impregnation in 1, 5 and 10 wt% loadings referred to iron and subsequently calcined at 600 °C. In addition to a Grignard compound, an aluminum organyl and a lithium organyl were applied as reducing agents for the formation of nanoparticles. Thereby, three model catalysts were obtained, which differ in the second metal and the formed structure of the iron species. As a reference catalyst, the iron precursor was directly brought on the support without generation of nanoparticles preliminary and treated similar to the other catalysts. In accordance to the reasons outlined in the introduction, section 1.3.2.3, the performances of all catalysts were tested in CO oxidation. As expected, all catalysts show significant diverse characteristics in their structure and in CO oxidation activity, which allows the establishment of a detailed structure-activity correlation.

3.1   Conspectus

Unexpectedly, the catalyst prepared as reference without reduction by a metal organic compound prior to application on the support material showed the best catalytic performance on CO oxidation of the investigated catalyst systems. Hence, this catalyst system is the subject matter of the first publication in this chapter, section 3.2. Through application of several analytic and spectroscopic techniques - X-ray diffraction, specific surface area determination according BET method, Mößbauer-, diffuse reflectance UV/Vis- and X-ray absorption spectroscopy - isolated and tetrahedral coordinated Fe^{III} centers and $AlFeO_3$ phases could be identified to be a structural requirement for high catalytic activity in CO oxidation. The catalyst structure is strongly dependent on the amount of iron present on the surface. With 1 wt% loading, a relatively high amount of isolated, tetrahedrally coordinated sites could be determined, which decreases with higher loadings in favor of larger iron oxidic agglomerates and γ-Fe_2O_3 phases. This trend is also reflected in the catalytic activity, which also decreases with increasing loading.

A very similar behavior can be observed for the catalyst systems, which are subject of the second publication in this chapter (3.3). Here, metal organic compounds were used in the preparation process and the second metal introduced in this way had a certain influence on the catalyst structure and its activity in CO oxidation. The catalysts prepared using a lithium organyl show a drastic decrease in specific surface area with higher catalyst loadings. This can be explained by the formation of higher agglomerates, γ-Fe_2O_3 and even $AlLiO_3$ phases already at relatively low loadings, as verified by X-ray diffraction, diffuse reflection UV/Vis- and X-ray absorption spectroscopy. These larger phases seem to block pores and cause the decrease of accessible active sites and with this of the catalytic activity.

The catalysts a magnesium organyl was applied in the preparation process showed a significantly higher catalytic activity. The specific surface area was relatively independent on the iron loading and only moderate formation of larger γ-Fe_2O_3 phases compared to the lithium catalyst system could be detected.

Application of an aluminum organyl in the preparation process lead to catalysts with the highest activity of the bimetallic systems. This could be correlated to the highest amount of tetrahedrally coordinated and isolated iron centers at all loadings. Furthermore, an increase in surface area was detected with higher loadings, which could be due to an integration of the particles into the support lattice. This could be plausible, since aluminum atoms are undoubtedly present on the nanoparticle surface after reduction, which can easily be incorporated under calcination conditions at 600 °C.

3.2 A New Iron-Based Carbon Monoxide Oxidation Catalyst

Participations in this publication

H. Huang, V. Schünemann: Mößbauer spectroscopy;
R. Schoch, M. Bauer: preparation, catalytic tests, X-ray diffraction, UV/Vis spectroscopy, XAFS analysis

★ ChemPubSoc
Europe

A New Iron-Based Carbon Monoxide Oxidation Catalyst: Structure–Activity Correlation

Roland Schoch,[a] Heming Huang,[b] Volker Schünemann,[b] and Matthias Bauer*[a]

A new iron-based catalyst for carbon monoxide oxidation, as a potential substitute for precious-metal systems, has been prepared by using a facile impregnation method with iron tris-acetylacetonate as a precursor on γ-Al_2O_3. Light-off and full conversion temperatures as low as 235 and 278 °C can be reached. However, the catalytic activity strongly depends on the loading; lower loadings perform better than higher ones. The different activities can be explained by variations of the structures formed. The structures are thoroughly characterized by a multimethodic approach by using X-ray diffraction, Brunauer–Emmett–Teller surface areas, and Mössbauer spectroscopy combined with diffuse reflectance UV/Vis and X-ray absorption spectroscopy. Consequently, isolated tetrahedrally coordinated Fe^{3+} centers and phases of $AlFeO_3$ are identified as structural requirements for high activity in the oxidation of carbon monoxide.

1. Introduction

Carbon monoxide oxidation is one of the catalytic reactions of utmost importance to daily life.[1] It removes highly toxic carbon monoxides from any type of exhaust gases, such as automotive engines and industrial plants. State of the art catalysts consist of noble metals such as gold, palladium, and platinum on different supports.[2] Although the catalytic performance of such noble-metal catalyst systems will present a benchmark for many years, rising prices for these materials are on the way to outcompete their usage. This issue becomes even more serious upon considering the numerous applications of noble metals in green chemistry. Fuel cells[3] and biomass conversion[4] catalysts rely mainly on platinum and will cause a further shortage of noble-metal resources. Moreover, the toxic nature of noble-metal exhaust gas catalysts released to the environment is still discussed controversially.[5] It is therefore highly desirable to have nontoxic, earth-abundant alternatives to these noble-metal-based catalysts available. One of the very rare elements that fulfils both requirements is iron. Other transition metals, such as cobalt or manganese, show better performance than iron, but are very sensitive to catalyst poisoning and deactivation.[6] Due to its presence in enzymes, iron even can be considered as bio-compatible.

Few examples of carbon monoxide oxidation on iron catalysts are known. Carriazo et al. modified a natural bentonite clay by intercalation to obtain higher iron and aluminum con-

tents and, in addition to 200 nm iron oxide agglomerates, iron nanoparticles of 15–25 nm.[7] Application of this catalyst in CO oxidation showed a conversion of about 30 % at 400 °C. Lin et al. prepared iron oxide nanoparticles containing Fe_3O_4 and FeO with a diameter smaller than 4 nm through precipitation and used them as catalysts.[8] At ambient temperature, this unsupported catalyst already shows 37 % conversion and at 100 °C 60 % of CO reacted to form CO_2. Temperatures needed for full conversion were not determined in this study. Hajaligol et al. tested commercially available nanoparticles (NANOCAT), which showed at least partly comparable size.[9] The majority of these particles had diameters of 3–5 nm. The other fraction was much larger at 24 nm. They discovered that NANOCAT consisted of γ-Fe_2O_3, FeOOH, and $Fe(OH)_3$ and catalyzed CO oxidation completely at 350 °C. It should be noted that this system also contains the active iron compound in its pure, unsupported form.

For technological applications, immobilization of the active species on an easy to handle support is mandatory. In 1988 Walker et al. investigated TiO_2 and γ-Al_2O_3 as supports for iron oxide as a catalyst in the oxidation of CO and propene.[10] They impregnated the supports with iron nitrate and after calcination achieved full conversion to CO_2 at 479 (Fe_2O_3/TiO_2) and 397 °C (Fe_2O_3/Al_2O_3). Szegedi et al. synthesized a Fe-MCM-41 silica catalyst with iron particles of 3–4 nm in diameter and a full conversion temperature of 320–350 °C.[11] Through coprecipitation and calcination, Laguna et al. achieved Ce–Fe mixed oxides, which removed CO completely at 275 °C.[12] By synthesizing an Fe_3O_4@SiO_2 nanocomposite catalyst with iron oxide particles of 15.5 nm, McFarland et al. reached complete conversion at 270 °C[13] and claimed Fe_3O_4 as the active species. Recently, Tepluchin et al. reported alumina-supported iron catalysts for CO oxidation.[14] By using incipient wetness impregnation of alumina with $Fe(NO_3)_3$, full conversion of 500 ppm in

[a] R. Schoch, Prof. Dr. M. Bauer
Fakultät für Naturwissenschaften, Department Chemie
Universität Paderborn, Warburger Straße 100
33098 Paderborn (Germany)
E-mail: matthias.bauer@upb.de

[b] H. Huang, Prof. Dr. V. Schünemann
Technische Universität Kaiserslautern, Fachbereich Physik
Erwin-Schrödinger-Straße 46, 67663 Kaiserslautern (Germany)

5 vol% O_2 could be achieved at 300 °C with a catalyst containing 20% iron.

Herein, we present the facile preparation of γ-Al_2O_3-supported iron catalysts by using the simple, inexpensive metal–organic precursor iron tris-acetylacetonate, $[Fe(acac)_3]$. As demonstrated in the following, these systems show very good catalytic activity compared with those reported in the literature at low loadings between 1 and 10%. Through characterization with X-ray absorption spectroscopy (XAS), diffuse reflectance optical absorption (DRUVS), and Mössbauer spectroscopy, as well as powder X-ray diffraction (XRD), the identification of characteristic structural features and a structure–activity correlation is deduced for these new catalysts for lean CO oxidation conditions. Because these catalysts provide an inexpensive alternative to noble-metal catalysts and the γ-Al_2O_3 support is used successfully in many technical applications, the results presented herein can be harnessed as a starting point for the rational design of iron-based CO oxidation catalysts.

2. Results and Discussion

Figure 1 shows the catalytic activity for the conversion of CO into CO_2 by catalysts prepared by impregnation of γ-Al_2O_3 with $[Fe(acac)_3]$ at loadings of 1, 5, and 10 wt% iron followed by calcination in air at 600 °C for 2 h (Table 1).

The light-off, half, and full conversion temperatures are 235, 257, and 278 °C for 1 wt% Fe; 250, 298, and 346 °C for 5 wt% Fe; and 235, 332, and 426 °C for 10 wt% Fe. At full conversion, TOFs of 0.01040 (1 wt% Fe), 0.00208 (5 wt% Fe), and

0.00104 s^{-1} (10 wt% Fe) were ascertained. This trend is the reverse of that found previously.[14] Such a performance has not yet been achieved by alumina-supported iron catalysts in CO oxidation reactions, as outlined in the Introduction. Compared with the most active systems, the catalyst with 1 wt% loading is as active as Fe–Ce mixed oxides and $Fe_3O_4@SiO_2$.[12,13] In the following sections, different catalytic activities are related to structural characteristics obtained with different loadings by means of a multitude of analytic methods.

Determination of the specific surface area of the calcinated catalysts through the Brunauer–Emmett–Teller (BET) method showed, for all loadings, a few smaller values than that of pure γ-Al_2O_3 (176 $m^2 g^{-1}$). The catalyst impregnated with 1 wt% Fe exhibits a specific surface area that is very similar to that of the pure support, whereas the 5% loaded catalyst had a surface area of 122 $m^2 g^{-1}$ and the 10% loaded catalyst had a surface area of 130 $m^2 g^{-1}$. The decrease in surface area correlates with the loading dependency of catalytic activity in CO oxidation. Despite the clear effects of loading on the BET surface area, no indications of a macroscopic iron-containing phase could be identified in powder XRD measurements. Only the well-known reflexes of γ-Al_2O_3 can be observed in Figure 2, in which a phys-
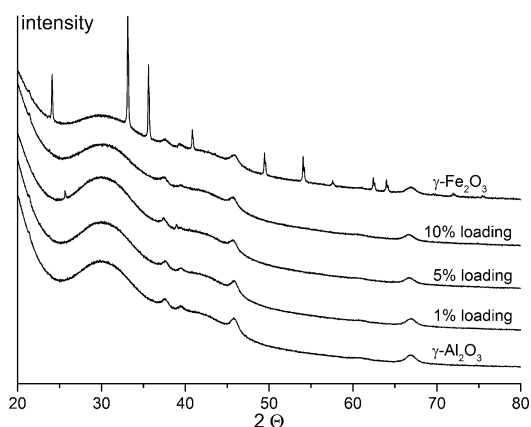
Figure 2. Powder X-ray diffractograms of $[Fe(acac)_3]$-impregnated and calcined catalysts with varying loadings. Diffractograms of the γ-Al_2O_3 support and a physical mixture of γ-Fe_2O_3 were recorded as references.

Figure 1. Catalytic conversion of CO (X) of catalysts impregnated with $[Fe(acac)_3]$ by using 1 (——), 5 (-----), and 10 wt% (•••••) Fe loadings. Conditions: 1000 ppm CO, 10% O_2 in N_2, total flow: 500 mL min^{-1}.

Table 1. Light off, half, and full conversion and turnover frequencies (TOFs; at full conversion) of the synthesized catalysts dependent on the iron loading.

Iron loading [wt%]	$T_{light off}$ [°C]	T_{50} [°C]	T_{100} [°C]	TOF [s^{-1}]
1	235	257	278	0.01040
5	250	298	346	0.00208
10	235	332	426	0.00104

ical mixture of γ-Al_2O_3 and γ-Fe_2O_3 is also shown for comparison. Even after application as a catalyst in CO oxidation, no other phases could be detected by XRD (see Figures SI1 and SI2 in the Supporting Information). It is thus clear that amorphous X-ray structures are present, which can only be characterized by short-range sensitive methods. To relate the structure on an atomic length scale to the catalytic performance, DRUVS spectroscopy is one of the methods available, because it probes the electronic structure of iron centers, which are, in turn, affected by the different possible coordination geometries and the degree of oligomerization. The assignment of DRUVS-signals for Fe^{III} was the subject of numerous investigations in the past decade.[15] Essentially, symmetry-dependent

charge-transfer signals (t$_1$→t$_2$, t$_1$→e) are visible in iron DRUVS spectra. Also, d–d transitions are possible, but are spin-forbidden, and therefore, are very weak and not visible in the spectra presented herein. Bands between $\lambda = 200$ and 333 nm belong to isolated tetrahedrally coordinated Fe^{III} ions, whereas bands between $\lambda = 333$ and 400 nm are related to octahedrally coordinated Fe^{III} ions. From $\lambda = 400$ to 450 nm, bands are assigned to oligomeric Fe$_x$O$_y$ clusters. Above a wavelength of $\lambda = 450$ nm, only signals of small Fe$_2$O$_3$-particles are visible.

The experimental DRUVS spectra of the catalysts with 1, 5, and 10% loading before and after CO oxidation are given in Figure 3; the underlying signals are summarized in Table 2. Even after usage in CO oxidation, the signals corresponding to tetra- ($\lambda \approx 270$ and 301 nm) and octahedral ($\lambda \approx 350$ nm) species and bigger agglomerates ($\lambda \approx 455$, 510, and 570 nm) are found at nearly the same wavelengths, with differing intensities.

According to DRUVS analysis, the amount of tetrahedrally coordinated centers decreases with increasing loading and after usage as a CO oxidation catalyst. This trend mirrors the dependence of the activity on the iron loading, as seen in Figure 1. The percentage of octahedrally coordinated sites and bigger oxidic cluster of 1 and 5% loaded catalysts are almost unchanged as the catalyst is used, whereas the amount of Fe$_x$O$_y$ clusters increases significantly on 10% loaded catalysts after application in CO oxidation. For the 5% loaded catalysts,
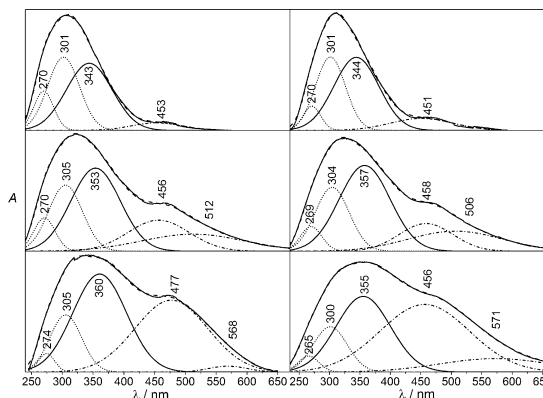
Figure 3. DRUVS spectra of 1 (top), 5 (middle), and 10% (bottom) loaded catalyst with corresponding unfolding. Left: after calcination at 600 °C, right: after application as a catalyst in CO oxidation. ••••• tetrahedral coordination, —— octahedral coordination, –•–• Fe$_x$O$_y$ cluster.

a fifth contribution appears at $\lambda \approx 510$ nm and for the 10% loaded catalyst at about $\lambda = 570$ nm; this contribution indicates the presence of a second Fe$_x$O$_y$ species.

To gain more detailed insight into the local structure of the iron centers, especially beyond direct Fe—O coordination, the element-specific method XAS was applied;[16] this has already been used to study CO oxidation reactions.[14,17] As seen in Figure 4, the X-ray absorption near-edge structure (XANES) spectra exhibited a pre-edge signal at 7.114 keV and a second feature at 7.124 keV that were independent of the iron content or whether the catalyst was applied in CO oxidation (XANES spectra of the catalysts after application in CO oxidation are shown in Figure SI3 in the Supporting Information; the energies of the prepeak and main edge are tabulated in Table SI1 in the Supporting Information). In general, the prepeak intensity of around 0.1 implies a deviation from centrosymmetric symmetry, that is, contributions of a tetrahedral coordination environment.[18] However, the 1 wt% samples exhibit a slightly higher prepeak intensity, which is in line with the larger fraction of tetrahedral centers deduced from DRUVS spectroscopy. The prepeak position is characteristic for iron in the oxidation state +3,[18c,19] which is also backed

Table 2. Summary of the DRUVS signals of the catalysts before and after CO oxidation and calculated coordination number of iron.

Sample	Signal [nm]	Assignment[a]	Percentage [%]	Calc. coordination number of 1st Fe—O contribution
1 wt% calcined	270	[4]Fe	47.2	5.1 ± 0.3
	301	[4]Fe		
	343	[6]Fe	46.8	
	453	Fe$_x$O$_y$	5.8	
1 wt% after CO oxidation	270	[4]Fe	39.3	5.2 ± 0.3
	301	[4]Fe		
	344	[6]Fe	49.3	
	451	Fe$_x$O$_y$	11.2	
5 wt% calcined	270	[4]Fe	27.5	5.4 ± 0.3
	305	[4]Fe		
	353	[6]Fe	38.3	
	456	Fe$_x$O$_y$	34.1	
	512	Fe$_x$O$_y$		
5 wt% after CO oxidation	269	[4]Fe	25.8	5.5 ± 0.2
	304	[4]Fe		
	357	[6]Fe	41.8	
	458	Fe$_x$O$_y$	32.2	
	506	Fe$_x$O$_y$		
10 wt% calcined	274	[4]Fe	16.4	5.7 ± 0.3
	305	[4]Fe		
	360	[6]Fe	40.9	
	477	Fe$_x$O$_y$	42.6	
	566	Fe$_x$O$_y$		
10 wt% after CO oxidation	265	[4]Fe	13.8	5.7 ± 0.2
	300	[4]Fe		
	355	[6]Fe	30.3	
	456	Fe$_x$O$_y$	55.7	
	571	Fe$_x$O$_y$		

[a] [4]Fe: tetrahedrally coordinated iron center. [6]Fe: octahedrally coordinated iron center.
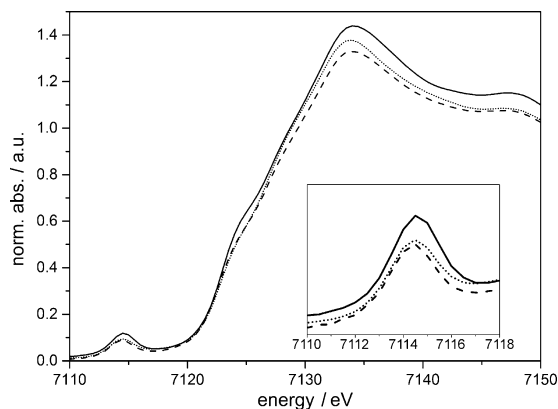
Figure 4. XANES spectra of [Fe(acac)$_3$]-impregnated catalysts with 1 (——), 5 (-----), and 10 wt% (•••••) Fe loadings after calcination at 600 °C.
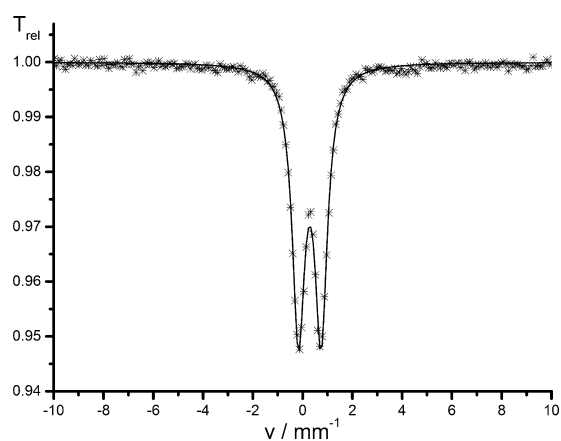
Figure 5. Mössbauer spectrum of the catalyst loaded with 10 wt% [Fe(acac)$_3$] and calcined at 600 °C.

by Mössbauer spectroscopy. Only the catalyst with 10% loading after calcination was subjected to such measurements due to the superior signal quality. The according result is displayed in Figure 5. With an isomer shift of 0.29 mm s^{-1} at ambient temperature, Fe^{3+} was the only oxidation state species could be verified[20] (see Table SI2 in the Supporting Information).

In the first step of the EXAFS analysis different iron oxide structures (Fe_3O_4,[21] α-Fe_2O_3,[22] γ-Fe_2O_3,[23] and FeO[24]) were fitted to the experimental data. However, no satisfactory fit could be obtained by using the crystallographic parameters. Due to the results of Mössbauer spectroscopy and XANES analysis, from which exclusively Fe^{3+} was found, Fe_3O_4 and FeO could be excluded. It was then generally possible to adjust oxygen at a distance of 1.9 Å and an iron shell between 3.0 and 3.3 Å in all samples. The Fe—O contributions match very well to the γ-Fe_2O_3 structure, but the Fe—Fe contributions with only one shell between 3 and 3.4 Å are not in agreement with

this iron oxide modification, which was characterized by two shells at 2.95 and 3.45 Å (cf. Table 3). Nonetheless, a certain fraction of γ-Fe_2O_3 has to be present, since tetrahedrally coordinated iron centers were found by DRUVS and XANES spectroscopy. γ-Fe_2O_3 crystalizes in a defect spinel structure, in which iron occupies tetrahedral sites as well as octahedral sites. α-Fe_2O_3 is characterized through a corundum structure, in which iron is solely octahedrally coordinated; this disagrees with the results from DRUVS and XANES analysis. Therefore, the presence of α-Fe_2O_3 can be excluded. An additional aluminum shell was necessary to improve the quality of fit, which yielded a Fe—Al distance of 3.3 Å that was independent of loading and treatment of the catalyst. This represents a typical distance in iron–aluminum oxides (see Table 3). The defect spinel $AlFeO_3$ is the only iron–aluminum oxide, in which iron is solely present in the oxidation state +3. Therefore, a mixture of $AlFeO_3$ and γ-Fe_2O_3 can be assumed. This assumption is backed up by the fact that $AlFeO_3$ can be understood as a mixed phase consisting of two defect spinels, γ-Fe_2O_3 and γ-Al_2O_3, which was used as a support.[25]

To refine the EXAFS analysis, in a second step, the individual contributions to the EXAFS spectra were Fourier filtered, as shown in Figures 6 and 7 (the corresponding $\chi(k)$ spectra are

Figure 6. Fourier-transformed and Fourier-filtered EXAFS spectra of the examined catalysts after calcination. Top: 1% loading, middle: 5% loading, bottom: 10% loading. Left: Fourier filtered from 1 to 2.5 Å (2 oxygen shells), right: Fourier filtered from 2.5 to 3.7 Å (iron, aluminum, and oxygen shell).

given in Figures SI4 and SI5 in the Supporting Information). In this approach, the contributions between 1.0 and 2.5 Å, which contained the first two oxygen shells, were fitted separately from two metal shells (iron and aluminum) and a further oxygen shell in the range 2.5–3.7 Å (see Table 3). Such a procedure is well accepted in the case of complex structures and allows the correlation between the shells in the fitting procedure to be reduced.[28]

With this method two oxygen shells at around 1.85 and 1.95 Å could be adjusted for all analyzed catalysts. They can be assigned to tetra- (1.85 Å) and octahedral (1.95 Å) environments of the iron centers in the sample.[26, 27] In the case of the

Table 3. Structural parameters obtained by EXAFS analysis.

Sample	Abs—Bs[a]	N(Bs)[b]	R(Abs—Bs) [Å][c]	σ [Å⁻¹][d]	R [%][e] E$_f$ [eV][f] Afac[g]
1 wt% calcinated	Fe—O	2.3±0.11	1.872±0.018	0.089±0.008	19.15
	Fe—O	2.5±0.12	1.936±0.019	0.097±0.009	6.544 0.8496
	Fe—Fe	0.4±0.04	3.041±0.030	0.050±0.005	3.835
	Fe—Al	2.5±0.25	3.370±0.033	0.112±0.011	8.309
	Fe—O	7.7±0.77	3.486±0.034	0.063±0.006	0.8690 N(Fe)/N(Al) 0.16
1 wt% after CO oxidation	Fe—O	1.4±0.07	1.872±0.018	0.074±0.007	13.63
	Fe—O	3.0±0.15	1.958±0.019	0.100±0.010	4.954 0.8913
	Fe—Fe	0.6±0.06	3.003±0.030	0.112±0.011	2.060
	Fe—Al	2.2±0.22	3.360±0.033	0.055±0.005	8.749
	Fe—O	7.2±0.72	3.481±0.034	0.039±0.003	0.8982 N(Fe)/N(Al) 0.27
5 wt% calcinated	Fe—O	2.3±0.11	1.836±0.018	0.063±0.006	29.31
	Fe—O	3.1±0.15	1.960±0.019	0.081±0.008	8.986 0.8144
	Fe—Fe	0.4±0.04	3.212±0.032	0.032±0.003	5.656
	Fe—Al	1.8±0.18	3.345±0.033	0.059±0.005	9.229
	Fe—O	5.9±0.59	3.459±0.034	0.032±0.003	0.7580 N(Fe)/N(Al) 0.67
5 wt% after CO oxidation	Fe—O	1.4±0.07	1.853±0.018	0.074±0.007	12.55
	Fe—O	2.3±0.11	1.957±0.019	0.081±0.008	5.675 0.8429
	Fe—Fe	1.8±0.18	3.397±0.033	0.032±0.003	2.097
	Fe—Al	2.7±0.27	3.360±0.033	0.063±0.006	6.931
	Fe—O	7.4±0.74	3.460±0.034	0.071±0.007	0.7395 N(Fe)/N(Al) 0.67
10 wt% calcinated	Fe—O	1.6±0.08	1.857±0.018	0.050±0.005	12.62
	Fe—O	4.0±0.20	1.973±0.019	0.092±0.009	5.100 0.7433
	Fe—Fe	2.2±0.22	3.261±0.032	0.081±0.005	3.75
	Fe—Al	2.3±0.20	3.352±0.035	0.084±0.008	7.475
	Fe—O	9.1±0.91	3.457±0.034	0.077±0.007	0.8142 N(Fe)/N(Al) 0.95
10 wt% after CO oxidation	Fe—O	1.5±0.07	1.876±0.018	0.071±0.007	13.77
	Fe—O	2.2±0.11	1.972±0.019	0.102±0.010	4.917 0.7288
	Fe—Fe	2.2±0.22	3.350±0.033	0.050±0.005	2.842
	Fe—Al	2.6±0.26	3.333±0.033	0.081±0.008	8.428
	Fe—O	8.4±0.84	3.413±0.034	0.112±0.011	0.7601 N(Fe)/N(Al) 0.85
Crystal structures used as references					
AlFeO$_3$[26]	Fe—O	2	1.880		
	Fe—O	4	2.0947		
	Fe—Fe	2	3.078		
	Fe—Al	5.5	3.196		
	Fe—O	1.5	3.296		
	Fe—Fe	3	3.348		
γ-Fe$_2$O$_3$[27]	Fe—O	2	1.891		
	Fe—O	3	2.035		
	Fe—Fe	3	2.947		
	Fe—Fe	9	3.455		
	Fe—O	6	3.471		

[a] Abs = X-ray absorbing atom, Bs = backscattering atom. [b] Number of backscattering atoms. [c] Distance of absorbing atom to backscattering atom. [d] Debye–Waller-like factor. [e] Fit index. [f] Fermi energy, which accounts for the shift between theory and experiment. [g] Amplitude reducing factor.

py shows a tetrahedral amount of 47%, whereas the EXAFS analysis yields 60%. With 5% iron loading, the fraction of tetrahedrally coordinated iron decreases to 28 (DRUVS) and 30% (EXAFS), and with 10% loading to 16.4% by DRUVS and 20% by EXAFS. After application in CO oxidation, the EXAFS results are not in such a striking agreement with the UV/Vis measurements. EXAFS seems to overestimate the fraction of tetrahedral environments at least by a factor of 2 in comparison to DRUVS: EXAFS yields 80, 38, and 41% and DRUVS 40, 26, and 14% for 1, 5, and 10% loading, respectively. The simplest explanation for this difference is the significantly increased noise level of the used catalyst, which is clear in the raw spectra (see Figure SI6 in the Supporting Information). One consequence is the non-physical low total Fe—O coordination number of approximately four.[29] In addition to the low signal-to-noise ratio, this can be caused by sintering of the catalyst particles under the reaction conditions.[30,31] Moreover, the fifth moment in the analysis of the DRUVS spectra was assigned to an octahedral iron species. Although tetrahedral iron centers are expected to absorb at a lower wavelength, this fifth moment might contain also Fe—O coordination numbers lower than six.

The second part of the Fourier-filtered spectra were adjusted by an iron shell at 3.0–3.3 Å, aluminum at 3.3 Å, and oxygen at 3.4 Å. For the as-prepared catalysts, the Fe—Fe distance increases systematically with higher loading, whereas the distances of Fe—Al and Fe—O are invariant with respect to the Fe loading. For 1% Fe, the Fe—Fe distance

catalysts, which were not applied in CO oxidation, the coordination numbers showed the same trend as the average coordination numbers deduced from DRUVS spectroscopy. Analysis of the calcined catalyst with 1% loading by DRUVS spectroscopy of 3.04 Å is in very good agreement with the distance of Fe in AlFeO$_3$ (3.07 Å[26]). However, the longer Fe—Fe distance in AlFeO$_3$ (3.35 Å[26]) could not be detected. With increasing Fe content, the Fe—Fe distance increases to 3.21 (5 wt% Fe) and
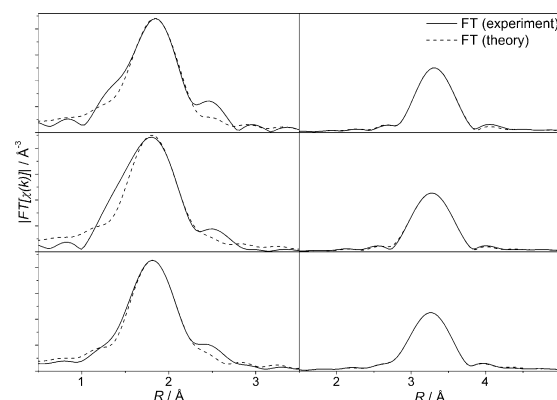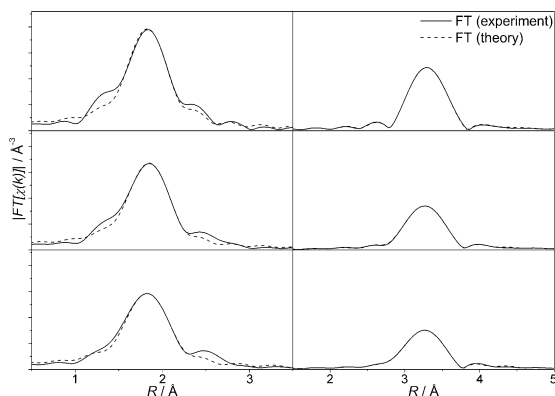
Figure 7. Fourier transformed and Fourier filtered EXAFS spectra of the examined catalysts after application in CO oxidation. Top: 1% loading, middle: 5% loading, bottom: 10% loading. Left: Fourier filtered from 1 to 2.5 Å (2 oxygen shells), right: Fourier filtered from 2.5 to 3.7 Å (iron, aluminum, and oxygen shell).

3.37 Å (10 wt% Fe); thus approaching a typical Fe—Fe distance in γ-Fe_2O_3 of 3.45 Å.[32] However, the short Fe—Fe contribution in γ-Fe_2O_3 (2.95 Å[32]) could not be fitted with statistical significance in any of the samples. The Fe—Fe coordination number increases with growing loading from 0.4 (1%) to 2.2 (10%). Therefore, the formation of pre-Fe_2O_3 structures in small particles with higher loading is deduced; this is in line with the missing iron oxide reflexes in the XRD measurements.

The Fe—Al contribution could be unequivocally assigned, since any other backscatterer yielded a lower quality of fit. Such contributions were postulated by Tepluchin et al., but could not be confirmed, since the EXAFS data presented were not analyzed by adjusting theoretical models.[14] However, the Fe—Al distance of around 3.35 Å increased compared with the crystal structure of $AlFeO_3$ (3.20 Å[26]). Because the alumina support was impregnated with the iron precursor, this elongated Fe—Al bond could be attributed to surface effects. Although the Fe—Al coordination number shows only small variations with loading, it is important to note that the relative ratio of Fe/Al found in the local surrounding of the Fe centers changes drastically from 0.16 (1%) to 0.67 (5%) to 0.95 (10% loading). The fraction of Fe—Fe pairs thus increases with increased loading. Following the assignment of iron–iron pairs in the 5 and 10% sample to iron oxide structures, this is interpreted as an increase in the size of the iron oxide particles with higher iron loading. Nonetheless, all samples exhibit characteristic Fe—Al contributions. After the reaction, the three contributions of Fe—Fe, Fe—Al, and Fe—O at higher distances remain mostly unchanged with regard to the distances found. However, it should be noted that the coordination numbers of the Fe—Fe and Fe—Al contributions increase in the 5 and 10 wt% Fe catalysts, which can be generally explained by growth of the according particles.

3. Conclusions

The impregnation of γ-Al_2O_3 with [$Fe(acac)_3$] followed by calcination in air at 600 °C presented a facile route for the preparation of active iron-based CO oxidation catalysts. In contrast to previous studies, the most active system was achieved with 1 wt% loading, followed by 5 and 10 wt%, respectively, accompanied by a successive drop in the BET surface area from 176 to 122 $m^2 g^{-1}$. As no X-ray crystalline species was detected by means of XRD, short-range sensitive methods were applied to elucidate the structure of the catalyst and to establish a structure–activity correlation. Through DRUVS spectroscopy, a decrease in tetrahedrally coordinated isolated iron centers and an increase in Fe_xO_y particles with increasing loadings and decreasing catalytic activity were detected. These iron centers contained the oxidation state Fe^{3+} exclusively, as proved by Mössbauer and XANES spectroscopy.

A final identification of the iron-containing phase was then achieved in the first thorough EXAFS evaluation on such systems. Analysis of the nearest neighbor oxygen shells confirmed the results of DRUVS spectroscopy with respect to the ratio of tetrahedral and octahedral coordination sites in the catalysts. The most active catalyst with 1 wt% iron loading showed the highest fraction of tetrahedrally coordinated Fe^{3+} centers. Moreover, this catalyst was characterized by the presence of Fe—O—Al groups. The only iron–aluminum oxidic species with tetrahedrally coordinated iron sites was $AlFeO_3$. As the catalytic activity decreased with higher loadings, the activity must be correlated to the amount of $AlFeO_3$ or isolated tetrahedrally coordinated Fe^{3+} centers within the γ-Al_2O_3 structure or on its surface. In contrast, the less active catalysts containing 5 and 10 wt% iron showed increasing amounts of iron oxide, whereas the amount of $AlFeO_3$ stagnated and the amount of tetrahedral isolated iron centers decreased.

Based on these findings, the following structural characteristics could be considered as prerequisites for a high catalytic CO oxidation activity under oxygen-rich conditions: 1) coordinatively unsaturated iron centers in a tetrahedral environment, and 2) a Fe—O—Al structure motif present as isolated Fe centers in an alumina environment or in very small particles.

Based on this structure–activity correlation, the following scenario (Scheme 1), which explains the different activities, is proposed: $AlFeO_3$ as a "mixed phase" of γ-Fe_2O_3 and γ-Al_2O_3 is only formed on the surface of the support. At the border of
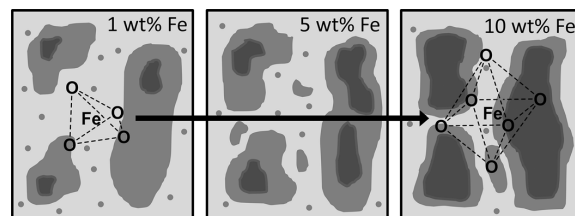
Scheme 1. Summary of the structures formed according to spectroscopic data. Gray spots: isolated iron centers, gray fields: $AlFeO_3$, black fields: γ-Fe_2O_3.

the AlFeO$_3$ phase, isolated tetrahedrally coordinated iron centers are present on the alumina support, due to the crystal structures of γ-Al$_2$O$_3$, γ-Fe$_2$O$_3$, and AlFeO$_3$ and the tendency of iron and aluminum to substitute each other in the spinel defect structures present.[25] With increasing loadings, iron oxide is formed on the AlFeO$_3$ phase, which covers the catalytic active centers gradually until γ-Fe$_2$O$_3$ is exclusively accessible for catalysis.

As all catalysts also show purely oxidic structures, it is suspected that these species also show a certain amount of activity, which also follows from already existing studies.[8–10, 13]

We presented a thorough spectroscopic characterization of iron-based CO oxidation catalysts, and we were able to establish a structure–activity correlation in highly disordered X-ray amorphous systems; future studies need to focus on the individual activity of defined iron oxides and iron aluminum oxides. Special emphasis needs to be given to particle size effects and defect structures. Finally, a spectroscopic investigation of the reaction mechanism is a great challenge on the way to the development of a competitive iron-based CO oxidation catalyst.

Experimental Section

The catalysts were prepared by impregnation of γ-Al$_2$O$_3$ with a solution of [Fe(acac)$_3$] in a mixture of equal amounts of tetrahydrofuran (THF) and N-methylpyrrolidone (NMP). [Fe(acac)$_3$] was purchased in high purity from Sigma Aldrich. The [Fe(acac)$_3$] concentration was 0.25 mol L^{-1} and the amount of solution was tuned with respect to the intended loadings. The support was suspended in THF and rigorously stirred, while the [Fe(acac)$_3$] mixture was added slowly. Afterwards the solvents were removed at 150 °C in vacuum and the catalysts were calcinated in air at 600 °C.

For catalytic tests in CO oxidation, a quartz glass tube was used as a plugged flow reactor with an inner diameter of 7.83 mm. The catalysts were granulated with a particle size of 125– 250 μm. The as-prepared catalyst (200 mg) was diluted with glass beads (800 mg) to gain a fill height of 10 mm. For CO oxidation, a reaction mixture of 1000 ppm CO and 10 % O$_2$ in nitrogen and a total flow of 500 mL min^{-1} was used. While the catalyst was heated up to 500 °C with a heating rate of 3 °C min^{-1}, the CO concentration in exhaust gas was detected by means of an Uras 10E infrared spectrometer from Hartmann&Braun.

For determination of the specific surface area through the BET method, the samples were activated at 600 °C under vacuum for 16 h before the measurement was performed by using a Belsorp mini II from BEL Japan.

XRD measurements were performed with a Bruker D8 Advance diffractometer by using Cu Kα radiation. The angle range was 2Θ= 80.31° with a step interval of 2.5 s and a step size of 2Θ= 0.01639770°. The sample was rotated during measurements. A mechanical mixture of 10 wt% α-Fe$_2$O$_3$ in γ-Al$_2$O$_3$ was investigated as a reference. The resulting diffractogram is shown in the Supporting Information.

DRUVS was performed by using a Lambda 18 spectrometer from PerkinElmer. For data refinement, an exponential function was used to subtract the background. Afterwards Gaussian-type functions were used to fit the spectra.

Mössbauer spectra were recorded by using a spectrometer in the constant-acceleration mode and by using a closed cycle cryostat. Isomer shifts were given relative to α-Fe at room temperature. The spectra were analyzed by least-squares fits by using Lorentzian line shapes by means of the Vinda Add On for Excel 2003.[33]

XAS experiments were performed at beamline X1 at the HASYLAB (Hamburger Synchrotronstrahlungslabor) in Hamburg (Germany) and at the XAS beamline at ANKA (Angströmquelle Karlsruhe) in Karlsruhe (Germany). The measurements at the iron k-edge (7.112 keV) were performed by using a Si(311) double-crystal monochromator. All samples were measured in pellet form at ambient temperature. Iron foil was used as a reference. For data evaluation, a Victoreen-type polynomial was subtracted from the spectrum to remove the background.[34] Energy E_0 was ascertained by using the first inflection point of the resulting spectrum. A piecewise polynomial was used to determine the smooth part of the spectrum. It was optimized to gain minimal low-R components of the resulting Fourier transformation. The background-corrected spectrum was divided by its smoothed part and the photon energy was converted to photoelectron wavenumber k. For evaluation of the EXAFS spectra, the resulting functions were weighted with k^3 and calculated with EXCURVE98, which worked based on the EXAFS function and according to Equation (1) in terms of radial distribution functions:[35]

$$\chi(k) = \sum_j S_0^2(k) \frac{N_j}{kr_j^2} F_j(k)\, e^{-2\sigma_j^2 k^2}\, e^{-\frac{2r_j}{\lambda(k)}} \sin\left[2kr_j + \varphi_{ij}(k)\right] \quad (1)$$

In this function the amplitude reducing factor $S_0^2(k)$ and the mean free path length λ account for inelastic effects. The number of backscattering atoms N_j, their average distance r_j to the X-ray absorbing atom and the degree of their disorder, reflected in the Debye-Waller like factor σ_j^2, are structural parameters. The backscattering amplitude $F_j(k)$ and the phase shift $\varphi_{ij}(k)$ are element specific parameters.

For EXAFS analysis Fourier filtering was necessary. As mentioned previously, analysis was treated in two separated processes to avoid correlations in the fitting. For this, filtering was performed in the area of 1–2.5 Å for the first two oxygen shells and in the area of 2.5–3.7 Å for the higher shells. The number of independent points, N_{ind}, was calculated by using Equation (2) for every fit to prevent overinterpretation by using too many parameters:[35b]

$$N_{ind} = \frac{2\Delta k \Delta R}{\pi} \quad (2)$$

in which Δk is the range used in k space and ΔR is the range in which distances were fitted. The accuracy of the determined distances was 1%; it was 10% for the Debye–Waller-like factor;[16a] and 5–15% for the coordination numbers, depending on the distance. The amplitude reducing factor was iterated free in every fit.

[1] a) L. Boisvert, I. Goldberg, *Acc. Chem. Res.* **2012**, *45*, 899–910; b) G. J. Hutchings, *J Mater. Chem.* **2009**, *19*, 1222; c) A. Russell, W. S. Epling, *Catal. Rev.* **2011**, *53*, 337–423; d) G. Salek, P. Alphonse, P. Dufour, S. Guillemet-Fritsch, C. Tenailleau, *Appl. Catal. B* **2014**, *147*, 1–7; e) X. Zhang, Z. Qu, F. Yu, Y. Wang, *Chin. J. Catal.* **2013**, *34*, 1277–1290; f) A. K. Kandalam, B. Chatterjee, S. N. Khanna, B. K. Rao, P. Jena, B. V. Reddy, *Surf. Sci.* **2007**, *601*, 4873–4880; g) B. V. Reddy, S. N. Khanna, *Phys. Rev. Lett.* **2004**, *93*, 068301.

[2] a) J.-D. Grunwaldt, C. Kiener, C. Wögenbauer, A. Baiker, *J. Catal.* **1999**, *181*, 223–232; b) M. Bandyopadhyay, O. Korsak, M. W. E. Van den Berg, W. Grünert, A. Birkner, W. Li, F. Schüth, H. Gies, *Microporous Mesoporous Mater.* **2006**, *89*, 158–163; c) T. Zheng, J. He, Y. Zhao, W. Xia, J. He, *J. Rare Earths* **2014**, *32*, 97–107; d) J. M. Herreros, S. S. Gill, I. Lefort, A. Tsolakis, P. Millington, E. Moss, *Appl. Catal. B* **2014**, *147*, 835–841; e) A. Russell, W. S. Epling, *Catal. Rev. Sci. Eng.* **2011**, *53*, 337–423; f) A. Boubnov, S. Dahl, E. Johnson, A. Puig Molina, S. Bredmose Simonsen, F. Morales Cano, S. Helveg, L. J. Lemus-Yegres, J.-D. Grunwaldt, *Appl. Catal. B* **2012**, *126*, 315–325; g) P. Glatzel, J. Singh, K. O. Kvashnina, J. A. van Bokhoven, *J. Am. Chem. Soc.* **2010**, *132*, 2555–2557.

[3] a) U. Lucia, *Renewable Sustainable Energy Rev.* **2014**, *30*, 164–169; b) L. Carrette, K. A. Friedrich, U. Stimming, *ChemPhysChem* **2000**, *1*, 162–193.

[4] a) A. Kruse, A. Funke, M.-M. Titirici, *Curr. Opin. Chem. Biol.* **2013**, *17*, 515–521; b) J. C. Serrano-Ruiz, R. M. West, J. A. Dumesic, *Annu. Rev. Chem. Biomol. Eng.* **2010**, *1*, 79–100.

[5] a) S. Zimmermann, J. Messerschmidt, A. von Bohlen, B. Sures, *Environ. Res.* **2005**, *98*, 203–209; b) K. Kalbitz, D. Schwesig, W. Wang, *Sci. Total Environ.* **2008**, *405*, 239–245; c) H. M. Prichard, P. C. Fisher, *Environ. Sci. Technol.* **2012**, *46*, 3149–3154.

[6] S. Royer, D. Duprez, *ChemCatChem* **2011**, *3*, 24–65.

[7] J. G. Carriazo, M. A. Centeno, J. A. Odriozola, S. Moreno, R. Molina, *Appl. Catal. A* **2007**, *317*, 120–128.

[8] H.-Y. Lin, Y.-W. Chen, W.-J. Wang, *J. Nanopart. Res.* **2005**, *7*, 249–263.

[9] P. Li, D. E. Miser, S. Rabiei, R. T. Yadav, M. R. Hajaligol, *Appl. Catal. B* **2003**, *43*, 151–162.

[10] J. S. Walker, G. I. Straguzzi, W. H. Manogue, G. C. Schuit, *J. Catal.* **1988**, *110*, 298–309.

[11] Á. Szegedi, M. Hegedűs, J. L. Margitfalvi, I. Kiricsi, *Chem. Commun.* **2005**, 1441–1443.

[12] O. H. Laguna, M. A. Centeno, G. Arzamendi, L. M. Gandía, F. Romero-Sarria, J. A. Odriozola, *Catal. Today* **2010**, *157*, 155–159.

[13] J.-N. Park, P. Zhang, Y.-S. Hu, E. W. McFarland, *Nanotechnology* **2010**, *21*, 225708 1–225708 8.

[14] M. Tepluchin, M. Casapu, A. Boubnov, H. Lichtenberg, D. Wang, S. Kureti, J.-D. Grunwaldt, *ChemCatChem* **2014**, *6*, 1763–1773.

[15] a) M. S. Kumar, M. Schwidder, W. Grünert, A. Brückner, *J. Catal.* **2004**, *227*, 384–397; b) M. Schwidder, M. S. Kumar, K. Klementiev, M. M. Pohl, A. Brückner, W. Grünert, *J. Catal.* **2005**, *231*, 314–330; c) E. J. M. Hensen, Q. Zhu, M. M. R. M. Hendrix, A. R. Overweg, P. J. Kooyman, M. V. Sychev,

R. A. van Santen, *J. Catal.* **2004**, *221*, 560–574; d) J. Janas, J. Gurgul, R. P. Socha, T. Shishido, M. Che, S. Dzwigaj, *Appl. Catal. B* **2009**, *91*, 113–122; e) J. Pérez-Ramírez, A. Gallardo-Llmas, *J. Phys. Chem. B* **2005**, *109*, 20529–20538.

[16] a) D. C. Koningsberger, B. L. Mojet, G. E. van Dorssen, D. E. Ramaker, *Top. Catal.* **2000**, *10*, 143–155; b) F. W. Lytle, *J. Synchrotron Radiat.* **1999**, *6*, 123–134.

[17] S. Yao, K. Mudiyanselage, W. Xu, A. C. Johnston-Peck, J. C. Hanson, T. Wu, D. Stacchiola, J. A. Rodriguez, H. Zhao, K. A. Beyer, K. W. Chapman, P. J. Chupas, A. Martínez-Arias, R. Si, T. B. Bolin, W. Liu, S. D. Senanayake, *ACS Catal.* **2014**, *4*, 1650–1661.

[18] a) D. K. Bora, A. Braun, S. Erat, O. Safonova, T. Graule, E. C. Constable, *Curr. Appl. Phys.* **2012**, *12*, 817–825; b) H. Okudera, A. Yoshiasa, K. Murai, M. Okube, T. Takeda, S. Kikkawa, *J. Mineral. Petrol. Sci.* **2012**, *107*, 127–132; c) J. D. S. Walker, A. P. Grosvenor, *J. Solid State Chem.* **2013**, *197*, 147–153; d) M. Bauer, H. Bertagnolli, *Methods in Physical Chemistry*, Wiley-VCH, Weinheim, **2012**, pp. 231–269; e) M. Bauer, C. Gastl, *Phys. Chem. Chem. Phys.* **2010**, *12*, 5575–5584; f) M. Bauer, T. Kauf, J. Christoffers, H. Bertagnolli, *Phys. Chem. Chem. Phys.* **2005**, *7*, 2664–2670.

[19] L. Signorini, L. Pasquini, L. Savini, R. Carboni, F. Boscherini, E. Bonetti, A. Giglia, M. Pedio, N. Mahne, S. Nannarone, *Phys. Rev. B* **2003**, *68*, 195423.

[20] a) M. D. Carvalho, F. Henriques, L. P. Ferreira, M. Godinho, M. M. Cruz, *J. Solid State Chem.* **2013**, *201*, 144–152; b) L. Heller-Kallai, I. Rozenson, *Phys. Chem. Miner.* **1981**, *7*, 223–228.

[21] A. A. Claasen, *Proc. Phys. Soc.* **1925**, *38*, 482–487.

[22] C. Pecharromán, T. González-Carreño, J. E. Iglesias, *Phys. Chem. Miner.* **1995**, *22*, 21–29.

[23] E. N. Maslen, V. A. Streltsov, N. R. Streltsova, N. Ishizawa, *Acta Crystallogr. B* **1994**, *50*, 435–441.

[24] E. R. Jette, F. Foote, *J. Chem. Phys.* **1933**, *1*, 29–36.

[25] R. M. Cornell, U. Schwertmann, *The Iron Oxides: Structure, Properties, Reactions, Occurrences and Uses*, 2edndedWiley-VCH, Weinheim, **2003**.

[26] F. Bouree, J.-L. Baudour, E. El Badraoui, J. Musso, C. Laurent, A. Rousset, *Acta Crystallogr. Sect. B* **1996**, *52*, 217–222.

[27] V. Petkov, P. D. Cozzoli, R. Buonsanti, R. Cingolani, Y. Ren, *J. Am. Chem. Soc.* **2009**, *131*, 14264–14266.

[28] M. Bauer, H. Bertagnolli, *J. Phys. Chem. B* **2007**, *111*, 13756–13764.

[29] It should be noted here that the fraction of tetrahedral species was determined by using the ratio of coordination numbers at 1.85 and 1.95 Å, respectively.

[30] A catalyst sample from the reactor was used without further treatment after the reaction.

[31] K.-q. Lu, E. A. Stern, *Nucl. Instrum. Methods Phys. Res.* **1983**, *212*, 475–478.

[32] J. E. Jørgensen, L. Mosegaard, L. E. Thomsen, T. R. Jensen, J. C. Hanson, *J. Solid State Chem.* **2007**, *180*, 180–185.

[33] http://users-phys.au.dk/hpg/vinda.htm.

[34] a) T. S. Ertel, H. Bertagnolli, S. Hückmann, U. Kolb, D. Peter, *Appl. Spectrosc.* **1992**, *46*, 690–698; b) M. Newville, P. Livins, Y. Yacoby, J. J. Rehr, E. A. Stern, *Phys. Rev. B* **1993**, *47*, 14126–14131.

[35] a) N. Binsted, S. S. Hasnain, *J. Synchrotron Radiat.* **1996**, *3*, 185–196; b) N. Binsted, F. Mosselmans, *EXCURV98 Manual*, Daresbury.

CHEMPHYSCHEM

Supporting Information

A New Iron-Based Carbon Monoxide Oxidation Catalyst: Structure–Activity Correlation

Roland Schoch,[a] Heming Huang,[b] Volker Schünemann,[b] and Matthias Bauer*[a]

cphc_201402551_sm_miscellaneous_information.pdf

Ù˘]] [¦c꣠* ÁQ ┤ ¦{ ꦣ }

Powder X-ray diffraction: XRD spectra were taken from the catalysts before (figure SI-1) and after (figure SI-2) application in CO oxidation. Reference spectra of α-Fe$_2$O$_3$[1], γ-Fe$_2$O$_3$[2], AlFeO$_3$[3] and γ-Al$_2$O$_3$[4] were calculated from crystal structures using the program Mercury CSD 3.3.
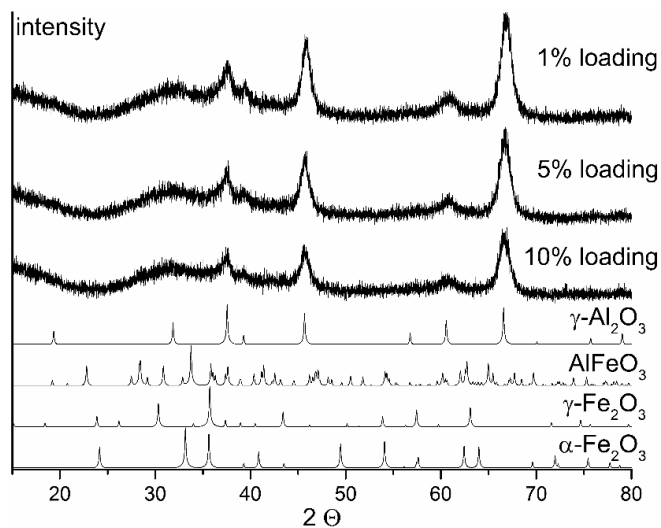
Figure SI-1: *XRD spectra of the catalysts after calcination at 600 °C and calculated reference spectra of γ-Al$_2$O$_3$, AlFeO$_3$, γ-Fe$_2$O$_3$ and α-Fe$_2$O$_3$.*
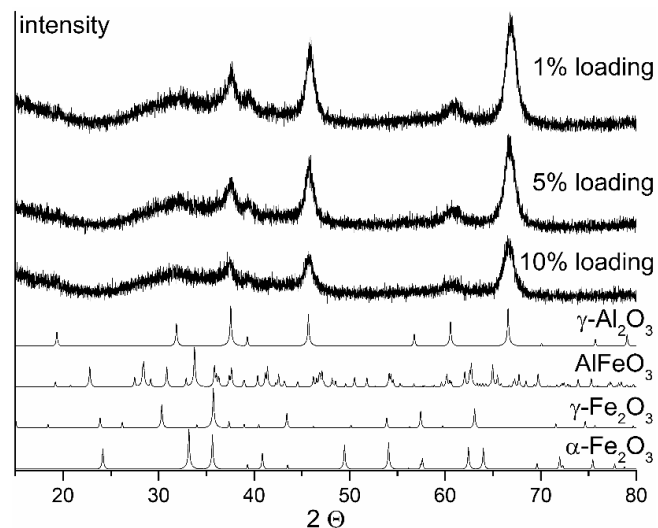
Figure SI-2: *XRD spectra of the catalysts after application in CO oxidation and calculated reference spectra of γ-Al$_2$O$_3$, AlFeO$_3$, γ-Fe$_2$O$_3$ and α-Fe$_2$O$_3$.*

EXAFS: The following graphs and tables contain further information about the X-ray absorption spectroscopic results referred to in the main text.
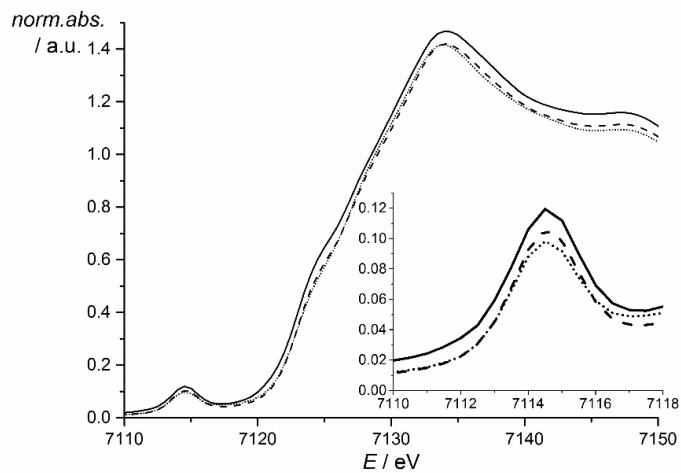
Figure SI-3: *XANES spectrum of the catalysts after application in CO oxidation. (—) 1 % loading, (---) 5 % loading, (⋯) 10 % loading*

Table SI-1: Pre-edge and main edge energies of all used catalysts determined with XANES analysis after calcination and after application as catalysts in CO oxidation.		
Sample	Pre-edge peak [eV]	Main edge [eV]
1 wt%, calcinated	7114.5	7123.7
5 wt%, calcinated	7114.5	7124.0
10 wt%, calcinated	7114.5	7124.1
1 wt%, after CO oxidation	7114.5	7123.7
5 wt%, after CO oxidation	7114.5	7124.0
10 wt%, after CO oxidation	7114.5	7124.2
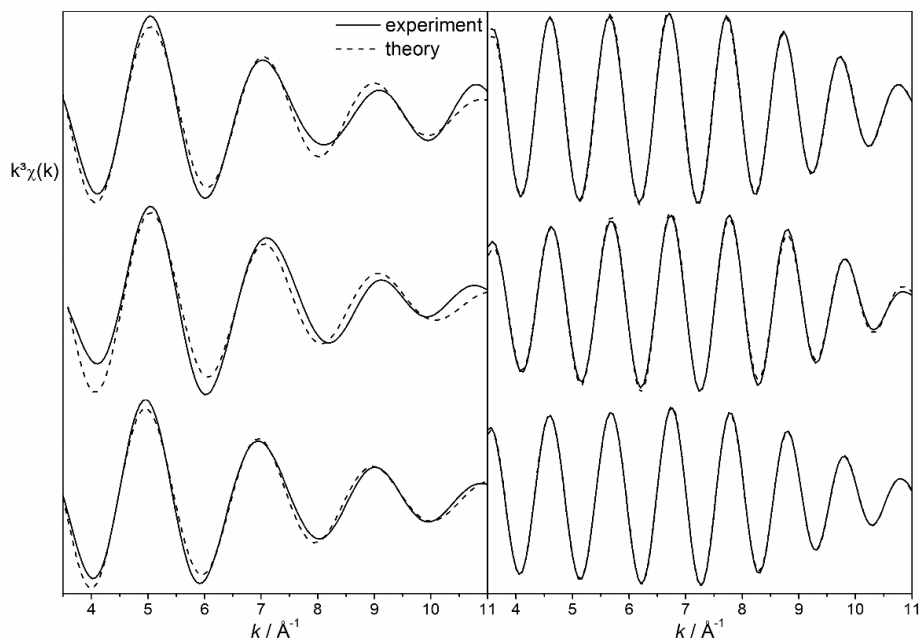
Figure SI-4: *Fourier filtered $k^3\chi(k)$ spectra and fits of the catalysts after calcination at 600 °C in air. Left: Fourier filtered from 1-2.5 Å, right: Fourier filtered from 2.5-3.7 Å. Top: 1 % loading, middle: 5 % loading, top: 10 %*
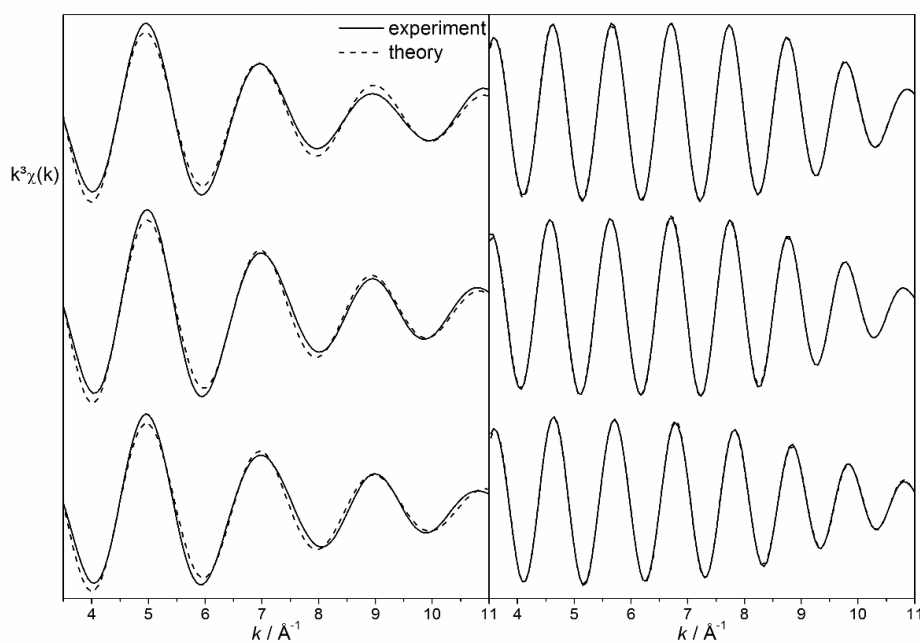
Figure SI-5: *Fourier filtered $k^3\chi(k)$ spectra and fits of the catalysts after application in CO oxidation. Left: Fourier filtered from 1-2.5 Å, right: Fourier filtered from 2.5-3.7 Å. Top: 1 % loading, middle: 5 % loading, top: 10 %*
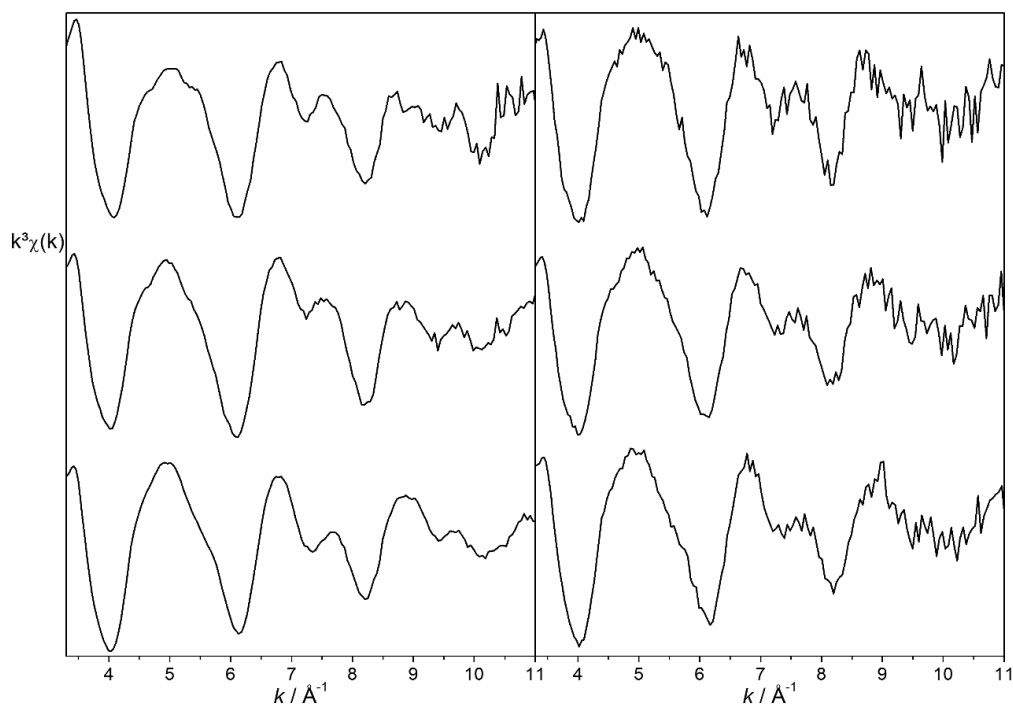
Figure SI-6: *$k^3\chi(k)$ raw spectra of catalysts after calcination at 600 °C under air (left) and after application as catalyst in CO oxidation (right). Top: 1 % loading, middle: 5 % loading, bottom: 10 % loading.*

<u>Mößbauer spectroscopy:</u> The following table contains all relevant Mössbauer parameters.

Table SI-2: Results and parameter of Mößbauer measurement.					
Sample	Temperature [K]	Isomer shift (δ) [mm/s]	Quadrupole shift ΔE_Q [mm/s]	Line width Γ [mm/s]	Relative area (I) [%]
10 wt%, calcinated	298	0.29	0.91	0.6	100
	77	0.39	0.90	0.6	100

Literature:

[1]   N. Pailhé, A. Wattiaux, M. Gaudon, A. Demourgues, *Journal of Solid State Chemistry* **2008**, *181*, 1040-1047.

[2]   C. Pecharromán, T. González-Carreño, J. E. Iglesias, *Phys. Chem. Minerals* **1995**, *22*, 21-29.

[3]   F. Bouree, J.-L. Baudour, E. Elbadraoui, J. Musso, C. Laurent, A. Rousset, *Acta Cryst.* **1996**, *B52*, 217-222.

[4]   G. Paglia, E. S. Bozin, S. J. L. Billinge, *Chem. Mater.* **2006**, *18*, 3242-3248.

3.3   Pollution Control Meets Sustainability

CHEMISTRY & SUSTAINABILITY

CHEMSUSCHEM

ENERGY & MATERIALS

EARTH ABUNDANCY

SUSTAINABILITY

X-RAY ANALYSIS

IRON

POLLUTION CONTROL

15/2016

Cover Picture:
Schoch and Bauer
Pollution Control Meets Sustainability:
Structure–Activity Studies on New Iron Oxide-Based
CO Oxidation Catalysts

WILEY-VCH   www.chemsuschem.org

A Journal of
ChemPubSoc
Europe

Pollution Control Meets Sustainability: Structure–Activity Studies on New Iron Oxide-Based CO Oxidation Catalysts

Roland Schoch and Matthias Bauer*[a]

A new class of catalysts for the oxidation of CO based on iron oxide as a biocompatible, earth-abundant and non-toxic metal is presented. The catalytic activities achieved with these catalysts provide promising milestones towards the substitution of noble metals in CO oxidation catalysts. The catalysts can be obtained by using iron core–shell nanoparticle precursors. The metal used for the shell material determines whether the iron core is integrated in or isolated from the support. The active iron site is effectively integrated into the γ-Al_2O_3 support if an aluminum shell is present in the core–shell precursor. When the metal used for the shell is different from the support, an isolated structure is formed. Using this directed synthesis approach, different iron oxide species can be obtained and their structural differences are linked to distinct catalytic activities, as demonstrated by combined in-depth analytical studies using XRD, X-ray absorption spectroscopy (XAS), UV/Vis, and Brunauer–Emmett–Teller (BET) analysis. The key species responsible for high catalytic activity is identified as isolated tetrahedrally coordinated Fe^{III} centers, whereas aggregation leads to a reduction in activity.

Introduction

The reduction of environmentally harmful emissions to minimize their destructive effects on the ecological system has become one of the most important technological challenges. Large parts of these emissions are exhaust gases from automotive engines and industrial plants.[1,2] CO is one of the most toxic substances in these gases. To prevent expositions of CO, catalysts are used for the oxidation of this poisonous gas to CO_2 in many applications. Currently, noble metals, such as Au, Pd, and Pt, are used as active species on different supports.[2,3] Although these metals have shown the best catalytic activity so far, the rising commodity prices of noble metals calls for alternatives to be found. The rise in price has resulted from an increase in the number of applications of these metals in other fields, for example, in information industry[4] or green chemistry, such as fuel cells[5] and biomass[6] conversion. Additionally, the toxicological effect of noble metal catalysts released into the environment is still under discussion.[7] Therefore, a sustainable alternative that is abundant, inexpensive and non-toxic is needed. Only a few metals, such as Mn, Fe, or Co, fulfill these requirements. Because of their presence in enzymes, they can all be considered as biocompatible.[8] Although Mn and Co catalysts both show better catalytic activity than Fe catalysts for the oxidation of CO, they are very sensitive to catalyst poisoning and deactivation.[9]

Therefore, Fe moved into the focus as a CO oxidation catalyst. However, catalyst systems based on Fe as the only active

compound are rare. Li et al. investigated commercially available iron oxide nanoparticles (NANOCAT©), which could be used for the complete removal of CO at 350 °C.[10] They verified the presence of three iron oxide phases [i.e., γ-Fe_2O_3, FeOOH, and $Fe(OH)_3$] and found two different particle size fractions of 3–5 nm and 24 nm. Carriazo et al. modified natural bentonite clay by intercalation to increase its Fe and Al content.[11] Fe nanoparticles with a size of 15–25 nm could be obtained beside larger iron oxide agglomerates with diameters of 200 nm. Thirty percent of CO could be removed at a temperature of 400 °C. The temperature for full conversion was not investigated. Lin et al. synthesized iron oxide nanoparticles containing Fe_3O_4 and FeO phases through precipitation methods.[12] The nanoparticles were smaller than 4 nm and already showed 37 % conversion at ambient temperature. Sixty percent of CO was removed at 100 °C; however, the temperature necessary for full conversion was not ascertained.

For stability reasons, active species are often immobilized on a support in technical applications. Furthermore, synergetic effects between the active species and the support can be utilized to increase the catalytic performance.[9] Laguna et al. prepared iron oxide and Fe–Ce mixed oxide catalysts using a microemulsion method and observed large differences in the temperature needed for full conversion of CO to CO_2.[13] Although the catalyst composed of pure iron oxide showed complete removal of CO at 375 °C, only 285 °C was necessary for a mixed Fe–Ce oxide catalyst. Walker et al. reported the influence of the support on the catalytic performance of iron oxide catalysts for the oxidation of CO and propene.[14] They prepared iron oxide catalysts by impregnation of TiO_2 and γ-Al_2O_3 support materials with iron nitrate followed by calcination. Complete conversion of CO was achieved with the catalyst composed of Fe_2O_3 immobilized on TiO_2 and γ-Al_2O_3 at

[a] R. Schoch, Prof. Dr. M. Bauer
Fakultät für Naturwissenschaften, Department Chemie
Universität Paderborn
Warburger Straße 100, 33098 Paderborn (Germany)
E-mail: matthias.bauer@uni-paderborn.de

Supporting Information for this article can be found under:
http://dx.doi.org/10.1002/cssc.201600508.

479 and 397 °C, respectively. Szegedi et al. synthesized a Fe-MCM-41 silica catalyst with 3–4 nm Fe nanoparticles, which showed full conversion at 320–350 °C.[15] A SiO_2-supported iron oxide catalyst was reported by Park et al.[16] The nanocomposite catalyst with 15.5 nm Fe_3O_4 particles as the active species achieved full conversion at 270 °C. Tepluchin et al. investigated the activity of Fe catalysts that were prepared in two different ways—incipient wetness impregnation[17] and a flame spray method.[18] The catalyst prepared through incipient wetness impregnation with an Fe loading of 20 wt% showed complete removal of CO at 300 °C. A mixture of Fe_2O_3 and FeO species with a loading of 15 wt% Fe was obtained using the flame spray method, which removed 50% of CO at 300 °C. In summary, the literature values for the temperature needed for full CO conversion using Fe catalysts start at 270 °C. However, structural investigations to explain the activity are not provided. In contrast, some theoretical work addressed the oxidation of CO on pure[19] and SiO_2-supported iron oxides[20] as well as the adsorption and desorption behavior of CO_2 on α-Fe_2O_3.[21]

In a recent study we presented an iron oxide catalyst supported on γ-Al_2O_3 that consisted of isolated Fe centers incorporated in the Al_2O_3 support and small γ-Fe_2O_3 nanoparticles.[22] Full conversion of CO at a temperature of 278 °C was achieved using a catalyst with 1 wt% Fe loading. This study suggested that tetrahedrally coordinated Fe species are responsible for the high catalytic activity. Hnat et al. observed the same phenomenon in their investigation of single tetrahedrally coordinated Fe^{III} sites in FeSi-BEA (beta polymorph A-type) zeolites for oxidation of CO using FTIR, UV/Vis, and TPR (temperature-programmed reduction).[23] To substantiate these results further, it is desirable to prepare catalysts that contain Fe sites with a defined chemical and structural environment. In this paper, we propose a new approach to achieve this aim based on the application of core–shell nanoparticles (see Figure 1) as precursors. The nanoparticles contain the active Fe

Figure 1. Representation of the working hypothesis introducing the integrating and isolating structure formation approaches using core–shell nanoparticles for Fe-based CO oxidation catalysts.

metal in the core surrounded by a second metal shell. The shell metal is defined by the metal–organic compound used to reduce the Fe precursor $Fe(acac)_3$ (acac = acetylacetonate) during the preparation of the nanoparticle (Figure 1). These

core–shell particles are then used to impregnate alumina γ-Al_2O_3 followed by calcination.

Two different structures are formed depending on the metal used for the shell. First, if the shell is composed of a metal that is identical to the metal in the oxide support—in this case Al—this facilitates the effective distribution of Fe sites on the support surface. Because there is a chemical connectivity between Fe and Al centers in the Fe–Al core–shell particles, the assembling of the Al shells into the γ-Al_2O_3 lattice under calcination conditions consequently leads to effective incorporation of Fe^{III} ions onto the Al_2O_3 surface (Figure 1). We call this an "integrating structure formation". This effect is not present if the shell consists of a metal that is different to the support. In this case, the metal shell isolates the Fe core from the support and prevents the incorporation of Fe^{III} ions into the Al_2O_3 lattice, which leads to the formation of larger oxide particles during calcination. Thus, this case is termed as an "isolating structure formation" (Figure 1). Integrating structure formation leads to isolated Fe centers, which have been proposed to be the active species in Fe-catalyzed CO oxidation in recent studies.[17, 18, 22] In contrast, isolating structure formation leads to larger iron oxide particles, which show reduced activity.[17, 18, 22, 23]

To gain a comprehensive understanding of this complex synthesis system, a multidimensional characterization using diffuse reflectance optical absorption, X-ray absorption spectroscopy (XAS) combined with powder XRD and Brunauer–Emmett–Teller (BET) surface analysis was used. The results from this study show that: 1) it is possible to generate active iron oxide-based CO oxidation catalysts that consist of major fractions of either tetrahedrally coordinated and isolated Fe^{III} centers or larger oxide particles using the integrating and isolating structure formation, respectively; and 2) tetrahedrally coordinated Fe^{III} sites are the active species in Fe-catalyzed CO oxidation.

Results and Discussion

All catalysts presented here use γ-Al_2O_3 as a support, which did not show any catalytic activity up to 650 °C before impregnation with Fe (Figure SI-2, Supporting Information). $AlPh_3$ was used for the synthesis of the Fe–Al core–shell precursors to prepare the catalysts using the integrating structure formation procedure and termed AlPh_X, where X = 01, 05, and 10 indicates 1, 5, or 10 wt% Fe loading, respectively. Two different isolating metal shells were introduced using PhMgBr and PhLi as precursors for the shell to prepare the catalysts using the isolating structure formation procedure and termed PhMgBr_X and PhLi_X using the same naming procedure as above. Details of the preparation are given in the Supporting Information. The short names for the prepared catalysts are summarized in Table 1.

Catalytic performance for the oxidation of CO

The light-off temperatures and the temperatures for half and full conversion of all the catalysts investigated for the oxidation of CO are shown in Figure 2. Additionally, the conversion graphs for the investigated catalysts are shown in Figure SI-1.

Table 1. Abbreviations used for the three investigated catalyst systems.

Metal organic compound	Structure formation	Fe loading [wt%]		
		1	5	10
AlPh$_3$	integrating	AlPh_01	AlPh_05	AlPh_10
PhMgBr	isolating	PhMgBr_01	PhMgBr_05	PhMgBr_10
PhLi	isolating	PhLi_01	PhLi_05	PhLi_10
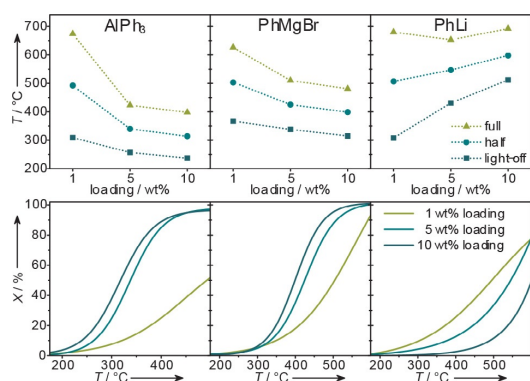
Figure 2. (top) Light-off temperature and temperature for half and full conversion of CO to CO$_2$ of the investigated catalysts depending on the reducing compound and the Fe loading of the catalyst. (bottom) CO conversions of the investigated catalysts with different Fe loadings.

Figure 3. Specific surface areas of the synthesized catalysts after calcination at 600 °C: AlPh_X (light green), PhMgBr_X (dark green), and PhLi_X (green). The regression for each type of catalyst is shown as a dashed line.

The AlPh_X catalysts show a characteristic behavior: the three measured temperature values are approximately 60 °C lower for the AlPh_01 catalyst compared with PhMgBr_01 and PhLi_01. In the case of 5 wt% loading (X=05), the difference increases to 85 °C (PhMgBr_05) and 200 °C (PhLi_05). A similar behavior is observed with 10 wt% Fe loading (X=10). Full conversion with 10 wt% Fe loading using AlPh_10 is reached at 398 °C, which competes with the best reported literature values if the amount of Fe is taken into account.

The PhMgBr_X catalysts show much higher temperature values but a similar trend to the AlPh_X catalysts. The PhLi_X catalysts also show higher characteristic temperature values, but interestingly, an inverse trend is observed for the dependence of the catalytic activity on the Fe loading.

The catalytic data provides first proof of the fundamental hypothesis concerning the preparation of iron oxide-based CO oxidation catalysts using the isolating and integrating structure formation approaches. The two methods yield catalysts with distinct activity. In the following, a detailed structure–activity analysis is used to show that the presented synthesis methods can be regarded as "semi-directed" towards iron sites of different coordination geometry and aggregation degree.

Specific surface area

The specific surface areas of all prepared catalysts are displayed in Figure 3. Although all the catalysts with 1 wt% loading (X=01) show surface areas of approximately 165 m^{2}g^{-1},

which is comparable to the pure γ-Al$_2$O$_3$ support (176 m^{2}g^{-1}), significant differences are observed with higher Fe loading. An upward trend of the specific surface area with higher loading is observed for the materials prepared using the integrating structure formation approach (AlPh_X). A much higher value of 206 m^{2}g^{-1} was observed for AlPh_10 compared with the pure support. In contrast, both materials prepared using the isolating structure formation approach had reduced surface areas with increasing Fe loading compared to the pure support. Because three values are not enough to establish a reasonable correlation between Fe loading and the specific surface area, more materials with various loadings need to be investigated to substantiate this trend.

Nevertheless, the surface area measurements are an impressive proof of the surface effects of the integrating and isolating structure formation approaches. The integrating approach leads to increased surface areas with higher loadings, whereas the isolating approach leads to reduced surface areas. This also indicates that larger iron oxide particles are formed when the isolating structure formation approach is used, which is in agreement with the model introduced above and described in Figure 1.

X-ray powder diffraction

The XRD diffractograms of the AlPh_X, PhMgBr_X, and PhLi_X catalysts are shown in Figures 4. Simulated patterns of the γ-Al$_2$O$_3$ support[24] and the different phases that can potentially be formed, such as γ-Fe$_2$O$_3$,[25] α-Fe$_2$O$_3$,[26] AlFeO$_3$,[27] and AlLiO$_2$,[28] are shown for comparison. The diffraction analysis provides the first structural proof for the validity of the isolating and integrating structure formation models introduced above. The effect of these two structure formation models is expected to be most significant at high loadings, as this favors the formation of larger crystalline Fe particles. Despite this, a formation of large crystalline Fe particles was not observed for the materials prepared with AlPh$_3$ as reducing and shell forming reagent using the integrating structure formation approach (AlPh_X). For all Fe loadings of 1, 5, and 10 wt% only the main reflexes of γ-Al$_2$O$_3$ are observable.[24] Only AlPH_10

CHEMSUSCHEM
Full Papers
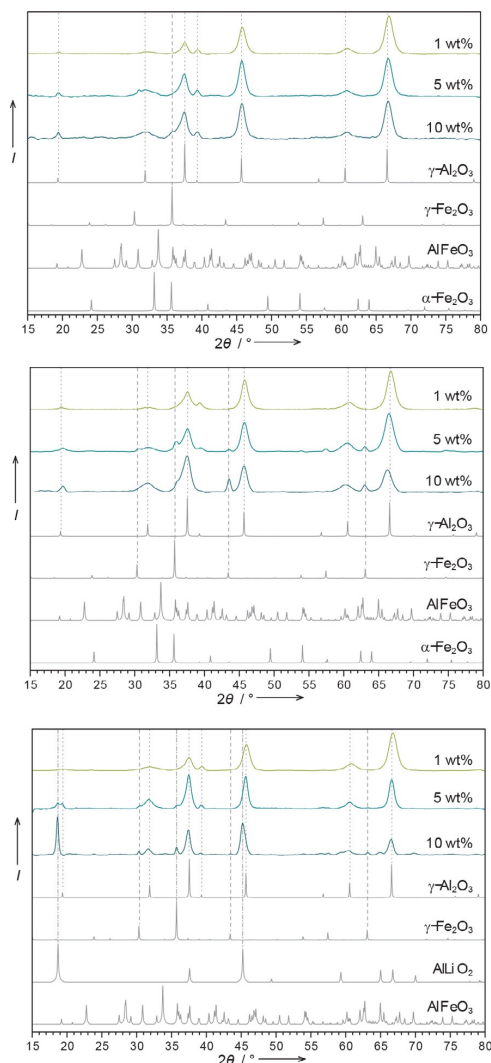
Figure 4. Powder XRD of the AlPh_X, PhMgBr_X, and PhLi_X catalysts. Calculated diffractograms of γ-Al₂O₃,[24] γ-Fe₂O₃,[25] AlFeO₃,[27] α-Fe₂O₃[26] and in case of PhLi_X AlLiO₂[28] are displayed for assignment of the peaks.

exhibited a minor fraction of γ-Fe₂O₃[25] at $2\theta = 36°$ (Figure 4). In contrast, more intense γ-Fe₂O₃[25] reflexes are found for PhMgBr_05, which increase significantly for PhMgBr_10 (Figure 4).

The isolating character of Li has a different effect on the final structure. The diffractograms of the catalysts prepared using PhLi (Figure 4) also exhibit γ-Fe₂O₃ reflexes, but with two additional signals; reflexes at $2\theta = 18°$ are visible in the diffractograms of PhLi_05 and PhLi_10, which are assigned to a AlLiO₂[28] phase.

Diffuse reflectance UV/Vis spectroscopy

To further elucidate the atomic structure of the formed iron oxide species short-range sensitive methods, such as diffuse reflectance UV/Vis spectroscopy (DRUVS), play an important role. DRUVS can be used to probe the electronic structure of Fe centers, which is affected by the coordination geometry and Fe–Fe contacts, that is, the degree of oligomerization. The assignment of Fe^{III} DRUVS signals has been the subject of numerous investigations over the past decade.[29] The bands in DRUVS spectra are attributed to charge transfer transitions ($t_1 \rightarrow t_2$, $t_1 \rightarrow e$), and the resulting energy depends on the symmetry of the Fe site. Transitions between d orbitals are also possible, but they are very weak owing to spin-forbiddance and usually not visible in the spectra. Commonly, bands between 200 and 300 nm are assigned to isolated tetrahedrally coordinated Fe^{III} centers. Octahedrally coordinated Fe^{III} ions can be found between 300 and 400 nm and bands between 400 and 450 nm indicate oligomeric Fe$_x$O$_y$ clusters. Bands at wavelengths larger than 450 nm are characteristic of Fe₂O₃ particles.[22] Signals corresponding to tetrahedral ($\lambda \approx 270$ and 300 nm) and octahedral ($\lambda \approx 335$ and 370 nm) coordination and bigger Fe$_x$O$_y$ agglomerates ($\lambda \approx 470$, 540, and 590 nm) are observed in the spectra of all the catalysts, as shown in Figure 5. Furthermore, Gaussian fitting curves used for the deconvolution of the spectra are also shown. Information about the underlying signals are listed in Table SI-6–8. The normalized areas of the fitted Gaussian curves were used to calculate the average coordination numbers (N) of iron by oxygen to obtain a trend for the coordination depending on the amount of loading and the formation model.

Based on the DRUVS analysis, the proportion of tetrahedral and octahedral coordination sites and the proportion of Fe$_x$O$_y$ oligomers (13%) in AlPh_01 differs significantly from AlPh_05 and AlPh_10, which show very similar distributions containing approximately 50% oligomers. Nonetheless, owing to the varying amount of isolated octahedral sites, the ratio of tetrahedral to octahedral sites is nearly identical at a value of 0.5 for each loading.

Although the overall trend is similar for the PhMgBr_X catalysts, the ratio of tetrahedral to octahedral sites was significantly reduced compared to the catalysts prepared using the integrating structure formation approach. This shows a clear correlation between the number of tetrahedral coordination sites and the catalytic activity. The PhLi_X catalysts show a further, more pronounced decrease of the amount of tetrahedrally coordinated iron sites, which is also in good agreement with the lowest catalytic activity of this catalyst.

X-ray absorption spectroscopy: XANES

To further substantiate the results of the DRUVS analysis, X-ray absorption spectroscopy was used as another powerful, element-specific, and short-range sensitive method,[30] which has successfully been used for the identification of related Fe species.[17,22,31] The X-ray absorption near edge structure (XANES) spectra of all the catalysts are shown in Figure 6. A pre-edge
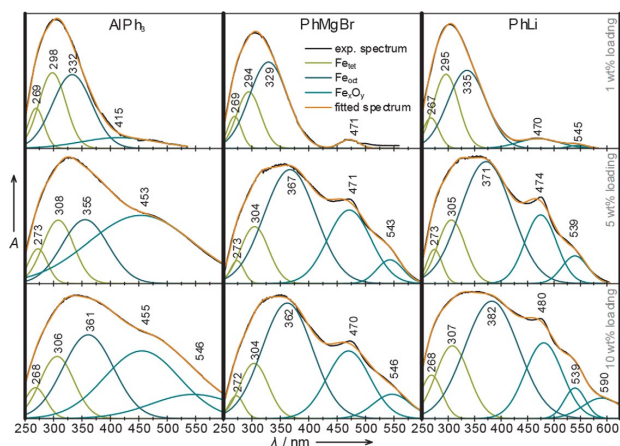
Figure 5. DRUVS spectra of the synthesized catalysts fitted with Gaussian curves dependent on Fe loading: (top) 1, (middle) 5, (bottom) 10 wt%.
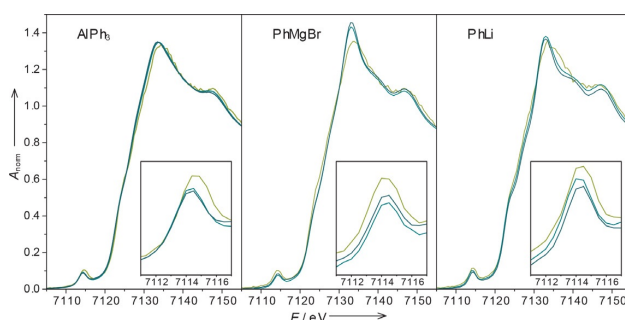
Figure 6. XAS of the investigated catalysts after calcination at 600 °C with Fe loadings of 1 (light green), 5 (middle green), and 10 wt% (dark green).

peak at 7114 eV is observed in all the spectra. Such pre-edge peaks are caused by 1s–3d transitions, which are forbidden in a centrosymmetric environment of the absorbing atom. A decrease in the coordination number, and associated with this, a loss of inversion symmetry, leads to a mixing of 4p and 3d states, which results in an increase of the pre-edge peak intensity. Therefore, the pre-edge peak in an iron K-edge spectrum can give information about the oxidation state, site distortion and the coordination number.[14,32–35] The pre-edge peak energy of 7114 eV for all measured catalysts is a clear indication of the presence of iron in a +3 oxidation state.[34] In general the energy and the relatively high pre-edge peak intensities in all the spectra of the investigated catalysts suggest a formation of γ-Fe$_2$O$_3$-related structures as the dominant phase.[34,35] The higher intensities of the pre-edge peaks in the spectra of the AlPh_01 and PhMgBr_01 catalysts can be explained by the increased proportion of tetrahedral iron sites. This agrees very well with the results of the DRUVS analysis, which showed that the proportion of tetrahedrally coordinated Fe^{III} is increased in these samples. The 1s–4p transitions are visible in the main-edge of an iron K-edge spectrum. Therefore,

the main-edge energy is besides to the oxidation state also sensitive to the coordination number of Fe. The main edge shifts to higher energies with increasing coordination number.[36] The shoulder at 7124 eV in the absorption edge of the Fe^{III} species can be assigned to a 4-coordinated Fe ion, whereas a feature at 7128 eV indicates a 6-coordinated environment.[32] Both features are observable in the spectra of all three catalyst types, independent of loading or application as catalyst (see Figures 6 and SI-7).

X-ray absorption spectroscopy: EXAFS

The EXAFS (extended X-ray absorption fine structure) spectra of the investigated systems are shown in Figure 7. Owing to the high complexity of the samples, the elaborated EXAFS data analysis is presented here in detail. In EXAFS analysis, the structure parameters of different iron oxides (i.e., α-Fe$_2$O$_3$,[25] γ-Fe$_2$O$_3$[37]) were used as starting point for the fitting process of the measured spectra. Because the XANES analysis excluded the presence of Fe in an oxidation state other than +3, FeO and Fe$_3$O$_4$ were not used as models. Adjustment of two O shells in the spectra of all three catalyst systems yields distances of 1.85 and 1.95 Å for all catalysts (see Tables 2, 3, and 4), which can be assigned to Fe—O pairs in a tetrahedral and octahedral coordination environment, respectively. The distances between the two O shells for the investigated systems are approximately 0.05 Å shorter than the distances in bulk Fe$_2$O$_3$ crystals (Table SI-12). This indicates that none of the spectra can be reproduced by using parameters from bulk Fe$_2$O$_3$. Further shells comprising Fe can be adjusted at distances of 2.95 and 3.45 Å for all catalysts. Comparison with crystal data (Table SI-12) reveals that these distances do not fit perfectly to α-Fe$_2$O$_3$ or γ-Fe$_2$O$_3$, but indicate that the formed structures are more similar to γ-Fe$_2$O$_3$. Considering the results of DRUVS and XRD measurements, it is clear that the adjustment of a crystalline iron oxide phase can only be used as a starting point. An adjustment of a further shell is indeed necessary to achieve a reasonable quality of fit. With an Al contribution at around 3.33 Å, the quality of fit can be increased significantly. The detailed results that can be extracted from the EXAFS data are discussed below.

EXAFS analysis of the AlPh_X catalysts show two O shells at 1.85 and 1.98 Å for all three Fe loadings (Table 2). The ratio of the tetrahedral to octahedral Fe sites, as deduced from the associated coordination numbers, decreases slightly with higher Fe loading. This trend is also apparent in the DRUVS spectra. The distance of the Fe shell at 2.98 Å is located between the Fe shell distances of the references γ-Fe$_2$O$_3$ and AlFeO$_3$. Therefore, the presence of very small γ-Fe$_2$O$_3$ structures or pre-γ-Fe$_2$O$_3$ structures, which are not detectable by XRD, cannot be ruled out. The distances of Al shells at 3.33 Å and Fe shells at 3.41 Å are also not dependent on Fe loading. The coordination number ratio of Fe to Al increases marginally with higher load-

Figure 7. EXAFS spectra of all the synthesized catalysts after Fourier transformation: (top) 1, (middle) 5, (bottom) 10 wt% loading.

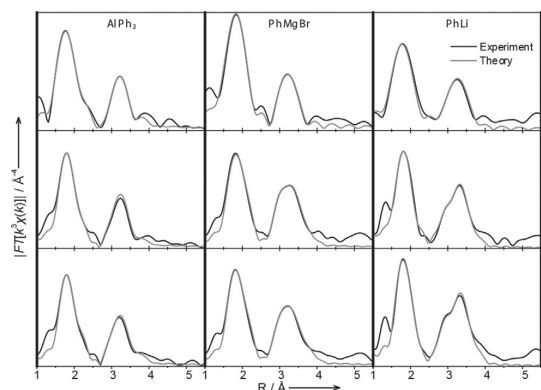ing. Because this number is a measure of the amount of Fe centers within an Fe and Al environment, it can be used to quantify the number of isolated Fe^{III} ions in the Al_2O_3 lattice versus oligomeric Fe species. According to the numbers given in Table 2, the amount of isolated centers decreases slightly with increasing Fe loading. Together with the results of the O shells, this trend is accompanied by a reduction in the amount of tetrahedral sites. Nonetheless, compared to the other two catalyst systems prepared using the isolating structure formation approach (Tables 3 and 4), the number of isolated tetrahedral sites and small iron oxide oligomers is significantly higher. The use of the materials as catalyst for the oxidation of CO does not cause significant changes to the structural parameters, as shown in detail in Tables SI-13–15.

The PhMgBr_X catalysts shows very comparable behavior to the AlPh_X catalysts (Table 3). However, the coordination numbers differ tremendously, especially with higher loadings. The $N(Fe)/N(Al)$ ratio for PhMgBr_01 is smaller than for AlPh_01, which is indeed reflected in the catalytic activity. This changes with 5 and 10 wt% Fe loading, in which $N(Fe)/N(Al)$ and the catalytic activity of PhMgBr_05 and PhMgBr_10 is inferior to those of AlPh_05 and AlPh_10. As can be seen in Figure SI-8–13, there are no substantial changes in the spectra of the catalysts after they were used in CO oxidation reactions.

The spectra of the PhLi_X catalysts (Figure 7) show coordination numbers of the two oxygen shells (Table 4) that are in full agreement with the results of the DRUVS analysis. A relatively high amount of tetrahedrally coordinated Fe centers for the catalysts loaded with 1 wt% Fe and a considerable decrease in the number of these sites with 5 and 10 wt% Fe loading is discernible. The distance of the first Fe–Fe shell in PhLi_01 indicates the presence of a major fraction of $AlFeO_3$. With higher loadings, the distance of this Fe–Fe pair shortens (2.69 Å), which is assigned to an increasing amount of γ-Fe_2O_3 and is also reflected in the increasing $N(Fe)/N(Al)$ ratio (Table 4) and is in agreement with the XRD results presented above. The $N(Fe)/N(Al)$ ratio of the PhLi_01 catalysts is twice as high as that for the PhMgBr_X catalysts and even three times that of the AlPh_X catalysts. This correlates very well with the catalytic activity. As can be seen in Figures SI-12 and SI-13, only small differences are observed in the spectra of the catalysts after they were used in CO oxidation reactions (see also Table SI-15).

Conclusions

Fe is a promising substitute for noble metals in catalysts for the oxidation of CO for environmental protection. The development of a new synthesis strategy for the preparation of Al-supported iron oxide catalysts for CO oxidation and the thorough catalytic and analytic measurements conducted using Brunauer–Emmett–Teller (BET), XRD, diffuse reflectance UV/Vis spectroscopy (DRUVS), and X-ray absorption spectroscopy (XAS) marks two milestones towards the establishment of sustainable catalytic systems based on iron:

1) Fe-core–metal-shell precursors can be used to achieve defined structures of the Fe species in the final catalyst by variation of the shell metal. The integrating structure formation approach with a nanoparticle species consisting of an Fe core and a shell containing the same metal as the support—here Al as in the support γ-Al_2O_3—produces a large proportion of isolated Fe sites, which can be preserved even at high loadings of 10 wt% Fe. In contrast, the isolating structure formation approach with shell metals different from the support—here Mg and Li—leads to larger agglomerates of iron oxide particles or mixed oxides with the support, with only a small proportion of isolated iron sites.

2) Isolated tetrahedral Fe^{III} sites are correlated to high catalytic activity. The most active catalysts pre-

Table 2. Structural parameters obtained by EXAFS analysis of catalyst synthesized applying $AlPh_3$ (integrating structure approach).

Sample	Abs(Bs)[a]	N(Bs)[b]	Abs–Bs[c] [Å]	σ[d] [Å^{-1}]	R[e] [%]	E[f] [eV]	Afac[g]	N(Fe)/ N(Al)
AlPh_01	Fe(O)	1.8 ± 0.09	1.837 ± 0.018	0.039 ± 0.003	30.04	3.916	0.9745	0.39
	Fe(O)	3.3 ± 0.16	1.988 ± 0.019	0.087 ± 0.008				
	Fe(Fe)	0.1 ± 0.01	2.959 ± 0.029	0.032 ± 0.003				
	Fe(Al)	5.3 ± 0.53	3.343 ± 0.033	0.122 ± 0.011				
	Fe(Fe)	2.0 ± 0.20	3.428 ± 0.034	0.097 ± 0.009				
AlPh_05	Fe(O)	1.7 ± 0.09	1.854 ± 0.018	0.055 ± 0.005	30.15	4.759	0.8577	0.50
	Fe(O)	3.6 ± 0.18	1.976 ± 0.019	0.095 ± 0.009				
	Fe(Fe)	0.3 ± 0.03	2.987 ± 0.029	0.092 ± 0.009				
	Fe(Al)	6.4 ± 0.64	3.320 ± 0.033	0.112 ± 0.011				
	Fe(Fe)	2.9 ± 0.29	3.406 ± 0.034	0.112 ± 0.011				
AlPh_10	Fe(O)	1.5 ± 0.07	1.861 ± 0.018	0.045 ± 0.004	27.59	3.173	0.8385	0.69
	Fe(O)	3.8 ± 0.19	1.994 ± 0.019	0.092 ± 0.009				
	Fe(Fe)	0.6 ± 0.06	3.009 ± 0.030	0.097 ± 0.009				
	Fe(Al)	5.3 ± 0.53	3.330 ± 0.033	0.112 ± 0.011				
	Fe(Fe)	3.1 ± 0.31	3.413 ± 0.034	0.112 ± 0.011				

[a] Abs: X-ray absorbing atom, Bs: backscattering atom. [b] Number of backscattering atoms. [c] Distance of absorbing atom to backscattering atom. [d] Debye–Waller-like factor. [e] Fit index. [f] Fermi energy, which accounts for the shift between theory and experiment. [g] Amplitude reducing factor.

Table 3. Structural parameters obtained by EXAFS analysis of catalyst synthesized applying PhMgBr (isolating structure approach).

Sample	Abs(Bs)[a]	N(Bs)[b]	Abs–Bs[c] [Å]	σ[d] [Å^{-1}]	R[e] [%]	E[f] [eV]	Afac[g]	N(Fe)/ N(Al)
PhMgBr_ 01	Fe(O)	1.4 ± 0.07	1.877 ± 0.018	0.071 ± 0.007	31.86	6.676	1.024	0.24
	Fe(O)	3.9 ± 0.19	1.921 ± 0.019	0.112 ± 0.011				
	Fe(Fe)	0.6 ± 0.06	3.019 ± 0.030	0.087 ± 0.008				
	Fe(Al)	3.7 ± 0.37	3.264 ± 0.032	0.122 ± 0.011				
	Fe(Fe)	0.3 ± 0.03	3.476 ± 0.034	0.039 ± 0.003				
PhMgBr_ 05	Fe(O)	1.1 ± 0.05	1.846 ± 0.018	0.032 ± 0.003	28.82	3.082	0.8663	0.84
	Fe(O)	4.4 ± 0.22	1.985 ± 0.019	0.084 ± 0.008				
	Fe(Fe)	1.0 ± 0.10	2.996 ± 0.029	0.074 ± 0.007				
	Fe(Al)	5.2 ± 0.52	3.339 ± 0.033	0.102 ± 0.010				
	Fe(Fe)	3.4 ± 0.34	3.469 ± 0.034	0.112 ± 0.011				
PhMgBr_ 10	Fe(O)	1.2 ± 0.01	1.855 ± 0.018	0.032 ± 0.003	27.90	2.682	0.8585	1.01
	Fe(O)	4.3 ± 0.21	1.992 ± 0.019	0.084 ± 0.008				
	Fe(Fe)	1.6 ± 0.16	3.011 ± 0.030	0.095 ± 0.009				
	Fe(Al)	5.4 ± 0.54	3.368 ± 0.033	0.112 ± 0.011				
	Fe(Fe)	3.9 ± 0.39	3.468 ± 0.034	0.112 ± 0.011				

[a] Abs: X-ray absorbing atom, Bs: backscattering atom. [b] Number of backscattering atoms. [c] Distance of absorbing atom to backscattering atom. [d] Debye–Waller-like factor. [e] Fit index. [f] Fermi energy, which accounts for the shift between theory and experiment. [g] Amplitude reducing factor.

Table 4. Structural parameters obtained by EXAFS analysis of catalyst synthesized applying PhLi (isolating structure approach).

Sample	Abs(Bs)[a]	N(Bs)[b]	Abs–Bs [c] [Å]	σ[d] [Å^{-1}]	R[e] [%]	E[f] [eV]	Afac[g]	N(Fe)/ N(Al)
PhLi_01	Fe(O)	1.7 ± 0.08	1.854 ± 0.018	0.055 ± 0.005	34.66	2.698	0.8233	1.11
	Fe(O)	3.4 ± 0.17	1.963 ± 0.019	0.112 ± 0.011				
	Fe(Fe)	2.6 ± 0.26	3.075 ± 0.030	0.112 ± 0.011				
	Fe(Al)	2.7 ± 0.27	3.255 ± 0.032	0.122 ± 0.011				
	Fe(Fe)	0.4 ± 0.04	3.497 ± 0.034	0.039 ± 0.003				
PhLi_05	Fe(O)	1.2 ± 0.06	1.862 ± 0.018	0.067 ± 0.006	35.89	3.854	0.9098	1.50
	Fe(O)	4.2 ± 0.21	1.933 ± 0.019	0.107 ± 0.010				
	Fe(Fe)	0.5 ± 0.05	2.963 ± 0.029	0.039 ± 0.003				
	Fe(Al)	1.6 ± 0.16	3.262 ± 0.032	0.039 ± 0.003				
	Fe(Fe)	1.9 ± 0.19	3.460 ± 0.034	0.092 ± 0.009				
PhLi_10	Fe(O)	1.4 ± 0.07	1.831 ± 0.018	0.032 ± 0.003	32.59	3.210	0.7909	2.33
	Fe(O)	3.9 ± 0.19	1.951 ± 0.019	0.071 ± 0.007				
	Fe(Fe)	0.8 ± 0.08	2.963 ± 0.029	0.050 ± 0.005				
	Fe(Al)	1.8 ± 0.18	3.264 ± 0.032	0.032 ± 0.003				
	Fe(Fe)	3.4 ± 0.34	3.460 ± 0.034	0.100 ± 0.010				

[a] Abs: X-ray absorbing atom, Bs: backscattering atom. [b] Number of backscattering atoms. [c] Distance of absorbing atom to backscattering atom. [d] Debye–Waller-like factor. [e] Fit index. [f] Fermi energy, which accounts for the shift between theory and experiment. [g] Amplitude reducing factor.

pared by the integrating structure formation approach contain a major fraction of isolated tetrahedral coordinated Fe^{III} ions incorporated in the alumina support surface lattice. The activity of such coordinatively unsaturated sites is suspected to be caused by the possibility to coordinate to either CO or O$_2$ in a dissociative process.[19]

Consequently, the directed preparation of monodisperse isolated tetrahedral Fe^{III} species on Al$_2$O$_3$ or other supports is identified as a key challenge for the future. As established by the results in this work, bimetallic Fe precursors, in which the second metal is identical to the constituent metal in the support, are a promising way to achieve this aim. According to the presented results, if the second metal used to form the shell is different from the support, highly agglomerated iron oxide structures with inferior activity are produced. The role of the metals, especially Li, which showed very low activity, needs to be further investigated as they influence the redox behavior of iron oxide.[38]

It is remarkable that the catalysts did not show any significant changes in their spectroscopic signatures after they were used for the oxidation of CO, indicating a high structural stability; the catalysts prepared using the integrating structure formation approach showed superior structural stability than those prepared using the isolating structure formation approach. To further promote iron oxide-based catalyst systems as a sustainable alternative to noble metal systems, further reduction of the light-off temperature below 200 °C needs to be achieved.

Experimental Section

Materials. Unless stated below, all chemicals were purchased from Sigma–Aldrich. Iron(III) tris-acetylacetonate [Fe(acac)$_3$] was dissolved under an inert atmosphere in a 1:1 volumetric mixture of tetrahydrofuran (THF, purity ≥99.9 %, anhydrous) and N-methy-2-pyrrolidone (NMP, purity 99.5 %, anhydrous) to obtain a solution with a concentration of 0.25 mol L^{-1}. Four equivalents of the metal organic reducing reagent were added slowly to this solution under vigorous stirring. Phenyl magnesium bromide (PhMgBr, 3 M in diethyl ether), triphenyl aluminum (AlPh$_3$, 1 M in dibutyl ether) or phenyl lithium (PhLi, 1.8 M in dibutyl ether) were used as the reducing agents. In the second step, the reaction mixture was slowly added in varying amounts to a rigorously stirred suspension of γ-Al$_2$O$_3$ in THF to obtain nominal catalyst loadings of 1, 5, and 10 wt % Fe referred to the mass of Fe on the support. The solvents were removed at 150 °C under vacuum and the catalysts were calcined at 600 °C for 3 h under air. γ-Al$_2$O$_3$ was synthesized using aluminum oxide hydroxide PURAL-B (Sasol) as precursor by calcination at 600 °C for 3 h under air to obtain the support material.

Catalytic activity. The catalytic activity for the oxidation of CO was tested in a quartz glass plug flow reactor with an internal diameter of 7.8 mm. 200 mg of the catalyst was used in granulated form with particle sizes of 125–250 μm and diluted with 800 mg of glass beads to gain a fill height of 10 mm in the reactor tube. The composition of the gas used for the catalytic tests was 1000 ppm CO and 10 % O$_2$ balanced in N$_2$ with a total flow of 500 mL min^{-1}, resulting in a space velocity of 17.3 s^{-1}. The catalyst was heated at a rate of 3 °C min^{-1} up to 600 °C and the CO concentration in the exhaust gas was detected using an Uras 10E infrared spectrometer from Hartmann&Braun. A

Boltzmann function was fit to the data and the inflection point was used to determine the half-conversion temperature. The intersection points of a tangent applied at the inflection point with 0 and 100% conversion were defined as light-off and full conversion temperatures.

Characterization. The specific surface areas of the catalysts were determined using the BET method. Before the measurement using a Belsorp mini II from BEL Japan, the samples were activated at 300°C under vacuum for 2 h. Powder XRD measurements were performed in reflection mode on a Siemens d5005 using CuKα radiation and rotating samples. Data was recorded between $2\theta = 15°$ and $2\theta = 80°$ with a step size of $2\theta = 0.0163977°$ and an acquisition time of 2.5 s per point. DRUVS was performed using a Lambda 18 spectrometer from PerkinElmer. An exponential function was subtracted from the spectra for background removal. Gaussian-type functions were used to fit the spectra. During the course of this, as few Gaussian-type functions as possible were adjusted to obtain satisfactory χ^2_{red} error values with a magnitude of 10^{-5} (values listed in Table SI-2–4). XAS experiments were performed at the beamline X1 of HASYLAB (Hamburger Synchrotronstrahlungslabor) in Hamburg (Germany). The measurements at the iron K-edge (7.112 keV) were performed using a Si (111) double-crystal monochromator with an Fe foil as energy reference material for calibration of the monochromator. All the samples were measured in pellet form and at ambient temperature. For data evaluation, a Victoreen-type polynomial was subtracted from the spectrum to remove the background.[39] Energy E_0 was ascertained by using the first inflection point of the resulting spectrum. For evaluation of the EXAFS spectra, fitting functions were calculated with EXCURVE98, which worked based on the EXAFS function. See the Supporting Information for more detailed information.

[1] a) L. Boisvert, K. I. Goldberg, *Acc. Chem. Res.* **2012**, *45*, 899–910; b) G. J. Hutchings, *J. Mater. Chem.* **2009**, *19*, 1222–1235; c) G. Salek, P. Alphonse, P. Dufour, S. Guillemet-Fritsch, C. Tenailleau, *Appl. Catal. B* **2014**, *147*, 1–7; d) X. Zhang, Z. Qu, F. Yu, Y. Wang, *Chin. J. Catal.* **2013**, *34*, 1277–1290; e) A. K. Kandalam, B. Chatterjee, S. N. Khanna, B. K. Rao, P. Jena, B. V. Reddy, *Surf. Sci.* **2007**, *601*, 4873–4880; f) B. V. Reddy, S. N. Khanna, *Phys. Rev. Lett.* **2004**, *93*, 683011–683014.

[2] A. Russell, W. S. Epling, *Catal. Rev. Sci. Eng.* **2011**, *53*, 337–423.

[3] a) J.-D. Grunwaldt, C. Kiener, C. Wögerbauer, A. Baiker, *J. Catal.* **1999**, *181*, 223–232; b) M. Bandyopadhyay, O. Korsak van den Berg, M. W. E., W. Grünert, A. Birkner, W. Li, F. Schüth, H. Gies, *Microporous Mesoporous Mater.* **2006**, *89*, 158–163; c) T. Zheng, J. He, Y. Zhao, W. Xia, J. He, *J. Rare Earths* **2014**, *32*, 97–107; d) J. M. Herreros, S. S. Gill, I. Lefort, A. Tsolakis, P. Millington, E. Moss, *Appl. Catal. B* **2014**, *147*, 835–841; e) A. Boubnov, S. Dahl, E. Johnson, A. Puig Molina, S. Bredmose Simonsen, F. Morales Cano, S. Helveg, L. J. Lemus-Yegres, J.-D. Grunwaldt, *Appl. Catal. B* **2012**, *126*, 315–325; f) P. Glatzel, J. Singh, K. O. Kvashnina, J. A. van Bokhoven, *J. Am. Chem. Soc.* **2010**, *132*, 2555–2557.

[4] P. J. Loferski, *2012 Minerals Yearbook: Platinum-Group Metals*.

[5] a) U. Lucia, *Renewable Sustainable Energy Rev.* **2014**, *30*, 164–169; b) L. Carrette, K. A. Friedrich, U. Stimming, *ChemPhysChem* **2000**, *1*, 162–193.

[6] a) A. Kruse, A. Funke, M.-M. Titirici, *Curr. Opin. Chem. Biol.* **2013**, *17*, 515–521; b) J. C. Serrano-Ruiz, R. M. West, J. A. Dumesic, *Annu. Rev. Chem. Biomol. Eng.* **2010**, *1*, 79–100.

[7] a) K. Kalbitz, D. Schwesig, W. Wang, *Sci. Total Environ.* **2008**, *405*, 239–245; b) H. M. Prichard, P. C. Fisher, *Environ. Sci. Technol.* **2012**, *46*, 3149–3154; c) S. Zimmermann, J. Messerschmidt, A. von Bohlen, B. Sures, *Environ. Res.* **2005**, *98*, 203–209.

[8] a) V. Krewald, M. Retegan, D. A. Pantazis, *Top. Curr. Chem.* **2015**, *371*, 23–48; b) M. Giedyk, K. Goliszewska, D. Gryko, *Chem. Soc. Rev.* **2015**, *44*, 3391–3404; c) M. C. Frise, P. A. Robbins, *J. Appl. Physiol.* **2015**, *119*, 1421–1431.

[9] S. Royer, D. Duprez, *ChemCatChem* **2011**, *3*, 24–65.

[10] P. Li, D. E. Miser, S. Rabiei, R. T. Yadav, M. R. Hajaligol, *Appl. Catal. B* **2003**, *43*, 151–162.

[11] J. G. Carriazo, M. A. Centeno, J. A. Odriozola, S. Moreno, R. Molina, *Appl. Catal. A* **2007**, *317*, 120–128.

[12] H.-Y. Lin, Y.-W. Chen, W.-J. Wang, *J. Nanopart. Res.* **2005**, *7*, 249–263.

[13] O. H. Laguna, M. A. Centeno, M. Boutonnet, J. A. Odriozola, *Appl. Catal. B* **2011**, *106*, 621–629.

[14] J. S. Walker, G. I. Straguzzi, W. H. Manogue, G. C. Schuit, *J. Catal.* **1988**, *110*, 298–309.

[15] Á. Szegedi, M. Hegedűs, J. L. Margitfalvi, I. Kiricsi, A. Szegedi, M. Hegedus, J. L. Margitfalvi, I. Kiricsi, *Chem. Commun.* **2005**, 1441–1443.

[16] J.-N. Park, P. Zhang, Y.-S. Hu, E. W. McFarland, *Nanotechnology* **2010**, *21*, 225708.

[17] M. Tepluchin, M. Casapu, A. Boubnov, H. Lichtenberg, Di Wang, S. Kureti, J.-D. Grunwaldt, *ChemCatChem* **2014**, *6*, 1763–1773.

[18] M. Tepluchin, D. K. Pham, M. Casapu, L. Mädler, S. Kureti, J.-D. Grunwaldt, *Catal. Sci. Technol.* **2015**, *5*, 455–464.

[19] S. Wagloehner, D. Reichert, D. Leon-Sorzano, P. Balle, B. Geiger, S. Kureti, *J. Catal.* **2008**, *260*, 305–314.

[20] H. Randall, R. Doepper, A. Renken, *Ind. Eng. Chem. Res.* **1997**, *36*, 2996–3001.

[21] C. Breyer, D. Reichert, J. Seidel, R. Huttl, F. Mertens, S. Kureti, *Phys. Chem. Chem. Phys.* **2015**, *17*, 27011–27018.

[22] R. Schoch, H. Huang, V. Schünemann, M. Bauer, *ChemPhysChem* **2014**, *15*, 3768–3775.

[23] I. Hnat, I. Kocemba, J. Rynkowski, T. Onfroy, S. Dzwigaj, *Catal. Today* **2011**, *176*, 229–233.

[24] L. Smrcok, V. Langer, J. Krestan, *Acta Crystallogr. Sect. C* **2006**, *62*, i83–84.

[25] C. Pecharromán, T. González-Carreño, J. Iglesias, *Phys. Chem. Miner.* **1995**, *22*, 21–29.

[26] N. Pailhé, A. Wattiaux, M. Gaudon, A. Demourgues, *J. Solid State Chem.* **2008**, *181*, 1040–1047.

[27] F. Bouree, J.-L. Baudour, E. El Badraoui, J. Musso, C. Laurent, A. Rousset, *Acta Crystallogr. Sect. B* **1996**, *52*, 217–222.

[28] M. Marezio, *J. Chem. Phys.* **1966**, *44*, 3143.

[29] a) E. J. M. Hensen, Q. Zhu, M. M. R. M. Hendrix, A. R. Overweg, P. J. Kooyman, M. V. Sychev, R. A. van Santen, *J. Catal.* **2004**, *221*, 560–574; b) M. Schwidder, M. S. Kumar, K. Klementiev, M.-M. Pohl, A. Brückner, W. Grünert, *J. Catal.* **2005**, *231*, 314–330; c) J. Janas, J. Gurgul, R. P. Socha, T. Shishido, M. Che, S. Dzwigaj, *Appl. Catal. B* **2009**, *91*, 113–122; d) M. S. Kumar, M. Schwidder, W. Grünert, A. Brückner, *J. Catal.* **2004**, *227*, 384–397; e) J. Pérez-Ramírez, A. Gallardo-Llamas, *J. Phys. Chem. B* **2005**, *109*, 20529–20538.

[30] a) F. W. Lytle, *J. Synchrotron Radiat.* **1999**, *6*, 123–134; b) D. C. Koningsberger, B. L. Mojet, G. E. van Dorssen, D. E. Ramaker, *Top. Catal.* **2000**, *10*, 143–155.

[31] S. Yao et al., *ACS Catal.* **2014**, *4*, 1650–1661.

[32] J. D. Walker, A. P. Grosvenor, *J. Solid State Chem.* **2013**, *197*, 147–153.

[33] a) M. Bauer, C. Gastl, *Phys. Chem. Chem. Phys.* **2010**, *12*, 5575–5584; b) M. Bauer, T. Kauf, J. Christoffers, H. Bertagnolli, *Phys. Chem. Chem. Phys.* **2005**, *7*, 2664–2670; c) R. Schäfer, P. C. Schmidt (Eds.) *Methods in Physical Chemistry. X-Ray Absorption Spectroscopy—The Method and Its Applications*, Wiley-VCH Verlag, Weinheim, **2012**.

[34] D. K. Bora, A. Braun, S. Erat, O. Safonova, T. Graule, E. C. Constable, *Curr. Appl. Phys.* **2012**, *12*, 817–825.

[35] H. Okudera, A. Yoshiasa, K. Murai, M. Okube, T. Takeda, S. Kikkawa, *J. Mineral. Petrol. Sci.* **2012**, *107*, 127–132.

[36] a) A. P. Grosvenor, J. E. Greedan, *J. Phys. Chem. C* **2009**, *113*, 11366–11372; b) M. W. Gaultois, J. E. Greedan, A. P. Grosvenor, *J. Electron Spectrosc. Relat. Phenom.* **2011**, *184*, 192–195.

[37] E. N. Maslen, V. A. Streltsov, N. R. Streltsova, N. Ishizawa, *Acta Crystallogr. Sect. B* **1994**, *50*, 435–441.

[38] Q. Imtiaz, N. S. Yüzbasi, P. M. Abdala, A. M. Kierzkowska, W. van Beek, M. Broda, C. R. Müller, *J. Mater. Chem. A* **2016**, *4*, 113–123.

[39] a) M. Newville, P. Līviņš, Y. Yacoby, J. J. Rehr, E. A. Stern, *Phys. Rev. B* **1993**, *47*, 14126–14131; b) T. S. Ertel, H. Bertagnolli, S. Hückmann, U. Kolb, D. Peter, *Appl. Spectrosc.* **1992**, *46*, 690–698.

CHEMISTRY & SUSTAINABILITY

CHEM**SUS**CHEM

ENERGY & MATERIALS

Supporting Information

Pollution Control Meets Sustainability: Structure–Activity Studies on New Iron Oxide-Based CO Oxidation Catalysts

Roland Schoch and Matthias Bauer*[a]

cssc_201600508_sm_miscellaneous_information.pdf

EXPERIMENTAL

To facilitate the nomenclature of the catalysts, the following abbreviations were used for the

catalysts after their use in CO oxidation:

Table SI-1: Abbreviations used for the synthesized catalysts after application in CO oxidation reaction

dependent on reducing compound and iron loading (1, 5, 10 wt%).

Metal organic compound	$AlPh_3$	PhMgBr	PhLi
Structure formation	integrating	Isolating	
1 wt% loading	AlPh_01_u	PhMgBr_01_u	PhLi_01_u
5 wt% loading	AlPh_05_u	PhMgBr_05_u	PhLi_05_u
10 wt% loading	AlPh_10_u	PhMgBr_10_u	PhLi_10_u

CATALYSIS

The catalytic activities of all synthesized catalysts in dependence of the organometallic compound,

which was used in preparation process and of iron loading are given in Figure SI- 1. The measurement

parameter are mentioned in the main paper. Additionally, the pure support without iron application

was tested in CO oxidation in the same fashion, than the prepared catalysts and showed absolutely

no activity, as ca be seen in figure SI-2. As can be seen, the pure support shows no conversion.
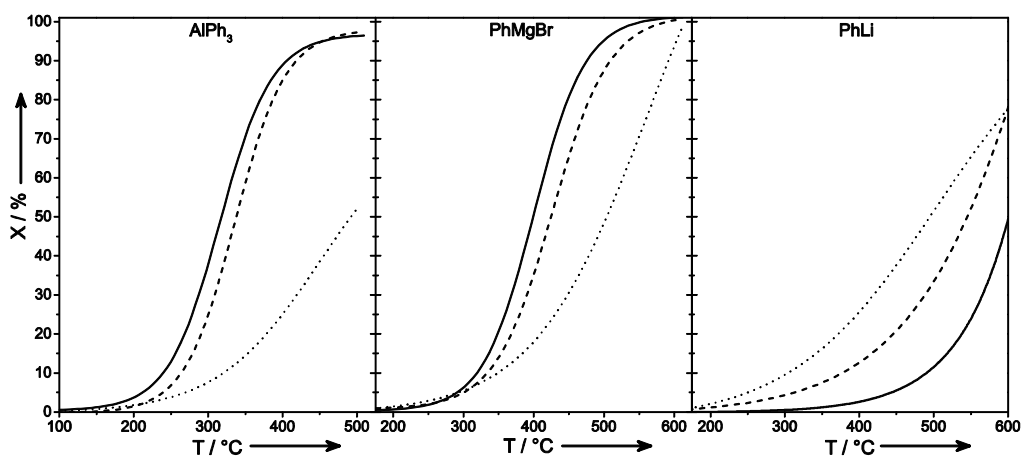
Figure SI- 1: Catalytic performances of the synthesized catalysts with loadings of 1 wt% (⋯), 5 wt% (---) and

10 wt% (—).
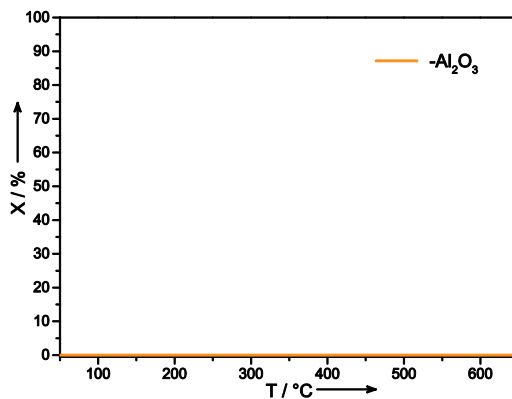
Figure SI- 2: *Catalytic activity in CO oxidation of the pure support γ-Al₂O₃.*

To determine the temperature for half conversion of a catalyst, the inflection point of a fitted Boltzmann function was used. The temperatures for light-off and full conversion were determined by intersection points of a tangent fitted in the inflection point of the Boltzmann fit and 0 % resp. 100 % conversion. Since not in all cases full conversion was reached until the maximum measured temperature of 600 °C, a theoretical value was calculated this way. The resulting functions are shown in Figure SI- *3* to Figure **SI- *5*** and the corresponding fitting values in Table SI- 2Table SI- **4**.

Figure SI- 3: CO oxidation conversion curves oft he catalysts synthesized with AlPh₃ with fitted Boltzmann and linear functions for the determination of light-off and full conversion temperatures (orange) and half conversion temperatures (blue).

Table SI- 2: Fitting parameter and errors of the adjustments of Boltzmann function and linear fit carried out for the determination of light-off, half and full conversion temperature of catalysts prepared using AlPh₃.

Boltzmann function			$y = A_2 + \dfrac{A_1 - A_2}{1 + e^{\frac{x - x_0}{dx}}}$				
1 wt% loading			5 wt% loading			10 wt% loading	
	Value	Error		Value	Error		Value	Error
A_1	-0.22866	0.04663	A_1	-0.2703	0.03076	A_1	0.36315	0.02702
A_2	76.95932	0.70559	A_2	97.97015	0.04948	A_2	96.76646	0.04002
x_0	449.47966	1.27961	x_0	336.3148	0.07422	x_0	315.7074	0.06825
dx	68.55202	0.49895	dx	33.85441	0.06659	dx	34.77345	0.06107
χ^2_{red}	1.41897		χ^2_{red}	1.2703		χ^2_{red}	1.09383	
r^2_{corr}	0.99418		r^2_{corr}	0.99919		r^2_{corr}	0.9993	
Linear fit			$y = mx + b$				
1 wt% loading			5 wt% loading			10 wt% loading	
	Value	Error		Value	Error		Value	Error
m	0.27385	7.101E-4	m	0.63463	0.00815	m	0.62068	0.00718
b	-84.73667	0.32165	b	-164.269	2.69648	b	-147.160	0.00718
r^2_{corr}	0.99985		r^2_{corr}	0.99589		r^2_{corr}	0.9972	
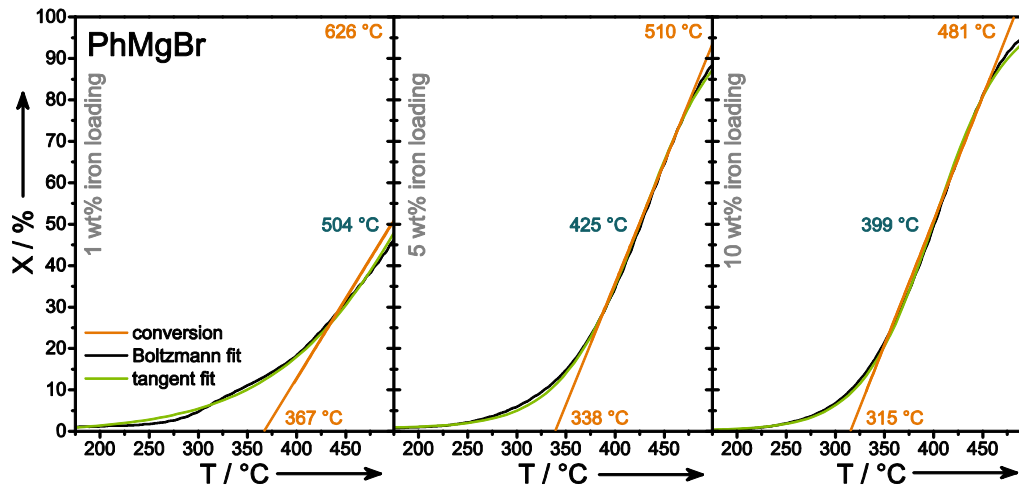
Figure SI- 4: CO oxidation conversion curves oft he catalysts synthesized with PhMgBr with fitted Boltzmann and linear functions for the determination of light-off and full conversion temperatures (orange) and half conversion temperatures (blue).

Table SI- 3: Fitting parameter and errors of the adjustments of Boltzmann function and linear fit carried out for the determination of light-off, half and full conversion temperature of catalysts prepared using PhMgBr.

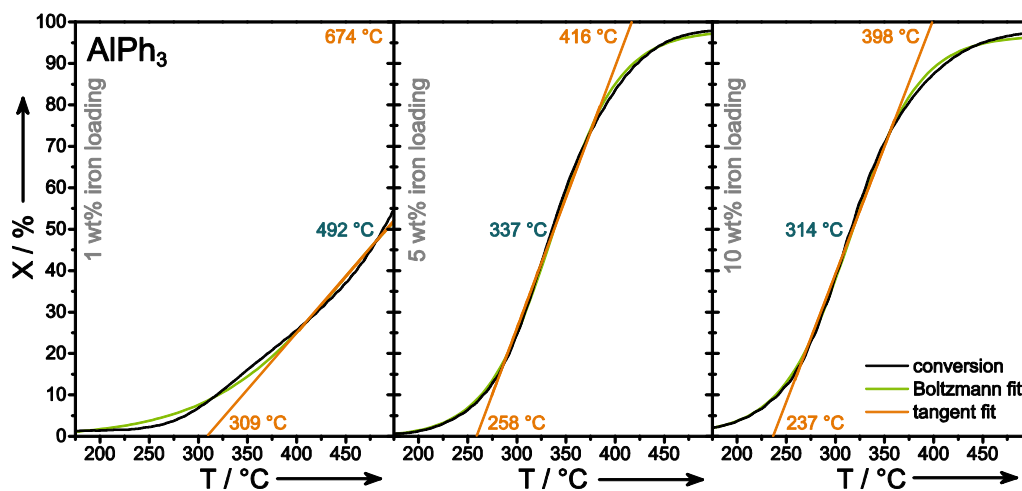| Boltzmann function							
			$y = A_2 + \dfrac{A_1 - A_2}{1 + e^{\frac{x-x_0}{dx}}}$				
1 wt% loading			5 wt% loading			10 wt% loading	
	Value	Error		Value	Error		Value	Error
A_1	-0.33102	0.02755	A_1	0.7548	0.02084	A_1	0.2165	0.01965
A_2	151.3028	0.633	A_2	101.70803	0.04802	A_2	101.41149	0.03394
x_0	560.64905	0.68395	x_0	426.6997	0.07506	x_0	400.38572	0.0593
dx	80.89028	0.2311	dx	40.50467	0.06438	dx	36.43096	0.05193
χ^2_{red}	1.11797		χ^2_{red}	1.00691		χ^2_{red}	0.92872	
r^2_{corr}	0.99859		r^2_{corr}	0.99932		r^2_{corr}	0.99946	
Linear fit			$y = mx + b$				
1 wt% loading			5 wt% loading			10 wt% loading	
	Value	Error		Value	Error		Value	Error
m	0.38633	0.00731	m	0.58035	0.00494	m	0.59961	0.00883
b	-141.9592	3.67192	b	-196.285	2.0882	b	-188.959	3.49649
r^2_{corr}	0.98795		r^2_{corr}	0.99884		r^2_{corr}	0.99546	
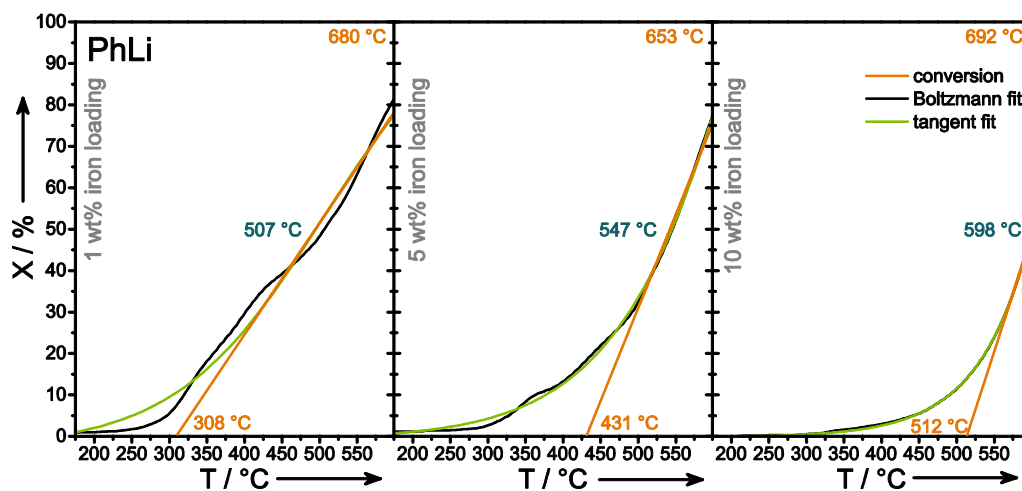
Figure SI- 5: CO oxidation conversion curves oft he catalysts synthesized with PhLi with fitted Boltzmann and linear functions for the determination of light-off and full conversion temperatures (orange) and half conversion temperatures (blue).

Table SI- 4: Fitting parameter and errors of the adjustments of Boltzmann function and linear fit carried out for the determination of light-off, half and full conversion temperature of catalysts prepared using PhLi.

Boltzmann function		$y = A_2 + \dfrac{A_1 - A_2}{1 + e^{\frac{x - x_0}{dx}}}$				
1 wt% loading		5 wt% loading		10 wt% loading		
	Value	Error		Value	Error		Value	Error
A_1	-2.60498	0.09635	A_1	-0.70211	0.02864	A_1	-0.15819	0.00913
A_2	107.46789	0.94529	A_2	307.41464	6.71846	A_2	47075.98	291766.13
x_0	503.77259	1.74659	x_0	705.87813	3.23466	x_0	1074.6503	431.04928
dx	97.34016	0.82098	dx	98.85137	0.41135	dx	69.23132	0.24099
χ^2_{red}	6.55309		χ^2_{red}	0.92438		χ^2_{red}	0.1845	
r^2_{corr}	0.98942		r^2_{corr}	0.99798		r^2_{corr}	0.99844	
Linear fit		$y = mx + b$				
1 wt% loading		5 wt% loading		10 wt% loading		
	Value	Error		Value	Error		Value	Error
m	0.23897	0.00102	m	0.45066	0.00996	m	0.55575	0.0049
b	-83.04558	0.51602	b	-194.436	5.50839	b	-284.910	2.8536
r^2_{corr}	0.99952		r^2_{corr}	0.99176		r^2_{corr}	0.99474	

Additionally turn-over frequencies are calculated for the investigated catalysts at 400 °C, which is a typical light-off temperature for a three-way catalyst in automobiles [1] and listed in Table **SI- 5**. The values cannot be used as meaningful description for the different catalytic performances of intedgrated and isolated structures, due to the fact that the real number of accesible catalytic active sites could not be determined. Instead, the total numbers of present Fe sites are used in the calculation, which lead to a decrease of TOFs for every catalys system with higher loading. Nevertheless, the general trends of the different catalytic performances are visible. For every loading the TOFs of AlPh$_3$ catalysts are the highest followed by the TOFs of PhMgBr and PhLi with the lowest TOF.

Table SI- 5: Calculated turn-over frequencies of the syntheszed catalysts in CO oxidation at 400 °C.

Catalyst	Loading [%]	TOF [s^{-1}]
AlPh$_3$	1	$2.67 \cdot 10^{-3}$
	5	$1.70 \cdot 10^{-3}$
	10	$9.20 \cdot 10^{-4}$
PhMgBr	1	$1.94 \cdot 10^{-3}$
	5	$7.16 \cdot 10^{-4}$
	10	$5.47 \cdot 10^{-4}$
PhLi	1	$2.63 \cdot 10^{-3}$
	5	$2.66 \cdot 10^{-4}$
	10	$5.47 \cdot 10^{-5}$

DIFFUSE REFLECTANCE UV/VIS SPECTROSCOPY

DRUVS spectra and the corresponding extracted impulse fittings of the synthesized iron catalysts after application in CO oxidation reaction are shown in Figure **SI- 6**. Detailed information are displayed in Table SI- 6 to Table SI- 8. Since in case of AlPh_10_u after application as catalyst in CO oxidation not enough sample could be isolated, no DRUVS characterization is possible.

Calculation of average coordination numbers from DRUVS spectra was carried out by comparison of the normalized areas of the fitted Gaussian curves. Bands between 200 and 300 nm were assigned to tetrahedral coordination, bands between 300 and 400 nm were assigned to octahedral coordination. Bands with wavelengths above 400 nm are assigned to oligomeric Fe_xO_y. In order to be able to account for these structures in the quantification of tetrahedral and octahedral sites, a γ-Fe_2O_3 structure is assumed. According to the coordination numbers in the γ-Fe_2O_3 crystal structure, tetrahedral and octahedral fractions are considered in the calculations. Due to the defect spinel structure of γ-Fe_2O_3 ($\{Fe^{+3}\}_{tet}\{Fe_{5/3}^{+3}+\square_{1/3}\}_{oct}O_4$)[22] ($\square$=defect position) 37.5 % of all iron sites are attributed to tetrahedral coordination and 62.5 % to octahedral coordination.

For all catalysts application in CO oxidation reaction had only a small influence on the proportional distribution of the coordination. Only a slight decrease of the amount of tetrahedrally coordinated centers and a small increase of octahedrally coordinated centers could be detected.
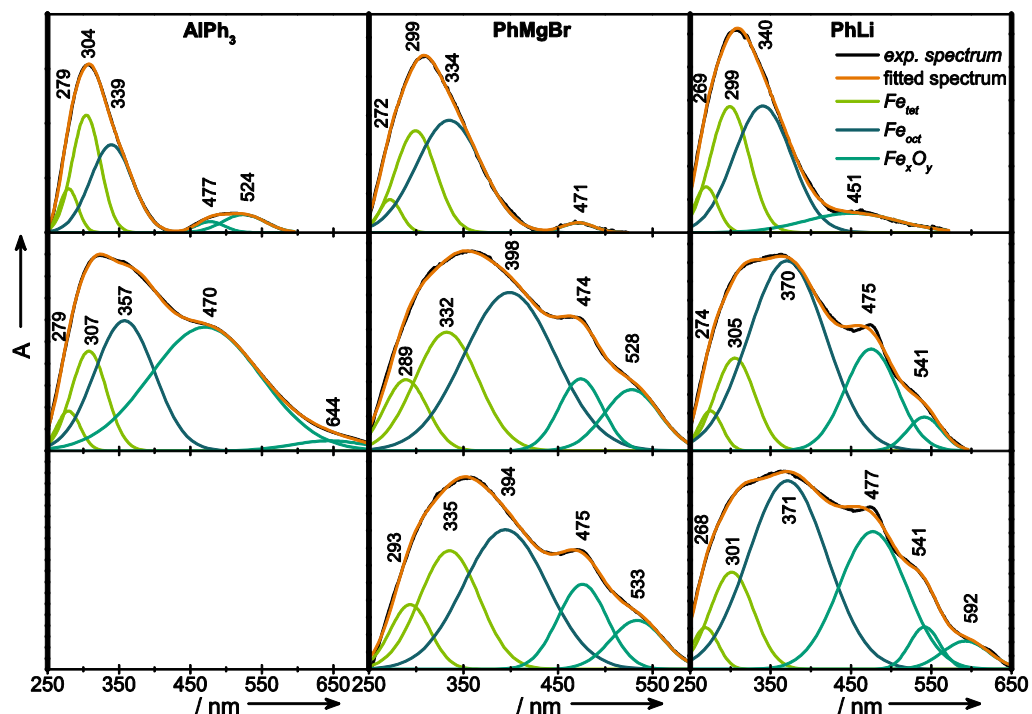
Figure SI- 6: DRUVS spectra of the synthesized catalysts after application in CO oxidation fitted with Gaussian curves dependent on iron loading. Top: 1 wt% loading, middle: 5 wt% loading, bottom: 10 wt% loading.

Table SI- 6: DRUVS signals of the catalysts synthesized using AlPh$_3$ and assignments to coordination and calculated coordination numbers for iron centers.

Sample	Signal [nm]	Error of Fit χ^2_{red}	Assignment [a]	Percentage [%]	Calc. coord number of 1st and 2nd Fe-O contribution
AlPh_01	269		[4]Fe	41.8	1.9
	298	1.224·10^{-5}			
	332		[6]Fe	45.4	3.2
	415		Fe$_x$O$_y$	12.9	
AlPh_01_u	279		[4]Fe	46.3	2.0
	304				
	339	1.238·10^{-6}	[6]Fe	41.6	2.9
	477		Fe$_x$O$_y$	12.2	
	524				
AlPh_05	272		[4]Fe	23.8	1.7
	309	1.466·10^{-5}			
	359		[6]Fe	28.6	3.5
	460		Fe$_x$O$_y$	47.6	

	656				
AlPh_05_u	279		[4]Fe	16.7	1.3
	307				
	357	$9.258 \cdot 10^{-6}$	[6]Fe	29.1	3.8
	470		Fe_xO_y	54.3	
	644				
AlPh_10	268		[4]Fe	19.6	1.5
	306				
	361	$3.017 \cdot 10^{-5}$	[6]Fe	30.1	3.7
	455		Fe_xO_y	50.4	
	546				
	[a] [4]Fe: tetrahedrally, [6]Fe: octahedrally coordinated iron center				

Table SI- 7: DRUVS signals of the catalysts synthesized using PhMgBr and assignments to coordination and

calculated coordination numbers for iron centers.

Sample	Signal [nm]	Error of Fit χ^2_{red}	Assignment [a]	Percentage [%]	Calc. coord number of 1st and 2nd Fe-O contribution
PhMgBr_01	269		[4]Fe	34.3	1.4
	294	$1.510 \cdot 10^{-5}$			
	329		[6]Fe	62.5	3.9
	471		Fe_xO_y	3.2	
PhMgBr_01_u	272		[4]Fe	39.1	1.6
	299	$5.727 \cdot 10^{-6}$			
	334		[6]Fe	58.4	3.6
	471		Fe_xO_y	2.5	
PhMgBr_05	273		[4]Fe	16.5	1.1
	304				
	367	$3.599 \cdot 10^{-5}$	[6]Fe	50.7	3.6
	471		Fe_xO_y	32.8	
	543				
PhMgBr_05_u	289		[4]Fe	9.7	0.7
	332		[6]Fe	69.5	5.0
	398	$4.487 \cdot 10^{-5}$			
	474		Fe_xO_y	20.8	
	528				
PhMgBr_10	272		[4]Fe	16.5	1.2
	304				
	362	$5.114 \cdot 10^{-5}$	[6]Fe	50.4	4.3
	470		Fe_xO_y	33.1	
	546				
PhMgBr_10_u	293		[4]Fe	9.2	0.7
	335		[6]Fe	66.7	4.9
	394	$3.294 \cdot 10^{-5}$			
	475		Fe_xO_y	24.1	
	533				

			[a] [4]Fe: tetrahedrally, [6]Fe: octahedrally coordinated iron center

Table SI- 8: DRUVS signals of the catalysts synthesized using PhLi and assignments to coordination and calculated coordination numbers for iron centers.

Sample	Signal [nm]	Error of Fit χ^2_{red}	Assignment [a]	Percentage [%]	Calc. coord number of 1st and 2nd Fe-O contribution
PhLi_01	267		[4]Fe	40.7	1.7
	295	7.643·10⁻⁵			
	335		[6]Fe	51.4	3.4
	470		FexOy	7.9	
	545				
PhLi_01_u	269		[4]Fe	39.4	1.8
	299	9.289·10⁻⁶			
	340		[6]Fe	48.6	3.4
	451		FexOy	12.0	
PhLi_05	273		[4]Fe	19.9	1.2
	305				
	371	8.498·10⁻⁵	[6]Fe	55.0	4.2
	474		FexOy	25.2	
	539				
PhLi_05_u	274		[4]Fe	18.0	1.1
	305				
	370	5.311·10⁻⁵	[6]Fe	56.8	4.4
	475		FexOy	25.3	
	541				
PhLi_10	268		[4]	24.0	1.4
	307				
	382	4.431·10⁻⁵	[6]	45.4	3.9
	480		FexOy	30.6	
	539				
	590				
PhLi_10_u	268		[4]	16.7	1.2
	301		[6]	46.3	4.2
	371	6.470·10⁻⁵			
	477		FexOy	37.1	
	541				
	592				
	[a] [4]Fe: tetrahedrally, [6]Fe: octahedrally coordinated iron center				

X-RAY ABSORPTION SPECTROSCOPY

X-ray absorption spectroscopy (XAS) experiments were performed at the beamline X1 of HASYLAB (Hamburger Synchrotronstrahlungslabor) in Hamburg (Germany). Application of a Si(111) double-

crystal monochromator delivers an energy resolution of $\frac{\Delta E}{E} = 2 \cdot 10^{-4}$ at the iron K-edge at 7112 eV.

Higher harmonics during the measurement have been rejected by tilting the second monochromator

crystal. The spectra of the 1 wt% loaded catalysts were recorded in fluorescence mode with a five

element Ge-detector, while for higher loadings transmission mode using ionization chambers was

applied. Energy calibration of the monochromator during transmission measurements was carried

out by using a third ionization chamber with an iron foil simultaneously to the sample spectrum. For

fluorescence mode spectra the iron foil was measured before and after the sample spectra. As can be

seen in *Table SI- 9* the parameter for data acquisition were varied in pre-edge, edge and post-edge

range. In EXAFS range the measurement time per point was increased as follows:

$$t_{measure} = t_{starting\ point} \cdot \left(\frac{wave\ vector\ E_{current}}{wave\ vector\ E_{starting\ point}} \right)^{exponent}$$

Whereby $t_{starting\ point} = 0.4\ s$ and $exponent = 1.7$.

Table SI- 9: Acquisition procedure of the carried out XAS experiments. Parameters were varied in three energy

ranges.

Energy ranges [eV]	ΔE [eV]	t [s]
6912…7072	5	0.4
7072…7152	0.5	0.4
7152…8010	0.5	0.4 … 4.64

For data evaluation a Victoreen-type polynomial was subtracted from the spectrum to remove the

background [1]. Energy E_0 was ascertained by using the first inflection point of the resulting spectrum.

A piecewise polynomial was used to determine the smooth part of the spectrum. It was optimized to

gain minimal low-R components of the resulting Fourier transformation. The background-corrected

spectrum was divided by its smoothed part and the photon energy was converted to photoelectron

wavenumber *k*. For evaluation of the EXAFS spectra, the resulting functions were weighted with k^3

and calculated with EXCURVE98, which worked based on the EXAFS function and according to

equation 1 in terms of radial functions [2,3]:

$$\chi(k) = \sum_j S_0^2(k) \frac{N_j}{kr_j^2} F_j(k) e^{-2\sigma_j^2 k^2} e^{-\frac{2r_j}{\lambda(k)}} sin[2kr_j + \varphi_{ij}(k)] \tag{1}$$

In this function the amplitude reducing factor $S_0^2(k)$ and the mean free path length λ account for inelastic effects. The number of backscattering atoms N_j, their average distance r_j to the X-ray absorbing atom and the degree of their disorder, reflected in the Debye-Waller-like factor σ_j^2, are structural parameters. In addition, backscattering amplitude $F_j(k)$ and phase shift $\varphi_{ij}(k)$ are element specific parameters. For EXAFS analysis the number of independent points N_{ind} was calculated using equation 2 for every fit to prevent overinterpretation by using too many parameters [3]:

$$N_{ind} = \frac{2\Delta k \Delta R}{\pi} \qquad\qquad (2)$$

Here Δk is the range used in k space and ΔR is the range in which distances were fitted. In *Table SI- 10* the number of independent points for every spectrum is listed:

Table SI- 10: Determined number of independent points (N_{ind}) for EXAFS analysis.

Reduction compound	Treatment	Loading [%]	N_{ind}
AlPh$_3$	Calcinated	1	20.3
		5	25.4
		10	25.4
	After application as catalyst	1	25.4
		5	25.4
		10	25.4
PhMgBr	Calcinated	1	17.8
		5	25.4
		10	25.4
	After application as catalyst	1	17.8
		5	25.4
		10	25.4
PhLi	Calcinated	1	17.8
		5	28.0
		10	28.0
	After application as catalyst	1	22.9
		5	25.4
		10	25.4

The accuracy of the determined distances was 1 %; it was 10 % for the Debye-Waller-like factor[4]; and 5-15 % for the coordination numbers, depending on the distance.

In Figure SI- 7 the X-ray absorption spectra of the investigated catalysts after application in CO oxidation are shown. The energetic positions of the pre-peaks and absorption edges are for all catalysts very similar. The pre-peak for all investigated catalysts is located between 7114.0 eV and 7114.5 eV, while the main edge is found between 7122.5 eV and 7122.9 eV. These energetic positions, which are characteristic for iron in the oxidation state +3, do not change during application as catalysts in CO oxidation, as demonstrated in Table SI- 11.
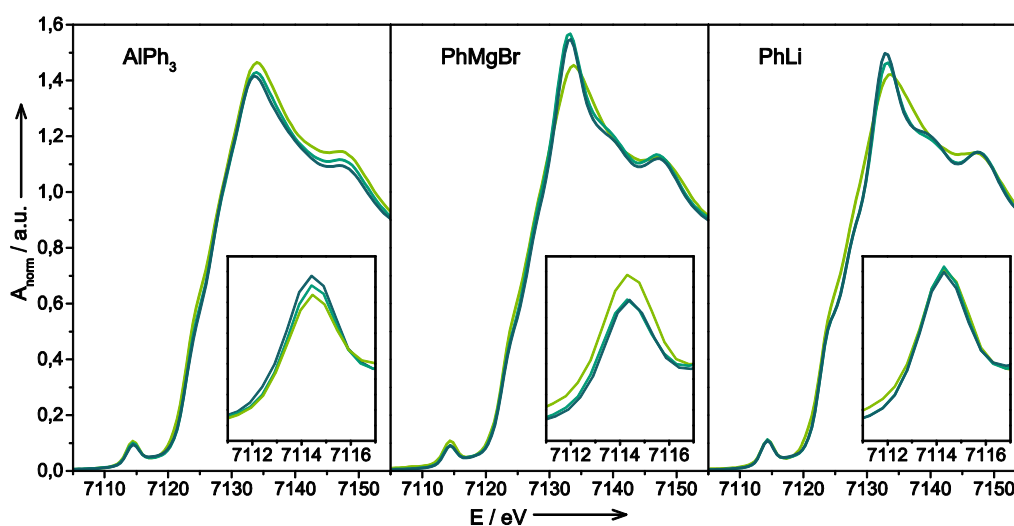
Figure SI- 7: X-ray absorption spectra of the investigated catalysts after application in CO oxidation reaction with iron loadings of 1 wt% (light green), 5 wt% (middle green) and 10 wt% (dark green).

Table SI- 11: Pre-peak and Fe K-edge energies of the investigated catalysts.

Sample	Pre-peak [eV]	Edge energy [eV]
AlPh_01	7114.3	7122.5
AlPh_01_u	7114.4	7122.9
AlPh_05	7114.5	7122.5
AlPh_05_u	7114.4	7122.9
AlPh_10	7114.5	7112.5
AlPh_10_u	7114.4	7122.9
PhMgBr_01	7113.9	7122.5
PhMgBr_01_u	7114.3	7122.8
PhMgBr_05	7114.5	7122.5
PhMgBr_05_u	7114.4	7122.7
PhMgBr_10	7114.5	7122.5

PhMgBr_10_u	7114.4	7122.5
PhLi_01	7114.5	7122.5
PhLi_01_u	7114.3	7122.8
PhLi_05	7114.0	7122.5
PhLi_05_u	7114.3	7122.5
PhLi_10	7114.5	7122.5
PhLi_10_u	7114.3	7122.5

EXAFS

Due to space reasons only the Fourier-transformed EXAFS spectra of the catalysts after calcination are shown in the main paper. Therefore in Figure SI- 8 to Figure SI- 13 $k^3\chi(k)$ and the Fourier transformation of all catalysts after calcination and after application in CO oxidation are pictured. The corresponding fitting parameter of EXAFS analysis can be found in Table SI- 13 to Table SI- 15.

In general all catalysts show very similar backscatterer numbers and types of backscatterers and nearly the same atom distances – independent on their use in CO-oxidation. A small increase of bigger agglomerates is detectable with regard on the Fe/Al-ratio, which is in good agreement to the results from DRUVS analysis.

Table SI- 12: Type, number and distances of backscatterers in reference materials received through crystal structures.

Sample	Abs-Bs[a]	N(Bs)[b]	R(Abs-Bs) [Å][c]
AlFeO$_3$[24]	Fe-O	2	1.880
	Fe-O	4	2.097
	Fe-Fe	2	3.078
	Fe-Al	5.5	3.196
	Fe-O	2	3.320
	Fe-Fe	3	3.349
γ-Fe$_2$O$_3$[35]	Fe-O	2	1.891
	Fe-O	3	2.035
	Fe-Fe	3	2.947
	Fe-Fe	9	3.455
	Fe-O	6	3.471
α-Fe$_2$O$_3$[36]	Fe-O	3	1.942
	Fe-O	3	2.104
	Fe-Fe	4	2.943
	Fe-Fe	3	3.352
	Fe-O	3	3.384

[a] Abs: X-ray absorbing atom, Bs:backscattering atom. [b] Number of backscattering atoms. [c] Distance of absorbing atom to backscattering atom.

AlPh3
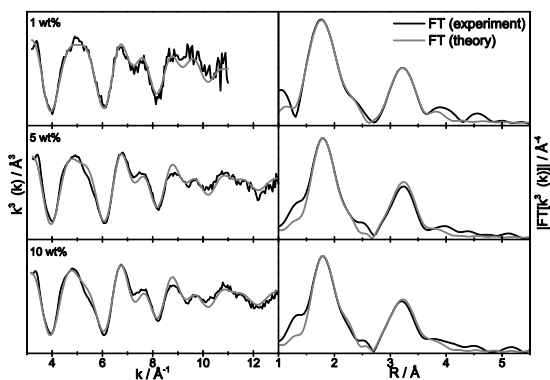
Figure SI- 8: EXAFS spectra k³χ(k) (left) and the corresponding Fourier transformed functions (right) of AlPh_01 (top), AlPh_05 (middle) and AlPh_10 (bottom) after calcination at 600 °C.

Figure SI- 9: EXAFS spectra k³χ(k) (left) and the corresponding Fourier transformed functions (right) of AlPh_01_u (top), AlPh_05_u (middle) and AlPh_10_u (bottom) after application as catalyst in CO oxidation.

Table SI- 13: Results and parameters obtained through EXAFS analysis of the AlPh$_3$ system after use in CO oxidation.

Sample	Abs-Bs[a]	N(Bs)[b]	R(Abs-Bs) [Å][c]	σ [Å⁻¹][d]	R [%][e] Ef [eV][f] Afac[g]
AlPh_01_u	Fe-O	2.0±0.10	1.882±0.018	0.097±0.009	32.26
	Fe-O	2.9±0.15	1.989±0.019	0.112±0.011	3.819

113

	Fe-Fe	0.2±0.02	3.007±0.030	0.055±0.005	1.280
	Fe-Al	5.0±0.50	3.357±0.033	0.112±0.011	
	Fe-Fe	2.5±0.25	3.417±0.034	0.112±0.011	
				N(Fe)/N(Al)	0.54
AlPh_05_u	Fe-O	1.4±0.70	1.874±0.018	0.059±0.005	24.64
	Fe-O	3.8±0.19	1.976±0.019	0.112±0.011	3.696
	Fe-Fe	0.1±0.01	3.005±0.030	0.045±0.004	1.009
	Fe-Al	5.4±0.54	3.328±0.033	0.112±0.011	
	Fe-Fe	2.5±0.25	3.402±0.034	0.112±0.011	
				N(Fe)/N(Al)	0.48
AlPh_10_u	Fe-O	2.0±0.10	1.885±0.018	0.074±0.007	23.37
	Fe-O	3.8±0.19	1.994±0.019	0.112±0.011	3.173
	Fe-Fe	0.6±0.06	3.009±0.030	0.102±0.010	0.8639
	Fe-Al	5.3±0.53	3.333±0.033	0.112±0.011	
	Fe-Fe	3.1±0.31	3.413±0.034	0.112±0.011	
				N(Fe)/N(Al)	0.69

[a] Abs=X-ray absorbing atom, Bs=backscattering atom; [b] Number of backscattering atoms; [c] Distance of absorbing atom to backscattering atom; [d] Debye-Waller like factor; [e] Fit index; [f] Fermi energy, which accounts for the shift between theory and experiment; [g] Amplitude reducing factor.

PhMgBr

Figure SI- 10: EXAFS spectra k³χ(k) (left) and the corresponding Fourier transformed functions (right) of PhMgBr_01 (top), PhMgBr_05 (middle) and PhMgBr_10 (bottom) after calcination at 600 °C.
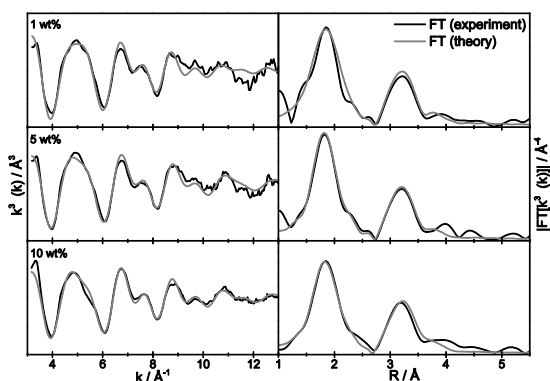
Figure SI- 11: EXAFS spectra k³χ(k) (left) and the corresponding Fourier transformed functions (right) of

PhMgBr_01_u (top), PhMgBr_05_u (middle) and PhMgBr_10_u (bottom) after application as catalyst in CO

oxidation.

Table SI- 14: Results and parameters obtained through EXAFS analysis of the PhMgBr system after use in CO

oxidation.

Sample	Abs-Bs[a]	N(Bs)[b]	R(Abs-Bs) [Å][c]	σ [Å⁻¹][d]	R [%][e] Ef [eV][f] Afac[g]
PhMgBr_01_u	Fe-O	1.6±0.08	1.879±0.018	0.112±0.011	27.92
	Fe-O	3.7±0.18	1.923±0.019	0.112±0.011	6.887
	Fe-Fe	0.6±0.06	3.029±0.030	0.097±0.009	1.115
	Fe-Al	3.7±0.37	3.264±0.032	0.112±0.011	
	Fe-Fe	0.3±0.03	3.478±0.034	0.097±0.009	
			N(Fe)/N(Al)	0.24	
PhMgBr_05_u	Fe-O	1.1±0.05	1.888±0.018	0.039±0.003	28.62
	Fe-O	5.3±0.26	1.999±0.019	0.112±0.011	1.723
	Fe-Fe	2.7±0.27	3.024±0.030	0.107±0.010	0.8908
	Fe-Al	4.9±0.49	3.413±0.034	0.112±0.011	
	Fe-Fe	4.8±0.48	3.494±0.034	0.112±0.011	
			N(Fe)/N(Al)	1.53	
PhMgBr_10_u	Fe-O	0.8±0.04	1.881±0.018	0.032±0.003	24.57
	Fe-O	5.0±0.25	1.996±0.019	0.105±0.001	0.1563
	Fe-Fe	2.8±0.28	3.033±0.030	0.110±0.011	0.8838
	Fe-Al	6.2±0.62	3.439±0.034	0.112±0.011	
	Fe-Fe	5.2±0.52	3.490±0.034	0.112±0.011	
			N(Fe)/N(Al)	1.29	

[a] Abs=X-ray absorbing atom, Bs=backscattering atom; [b] Number of backscattering atoms; [c] Distance of absorbing atom to backscattering atom; [d] Debye-Waller like factor; [e] Fit index; [f] Fermi energy, which accounts for the shift between theory and experiment; [g] Amplitude reducing factor.
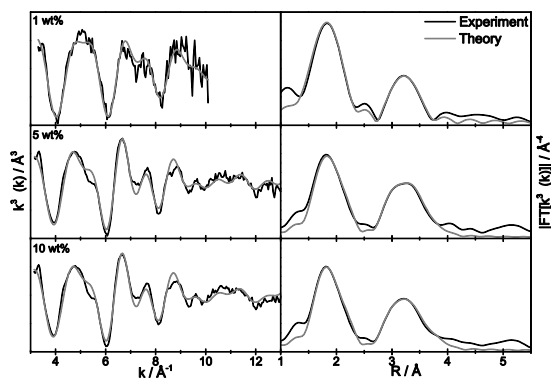
PhLi
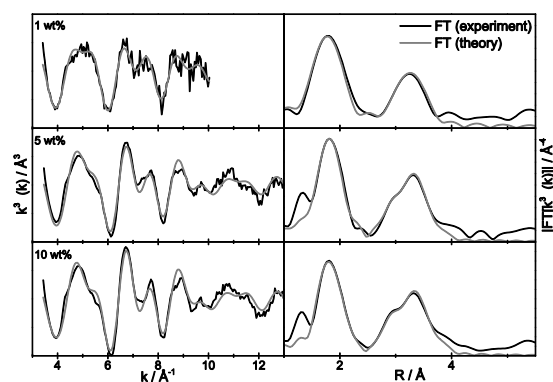
Figure SI- 12 EXAFS spectra $k^3\chi(k)$ (left) and the corresponding Fourier transformed functions (right) of PhLi_01 (top),PhLi_05 (middle) and PhLi_10 (bottom) after calcination at 600 °C.
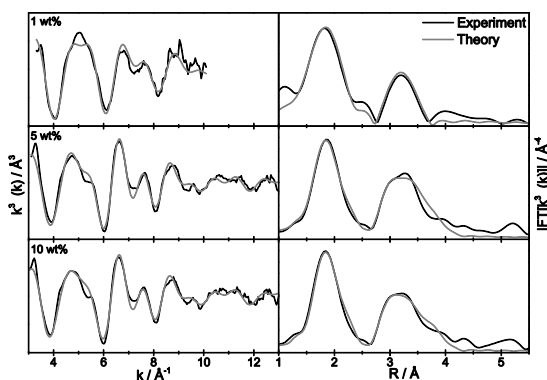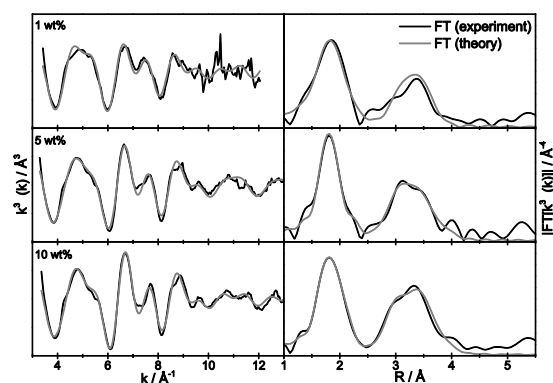

Figure SI- 13: EXAFS spectra $k^3\chi(k)$ (left) and the corresponding Fourier transformed functions (right) of PhLi_01_u (top), PhLi_05_u (middle) and PhLi_10_u (bottom) after application as catalyst in CO oxidation.

Table SI- 15: Results and parameters obtained through EXAFS analysis of the PhLi system after use in CO oxidation.

Sample	Abs-Bs[a]	N(Bs)[b]	R(Abs-Bs) [Å][c]	σ [Å^{-1}][d]	R [%][e] E$_f$ [eV][f]
PhLi_01_u	Fe-O	1.9±0.09	1.858±0.018	0.084±0.008	35.19

	Fe-O	3.8±0.19	1.967±0.019	0.032±0.003	2.763
	Fe-Fe	2.5±0.25	3.082±0.030	0.112±0.011	0.7788
	Fe-Al	3.1±0.31	3.258±0.032	0.112±0.011	
	Fe-Fe	0.6±0.06	3.523±0.035	0.032±0.003	
			N(Fe)/N(Al)	1.00	
PhLi_05_u	Fe-O	1.4±0.07	1.873±0.018	0.039±0.003	28.44
	Fe-O	4.4±0.22	1.969±0.019	0.107±0.010	-0.4493
	Fe-Fe	2.7±0.27	3.024±0.030	0.107±0.010	0.7893
	Fe-Al	4.9±0.49	3.404±0.034	0.112±0.011	
	Fe-Fe	5.5±0.55	3.457±0.034	0.112±0.011	
			N(Fe)/N(Al)	1.67	
PhLi_10_u	Fe-O	1.3±0.06	1.832±0.018	0.045±0.004	24.52
	Fe-O	4.2±0.21	1.956±0.019	0.081±0.008	1.349
	Fe-Fe	2.6±0.26	2.996±0.029	0.102±0.010	0.770
	Fe-Al	4.9±0.49	3.379±0.033	0.112±0.011	
	Fe-Fe	6.7±0.67	3.450±0.034	0.112±0.011	
			N(Fe)/N(Al)	1.89	

[a] Abs=X-ray absorbing atom, Bs=backscattering atom; [b] Number of backscattering atoms; [c] Distance of absorbing atom to backscattering atom; [d] Debye-Waller like factor; [e] Fit index; [f] Fermi energy, which accounts for the shift between theory and experiment; [g] Amplitude reducing factor.

References:

[1] H.-Y. Chen, H.-L. Chang, *Johnson Matthey Technol. Rev.* **2015**, *59*, 64–67.

[2] a) L. Boisvert, K. I. Goldberg, *Acc. Chem. Res.* **2012**, *45*, 899–910; b) G. J. Hutchings, *J. Mater. Chem.* **2009**, *19*, 1222–1235; c) G. Salek, P. Alphonse, P. Dufour, S. Guillemet-Fritsch, C. Tenailleau, *Appl. Catal. B* **2014**, *147*, 1–7; d) X. Zhang, Z. Qu, F. Yu, Y. Wang, *Chin. J. Catal.* **2013**, *34*, 1277–1290; e) A. K. Kandalam, B. Chatterjee, S. N. Khanna, B. K. Rao, P. Jena, B. V. Reddy, *Surf. Sci.* **2007**, *601*, 4873–4880; f) B. V. Reddy, S. N. Khanna, *Phys. Rev. Lett.* **2004**, *93*, 683011–683014;

[3] A. Russell, W. S. Epling, *Catal. Rev. - Sci. Eng.* **2011**, *53*, 337–423.

[4] a) J.-D. Grunwaldt, C. Kiener, C. Wögerbauer, A. Baiker, *J. Catal.* **1999**, *181*, 223–232; b) M. Bandyopadhyay, O. Korsak, van den Berg, M. W. E., W. Grünert, A. Birkner, W. Li, F. Schüth, H. Gies, *Microporous Mesoporous Mater.* **2006**, *89*, 158–163; c) T. Zheng, J. He, Y. Zhao, W. Xia, J. He, *J. Rare Earths* **2014**, *32*, 97–107; d) J. M. Herreros, S. S. Gill, I. Lefort, A. Tsolakis, P. Millington, E. Moss, *Appl. Catal. B* **2014**, *147*, 835–841; e) A. Boubnov, S. Dahl, E. Johnson, A. Puig Molina, S. Bredmose Simonsen, F. Morales Cano, S. Helveg, L. J. Lemus-Yegres, J.-D. Grunwaldt, *Appl. Catal. B* **2012**, *126*, 315–325; f) P. Glatzel, J. Singh, K. O. Kvashnina, van Bokhoven, Jeroen A., *J. Am. Chem. Soc.* **2010**, *132*, 2555–2557;

[5] P. J. Loferski, *2012 Minerals Yearbook: Platinum-Group Metals*.

[6] a) U. Lucia, *Renewable Sustainable Energy Rev.* **2014**, *30*, 164–169; b) L. Carrette, K. A. Friedrich, U. Stimming, *ChemPhysChem* **2000**, *1*, 162–193;

[7] a) A. Kruse, A. Funke, M.-M. Titirici, *Curr. Opin. Chem. Biol.* **2013**, *17*, 515–521; b) J. C. Serrano-Ruiz, R. M. West, J. A. Dumesic, *Annu. Rev. Chem. Biomol. Eng.* **2010**, *1*, 79–100;

[8] a) K. Kalbitz, D. Schwesig, W. Wang, *Sci. Total Environ.* **2008**, *405*, 239–245; b) H. M. Prichard, P. C. Fisher, *Environ. Sci. Technol.* **2012**, *46*, 3149–3154; c) S. Zimmermann, J. Messerschmidt, A. von Bohlen, B. Sures, *Environ. Res.* **2005**, *98*, 203–209;

[9] S. Royer, D. Duprez, *ChemCatChem* **2011**, *3*, 24–65.

[10] P. Li, D. E. Miser, S. Rabiei, R. T. Yadav, M. R. Hajaligol, *Appl. Catal. B* **2003**, *43*, 151–162.

[11] J. G. Carriazo, M. A. Centeno, J. A. Odriozola, S. Moreno, R. Molina, *Appl. Catal. A* **2007**, *317*, 120–128.

[12] H.-Y. Lin, Y.-W. Chen, W.-J. Wang, *J. Nanopart. Res.* **2005**, *7*, 249–263.

[13] O. H. Laguna, M. A. Centeno, M. Boutonnet, J. A. Odriozola, *Appl. Catal. B* **2011**, *106*, 621–629.

[14] J. S. Walker, G. I. Straguzzi, W. H. Manogue, G. C. Schuit, *J. Catal.* **1988**, *110*, 298–309.

[15] J.-N. Park, P. Zhang, Y.-S. Hu, E. W. McFarland, *Nanotechnology* **2010**, *21*, 225708.

[16] M. Tepluchin, M. Casapu, A. Boubnov, H. Lichtenberg, Di Wang, S. Kureti, J.-D. Grunwaldt, *ChemCatChem* **2014**, *6*, 1763–1773.

[17] M. Tepluchin, D. K. Pham, M. Casapu, L. Mädler, S. Kureti, J.-D. Grunwaldt, *Catal. Sci. Technol.* **2014**, *5*, 455–464.

[18] R. Schoch, H. Huang, V. Schünemann, M. Bauer, *ChemPhysChem* **2014**, *15*, 3768–3775.

[19] I. Hnat, I. Kocemba, J. Rynkowski, T. Onfroy, S. Dzwigaj, *Catalysis Today* **2011**, *176*, 229–233.

[20] a) T. S. Ertel, H. Bertagnolli, S. Hückmann, U. Kolb, D. Peter, *Appl. Spectrosc.* **1992**, *46*, 690–698; b) M. Newville, P. Līviņš, Y. Yacoby, J. J. Rehr, E. A. Stern, *Phys. Rev. B* **1993**, *47*, 14126–14131;

[21] L. Smrcok, V. Langer, J. Krestan, *Acta Crystallogr., Sect. C* **2006**, *62*, i83-4.

[22] C. Pecharromán, T. González-Carreño, J. Iglesias, *Phys. Chem. Miner.* **1995**, *22*, 21–29.

[23] N. Pailhé, A. Wattiaux, M. Gaudon, A. Demourgues, *J. Solid State Chem.* **2008**, *181*, 1040–1047.

[24] F. Bouree, J.-L. Baudour, E. El Badraoui, J. Musso, C. Laurent, A. Rousset, *Acta Crystallogr., Sect. B* **1996**, *52*, 217–222.

[25] M. Marezio, *J. Chem. Phys.* **1966**, *44*, 3143.

[26] a) M. Schwidder, M. S. Kumar, K. Klementiev, M.-M. Pohl, A. Brückner, W. Grünert, *J. Catal.* **2005**, *231*, 314–330; b) Hensen, E. J. M., Q. Zhu, Hendrix, M. M. R. M., A. R. Overweg, P. J. Kooyman, M. V. Sychev, van Santen, R. A., *J. Catal.* **2004**, *221*, 560–574; c) J. Janas, J. Gurgul, R. P. Socha, T. Shishido, M. Che, S. Dzwigaj, *Appl. Catal. B* **2009**, *91*, 113–122; d) J. Pérez-Ramírez, A. Gallardo-Llamas, *J. Phys. Chem. B* **2005**, *109*, 20529–20538; e) M. S. Kumar, M. Schwidder, W. Grünert, A. Brückner, *J. Catal* **2004**, *227*, 384–397;

[27] R. Pérez Vélez, I. Ellmers, H. Huang, U. Bentrup, V. Schünemann, W. Grünert, A. Brückner, *J. Catal.* **2014**, *316*, 103–111.

[28] a) D. C. Koningsberger, B. L. Mojet, van Dorssen, G. E., D. E. Ramaker, *Top. Catal.* **2000**, *10*, 143–155; b) F. W. Lytle, *J. Synchrotron Rad.* **1999**, *6*, 123–134;

[29] S. Yao et al., *ACS Catal.* **2014**, *4*, 1650–1661.

[30] D. K. Bora, A. Braun, S. Erat, O. Safonova, T. Graule, E. C. Constable, *Curr. Appl. Phys.* **2012**, *12*, 817–825.

[31] H. Okudera, A. Yoshiasa, K. Murai, M. Okube, T. Takeda, S. Kikkawa, *J. Mineral. Petrol. Sci.* **2012**, *107*, 127–132.

[32] J. D. Walker, A. P. Grosvenor, *J. Solid State Chem.* **2013**, *197*, 147–153.

[33] a) R. Schäfer, P. C. Schmidt (Eds.) *Methods in Physical Chemistry. X-Ray Absorption Spectroscopy - the Method and Its Applications*, Wiley-VCH Verlag GmbH & Co. KGaA, Weinheim, Germany, **2012**; b) M. Bauer, C. Gastl, *Phys. Chem. Chem. Phys.* **2010**, *12*, 5575–5584; c) M. Bauer, T. Kauf, J. Christoffers, H. Bertagnolli, *Phys. Chem. Chem. Phys.* **2005**, *7*, 2664–2670;

[34] a) M. W. Gaultois, J. E. Greedan, A. P. Grosvenor, *J. Electron. Spectrosc. Relat. Phenom.* **2011**, *184*, 192–195; b) A. P. Grosvenor, J. E. Greedan, *J. Phys. Chem. C* **2009**, *113*, 11366–11372;

[35] E. N. Maslen, V. A. Streltsov, N. R. Streltsova, N. Ishizawa, *Acta Crystallogr., Sect. B* **1994**, *50*, 435–441.

[36] V. Petkov, P. D. Cozzoli, R. Buonsanti, R. Cingolani, Y. Ren, *J. Am. Chem. Soc.* **2009**, *131*, 14264–14266.

[37] S. C. Yu, J. S. Lee, S. F. Tung, C. L. Lan, *J. Geological Soc. China* **1999**, *42*, 349–358.

4

FINAL CONCLUSION & OUTLOOK

Iron proved to be a versatile applicable and active metal in both, homogeneous as well as heterogeneous catalysis with notable and promising performances. The application of multiple analytical techniques - especially the combination of standard methods (like UV/Vis-, Raman- and Mößbauer spectroscopy as well as X-ray powder diffraction and specific surface determination) with XAFS - allows the identification of the catalytically active species and a detailed view on its operating principles in a catalyst system. Knowledge about these conditions opens the full spectrum of possibilities to a targeted optimization of the catalyst's performance.

4.1 Summary of the work

The aim of this thesis was the synthesis and the investigation of iron-based catalysts in selected reactions - homogeneous as well as heterogeneous - to gain a deeper mechanistic understanding of the working principles and the catalytically active species.

In case of homogeneous iron-catalyzed cross-coupling reactions, the proposed active species and the reaction mechanism are still not clarified conclusively and are subject of controversial discussions. Nonetheless, the application of iron instead of noble metals as catalyst in this important carbon-carbon bond formation exhibits very promising results and has to be understood in detail to implement highly active iron-based catalyst systems. For these reasons, the intrinsic activation process of the iron precursor was investigated by XAFS analysis in combination with the determination of the consumed amount of reducing compound. In this way, it was possible to gain proof about the oxidation state and the structure of the iron species during the course of the reduction process and the resulting

catalytically active species. Therefore, a stepwise view on the system could be achieved by measurements after different equivalents of aryl-Grignard compound (PhMgCl) added to the iron precursor. Thus, the reduction of the Fe^{III} precursor towards Fe^{I} in the catalytically active species after reaction with three equivalents of reducing compound could be monitored. The results obtained by EXAFS analysis allow the assumption of $Fe_3(MgCl)_3L_3$ as a possible composition of the active species. Furthermore, XAFS investigations of a test reaction allowed the deduction of a reaction mechanism based on iron in the oxidation states +I and +III.

In case of heterogeneous catalyzed oxidation of carbon monoxide based on iron as active metal, only little is known about the reaction processes and the catalytically active species. Addressing the reasons for the application of iron in this reaction elucidated in chapter 1, model catalysts containing iron in different coordinations should be synthesized and tested in carbon monoxide oxidation regarding their catalytic activity. The main goal was to synthesize catalysts consisting of different structures and catalytic activities. By comparison of the catalyst structures investigated by various analytic techniques with their respective activities, conclusions can be drawn about structural requirements and iron coordinations, which are prerequisites for high catalytic performance. Knowledge about these coherences will allow to synthesize catalysts with outstanding performance by intentionally introducing these iron structures or coordinations. Originating from the catalyst system used in homogeneous cross-coupling reactions, small iron nanoparticles could be formed by addition of an excess of organometallic compound working as reducing agent. To extent the investigated system initially based on magnesium organyls, aluminum and lithium organyls were also applied as reducing compound. Thereby, aluminum and lithium organyls bearing the same organic residues like the Grignard compound were used (PhMgBr, $AlPh_3$, PhLi) to ensure the same reducing mechanism of the iron precursor. The obtained nanoparticles consist of small iron cluster and second metal atoms on the cluster surface introduced by the organometallic compound. These nanoparticles were brought on a γ-alumina support and were calcined preliminary to their application in carbon monoxide oxidation. All catalysts showed different activities and structures, which enabled a structure-activity correlation and an identification of isolated tetrahedrally coordinated Fe^{III} species as catalytically active centers. Furthermore, the influence of the second metal could be investigated. By application of $AlPh_3$ in the reduction process, iron cluster were formed with aluminum atoms on their surface. During the impregnation of γ-alumina with these nanoparticles followed by calcination a large proportion of isolated Fe sites were formed. This could be assigned to the presence of alumina atoms on the iron cluster surface, which enables an integration of the cluster into the alumina lattice and therefore prevents from agglomeration. In contrast, by utilization of PhMgBr and PhLi iron clusters are formed with magnesium respectively lithium atoms on their surface. The resulting catalysts showed a

lower activity than catalysts prepared using AlPh$_3$, due to a significantly higher amount of agglomerates and a minor proportion of isolated sites. Beside the initial approach to correlate the structures of the synthesized catalysts to their activities, also the synthesis of several catalyst systems, competitive to the performances of commercial available systems (under laboratory conditions), was possible. Nonetheless, the full conversion temperatures of the investigated catalysts are still higher than comparable precious metal systems. However, the minimal working temperature of a typical three-way catalyst of about 350 °C are by far high enough to reach full conversion with some of the investigated catalyst systems. Implementation of the gained knowledge about structural prerequisites will lead to catalysts with increased activity and to an improved catalytic performance.

4.2 Outlook

In a next step, time-dependent investigations of the catalytic species in cross-coupling reactions have to be carried out to obtain more information during the activation process about formed intermediates and a more detailed clarification of the active species structure. This effort appears to be extremely complex, since the reduction process proceeds very fast and the formed species are highly reactive, therefore instable and sensitive. To overcome these difficulties, different approaches are conceivable: 1) Application of a special designed polytetrafluoroethylene (PTFE) cell, which facilitates sample preparation and measurement under inert atmosphere in combination with relatively fast spectroscopic methods, such as Quick EXAFS or dispersive XAFS. 2) Stopped-flow setup, where the reactants were brought together in a mixing unit and afterwards directly lead in a thin-walled capillary, which allows XAFS measurements. This technique also requires fast spectroscopic methods. 3) Stabilization of the intermediate species by application of an electric potential. For this, a PTFE cell was developed in our work group, allowing cyclic voltammetry (CV) measurements through installation of electrodes additionally to sample preparation under inert atmosphere. 4) By implementation of a freeze-quench setup, the reaction mixture is frozen after a certain (short) time delay, which maintains the intermediates stable for the duration of a XAFS measurement. Hitherto, aryl (phenyl) Grignard compounds are used as reduction agents for the formation of the active species in cross-coupling reactions. The application of the new setups and techniques enables the investigations of alkyl Grignard compounds, which exhibit a different reduction mechanism due to the presence of β-H atoms on the organic residue.

Following the results of this work, the preparation of heterogeneous catalysts containing an amount of tetrahedrally coordinated isolated Fe^{III} species as high as possible have to be synthesized to reach high catalytic activities in CO oxidation. This could be achieved

by variation of the iron loading of the catalyst, change of the iron precursor or the use of $AlFeO_3$ in the preparation process. In course to achieve a more detailed understanding of the catalysts operation principles, in-operando investigations are indispensable since the catalyst structure and electronic state could differ from the ex-situ results. Until now, no cells were available, in which the catalyst can be measured in the same reaction conditions than in the laboratory reactor. An in-operando cell prototype was developed in our work group during the last months, which has similar dimensions and will be applied for the first time in nearest future. Beside spectroscopic improvements, isolation and characterization of the (bimetallic) nanoparticles formed in the reduction process should be carried out. By this, size, shape and metal distribution of the particles can be determined for example by transmission electron microscopy (TEM) and X-ray photoelectron spectroscopy (XPS). The size and shape of the nanoparticles could be dependent on the solvent. Therefore, the influence of a THF:NMP ratio variation and the addition of other stabilizing compounds such as tensides or polymers during the reduction process should be investigated. The influence of the second metal, present on the nanoparticle surface, on the catalyst structure and its catalytic performance in carbon monoxide oxidation could be studied in more detail through application of defined core-shell nanoparticles in the preparation process. In contrast, the support material also offers diverse modification opportunities. The preparation route of γ-alumina can be changed to obtain a higher specific surface area or other materials, like zirconia, tin oxide or titanium oxide can be used. Magnesia could be tested as support material for systems, where Grignard compounds were applied as reduction agent to obtain similar effects to the aluminum organyl/alumina system. Furthermore, the catalytic test reaction has to be modified to converge to more realistic emission gas conditions. This means addition of moisture to the gas mixture, an amount of oxygen similar to the concentration in exhaust gas, presence of sulfur oxide and even coating of a washcoat.

Summarizing, despite the development of iron catalysts is lagging behind the evolution of noble metal catalysts for several years, they show very promising results in the discussed homogeneous and heterogeneous applications. Iron-based catalysts still show some disadvantages compared to established noble metal-based catalyst systems (e.g. lower activity or stability), which can surely be overcome and thus offer a lot of potential for improvement. The increased effort in catalyst preparation compared to established, noble metal-based catalyst systems can be compensated by the significant price disparity between iron and noble metals. Through identification of the active species in the presented reactions, a purposive development of enhanced iron-based catalysts is now possible.

Bibliography

[1] J. Hagen, *Industrial catalysis: A practical approach 2nd ed.*, Wiley-VCH, Weinheim, **2008**.

[2] G. B. Kauffman, *Platinum Metals Rev.* **1999**, *43*, 122–128.

[3] A. Behr, P. Neubert, *Applied homogeneous catalysis*, Wiley-VCH, Weinheim, **2012**.

[4] A. Trofast, *12th Proceedings of Swedish Symposium of Catalysis: Larsson, R. (Ed.)*, **1981**.

[5] F. W. Ostwald, *Nature* **1902**, *65*, 522–526.

[6] J. R. Partington, *A history of chemistry 4th ed.*, Macmillan & Co., London, **1964**.

[7] H. Hildebrand, *Nobel Prize for Chemistry 1909 - Award Ceremony Speech*, **1909**.

[8] J. M. Thomas, W. J. Thomas, *Principles and practice of heterogeneous catalysis 2nd ed.*, Wiley-VCH, Weinheim, **2015**.

[9] B. H. Davis in *Handbook of heterogeneous catalysis*, *Vol. 1*, G. Ertl, H. Knözinger, F. Schüth, J. Weitkamp (Eds.), Wiley-VCH, Weinheim, **2008**.

[10] Badische Anilin- und Sodafabrik, *DE235421, assigned to BASF,* **1908**.

[11] I. Chorkendorff, J. W. Niemantsverdriet, *Concepts of modern catalysis and kinetics*, Wiley-VCH, Weinheim, **2005**.

[12] C. H. Bartholomew, R. J. Farrauto, *Fundamentals of industrial catalytic processes 2nd ed.*, Wiley-Interscience, Hoboken, **2010**.

[13] J. Heveling, *J. Chem. Educ.* **2012**, *89*, 1530–1536.

[14] M. Schmal, *Heterogeneous Catalysis and its Industrial Applications*, Springer International Publishing AG Switzerland, Cham, **2016**.

[15] P. T. Anastas, *Handbook of Green Chemistry*, Wiley-VCH, Weinheim, **2012**.

[16]   Nobel Media AB 2014. Web, *All Nobel Prizes in Chemistry* **Mar 23th, 2017**, *www.nobelprize.org/nobel_prizes/chemistry/laureates/*.

[17]   J. R. Anderson, M. Boudart (Eds.), *Catalysis: Science and Technology*, Vol. 7 of *Catalysis, Science and Technology*, Springer, Berlin and Heidelberg, **1985**.

[18]   B. Cornils, W. A. Herrmann, *Applied homogeneous catalysis with organometallic compounds 2nd ed.*, Wiley-VCH, Weinheim, **2002**.

[19]   B. Cornils, W. A. Herrmann, H.-W. Zanthoff, C.-H. Wong (Eds.), *Catalysis from A to Z: A concise encyclopedia 4th ed.*, Wiley-VCH, Weinheim, **2013**.

[20]   G. Ertl, H. Knözinger, F. Schüth, J. Weitkamp (Eds.), *Handbook of heterogeneous catalysis 2nd ed.*, Wiley-VCH, Weinheim, **2008**.

[21]   P. A. Jacobs, E. M. Flanigen, J. C. Jansen, H. van Bekkum (Eds.), *Introduction to zeolite science and practice 2nd ed.*, Vol. 137 of *Studies in surface science and catalysis*, Elsevier, Amsterdam, **2001**.

[22]   E. G. Derouane, F. Lemos, C. Naccache, F. R. Ribeiro, *Zeolite Microporous Solids: Synthesis, Structure, and Reactivity*, Vol. 352 of *NATO ASI Series, Series C: Mathematical and Physical Sciences, 1389-2185*, Springer Netherlands, Dordrecht, **1992**.

[23]   A. Corma, H. Garcia, *Eur. J. Inorg. Chem.* **2004**, 1143–1164.

[24]   J. A. Gladysz, *Chem. Rev.* **2002**, *102*, 3215–3216.

[25]   D. Ballard, *Adv. Catal.* **1973**, *23*, 263–325.

[26]   D. E. d. Vos, I. F. J. Vankelecom, P. A. Jacobs (Eds.), *Chiral catalyst immobilization and recycling*, Wiley-VCH, Weinheim, **2000**.

[27]   A. Kirschning, H. Monenschein, R. Wittenberg, *Angew. Chem.* **2001**, *113*, 670–701.

[28]   A. Kirschning, H. Monenschein, R. Wittenberg, *Angew. Chem. Int. Ed.* **2001**, *40*, 650–679.

[29]   G. Jas, A. Kirschning, *Chem. - Eur. J.* **2003**, *9*, 5708–5723.

[30]   A. M. Klibanov, *Anal. Biochem.* **1979**, *93*, 1–25.

[31]   K. M. Koeller, C. H. Wong, *Nature* **2001**, *409*, 232–240.

[32]   L. Cao, *Curr. Opin. Chem. Biol.* **2005**, *9*, 217–226.

[33]   E. A. Tomic, *J. Appl. Polym. Sci.* **1965**, *9*, 3745–3752.

[34] U. Müller, M. Hesse, H. Pütter, M. Schubert, D. Mirsch, *EP1674555, assigned to BASF,* **2006**.

[35] U. Müller, M. Schubert, F. Teich, H. Puetter, K. Schierle-Arndt, J. Pastré, *J. Mater. Chem.* **2006**, *16*, 626–636.

[36] R. Matsuda, R. Kitaura, S. Kitagawa, Y. Kubota, R. V. Belosludov, T. C. Kobayashi, H. Sakamoto, T. Chiba, M. Takata, Y. Kawazoe, Y. Mita, *Nature* **2005**, *436*, 238–241.

[37] A. G. Wong-Foy, A. J. Matzger, O. M. Yaghi, *J. Am. Chem. Soc.* **2006**, *128*, 3494–3495.

[38] H. K. Chae, D. Y. Siberio-Perez, J. Kim, Y. Go, M. Eddaoudi, A. J. Matzger, M. O'Keeffe, O. M. Yaghi, *Nature* **2004**, *427*, 523–527.

[39] G. Ferey, C. Mellot-Draznieks, C. Serre, F. Millange, J. Dutour, S. Surble, I. Margiolaki, *Science* **2005**, *309*, 2040–2042.

[40] F. Stallmach, S. Gröger, V. Künzel, J. Kärger, O. M. Yaghi, M. Hesse, U. Müller, *Angew. Chem.* **2006**, *118*, 2177–2181.

[41] F. Stallmach, S. Groger, V. Kunzel, J. Karger, O. M. Yaghi, M. Hesse, U. Muller, *Angew. Chem. Int. Ed.* **2006**, *45*, 2123–2126.

[42] S. Hermes, M.-K. Schröter, R. Schmid, L. Khodeir, M. Muhler, A. Tissler, R. W. Fischer, R. A. Fischer, *Angew. Chem.* **2005**, *117*, 6394–6397.

[43] S. Hermes, M.-K. Schroter, R. Schmid, L. Khodeir, M. Muhler, A. Tissler, R. W. Fischer, R. A. Fischer, *Angew. Chem. Int. Ed.* **2005**, *44*, 6237–6241.

[44] U. Müller, L. Lobree, M. Hesse, O. M. Yaghi, M. Eddaoudi, *EP1513823, assigned to BASF & University of Michigan,* **2003**.

[45] W. Mori, T. Sato, T. Ohmura, C. Nozaki Kato, T. Takei, *J. Solid State Chem.* **2005**, *178*, 2555–2573.

[46] H. L. Ngo, W. Lin, *Top. Catal.* **2005**, *34*, 85–92.

[47] M. A. Gotthardt, A. Beilmann, R. Schoch, J. Engelke, W. Kleist, *RSC Adv.* **2013**, *3*, 10676–10679.

[48] M. A. Gotthardt, R. Schoch, T. S. Brunner, M. Bauer, W. Kleist, *ChemPlusChem* **2015**, *80*, 188–195.

[49] S. Naito, T. Tanibe, E. Saito, T. Miyao, W. Mori, *Chem. Lett.* **2001**, *30*, 1178–1179.

[50] J. Perles, M. Iglesias, M.-Á. Martín-Luengo, M. Á. Monge, C. Ruiz-Valero, N. Snejko, *Chem. Mater.* **2005**, *17*, 5837–5842.

[51] National Research Council (U.S.), *Catalysis looks to the future*, National Academy Press, Washington, D.C, **1992**.

[52] J. N. Armor, *Appl. Catal., A* **2001**, *222*, 407–426.

[53] R. A. van Santen (Ed.), *Catalysis: An integrated approach 2nd ed.*, of *Studies in surface science and catalysis*, Elsevier, Amsterdam, **1999**.

[54] W. Vielstich (Ed.), *Handbook of fuel cells: Fundamentals, technology and applications*, Wiley Interscience, Hoboken, **2010**.

[55] S. Park, J. M. Vohs, R. J. Gorte, *Nature* **2000**, *404*, 265–267.

[56] S. Ha, R. Larsen, R. I. Masel, *J. Power Sources* **2005**, *144*, 28–34.

[57] A. Corma, H. Garcia, *Chem. Rev.* **2003**, *103*, 4307–4365.

[58] G. Centi, S. Perathoner, *Catal. Today* **2003**, *77*, 287–297.

[59] R. A. Sheldon, *Green Chem.* **2005**, *7*, 267.

[60] J. E. Herrera, L. Balzano, A. Borgna, W. E. Alvarez, D. E. Resasco, *J. Catal.* **2001**, *204*, 129–145.

[61] H. van Bekkum, P. Gallezot, *Top. Catal.* **2004**, *27*, 1–2.

[62] G. W. Huber, J. W. Shabaker, J. A. Dumesic, *Science* **2003**, *300*, 2075–2077.

[63] D. L. Huber, *Small* **2005**, *1*, 482–501.

[64] I. K. Mbaraka, B. H. Shanks, *J. Catal.* **2005**, *229*, 365–373.

[65] S. Varadarajan, D. J. Miller, *Biotechnol. Prog.* **1999**, *15*, 845–854.

[66] S. G. Masters, K. M. Eriksen, R. Fehrmann, *J. Mol. Catal. A: Chem.* **1997**, *120*, 227–233.

[67] J. J. McCarroll, S. R. Tennison, N. P. Wilkinson, *US Patent 4,600,571, assigned to The British Petroleum Company,* **1986**.

[68] A. I. Foster, P. G. James, J. J. McCarroll, S. R. Tennison, *US Patent 4,163,775, assigned to The British Petroleum Company,* **1979**.

[69] A. I. Foster, P. G. James, J. J. McCarroll, S. R. Tennison, *US Patent 4,250,057 assigned to The British Petroleum Company,* **1981**.

[70] V. Sadykov, L. Isupova, I. Zolotarskii, L. Bobrova, A. Noskov, V. Parmon, E. Brushtein, T. Telyatnikova, V. Chernyshev, V. Lunin, *Appl. Catal., A* **2000**, *204*, 59–87.

[71] I. V. Babich, J. A. Moulijn, *Fuel* **2003**, *82*, 607–631.

[72] J. A. Rob van Veen, J. K. Minderhoud, L. G. Huve, W. H. J. Stork in *Handbook of heterogeneous catalysis*, *Vol. 6*, G. Ertl, H. Knözinger, F. Schüth, J. Weitkamp (Eds.), Wiley-VCH, Weinheim, **2008**.

[73] A. Corma, F. V. Melo, S. Mendioroz, J. L. G. Fierro (Eds.), *Proceedings of the 12th ICC: Granada, Spain, July 9-14, 2000 ; Pt. A 1st ed.*, Vol. 130, A of *Studies in surface science and catalysis*, Elsevier, Amsterdam, **2000**.

[74] J. R. Rostrup-Nielsen, *Catal. Rev.: Sci. Eng.* **2004**, *46*, 247–270.

[75] D. R. Lide (Ed.), *CRC handbook of chemistry and physics: A ready-reference book of chemical and physical data 90th ed.*, CRC Press, Boca Raton, FL., **2010**.

[76] A. F. Hollemann, E. Wiberg, N. Wiberg, *Lehrbuch der anorganischen Chemie 102nd ed.*, de Gruyter, Berlin, **2007**.

[77] P. J. Loferski, *2012 Minerals Yearbook: Platinum-Group Metals*.

[78] U. Lucia, *Renewable Sustainable Energy Rev.* **2014**, *30*, 164–169.

[79] L. Carrette, K. A. Friedrich, U. Stimming, *ChemPhysChem* **2000**, *1*, 162–193.

[80] A. Kruse, A. Funke, M.-M. Titirici, *Curr. Opin. Chem. Biol.* **2013**, *17*, 515–521.

[81] J. C. Serrano-Ruiz, R. M. West, J. A. Dumesic, *Annu. Rev. Chem. Biomol. Eng.* **2010**, *1*, 79–100.

[82] Deutsche Börse AG, *Frankfurter Wertpapierbörse* **Oct. 11th 2016**, www.boerse–frankfurt.de/.

[83] K. Kalbitz, D. Schwesig, W. Wang, *Sci. Total Environ.* **2008**, *405*, 239–245.

[84] S. Zimmermann, J. Messerschmidt, A. von Bohlen, B. Sures, *Environ. Res.* **2005**, *98*, 203–209.

[85] N. Haus, S. Zimmermann, J. Wiegand, B. Sures, *Chemosphere* **2007**, *66*, 619–629.

[86] H. M. Prichard, P. C. Fisher, *Environ. Sci. Technol.* **2012**, *46*, 3149–3154.

[87] G. Ertl, H. Knözinger, J. Weitkamp (Eds.), *Environmental catalysis*, Wiley-VCH, Weinheim, **1999**.

[88] G. M. Mudd, *The "Limits of Growth" and 'Finite' Mineral Resources: Re-visiting the Assumptions and Drinking From That Half-Capacity Glass: 4th International Conference on Sustainability Engineering & Science: Transitions to Sustainability*, **Nov 30.-3 Dec 2010**.

[89] W. M. Czaplik, Dissertation, Universität zu Köln, Köln, **2009**.

[90] V. Krewald, M. Retegan, D. A. Pantazis, *Top. Curr. Chem.* **2015**, *371*, 23–48.

[91] M. Giedyk, K. Goliszewska, D. Gryko, *Chem. Soc. Rev.* **2015**, *44*, 3391–3404.

[92] M. C. Frise, P. A. Robbins, *J. Appl. Physiol.* **2015**, *119*, 1421–1431.

[93] M. Boudart, *Chem. Rev.* **1995**, *95*, 661–666.

[94] E. S. J. Lox in *Handbook of heterogeneous catalysis*, *Vol. 5*, G. Ertl, H. Knözinger, F. Schüth, J. Weitkamp (Eds.), Wiley-VCH, Weinheim, **2008**.

[95] P. Li, D. E. Miser, S. Rabiei, R. T. Yadav, M. R. Hajaligol, *Appl. Catal., B* **2003**, *43*, 151–162.

[96] K. C. Nicolaou, P. G. Bulger, D. Sarlah, *Angew. Chem. Int. Ed.* **2005**, *44*, 4442–4489.

[97] K. C. Nicolaou, P. G. Bulger, D. Sarlah, *Angew. Chem.* **2005**, *117*, 4516–4563.

[98] C. Bolm, J. Legros, J. Le Paih, L. Zani, *Chem. Rev.* **2004**, *104*, 6217–6254.

[99] G. F. Nordberg, B. A. Fowler, M. Nordberg, L. Friberg (Eds.), *Handbook on the toxicology of metals 3rd ed.*, Elsevier, Amsterdam, **2007**.

[100] B. Plietker in *Iron catalysis in organic chemistry*, B. Plietker (Ed.), Wiley-VCH, Weinheim, **2008**.

[101] A. d. Meijere, F. Diederich (Eds.), *Metal-catalyzed cross-coupling reactions 2nd ed.*, Wiley-VCH, Weinheim, **2004**.

[102] M. S. Kharasch, E. K. Fields, *J. Am. Chem. Soc.* **1941**, *63*, 2316–2320.

[103] M. Tamura, J. Kochi, *Synthesis* **1971**, 303–305.

[104] M. Tamura, J. K. Kochi, *J. Am. Chem. Soc.* **1971**, *93*, 1487–1489.

[105] R. J. P. Corriu, J. P. Masse, *J. Chem. Soc., Chem. Commun.* **1972**, 144.

[106] K. Tamao, K. Sumitani, M. Kumada, *J. Am. Chem. Soc.* **1972**, *94*, 4374–4376.

[107] R. S. Smith, J. K. Kochi, *J. Org. Chem.* **1976**, *41*, 502–509.

[108] J. K. Kochi, *Acc. Chem. Res.* **1974**, *7*, 351–360.

[109] S. M. Neumann, J. K. Kochi, *J. Org. Chem.* **1975**, *40*, 599–606.

[110] J. K. Kochi, *J. Organomet. Chem.* **2002**, *653*, 11–19.

[111] G. A. Molander, B. J. Rahn, D. C. Shubert, S. E. Bonde, *Tetrahedron Lett.* **1983**, *24*, 5449–5452.

[112] G. Cahiez, H. Avedissian, *Synthesis* **1998**, 1199–1205.

[113] N. Østergaard, B. T. Pedersen, N. Skjærbæk, P. Vedsø, M. Begtrup, *Synlett* **2002**, *11*, 1889–1891.

[114] B. Scheiper, M. Bonnekessel, H. Krause, A. Fürstner, *J. Org. Chem.* **2004**, *69*, 3943–3949.

[115] M. Seck, X. Franck, R. Hocquemiller, B. Figadère, J.-F. Peyrat, O. Provot, J.-D. Brion, M. Alami, *Tetrahedron Lett.* **2004**, *45*, 1881–1884.

[116] M. A. Fakhfakh, X. Franck, R. Hocquemiller, B. Figadère, *J. Organomet. Chem.* **2001**, *624*, 131–135.

[117] A. Leitner in *Iron catalysis in organic chemistry*, B. Plietker (Ed.), Wiley-VCH, Weinheim, **2008**.

[118] V. Fiandanese, G. Miccoli, F. Naso, L. Ronzini, *J. Organomet. Chem.* **1986**, *312*, 343–348.

[119] D. Noda, Y. Sunada, T. Hatakeyama, M. Nakamura, H. Nagashima, *J. Am. Chem. Soc.* **2009**, *131*, 6078–6079.

[120] A. C. Frisch, M. Beller, *Angew. Chem.* **2005**, *117*, 680–695.

[121] A. C. Frisch, M. Beller, *Angew. Chem. Int. Ed.* **2005**, *44*, 674–688.

[122] D. J. Cárdenas, *Angew. Chem.* **2003**, *115*, 398–401.

[123] D. J. Cardenas, *Angew. Chem. Int. Ed.* **2003**, *42*, 384–387.

[124] S. R. Chemler, D. Trauner, S. J. Danishefsky, *Angew. Chem.* **2001**, *113*, 4676–4701.

[125] S. R. Chemler, D. Trauner, S. J. Danishefsky, *Angew. Chem. Int. Ed.* **2001**, *40*, 4544–4568.

[126] M. R. Netherton, G. C. Fu, *Adv. Synth. Catal.* **2004**, *346*, 1525–1532.

[127] R. B. Bedford, D. W. Bruce, R. M. Frost, M. Hird, *Chem. Commun.* **2005**, 4161–4163.

[128] G. Cahiez, V. Habiak, C. Duplais, A. Moyeux, *Angew. Chem.* **2007**, *119*, 4442–4444.

[129] G. Cahiez, V. Habiak, C. Duplais, A. Moyeux, *Angew. Chem. Int. Ed.* **2007**, *46*, 4364–4366.

[130] R. B. Bedford, M. Betham, D. W. Bruce, S. A. Davis, R. M. Frost, M. Hird, *Chem. Commun.* **2006**, 1398–1400.

[131] K. Bica, P. Gaertner, *Org. Lett.* **2006**, *8*, 733–735.

[132] G. Cahiez, S. Marquais, *Pure Appl. Chem.* **1996**, *68*, 53–60.

[133] A. Fürstner (Ed.), *Active metals: Preparation, characterization, applications*, VCH, Weinheim, **1996**.

[134] I. Sapountzis, W. Lin, C. C. Kofink, C. Despotopoulou, P. Knochel, *Angew. Chem.* **2005**, *117*, 1682–1685.

[135] I. Sapountzis, W. Lin, C. C. Kofink, C. Despotopoulou, P. Knochel, *Angew. Chem. Int. Ed.* **2005**, *44*, 1654–1658.

[136] A. Fürstner, A. Leitner, M. Méndez, H. Krause, *J. Am. Chem. Soc.* **2002**, *124*, 13856–13863.

[137] A. Fürstner, A. Leitner, *Angew. Chem.* **2002**, *114*, 632–635.

[138] M. Nakamura, S. Ito, K. Matsuo, E. Nakamura, *Synlett* **2005**, 1794–1798.

[139] A. Fürstner, A. Leitner, *Angew. Chem. Int. Ed.* **2002**, *41*, 609–612.

[140] T. Kauffmann, *Angew. Chem.* **1996**, *108*, 401–418.

[141] T. Kauffmann, *Angew. Chem. Int. Ed.* **1996**, *35*, 386–403.

[142] B. Bogdanović, N. Janke, H.-G. Kinzelmann, *Chem. Ber.* **1990**, *123*, 1507–1516.

[143] B. Bogdanović, M. Schwickardi, *Angew. Chem.* **2000**, *112*, 4788–4790.

[144] B. Bogdanović, M. Schwickardi, *Angew. Chem. Int. Ed.* **2000**, *39*, 4610–4612.

[145] L. E. Aleandri, B. Bogdanović, C. Dürr, U. Wilczok, D. J. Jones, J. Rozière, *Phys. B* **1995**, 500–502.

[146] R. R. Rieke, M. S. Sell, W. R. Klein, T.-A. Chen, J. D. Brown, M. V. Hanson in *Active metals*, A. Fürstner (Ed.), VCH, Weinheim, **1996**, pp. 1–59.

[147] A. Fürstner, *Angew. Chem. Int. Ed.* **1993**, *32*, 164–189.

[148] A. V. Kavaliunas, R. D. Rieke, *J. Am. Chem. Soc.* **1980**, *102*, 5944–5945.

[149] A. V. Kavaliunas, A. Taylor, R. D. Rieke, *Organometallics* **1983**, *2*, 377–383.

[150] K. Jonas, L. Schieferstein, *Angew. Chem.* **1979**, *91*, 590.

[151] K. Jonas, L. Schieferstein, *Angew. Chem. Int. Ed.* **1979**, *18*, 549–550.

[152] K. Jonas, L. Schieferstein, C. Krüger, Y.-H. Tsay, *Angew. Chem.* **1979**, *91*, 590–591.

[153] K. Jonas, L. Schieferstein, C. Krüger, Y.-H. Tsay, *Angew. Chem. Int. Ed.* **1979**, *18*, 550–551.

[154] M. F. Semmelhack in *Organometallics in synthesis*, M. Schlosser (Ed.), John Wiley & Sons, Inc., Chichester, **2002**.

[155] R. M. Heck, R. J. Farrauto, S. T. Gulati, *Catalytic air pollution control: Commercial technology 3rd ed.*, John Wiley, Hoboken, **2009**.

[156] R. Burch, *Catal. Rev.: Sci. Eng.* **2004**, *46*, 271–334.

[157] P. Gabrielsson, H. G. Pedersen in *Handbook of heterogeneous catalysis*, *Vol. 5*, G. Ertl, H. Knözinger, F. Schüth, J. Weitkamp (Eds.), Wiley-VCH, Weinheim, **2008**.

[158] A. König, W. Held, T. Richter, *Top. Catal.* **2004**, *28*, 99–103.

[159] Verband der Automobilindustrie e. V., *AdBlue*, Berlin, **2013**.

[160] S. Roy, A. Baiker, *Chem. Rev.* **2009**, *109*, 4054–4091.

[161] M. Takeuchi, S. Matsumoto, *Top. Catal.* **2004**, *28*, 151–156.

[162] S. Matsumoto, *CatTech* **2000**, *4*, 102–109.

[163] S. Royer, D. Duprez, *ChemCatChem* **2011**, *3*, 24–65.

[164] L. D. Prockop, R. I. Chichkova, *J. Neurol. Sci.* **2007**, *262*, 122–130.

[165] M. Goldstein, *J. Emerg. Nurs.* **2008**, *34*, 538–542.

[166] S. M. El-Sheikh, F. A. Harraz, K. S. Abdel-Halim, *J. Alloys Compd.* **2009**, *487*, 716–723.

[167] A. Biabani-Ravandi, M. Rezaei, *Chem. Eng. J.* **2012**, *184*, 141–146.

[168] K. S. Abdel Halim, M. H. Khedr, M. I. Nasr, A. M. El-Mansy, *Mater. Res. Bull.* **2007**, *42*, 731–741.

[169] S. A. C. Carabineiro, N. Bogdanchikova, P. B. Tavares, J. L. Figueiredo, *RSC Adv.* **2012**, *2*, 2957–2965.

[170] A. A. Herzing, C. J. Kiely, A. F. Carley, P. Landon, G. J. Hutchings, *Science* **2008**, *321*, 1331–1335.

[171] X. Zhang, Z. Qu, F. Yu, Y. Wang, *Chin. J. Catal.* **2013**, *34*, 1277–1290.

[172] G. Águila, F. Gracia, P. Araya, *Appl. Catal., A* **2008**, *343*, 16–24.

[173] H.-H. Perkampus, *UV-Vis spectroscopy and its applications*, Springer, Berlin, Heidelberg, **2012**.

[174] J. Haber, *Pure Appl. Chem.* **1991**, *63*, 1227–1246.

[175] S. Lowell, J. E. Shields, M. A. Thomas, M. Thommes, *Characterization of Porous Solids and Powders: Surface Area, Pore Size and Density*, Springer Netherlands, Dordrecht, **2004**.

[176] S. J. Gregg, K. S. Sing, *Adsorption, surface area and porosity 2nd ed.*, Academic Press, London, **1982**.

[177] J. Rouquerol, D. Avnir, C. W. Fairbridge, D. H. Everett, J. M. Haynes, N. Pernicone, J. D. F. Ramsay, K. S. W. Sing, K. K. Unger, *Pure Appl. Chem.* **1994**, *66*, 1739–1758.

[178] F. Rouquerol, J. Rouquerol, K. S. W. Sing, *Adsorption by powders and porous solids: Principles, methodology, and applications*, Academic Press, San Diego, **1999**.

[179] G. Q. Lu, G. X. S. Zhao (Eds.), *Nanoporous materials: Science and engineering*, Vol. 4 of *Series on chemical engineering*, Imperial College Press, London, **2004**.

[180] A. V. Neimark, K. S. W. Sing, M. Thommes in *Handbook of heterogeneous catalysis*, *Vol. 2*, G. Ertl, H. Knözinger, F. Schüth, J. Weitkamp (Eds.), Wiley-VCH, Weinheim, **2008**.

[181] F. Schüth, K. S. W. Sing, J. Weitkamp (Eds.), *Handbook of porous solids*, Wiley-VCH, Weinheim, **2008**.

[182] K. S. W. Sing, *Pure Appl. Chem.* **1985**, *57*, 603–619.

[183] F. Gomez, R. Denoyel, J. Rouquerol, *Langmuir* **2000**, *16*, 4374–4379.

[184] V. Y. Gusev, *Langmuir* **1994**, *10*, 235–240.

[185] V. Medout-Marere, *J. Colloid Interface Sci.* **2000**, *228*, 434–437.

[186] C. H. Giles, D. Smith, A. Huitson, *J. Colloid Interface Sci.* **1974**, *47*, 755–765.

[187] G. Schay, L. G. Nagy, T. Szekrényesy, *Period. Polytech., Chem. Eng.* **1960**, *4*, 95–117.

[188] S. Brunauer, P. H. Emmett, E. Teller, *J. Am. Chem. Soc.* **1938**, *60*, 309–319.

[189] D. Everett, A. Langdon, P. Maher, *J. Chem. Thermodynamics* **1984**, *16*, 981–992.

[190] B. V. Zhmud, J. Sonnefeld, *J. Chem. Soc., Faraday Trans.* **1995**, *91*, 2965.

[191] A. de Keizer, E. M. van der Ent, L. K. Koopal, *Colloids Surf., A* **1998**, *142*, 303–313.

[192] R. J. Hunter, R. H. Ottewill, R. L. Rowell, *Zeta Potential in Colloid Science: Principles and Applications*, Elsevier Science, Burlington, **2013**.

[193] A. McClellan, H. Harnsberger, *J. Colloid Interface Sci.* **1967**, *23*, 577–599.

[194] Z. Király, I. Dékány, *J. Chem. Soc., Faraday Trans. 1* **1989**, *85*, 3373.

[195] Z. Király, I. Dékány, L. G. Nagy, *Colloids Surf., A* **1993**, *71*, 287–292.

[196] D. Herein in *Handbook of heterogeneous catalysis*, *Vol. 1*, G. Ertl, H. Knözinger, F. Schüth, J. Weitkamp (Eds.), Wiley-VCH, Weinheim, **2008**.

[197] J. K. Cockcroft, A. N. Fitch in *Powder diffraction*, R. E. Dinnebier, S. J. L. Billinge (Eds.), Royal Society of Chemistry, Cambridge, **2009**.

[198] C. Suryanarayana, M. G. Norton, *X-Ray Diffraction: A Practical Approach*, Springer, Boston, MA, **1998**.

[199] V. K. Pecharsky, P. Y. Zavalij, *Fundamentals of Powder Diffraction and Structural Characterization of Materials*, Springer US, Boston, **2009**.

[200] J. W. Niemantsverdriet, *Spectroscopy in catalysis: An introduction*, Wiley-VCH, Weinheim, **1993**.

[201] P. Georgopoulos, J. B. Cohen, *J. Catal.* **1985**, *92*, 211–215.

[202] R. E. Dinnebier, S. J. L. Billinge in *Powder diffraction*, R. E. Dinnebier, S. J. L. Billinge (Eds.), Royal Society of Chemistry, Cambridge, **2009**.

[203] R. E. Dinnebier, S. J. L. Billinge (Eds.), *Powder diffraction: Theory and practice*, Royal Society of Chemistry, Cambridge, **2009**.

[204] P. Canton, C. Meneghini, P. Riello, A. Benedetti in *In-situ spectroscopy of catalysts*, B. M. Weckhuysen (Ed.), American Scientific Publishers, Stevenson Ranch, **2004**.

[205] B. S. Clausen, H. Topsøe, *Catal. Today* **1991**, *9*, 189–196.

[206] H. Jung, W. J. Thomson, *J. Catal.* **1991**, *128*, 218–230.

[207] P. Scherrer, *DGZ Göttingen* **1918**, *2*, 98–100.

[208] L. H. Schwartz, J. B. Cohen, *Diffraction from materials*, of *Materials science and technology*, Academic Press, New York, **1977**.

[209] S. Sashital, *J. Catal.* **1977**, *50*, 479–493.

[210] J. Pielaszek, *J. Catal.* **1983**, *80*, 479–481.

[211] H. M. Rietveld, *Acta Crystallogr.* **1967**, *22*, 151–152.

[212] H. M. Rietveld, *J. Appl. Crystallogr.* **1969**, *2*, 65–71.

[213] R. A. Young (Ed.), *The Rietveld method*, Vol. 5 of *IUCr monographs on crystallography*, Oxford Univ. Press, Oxford, **1993**.

[214] D. C. Koningsberger, B. L. Mojet, G. E. van Dorssen, D. E. Ramaker, *Top. Catal.* **2000**, *10*, 143–155.

[215] G. Bunker, *Introduction to XAFS: A practical guide to X-ray absorption fine structure spectroscopy*, Cambridge University Press, Cambridge, **2010**.

[216] B. K. Teo, *EXAFS: Basic Principles and Data Analysis*, Vol. 9 of *Inorganic chemistry concepts*, Springer, Berlin, **1986**.

[217] G. F. Knoll, *Radiation detection and measurement 4th ed.*, Wiley, Hoboken, NJ, **2010**.

[218] M. Bauer, H. Bertagnolli, *Bunsen-Mag.* **2007**, *9*, 216–231.

[219] T. Yamamoto, *X-Ray Spectrom.* **2008**, *37*, 572–584.

[220] A. Bianconi, L. Incoccia, S. Stipcich (Eds.), *EXAFS and Near Edge Structure: Proceedings of the International Conference Frascati, Italy, September 13-17, 1982*, Vol. 27 of *Springer Series in Chemical Physics*, Springer, Berlin and Heidelberg, **1983**.

[221] D. C. Koningsberger, R. Prins (Eds.), *X-ray absorption: Principles, applications, techniques of EXAFS, SEXAFS and XANES*, Vol. 92 of *A Wiley Interscience publication*, Wiley, New York, **1988**.

[222] M. de Broglie, *Comptes. Rendus.* **1913**, *157*, 924–926.

[223] H. Fricke, *Phys. Rev.* **1920**, *16*, 202–215.

[224] G. Hertz, *Z. Phys.* **1920**, *3*, 19–25.

[225] A. E. Lindh, *Z. Phys.* **1921**, *6*, 303–310.

[226] A. E. Lindh, *Z. Phys.* **1925**, *31*, 210–218.

[227] A. E. Lindh, *Z. Phys.* **1930**, *63*, 106–113.

[228] B. Kievit, G. A. Lindsay, *Phys. Rev.* **1930**, *36*, 648–664.

[229] G. A. Lindsay, *Z. Phys.* **1931**, *71*, 735–738.

[230] D. Coster, J. Veldkamp, *Z. Phys.* **1931**, *70*, 306–316.

[231] D. Coster, J. Veldkamp, *Z. Phys.* **1932**, *74*, 191–208.

[232] W. Kossel, *Z. Phys.* **1920**, *1*, 119–134.

[233] R. de L. Kronig, *Z. Phys.* **1931**, *70*, 317–323.

[234] R. de L. Kronig, *Z. Phys.* **1932**, *75*, 191–210.

[235] R. de L. Kronig, *Z. Phys.* **1932**, *75*, 468–475.

[236] L. V. Azároff, *Rev. Mod. Phys.* **1963**, *35*, 1012–1021.

[237] D. E. Sayers, E. A. Stern, F. W. Lytle, *Phys. Rev. Lett.* **1971**, *27*, 1204–1207.

[238] E. A. Stern, *Phys. Rev. B* **1974**, *10*, 3027–3037.

[239] F. W. Lytle, D. E. Sayers, E. A. Stern, *Phys. Rev. B* **1975**, *11*, 4825–4835.

[240] E. A. Stern, D. E. Sayers, F. W. Lytle, *Phys. Rev. B* **1975**, *11*, 4836–4846.

[241] F. W. Lytle, D. E. Sayers, E. B. Moore, *Appl. Phys. Lett.* **1974**, *24*, 45–47.

[242] J. H. Sinfelt, G. H. Via, F. W. Lytle, *Catal. Rev.: Sci. Eng.* **1984**, *26*, 81–140.

[243] P. Eisenberger, B. M. Kincaid, *Chem. Phys. Lett.* **1975**, *36*, 134–136.

[244] B. M. Kincaid, P. Eisenberger, *Phys. Rev. Lett.* **1975**, *34*, 1361–1364.

[245] H. Winick in *Proceedings of the 1997 Particle Accelerator Conference*, IEEE Operations Center, Piscataway, NJ, **1998**, pp. 37–41.

[246] P. A. Lee, J. B. Pendry, *Phys. Rev. B* **1975**, *11*, 2795–2811.

[247] S. J. Gurman, R. F. Pettifer, *Philos. Mag. B* **1979**, *40*, 345–359.

[248] C. A. Ashley, S. Doniach, *Phys. Rev. B* **1975**, *11*, 1279–1288.

[249] P. L. Lee, F. Boehm, P. Vogel, *Phys. Lett. A* **1977**, *63*, 251–253.

[250] P. A. Lee, B.-K. Teo, A. L. Simons, *J. Am. Chem. Soc.* **1977**, *99*, 3856–3859.

[251] P. A. Lee, G. Beni, *Phys. Rev. B* **1977**, *15*, 2862–2883.

[252] T. M. Hayes, J. B. Boyce in *Solid state physics*, Vol. 37 of *Solid State Physics*, F. Seitz, H. Ehrenreich (Eds.), Academic Press, New York, **1981**, pp. 173–351.

[253] E. A. Stern, *Phys. Rev. B* **1993**, *48*, 9825–9827.

[254] J. S. Walker, G. I. Straguzzi, W. H. Manogue, G. C. Schuit, *J. Catal.* **1988**, *110*, 298–309.

[255] O. H. Laguna, M. A. Centeno, M. Boutonnet, J. A. Odriozola, *Appl. Catal., B* **2011**, *106*, 621–629.

[256] J. G. Carriazo, M. A. Centeno, J. A. Odriozola, S. Moreno, R. Molina, *Appl. Catal., A* **2007**, *317*, 120–128.

[257] A. K. Kandalam, B. Chatterjee, S. N. Khanna, B. K. Rao, P. Jena, B. V. Reddy, *Surf. Sci.* **2007**, *601*, 4873–4880.

[258] M. Tepluchin, M. Casapu, A. Boubnov, H. Lichtenberg, Di Wang, S. Kureti, J.-D. Grunwaldt, *ChemCatChem* **2014**, *6*, 1763–1773.